

JOURNAL OF NUCLEAR MATERIALS

A JOURNAL ON METALLURGY, CERAMICS AND SOLID
STATE PHYSICS IN THE NUCLEAR ENERGY INDUSTRY

EDITORS:

R. W. CAHN - BIRMINGHAM, ENGLAND - J. P. HOWE - CANOGA PARK, U.S.A.
P. LACOMBE - PARIS, FRANCE - S. T. KONOBEEVSKI - MOSCOW, U.S.S.R.

CONTENTS

J. S. O'NEILL, A. W. HEY and D. T. LIVEY, Density and permeability relationships in fabricated beryllia	125
N. A. HILL and J. W. S. JONES, The crystallographic dependence of low load indentation hardness in beryllium	138
D. M. DAVIES and J. W. MARTIN, The effect of inclusions on the fracture of uranium	156
J. PAIDASSI, M. L. POINTUD, R. CAILLAT et R. DARRAS, Contribution à l'étude de l'oxydation de l'uranium dans l'anhydride carbonique aux températures élevées	162
S. J. GREGG, R. J. HUSSEY and W. B. JEPSON, The high temperature oxidation of beryllium. Part III: In carbon dioxide, carbon monoxide and carbon monoxide-carbon dioxide mixtures	175
D. W. AYLMOORE, S. J. GREGG and W. B. JEPSON, The high temperature oxidation of beryllium. Part IV: In water vapour and in moist oxygen	190
J. T. WABER, W. M. OLSON and R. B. ROOF, Jr., Atmospheric corrosion tests of several delta-phase alloys of plutonium	201
J. C. BOKROS, Creep properties of a zirconium-hydrogen uranium alloy	216
P. LELONG, J. DOSDAT, J. BOGHEN et J. HÉRENGUEL, Observations micrographiques sur l'alliage Mg-Zr à 0,6 % en poids, chauffé dans l'hydrogène	222
<i>Letters to the Editors - Lettres aux Rédacteurs</i>	
S. STEEB, Elektronenbeugungs-Untersuchung an einkristallinen Schichten von Uranoxyden im Bereich von UO_2 bis U_4O_9	235
Mme J. BLOCH, Restauration thermique du paramètre de l' UO_2 faiblement irradié	237
A. G. KNAPTON and K. B. C. WEST, The compatibility of beryllium and uranium dioxide	239
L. T. LLOYD, P. LACOMBE, D. CALAIS and Mrs. N. SIMENEL, Temperature dependence of the slip direction for {110} slip in α -uranium	241



EDITORIAL ADVISORY BOARD — CONSEIL DES REDACTEURS

S. AAS (Kjeller, Norway)
 K. F. ALDER (Lucas Heights, Australia)
 P. ALBERT (Vitry, France)
 G. W. ARDLEY (Whetstone, U.K.)
 J. E. BURKE (Schenectady, U.S.A.)
 R. CAILLAT (Saclay, France)
 G. CHAUDRON (Vitry, France)
 H. CHISWIK (Argonne, U.S.A.)
 A. T. CHURCHMAN (Bristol, U.K.)
 A. S. COFFINBERRY (Los Alamos, U.S.A.)
 A. H. COTTELL (Cambridge, U.K.)
 R. L. CUNNINGHAM (Ottawa, Canada)
 C. DECROLY (Bruxelles, Belgium)
 M. D'HONT (Mol, Belgium)
 J. D. FAST (Eindhoven, Netherlands)
 H. M. FINNISTON (Newcastle, U.K.)
 J. FRIEDEL (Paris, France)
 E. GEBHARDT (Stuttgart, Germany)

E. GRISON (Saclay, France)
 B. R. HASIGUTI (Tokyo, Japan)
 J. HERENGUEL (Antony, France)
 L. K. JETTER (Oak Ridge, U.S.A.)
 E. KIESSLING (Stockholm, Sweden)
 K. LÜCKE (Aachen, Germany)
 B. LUSTMAN (Pittsburgh, U.S.A.)
 B. MADDIN (Philadelphia, U.S.A.)
 A. MERLINI (Milan, Italy)
 F. MURRAY (Harwell, U.K.)
 B. MYERS (Sydney, Australia)
 E. C. W. PERRYMAN (Culcheth, U.K.)
 J. A. L. ROBERTSON (Chalk River, Canada)
 J. A. SABATO (Buenos Aires, Argentina)
 K. TANGRI (Bombay, India)
 P. VACHET (Paris, France)
 J. WILLIAMS (Harwell, U.K.)

Papers or letters should be sent to one of the Editors,

R. W. CAHN (Dept. of Metallurgy, University of Birmingham, Birmingham 15, England).
 J. P. HOWE (Atomics International, P.O. Box 309, Canoga Park, California, U.S.A.).
 P. LACOMBE (Centre de Recherches Métallurgiques de l'Ecole des Mines, Blvd. St. Michel 60, Paris VI, France)
 S. T. KONOBEVSKI (U.S.S.R. Academy of Sciences) Leninsky Prospekt 14, Moscow V-71, U.S.S.R.

either directly or through a member of the Editorial Advisory Board.

Papers or letters should be written in English, French or German; papers should have a summary in the appropriate language. Translations of the summary into the two other languages and in Russian will be added by the Editors.

Instructions to contributors will be found in Vol. 1, No. 1 (pp. 111-112).

Books for review should be sent to one of the Editors.

The Journal of Nuclear Materials is published monthly.

The subscription price of a volume of 360 pages is Gld. 68.50 per volume, post-free.

Subscriptions should be sent to the publishers, North-Holland Publishing Company, P.O. Box 103, Amsterdam or to any subscription-agent.

No part of this issue may be reproduced in any form, by print, photoprint, microfilm or any other means without written permission from the publisher. Reprints, photoprints or microfilms are obtainable at cost from the publisher.

Les articles ou les lettres devront être envoyés à un des Rédacteurs-en-chef,

R. W. CAHN (Dept. of Metallurgy, University of Birmingham, Birmingham 15, England).
 J. P. HOWE (Atomics International, P.O. Box 309, Canoga Park, California, U.S.A.).
 P. LACOMBE (Centre de Recherches Métallurgiques de l'Ecole des Mines, 60 Bd. St. Michel, Paris VI, France)
 S. T. KONOBEVSKI (Académie des Sciences de l'U.S.S.R.) Leninsky Prospekt 14, Moscow V-71, U.S.S.R.

ou directement ou par un membre du Conseil des Rédacteurs.

Les articles ou les lettres devront être rédigés en anglais, français ou allemand, les articles avec un résumé dans la langue correspondante. Les traductions du résumé dans les deux autres langues et en russe seront ajoutées par les Rédacteurs-en-chef.

Les instructions aux auteurs se trouvent dans le Vol. 1, No. 2 (pp. 211-212).

Les livres (exemplaires de presse) devront être envoyés à un des Rédacteurs-en-chef.

Le Journal des Matériaux Nucléaires paraîtra tous les mois.

Prix de souscription par volume d'environ 360 pages: Gld. 68.50, franco.

Les abonnements devront être envoyés aux éditeurs, North-Holland Publishing Company, P.O. Box 103, Amsterdam, ou à votre librairie.

DENSITY AND PERMEABILITY RELATIONSHIPS IN FABRICATED BERYLLIA

J. S. O'NEILL, A. W. HEY and D. T. LIVEY

UKAEA Research Group, Metallurgy Division, AERE, Harwell, Didcot, Berks., UK

Received 13 May 1960

The permeability towards various gases of fabricated beryllia, ranging from 80-95 % theoretical density, has been measured. Permeability coefficients, B_0 and K_0 , are calculated from the Carman equation and gas flow through beryllia is compared with that through graphite.

The viscous permeability—density relationship for hot pressed beryllia is shown to be similar to that for metal powder compacts, and rapidly decreases to a negligible value at ≈ 95 % theoretical density.

Information on pore properties (number, size and tortuosity) is obtained from permeability equations. For the specimen examined, the pores are $\approx 1 \mu$ diameter, tortuous and relatively few in number. Comparison is made with graphite, and the pore structure of beryllia is discussed.

A minimum is observed in the plot of permeability coefficient (K) against mean pressure (\bar{p}) and an explanation is given in terms of pore size distribution for this and another type of observed plot.

On a mesuré la perméabilité vis-à-vis de différents gaz de la glucine élaborée ayant des densités variant de 80 à 95 % de la densité théorique. Les coefficients de perméabilité, B_0 et K_0 sont calculés à partir de l'équation de Carman et l'écoulement du gaz à travers la glucine a été comparé à celui à travers le graphite.

La relation entre perméabilité visqueuse et densité pour la glucine comprimée à chaud s'est révélée similaire à celle observée pour les compacts de poudre métallique. La perméabilité tend rapidement vers zéro quand la densité atteint 95 % de la densité théorique.

Les équations de perméabilité donnent des informations sur les propriétés des pores (nombre, grandeur et configuration plus ou moins tourmentée). Pour l'échantillon examiné, les pores ont environ 1μ de dia-

mètre, une forme tortueuse et se trouvent à des concentrations relativement faibles. La comparaison est faite avec le graphite et la structure des pores de la glucine est discutée.

On a observé un minimum dans la courbe de variation du coefficient de perméabilité (K) en fonction de la pression moyenne (\bar{p}). Une explication de cette courbe et d'un autre type de courbe observée est proposée en se basant sur la distribution des dimensions des pores.

Es wurde die Gasdurchlässigkeit von Berylliumoxydkörpern mit einer Dichte zwischen 80 und 95 % des theoretischen Wertes gemessen. Die Permeabilitätskoeffizienten B_0 und K_0 wurden aus der Carman-Gleichung berechnet. Der Gasstrom durch Berylliumoxyd wurde mit dem Gasstrom durch Graphit verglichen.

Für heissgepresste Berylliumoxydkörper besteht demnach eine gleichartige Beziehung zwischen der Durchlässigkeit bei viskoser Gasströmung und der Dichte wie für Metallpulverpresslinge. Die Durchlässigkeit geht gegen null bei 95 % der theoretischen Dichte.

Aus den Gleichungen für die Durchlässigkeit sind Angaben über die Art der Porosität (Zahl, Gestalt und Krümmung der Poren) zu entnehmen. Bei den untersuchten Proben hatten die Poren einen Durchmesser von etwa 1μ , waren gekrümmt und in verhältnismässig geringer Konzentration vorhanden. Es wurden Vergleiche mit Graphit angestellt. Die Porenstruktur von Berylliumoxyd wurde besprochen.

In der Darstellung des Permeabilitätskoeffizienten (K) gegen den mittleren Druck (\bar{p}) wurde ein Minimum festgestellt, das zusammen mit einer anderen Kurvenart mit Hilfe der Verteilung der Porengrösse erklärt wurde.

1. Introduction

Ceramic solids are generally fabricated by powder metallurgy methods, the techniques most commonly used being cold pressing and

sintering or hot pressing. The success of these operations depends on the elimination of the pores existing between, and in, the powder particles and rarely does either method produce

a body of theoretical density. In some cases the remaining porosity may be so small that the body is virtually impermeable to gases, but in others may be great enough for easy transport of gas. In either case, little is known of the pore structure of the body in terms of the number, size and tortuosity of pores, their size distribution, distribution throughout the body and the relative numbers of open and closed pores. Still further, the relative number of open pores which contribute to permeability is not known.

It is now important to know something of these factors because of the general increasing interest in ceramics which are impermeable to gases at high temperatures. In the nuclear field, for example, the pore structure of the ceramic fuel has an important bearing on fission gas behaviour. To elucidate pore structure, no single type of measurement will provide all the required data, and a combined approach involving measurement of permeability, pore size distribution, surface area and microscopic examination will probably provide the most complete answer.

In the work described here, the permeability of fabricated beryllia bodies has been measured, this being undertaken in the first place to provide specific values of permeability at given relative densities. From the data obtained, some information is also deduced regarding the pore structure of the samples studied.

2. Theory

The basic law of permeability theory is that due to Darcy ¹⁾, which states that the rate of flow of fluid through a porous solid is directly proportional to the pressure gradient causing flow. Nutting ²⁾ modified this to include the viscosity of the permeating medium and so obtained a permeability coefficient characteristic of the solid only. The modified law may be written:

$$K_D = \frac{v\eta}{\Delta p} \frac{L}{A} \quad (1)$$

where

K_D = Darcy coefficient of specific permeability.

v = Rate of gas flow (cc/sec) measured at the mean pressure.

η = Viscosity of the permeating fluid (poise).

Δp = Pressure difference across specimen (dynes/cm²).

L = Thickness of specimen (cm).

A = Area of specimen (cm²).

This equation describes the viscous flow of fluid through a porous solid and is valid for a wide range of pore sizes and mean pressures. But for gas flow through porous solids with a small pore diameter, two additional mechanisms contribute to the total gas flow:

1) *Slip flow*, independent of pressure, becomes important when the mean free path of the gas ($\bar{\lambda}$) is an appreciable fraction of the mean pore diameter (\bar{d}).

2) *Knudsen flow*, also independent of pressure, occurs when $\bar{\lambda} \gg \bar{d}$ so that molecules collide only with the walls and not with each other.

Carman ³⁾ proposed an equation to account for viscous and slip contributions to gas flow, as follows:

$$K = \frac{v\bar{p}}{\Delta p} \frac{L}{A} = \frac{B_0}{\eta} \bar{p} + \frac{4}{3} K_0 \sqrt{\frac{8RT}{\pi M}} \quad (2)$$

where

K = Total permeability coefficient (cm²/sec).

Δp = Pressure difference across specimen (dynes/cm²).

\bar{p} = Mean pressure in specimen (dynes/cm²).

B_0 = Permeability coefficient for viscous flow (cm²).

K_0 = Permeability coefficient for slip flow (cm).

R = Gas constant.

T = Absolute temperature.

M = Molecular weight of the permeating gas.

η = Viscosity (poise).

From the slope and intercept of the plot K vs \bar{p} , the coefficients B_0 and K_0 are obtained. When slip flow makes a negligible contribution, the line passes through the origin and $B_0 = K_D$. The equation has been tested experimentally by Carman ⁴⁾ on unconsolidated beds and recently, it has been shown that gas flow through

graphite, with a mean pore diameter of 0.8μ , obeys this equation ⁵).

Under those conditions where Knudsen flow alone is the mechanism of gas transport, the permeability coefficient is given by

$$K = \frac{4}{3} K_0' \sqrt{\frac{8RT}{\pi M}} \quad (3)$$

where K_0' = Permeability coefficient for Knudsen flow (cm).

3. Experimental Method

3.1. MATERIALS

The beryllia specimens, of which particulars are listed in table 1, were supplied in the form of plates $\frac{1}{8}$ " thick. With the exception of specimen 6, these were cut from blocks of beryllia hot pressed at 1650°C from dry powder originally calcined at 1650°C and subsequently treated by grinding and leaching as for the production of slip ⁶). Specimen 6 was prepared by cold pressing and sintering beryllia, which had been calcined to 1400°C for 1 hour, and subsequently mixed with 2 wt % CaO.

The density and porosity figures on all specimens, with the exceptions of A and C, were obtained by the normal volume displacement

method. On A and C, obvious variations in structure occurred across the specimens and the density, measured along any traverse by a β particle absorption method, showed considerable variation. The centre portion of both specimens, however, over which the permeability was measured, was found to be constant in density. Open and closed porosity figures cannot be determined by the β particle absorption method, and owing to the variation in density which exists, the figures obtained by volume displacement are not applicable to the high density area over which permeability was measured; no figures are therefore quoted. All other specimens had a uniform density throughout.

3.2. APPARATUS AND METHOD

While the permeability of most specimens shown in table 1 could be measured on one apparatus (Rig A) the higher density specimens were sufficiently impermeable to require construction of a second more sensitive apparatus (Rig B).

Fig. 1 shows the general arrangement of Rig A, the principle being that the quantity of gas flowing through the specimen of given cross sectional area is measured for fixed pressure

TABLE 1
Density and porosity figures on permeability specimens

Specimen	Density		Total porosity (P_T) (%)	Open porosity (P_o) (%)	$\frac{P_o}{P_T}$ (%)
	(g/cm ³)	(% theoretical)			
1	2.34	77.3	22.7	21.2	93.5
2	2.42	80.0	20.0	19.7	98.5
3	2.44	80.7	19.3	18.5	95.8
4	2.46	81.3	18.7	18.1	97.3
5	2.46	81.3	18.7	17.7	94.6
6	2.58	85.5	14.5	11.3	78.0
7	2.62	86.7	13.3	11.9	89.5
8	2.64	87.3	12.7	12.0	94.0
9	2.67	88.3	11.7	10.1	86.0
10	2.68	88.6	11.4	10.0	87.5
11	2.74	90.6	9.4	6.3	67.0
A	2.79	92.3	7.7	—	—
B	2.81	92.9	7.1	0.19	2.66
C	2.87	95.2	4.8	—	—

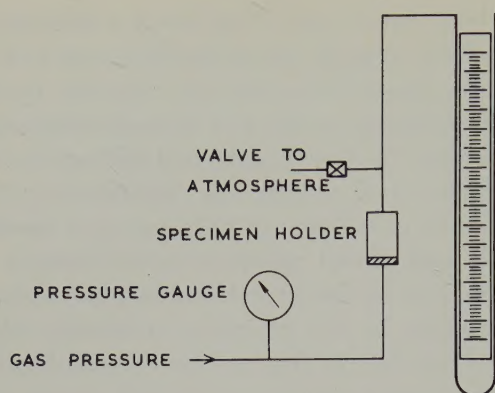


Fig. 1. Permeability apparatus — Rig. A.

drops across the specimen. This was done by allowing gas from the high pressure side to flow into the confined space of a capillary manometer and noting the change in height of the liquid column in the manometer.

The specimen was contained in a holder shown in fig. 2. It was squeezed between two rubber rings, the applied pressure forcing the rubber against the walls of the holder to improve the efficiency of the seal. To retain precise dimensions of the area under test, a short length of steel tubing was inserted in the inner bore of the rubber seal, the face of the tube in contact with the beryllia being tapered to a knife edge. With this arrangement, using a brass plate in the specimen position, no leak was detected up to a maximum pressure of 10 atmospheres (140 psi).

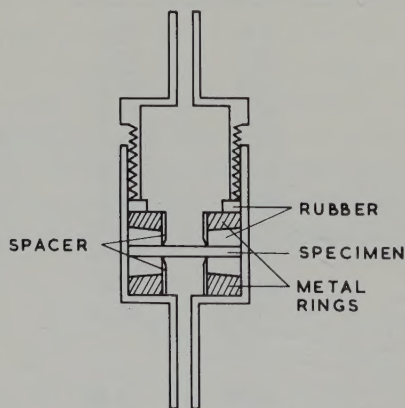


Fig. 2. Specimen holder.

The results obtained on Rig A with specimens 1-11 were of insufficient accuracy and were taken at mean pressures too high to provide information on the slip factor and as the permeability was also too high to permit data to be obtained with Rig B, the data for these specimens are restricted only to the viscous component.

The general arrangement of Rig B is shown in fig. 3. The rate of gas flow through the specimen was measured by observing the rate of pressure increase in a vacuum system of known volume (1380 cc), the specimen being the only appreciably permeable partition between the vacuum and the external pressure. This apparatus was used for specimens A, B and C and had the advantage that the mean pressure range 0.007×10^6 to 2.0×10^6 dynes/cm² could be in-

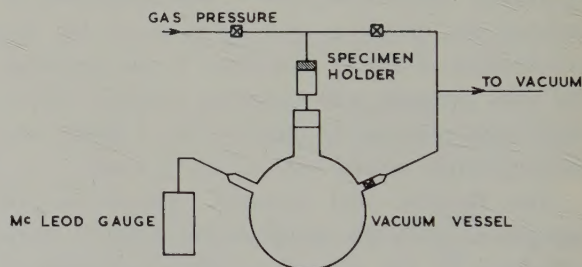


Fig. 3. Permeability apparatus — Rig. B.

vestigated, facilitating estimation of the slip factor. The pressure on the high pressure side could be varied from 10 mm Hg to 4 atmospheres and the vacuum system could be reduced to 10^{-4} mm Hg with observations of pressure increase made up to 10^{-1} mm Hg.

The specimen holder was basically similar to that in Rig A and was fitted to the all-glass vacuum vessel by way of a specially machined steel cone. Changes in vacuum were measured by a McLeod gauge joined permanently to the vacuum vessel.

The experimental procedure used was as follows. The natural leak rate was determined by pumping the system to below 10^{-4} mm Hg for at least 24 hours, isolating the vacuum vessel and, with vacuum on both sides of the specimen, observing the build up of pressure

in the vessel. Pressure build up was then observed with various nitrogen pressures applied to the specimen, pressure increase-time curves drawn and the slope measured after correcting for natural leak. With an impermeable metal blank in place of the specimen, the build up of pressure did not exceed the natural leak rate whatever the applied pressure, thus justifying the procedure described to determine natural leak.

4. Results

4.1. DATA OBTAINED IN RIG A: SPECIMENS 1-11

Details of typical results are shown in table 2 for specimen 9, and fig. 4 shows the data for all specimens 1 to 11.

4.2. DATA OBTAINED ON RIG B

Plots of K against \bar{p} for specimens A and C are shown in figs. 5 and 6 and values of B_0 and K_0 listed in table 4. Data on specimen C were difficult to obtain owing to the high density and a horizontal intercept is assumed at low pressure (shown dotted); the value of K_0 is therefore uncertain.

The permeability of specimen B was measured with various gases and a detailed examination with nitrogen gave the permeability curve in

fig. 7. This shows a minimum at low pressure and as far as is known is only the second record of a minimum in the permeability plot for a consolidated ceramic; minima for ceramics of higher porosity have been noted recently⁷).

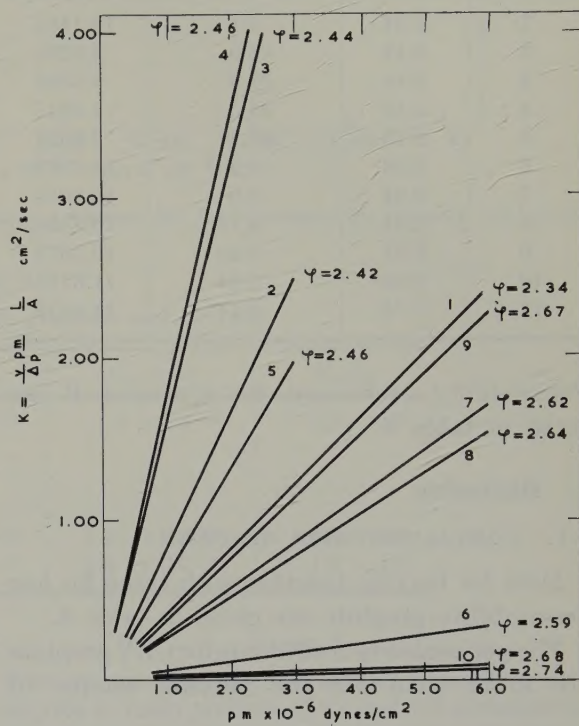


Fig. 4. Permeability — Mean Pressure Curves for Specimens 1-11.

TABLE 2

Permeability data on specimen 9 (density = 2.67 g/cc)

Length L (cm)	Area A (cm ²)	Δp	\bar{p}	Vol. N ₂ collected (cc)	Time (sec)	q_m (cc/sec)	$K = \frac{q_m \bar{p} L}{\Delta p A}$ (cm ² /sec)
		(dynes/cm ² × 10 ⁻⁶)					
0.334	0.316	0.207	1.121	3.92	53.0	0.067	0.383
		0.346	1.191	3.92	27.0	0.124	0.450
		0.484	1.260	3.92	18.3	0.173	0.465
		0.622	1.329	3.92	13.7	0.220	0.496
		0.761	1.398	3.92	10.7	0.267	0.512
		0.896	1.466	3.92	8.5	0.320	0.551
		1.035	1.535	3.92	6.8	0.383	0.600
		1.175	1.605	3.92	5.8	0.429	0.620
		1.312	1.614	3.92	5.0	0.476	0.642
		1.451	1.743	3.92	4.2	0.545	0.690
		1.590	1.813	3.92	3.9	0.564	0.678

From fig. 4, the permeability coefficients shown in table 3 were obtained.

TABLE 3
Permeability coefficients for specimens 1-11

Specimen	Density	Viscous flow coefficient B_0 ($\text{cm}^2 \times 10^{11}$)	$-\text{Log}_{10} B_0$
1	2.34	7.1	10.1487
2	2.42	15.0	9.8239
3	2.44	28.6	9.5436
4	2.46	31.3	9.5045
5	2.46	10.1	9.9957
6	2.58	0.93	11.0315
7	2.62	5.0	10.3010
8	2.64	4.15	10.3820
9	2.67	6.80	10.1675
10	2.68	0.21	11.6778
11	2.74	0.14	11.8539

Permeability coefficients for specimen B are listed in table 5.

5. Discussion

5.1. COMPARISON WITH GRAPHITE

Data for beryllia together with those for low permeability graphite are given in table 6.

The permeability coefficients for CEY graphite are lower than for the beryllia sample of

density 2.81 g/cc. Strict comparison of the materials however can only be made on the basis of actual gas flow through standard specimens under given conditions since the quantity of gas which flows by the viscous mechanism varies with pressure. The ratio of

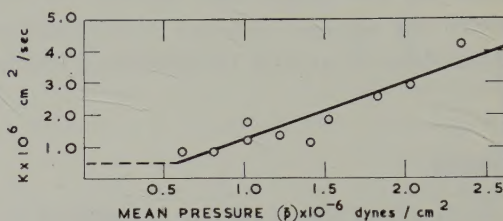


Fig. 6. Plot of permeability coefficient (K) against mean pressure (\bar{p}) for specimen C, density 2.87 g/cc.

TABLE 5
Permeability coefficients for specimen B with various gases

Gas	$B_0 \times 10^{15}$ (cm^2)	$K_0 \times 10^{10}$ (cm)
N ₂	2.03	1.27
CO ₂	2.02	1.29
H ₂	2.16	1.23
He	2.13	1.29

TABLE 4
Permeability coefficients for specimens A and C

Specimen	Density (g/cc)	Viscous flow coefficient B_0 (cm^2)	Slip flow coefficient K_0 (cm)	$-\text{Log}_{10} B_0$
A	2.79	5.2×10^{-15}	1.30×10^{-10}	14.2840
C	2.87	3.2×10^{-17}	(5.95×10^{-12})	16.4949

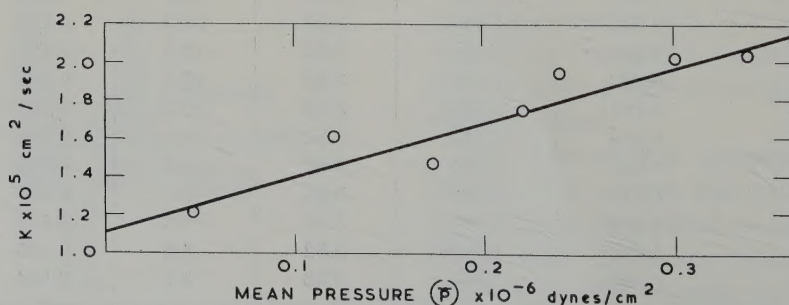


Fig. 5. Plot of permeability coefficient (K) against mean pressure (\bar{p}) for specimen A, density 2.79 g/cc.

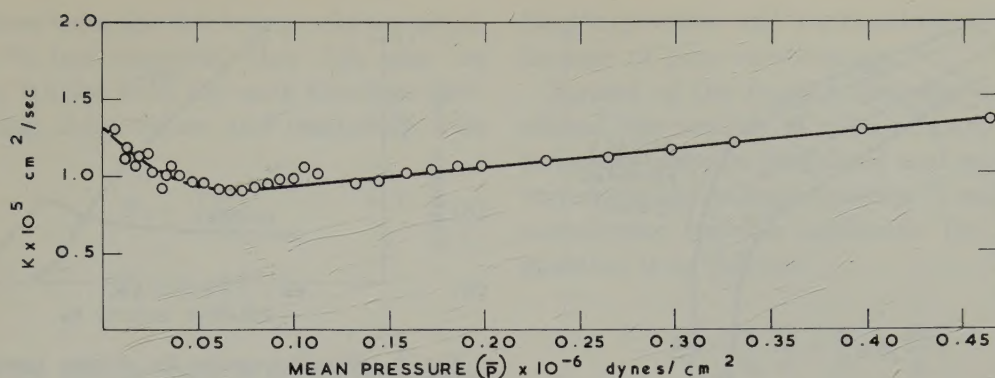


Fig. 7. Plot of permeability coefficient (K) against mean pressure (\bar{p}) for specimen B, density 2.81 g/cc.

TABLE 6

Permeability coefficients for graphite and beryllia

Material	B_0 (cm ²)	K_0 (cm)	K_0/B_0
Natl. Carbon Co. ⁸) CEY Extruded Graphite, ⊥ Extrusion Direction	$< 6.2 \times 10^{-18}$	3×10^{-11}	$> 0.5 \times 10^7$
Beryllia 2.81 g/cc	2.08×10^{-15}	1.27×10^{-10}	0.6×10^5
Beryllia 2.87 g/cc	3.2×10^{-17}	(5.9×10^{-12})	1.8×10^5

K_0/B_0 indicates the relative significance of slip and viscous flow, and therefore of the effect of pressure on the transport of gas. Because of the high ratio for CEY graphite, pressure variation has a minor influence on gas flow unless very high pressures are used, but with the BeO samples pressure variation is more significant. The specimen of density 2.81 g/cc will always transmit more gas than the CEY graphite, but at low pressure the ratio of gas flow will reach its limiting minimum value of $K_0(\text{BeO})/K_0(\text{CEY}) \approx 4$. With the higher density BeO sample, gas transport relative to the CEY graphite will be above unity at high pressure but fall below this as the pressure is reduced. Comparison of the gas flow at two values of mean pressure is made in table 7, taking B_0 for CEY graphite to be 10^{-18} cm².

5.2. PERMEABILITY-DENSITY RELATIONSHIP AND POROSITY

Open porosity may be subdivided into "blind" porosity and "through" porosity, the

TABLE 7

Flow of nitrogen gas through CEY graphite and beryllia at mean pressure of 0.5 and 9.5 atmospheres

Material	Ratio $\frac{\text{Gas flow through beryllia}}{\text{Gas flow through graphite}}$	
	Mean pressure 0.5×10^6 dynes/cm ²	Mean pressure 9.5×10^6 dynes/cm ²
Beryllia 2.81 g/cc	≈ 7	≈ 60
Beryllia 2.87 g/cc	≈ 0.25	≈ 1.0

blind pores being connected to one surface only of the specimen and the through pores to two or more surfaces; only the through pores contribute to permeability.

The viscous flow coefficients in tables 3 and 4 are plotted in fig. 8 and show considerable scatter. This is to be expected in view of the complexity of the factors influencing permeability, and is not an unusual feature of permeability data. A pronounced deflection shows up at 90 %–92 % theoretical density above which the

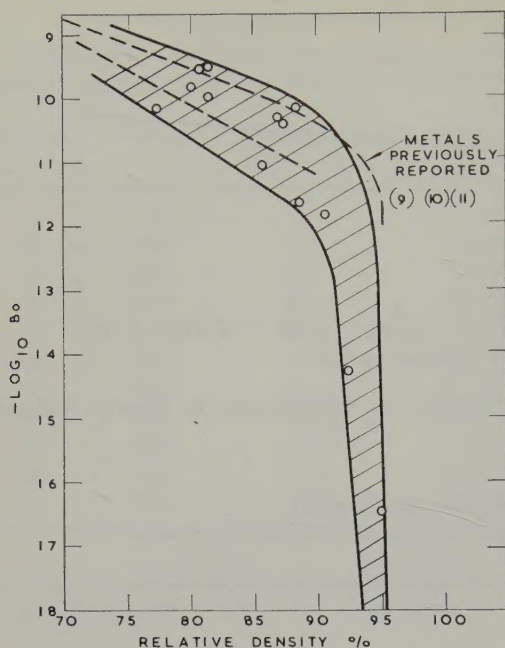


Fig. 8. Viscous permeability-density relationship for BeO with superimposed results for metals as reported in references ⁹, ¹⁰ and ¹¹).

permeability is a very sensitive function of density. The results agree well with those of Arthur ^{9,10,11}) on metal powder compacts, also plotted in fig. 8, but are extended to higher relative density at which the permeability is much lower.

It is clear that the viscous permeability coefficient tends to a negligible value at $\approx 95\%$ theoretical density and no gas flow could be detected on the apparatus with a sample of 96.5% theoretical density. It may be inferred therefore that the through porosity is zero above a relative density of $\approx 95\%$. This is in agreement with data on metal powder compacts ^{9,10,11}) which indicate the disappearance of open pores at $\approx 95-97\%$ theoretical density.

Data on the porosities of UO_2 compacts ¹²) also agree with the metal powder data on this point. From the permeability figures given here, and from the data on UO_2 and on hot compacted and sintered metal compacts, it seems conclusive that the porosity curves for both metals and ceramics are similar and approximate in general to that shown in fig. 9. Within the accuracy of

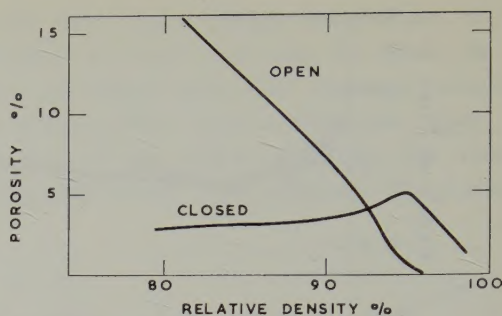


Fig. 9. Porosity curves for powder compacts.

the methods of measurement, these curves apply to both sintered and hot pressed materials.

It cannot be decided from any of the reported data at which point even the smallest pores, allowing only Knudsen flow, are eliminated; it is quite possible that they exist even above 97% theoretical density.

5.3. PORE PROPERTIES

Data on the pore properties can be obtained from eq. (4) below, which is a development of the Carman-Arnell equation ¹³) for viscous and slip flow in unconsolidated beds with uniform pore texture.

$$K = \frac{\varepsilon m^2}{k_0 q^2 \eta} \bar{p} + \frac{4}{3} \frac{\delta}{k_1} \frac{\varepsilon}{q^2} m \bar{v} \quad (4)$$

where

ε = "Through" porosity (cm^3/cm^3)

m = Mean hydraulic radius (cm) = $(\frac{1}{4} \times \text{Pore diameter}, \frac{1}{4} \bar{d})$

k_0 = Shape factor for viscous flow through non-circular capillaries

q = Tortuosity L_e/L where L_e = average actual path length through the porous solid and L = length of specimen

k_1 = Shape factor for slip and Knudsen flow in non-circular capillaries

δ = Constant which has values

$\delta_0 = 1$ for Knudsen flow and

$\delta_1 = 0.6-0.9$ for slip flow.

$$\bar{v} = \sqrt{\frac{8RT}{\pi M}}$$

The value of k_0 seems to vary from 2.0-2.5 ¹⁴) although higher values have been reported ¹⁵),

but in most cases $k_0 = 2.5$ is generally accepted. Carman¹⁶⁾ has suggested that δ/k_1 may be taken as 0.8 for both slip and Knudsen flow.

Inserting these values and comparing with eq. (2)

$$B_0 = \frac{\varepsilon m^2}{2.5 q^2}, \quad (5)$$

$$K_0 = 0.8 \frac{\varepsilon m}{q} \quad (6)$$

From the data in table 5 for various gases, a mean hydraulic radius of 0.33μ and a tortuosity $q = 20$ is calculated.

The mean hydraulic radius (0.33μ) corresponds to a mean pore size of 1.3μ and the tortuosity value is the highest which has been noted. There is confirmatory evidence to indicate that this pore size is of the correct order. Although a pore size distribution experiment could not be carried out because of the specimen size, experiments on another specimen of the same density gave the results shown in fig. 10. This shows the average pore entrance diameter to be of the order of 1μ .

No data have previously been reported on a material of such high relative density and on that account the very high tortuosity is not unexpected. This is not to be taken literally however as meaning an increase in the actual path length of ≈ 20 times the specimen length as it also includes loss of pressure head due to

local expansion and contractions of the gas because of pore constrictions.

Instead of the fraction of pores being considered, the number of pores of given size and tortuosity may be considered and eq. (4) converted into the Adzumi equation¹⁷⁾, modified for non-circular, tortuous capillaries. The resulting equation is as follows:

$$K = \frac{\pi \bar{p}}{10\eta} \frac{E_0}{q} + \frac{2}{3} \pi \delta_1 \frac{F_0}{q} \bar{v} \quad (7)$$

where $E_0 = nr^4$ and $F_0 = nr^3$, n being the number of capillaries per cm^2 of cross section and r , the mean capillary radius. It may be deduced that

$$r = \frac{E_0}{F_0} \quad \text{and} \quad n = \frac{(F_0)^4}{(E_0)^3}$$

From the data for specimen B in table 5, values of r and n are calculated as 0.655μ and 7.200 respectively. Two points may be noted with regard to these values:

(1) For CEY graphite, the respective values are $r < 0.0083 \mu$ and $n \simeq 11 \times 10^8$. There is therefore a great difference in pore structure between the two materials, flow through the graphite taking place in a very large number of very small pores – hence the predominance of slip flow in the graphite.

(2) The number of through pores in the beryllia is relatively small – on a linear basis, one pore every 117 microns. This is a much greater distance than the grain diameter ($\approx 20 \mu$). This result was confirmed only to the extent that micro-examination showed the distribution of pores to be non-uniform. Tests on other specimens, by mercury porosimetry, have also shown a marked non-uniformity of pore distribution in hot pressed beryllia. These observations suggest that the permeability is due to small volumes of the specimen with a density lower than that calculated for the bulk specimen. Such a pore structure could form by local internal shrinkage in the early stages of the fabrication process, as has been suggested for sintered beryllia¹⁸⁾.

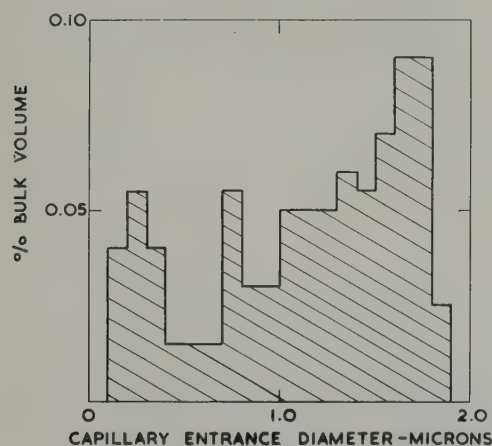


Fig. 10. Pore size distribution for hot pressed beryllia, density 2.81 g/cc.

5.4. OCCURRENCE OF A MINIMUM IN THE PERMEABILITY PLOT

As the mean free path of the permeating gas increases and becomes greater than the mean pore diameter, viscous and slip flow give way to Knudsen flow. With long single capillaries a minimum has been noted ⁴⁾ in the permeability plot in the region where Knudsen flow becomes predominant, as in fig. 11a and this has been accounted for on the basis of greater efficiency of the Knudsen process. Thus for slip flow:

$$K = \frac{1}{3} \delta_1 d_e \bar{v} \quad (8)$$

where δ_1 is a constant for a given system but has values ranging from 0.6–0.9. For Knudsen flow:

$$K = \frac{1}{3} \delta_0 d_e \bar{v} \quad (9)$$

where $\delta_0 = 1$. Between these limits δ varies with pressure and thus gives rise to a minimum in the permeability plot with K having the limiting value for Knudsen flow at zero pressure.

For gas flow in porous media, Pollard and Present ¹⁹⁾ have predicted that a minimum will not be observed, since in these materials the “capillaries” will be made up of short straight sections whose length is such that mean free paths much greater than the pore diameter will not exist. However, this work, and work recently published ⁷⁾ show that in ceramics and graphite a minimum may be observed, and that in the same materials, but not the same specimen, a horizontal portion sometimes shows up rather than the minimum ⁷⁾. This suggests that in these media the “capillaries” are sufficiently long for the Knudsen effect to be noted, and it seems not unreasonable to take a grain diameter for this length. For specimen B, the grain diameter is $\approx 20 \mu$ and l/d_e is therefore ≈ 20 where l is the capillary length and d_e is the diameter.

To account for a minimum in some cases and a horizontal portion in others, it seems likely, as already suggested ⁷⁾, that pore size distribution may have some influence. It is the purpose of this last section to show how this may arise on the basis of the explanation given above for the minimum in single capillaries.

The Adzumi equation may be generalised as follows for a pore size distribution.

$$K = \frac{\pi}{10\eta q} (n_1 r_1^4 + n_2 r_2^4 + \dots) \bar{p} + \left. \begin{aligned} &+ \frac{2\pi\delta_1}{3q} \bar{v} (n_1 r_1^3 + n_2 r_2^3 + \dots) \end{aligned} \right\} \quad (10)$$

where n_1 is the number of pores of tortuosity q and radius r_1 etc. per cm^2 . For the Knudsen range, the expression is

$$K = \frac{2\pi\delta_0}{3qk_1} \bar{v} (n_1 r_1^3 + n_2 r_2^3 + \dots) \quad (11)$$

where k_1 is the shape factor for Knudsen flow through non-circular capillaries. The Knudsen expression is identical to the slip flow expression in eq. (10) but for the substitution of δ_0/k_1 for δ_1 . The Knudsen coefficient will therefore be the greater if $\delta_0/k_1 > \delta_1$. As already noted $\delta_0 = 1$ and $\delta_1 = 0.6$ – 0.9 but the value of k_1 is somewhat indeterminate ²⁰⁾. Knudsen has suggested a general formula for flow in short capillaries and this appears to give reasonable correlation with existing data ²⁰⁾.

$$k_1 = 1 + \frac{16}{3} \frac{m}{l}. \quad (12)$$

For specimen B, taking $l = 20 \mu$ and $m = 0.35 \mu$, as previously calculated, this gives $k_1 = 1.094$ and therefore if $\delta_1 < 0.9$, the Knudsen coefficient, will be greater than the slip coefficient.

Assuming that this condition is fulfilled, then if the pore size distribution is wide, successive ranges of pores will come into the Knudsen range as measurements are taken at decreasing values of mean pressure and a minimum will show up on the permeability plot, as in fig. 11a. Alternatively if the pore size distribution is narrow, or the pores all of one size, and measure-

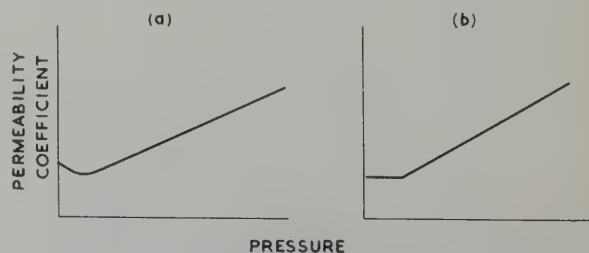


Fig. 11. Observed types of permeability plot.

ments are taken at increments of mean pressure such that at one pressure, no Knudsen flow is occurring while at the next (lower) pressure, Knudsen flow is occurring in all pores, then a horizontal plot, fig. 11b, results. If of course there is a negligible difference between δ_1 and δ_0/k_1 , a horizontal plot will result, irrespective of pore size distribution.

To test this explanation a calculation has been made of the permeability of the pore system shown in fig. 10. These data were taken on a specimen of the same density as specimen B, the permeability curve for which is given in fig. 7. For the calculation it is assumed that $\delta_1=0.6$, $k_1=1.094$, that Knudsen flow occurs when the mean free path of the gas becomes greater than the mean pore diameter and that the tortuosity $q=20$, as calculated for specimen B. This gives the permeability coefficients for the flow of nitrogen gas at 20° C as follows.

$$K_{\text{viscous}} = 0.88 \times 10^2 (n_1 r_1^4 + n_2 r_2^4 + \dots) \bar{p} \quad (13)$$

$$K_{\text{slip}} = 2.96 \times 10^3 (n_1 r_1^3 + n_2 r_2^3 + \dots) \quad (14)$$

$$K_{\text{Knudsen}} = 4.50 \times 10^3 (n_1 r_1^3 + n_2 r_2^3 + \dots). \quad (15)$$

The pore distribution of fig. 10 obtained by mercury porosimetry strictly refers to the pore entrance diameter but gives no information about the uniformity or otherwise of the pore diameter. However, for the purpose of the calculation made here, it is assumed that the data actually represent the diameters of uniform, though tortuous, pores passing through the specimen. The calculated numbers of pores

TABLE 8

Calculated numbers of pores for pore distribution of fig. 10

Size range (μ)	No. of pores per cm^2	No. of pores for permeability
0.1-0.2	63 630	21 210
0.2-0.3	25 620	8 540
0.3-0.4	10 500	3 500
0.4-0.5	3 822	1 274
0.5-0.6	2 646	882
0.6-0.7	1 218	406
0.7-0.8	5 460	1 820
0.8-0.9	2 342	781
0.9-1.0	1 911	637
1.0-1.1	2 625	878
1.1-1.2	2 215	738
1.2-1.3	1 890	630
1.3-1.4	1 943	647
1.4-1.5	1 554	518
1.5-1.6	1 732	577
1.6-1.7	1 984	661
1.7-1.8	1 764	588
1.8-1.9	441	147
Total	133 297	44 434

for different size ranges are shown in table 8. It is further assumed that the specimen is uniform with regard to its pore structure. i.e. there are equal numbers of pores of the same size passing through the specimen in any direction. Undoubtedly this assumption cannot be correct as the method of fabrication could lead to preferred alignment of pores and the non-uniformity of pore distribution quoted earlier is further evidence against it. Nevertheless, in the absence of detailed knowledge of

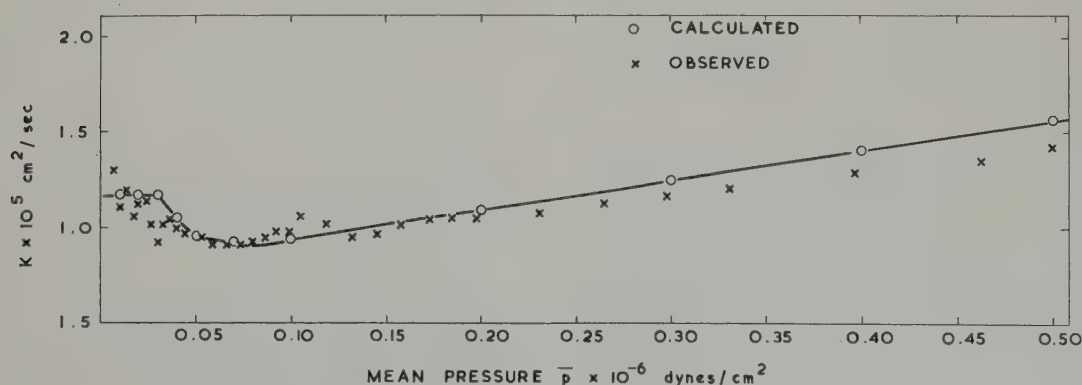


Fig. 12. Comparison of calculated and observed permeabilities for beryllia of density 2.81 g/cc.

pore density in different directions it is assumed that $\frac{1}{3}$ of the total pores contributes to permeability in one direction.

The calculated permeability curve from the above data is compared with the experimental one for specimen B in fig. 12 and shows good agreement. There is, however, a major discrepancy between the number of pores quoted in table 8, 44434, and the number calculated from the permeability data for specimen B, 7200. Permeability data however, are weighted in favour of the larger pores since these carry most of the gas. Thus, in table 8 the pores up to 0.6μ (35406) contribute only $\approx 3\%$ to the total gas flow. The larger pores, 9028 in number, account for the rest of the gas, and this number is in much better agreement with that calculated from the measured permeability. An alternative explanation of the discrepancy in pore numbers lies in the fact that mercury porosimetry measures pores connected only to one surface of the specimen as well as those which go through the specimen and the large majority of those noted in table 8 could belong to that category.

6. Conclusions

1. The permeability coefficients B_0 and K_0 for a hot pressed beryllia specimen of density 2.81 g/cc have been found to have the values $2.08 \times 10^{-15} \text{ cm}^2$ and $1.27 \times 10^{-10} \text{ cm}$ respectively. This gives gas flow rates higher than the best published data on graphite (CEY graphite). A higher density beryllia specimen (2.87 g/cc) was found to be comparable with CEY graphite in this respect. It is not expected that the permeability coefficients quoted here will apply to all beryllia of the same density, since grain size and method of fabrication are likely to have some influence.

2. The viscous permeability coefficient-density relationship has been shown to be similar to that for metal powder compacts over a limited range of density, and the coefficient tends to a negligible value at $\approx 95\%$ theoretical density. From data on metal powders, sintered UO_2 and hot pressed beryllia, it is concluded that the open porosity becomes zero at approx-

imately 95–97 % theoretical density as a general feature of bodies fabricated from powder.

3. The mean pore size calculated from permeability data for a specimen of density 2.81 g/cc is $\approx 1.3 \mu$, in reasonable agreement with porosimetry data taken on a different specimen of the same density. The concentration of through pores is calculated as 7200/cm² which compares with a low permeability graphite (CEY) having $\approx 11 \times 10^8$ pores/cm² of diameter $< 0.01 \mu$.

4. The permeability data and other evidence indicate that hot pressed beryllia shows local and considerable variations in density, so that a specimen of given density is composed of several regions of different density. This explains the relatively small concentration of pores.

5. A minimum has been noted at low pressure in the permeability plot K vs \bar{p} for a specimen of density 2.81 g/cc and an explanation has been put forward for this and another type of observed plot on the basis of pore size distribution.

Acknowledgments

The authors wish to express their thanks to Mr. I. Holland, Murex Ltd., Milford Haven, for supplying the specimens and to Mr. F. Dell, AERE, for the data on which fig. 10 is based. They also express their appreciation of the helpful advice given by Mr. J. Williams and Dr. P. Murray.

References

- 1) H. P. G. Darcy, Les Fontaines Publiques de la Ville de Dijon (Victor Dalmont, Paris, 1856)
- 2) P. G. Nutting, Bull. Am. Ass. Petrol. Geol. **14** (1934) 1337
- 3) P. C. Carman, Flow of Gases Through Porous Media (Butterworth Scientific Publications, London, 1956) Ch. III, p. 69
- 4) P. C. Carman, Proc. Roy. Soc. A **203** (1950) 55
- 5) J. M. Hutcheon, B. Longstaff and R. K. Warner, UKAEA (Harwell) Report, AERE CE/R 2335 (1957)
- 6) I. Holland and D. T. Livey, UKAEA (Harwell) Report AERE M/R 2850 (1959)
- 7) D. M. Grove and M. G. Ford, Nature **182** (1958) 999

- 8) S. D. Holdsworth, M. S. T. Price and F. Roberts, UKAEA (Harwell) Report, AERE CE/M 254 (1959)
- 9) G. Arthur, UKAEA (Harwell) Report, AERE M/R 1454 (1954)
- 10) G. Arthur, UKAEA (Harwell) Report, AERE M/R 1638 (1955)
- 11) G. Arthur, UKAEA (Harwell) Report, AERE M/R 1836 (1955)
- 12) J. Belle and B. Lustman, Westinghouse Atomic Power Div. (USA) Report, WAPD 184 (1957)
- 13) P. C. Carman and J. C. Arnell, Canad. J. Research A 26 (1948) 128
- 14) P. C. Carman, Flow of Gas Through Porous Media. (Butterworth Scientific Publications, London, 1956) Ch. I, p. 12
- 15) M. R. Wyllie and M. B. Spangler, Bull. Amer. Assoc. of Petroleum Geologists 36 (1943) 359
- 16) P. C. Carman, Flow of Gases Through Porous Media. (Butterworth Scientific Publications, London, 1956) Ch. III, p. 77
- 17) H. Adzumi, Bull. Chem. Soc. Japan 12 (1937) 304
- 18) D. T. Livey, N. Brett, I. Denton and P. Murray, UKAEA (Harwell) Report, AERE M/R 2794 (1959)
- 19) W. G. Pollard and R. D. Present, Phys. Rev. 73 (1948) 762
- 20) P. C. Carman, Flow of Gases Through Porous Media. (Butterworth Scientific Publications, London, 1956) Ch. III, p. 67

THE CRYSTALLOGRAPHIC DEPENDENCE OF LOW LOAD INDENTATION HARDNESS IN BERYLLIUM

N. A. HILL and J. W. S. JONES

UKAEA, Research Group: Metallurgy Division, Atomic Energy Research Establishment, Harwell, Didcot, Berks., UK

Received 28 June 1960

Low load indentation hardness measurements on beryllium are markedly dependent on orientation and surface condition. Machining produces a uniform surface layer with a hardness of 300 DPN on both single and polycrystalline beryllium. Removal by etching of 0.02 cm (0.008 in.) of surface reveals the marked crystallographic dependence viz 230 DPN on the basal plane and 70 DPN on prism plane for a single crystal, and 300-170 DPN depending on the angle of testing relative to the surface for highly oriented sheet. These variations can be related to the operative deformation mechanisms in a single crystal and the preferred orientation in the sheet. Similar, but less marked effects are found in less highly oriented sheet, tube and rod; in all cases the maximum hardness corresponds to the greatest concentration of basal planes.

Rotation of the diamond indenter in the basal plane of a single crystal gives no variation in hardness, but in both first and second order prism planes, there is a distinct variation which can be related to the beryllium crystal structure.

L'orientation et l'état de surface du béryllium influencent fortement les mesures de dureté sous faible charge. L'usinage donne une couche superficielle uniforme d'une dureté de 300 DPN, sur les monocristaux comme sur les polycristaux de béryllium. Si par attaque, on enlève 0,2 mm, on constate l'influence de la structure cristalline: l'on mesure 230 DPN sur le plan de base et 70 DPN sur le plan prismatique pour un monocristal et 300-170 DPN selon l'angle d'essai par rapport à la surface pour une tôle fortement orientée. Ces variations peuvent être reliées aux mécanismes de déformation opérant dans un monocristal et à l'orientation préférentielle dans la tôle. De même, dans des tôles fortement orientées, dans des

tubes et des barres, on a pu observer des effets similaires, quoique moins marqués. Dans tout les cas, la dureté maximale, correspond à la plus grande concentration de plans de base dans la texture.

La rotation du pénétrateur en diamant dans le plan de base d'un monocristal ne donne aucune variation dans la dureté, mais à la fois dans les plans du prisme de premier et de second ordre, il y a une variation distincte qu'on peut relier à la structure cristalline du béryllium.

Ergebnisse von Kleinlasthärtemessungen an Beryllium werden in ausgeprägtem Maße von der Kristallorientierung und dem Oberflächenzustand beeinflusst. Durch spanabhebende Bearbeitung wird auf Einkristallen und Vielkristallen eine Oberflächenschicht einheitlicher Vickershärte von 300 DPN erzeugt. Nach Abätzen einer 0,02 cm dicken Oberflächenschicht tritt die ausgeprägte Orientierungsabhängigkeit auf. So werden an Einkristallen auf der Basisfläche 230, auf einer Prismenfläche 70 DPN festgestellt, während bei stark texturhaltigem Blech je nach Größe des mit der Oberfläche eingeschlossenen Winkels Werte zwischen 300 und 170 DPN zu finden sind. Diese Unterschiede lassen sich mit dem wirksamen Verformungsmechanismus eines Einkristalls und mit der vorhandenen Kristallorientierung des Bleches in Zusammenhang bringen. Ähnliche, weniger deutliche Effekte wurden in schwächer texturhaltigen Blechen, Rohren und Stäben gefunden. Dabei ergaben sich stets die größten Härtewerte, wenn von der Messung die meisten Basisebenen erfasst wurden.

Eine Rotation des Diamant-Prüfkörpers in der Basisebene von Einkristallen bringt keine Änderung der Härtewerte. Dagegen ergibt sich in den Prismenflächen eine eindeutige Abhängigkeit, die mit der Struktur des Berylliums zu erklären ist.

1. Introduction

Beryllium single crystals have markedly anisotropic plastic properties¹⁾ and those of highly oriented polycrystalline beryllium are

also markedly dependent upon the direction of testing^{2, 3)}. Indentation hardness values have previously been reported¹⁾ for beryllium single crystals and extruded rods. In a single crystal

the basal plane was harder than the prism plane, and in an extruded rod, indentation parallel to the direction of extrusion (i.e. indentation into a concentration of prism planes) gave a lower hardness value than indentation at right angles to it (i.e. into a concentration of basal planes).

A detailed survey of the variation in low load indentation hardness values with direction of indentation for a single crystal and for sheet, rod and tube beryllium of known textures and varying surface condition is described in the following sections.

2. Experimental method

A Tukon automatic hardness tester which applies loads from 50 g up to 3 kg for a constant time of 15 sec was used throughout the investigations to be described. Preliminary experiments showed that there was a sharp rise in the scatter of results when the load was reduced below 200 g, so this load was used for the majority of tests. A similar limiting load for consistent results has been reported⁴⁾ for other metals. Using a load of 200 g, the automatic application of the load for a time of 15 sec was found to be adequate for attainment of equilibrium. Longer times of application (up to 1 hour) gave no measurable increase in the size of the impression.

A Knoop⁵⁾ diamond indenter, which gives an indent with the outline of a parallelogram in which the longer diagonal is approximately seven times the length of the shorter one, was used. The hardness values were obtained from measurements of the long diagonals. The results obtained were in every case the mean of five indentations obtained under identical conditions.

Cylindrical specimens were used in the investigation of the variation of hardness with the plane of indentation. The cylinders, approximately 2.5 cm long by 0.38 cm diameter, were machined on a jeweller's lathe and polished by rotation in contact with strips of emery paper soaked in paraffin, followed by a final light electropolish. The longer diagonal of the indenter was aligned parallel to the axis of the cylindrical specimen which was held in position in a Vee

groove in a steel block. Flat specimens, ground to expose the required surface, and polished on a normal series of metallographic emery papers soaked in paraffin were used to study variation of hardness with direction of test in a single plane; a brief electropolish was necessary to obtain a suitably flat surface to give "as machined" hardness values. To investigate the effect of surface condition, further electrolytic polishing was carried out on all the specimens. An electrolyte containing 40 % glycerol, 35 % orthophosphoric acid and 25 % sulphuric acid, which had been previously saturated with beryllium using a current density of 0.3 amps/cm², gave a bright smooth surface without pitting even after removal of 250 μ of metal.

A cylinder was machined from a single crystal (supplied by AWRE Aldermaston) with its axis parallel to a $[10\bar{1}0]$ direction. Hardness values were obtained at intervals of 10° round the circumference of the cylinder, firstly in the as-machined and polished condition and subsequently after removal of successive surface layers approximately 25 μ thick until a total of 250 μ of metal had been removed by electrolytic etching. The location of the (0001) basal plane was checked by Laue X-ray reflection photographs. The amount of asterism in these photographs also gave an indication of the amount of work hardening in the cylinder.

Flat specimens were ground from the single crystal with surfaces parallel to the (0001) basal plane and to $(10\bar{1}0)$ and $(11\bar{2}0)$ prism planes, to determine hardness variations with the direction of test in these planes, both as-polished and after removal of 250 μ of metal from the surface. The macro-hardness of the basal and prism planes was also determined using a load of 2 kg.

Cylinders were machined from sintered bar (provided by the UKAEA Industrial Group, Springfield) to obtain hardness values representative of polycrystalline beryllium having little or no preferred orientation.

The hardness of two types of sheet beryllium was studied. The first sheet was made by cross-rolling a piece of extruded flat beryllium

TABLE 1
Fabrication details of the beryllium sheet, rod and tube

Reference Number	Final form	Extrusion Details	Rolling Details
1	Sheet	Cold compacted powder extruded at 1050° C in a steel sheath to a flat bar (redn. in area 12:1)	Flat bar re-canned in steel, heated to 1050° C and rolled at right angles to the extrusion direction (reduction in thickness 5:1)
2	Sheet	—	Cold compacted and die forged at 1050° C under 10 tsi pressure reduced 33 % in the cross-direction and 80 % in the longitudinal direction by rolling at 1000° C
3	Rod	Cold compacted powder extruded at 1050° C to a round bar (redn. in area 20:1)	
4	Tube	Vacuum hot pressed billet extruded at 500° C to a tube (redn. in area 6:1)	
5	Tube	Sintered billet extruded to tube at 800° C (redn. in area 12:1)	
6	Tube	Sintered billet extruded to tube at 850° C (redn. in area 25:1)	
7	Tube	Sintered billet extruded to rod at 1050° C (20:1 redn. in area) rod drilled and re-extruded to tube at 850° C (12:1 redn. in area)	
8	Tube	Cold compacted powder extruded at 1050° C (50:1 redn. in area)	

(table 1) and showed a very strong "basal plane layer texture" with also a very marked alignment of (10 $\bar{1}$ 0) prism planes at right angles to the rolling direction. Cylinders were machined with axes parallel to maximum concentrations of [10 $\bar{1}$ 0] and [11 $\bar{2}$ 0] directions and indentations made at 10° intervals around the circumference after removal of up to 200 μ of metal from the surface by etching. Since the sheet texture was so marked, corresponding to a "pseudo single crystal", these specimens were used for investigation of hardness changes due to testing direction in a given "crystal plane" in polycrystalline material. A piece of the sheet surface (corresponding to a high concentration of basal planes) and a section through the sheet parallel to the rolling direction (corresponding to a high

concentration of (11 $\bar{2}$ 0) prism planes) were polished and 250 μ . of surface removed by etching. By rotating the long diagonal of the indenter through 10° after each indent, the variation of hardness with direction in these two planes was obtained. The macrohardness under a load of 2 kg was also determined for these two surfaces.

The second sheet had been rolled from a hot forged block (see table 1 for details). The pole figure shows a high concentration of basal planes almost parallel to the sheet surface but no marked prism plane texture. A cylinder cut from the sheet parallel to the rolling direction was polished and indented, 130 μ of surface removed by etching, and the hardness redetermined.

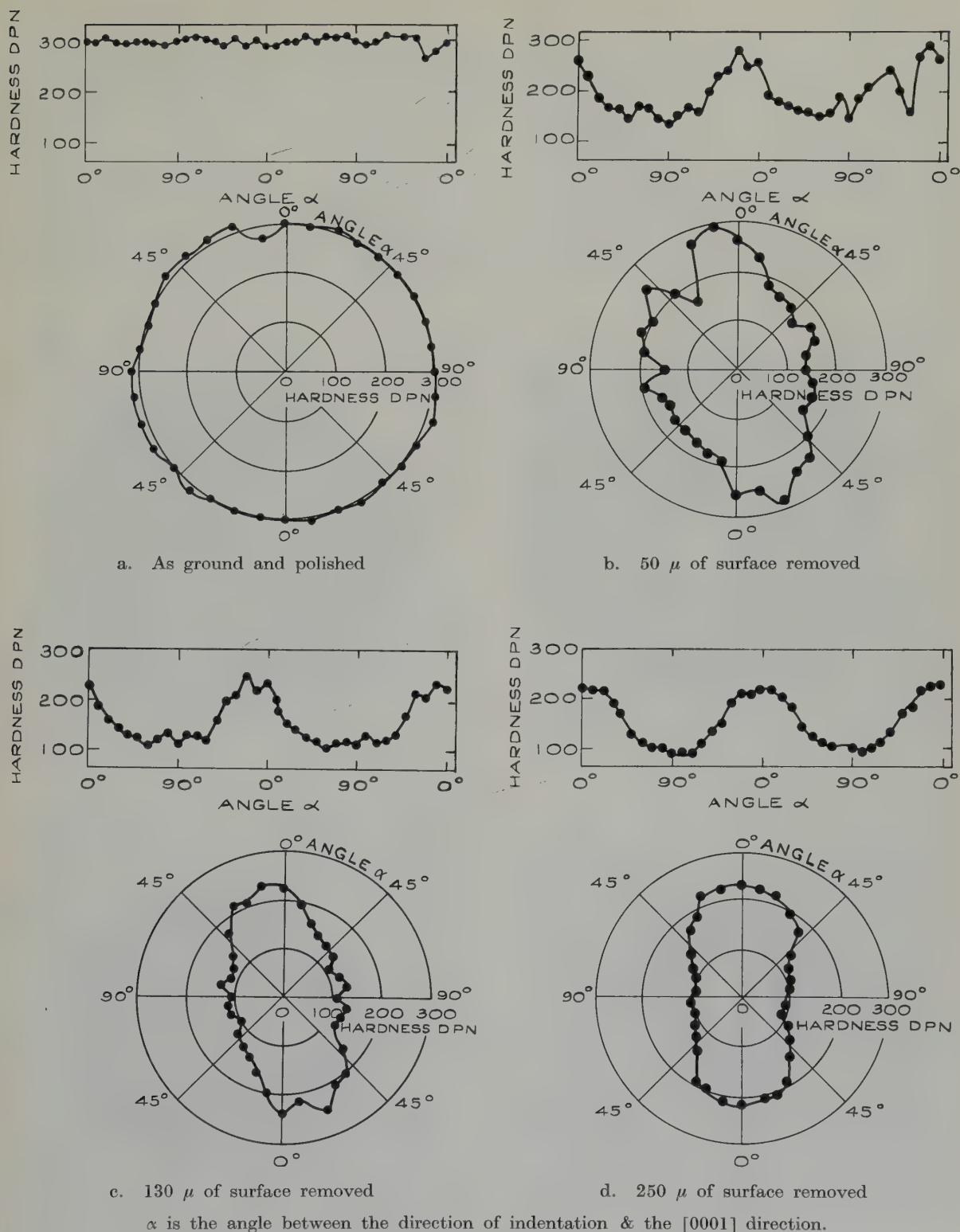


Fig. 1. Hardness variation on rotation of a single crystal cylinder about a $[10\bar{1}0]$ axis.

Five extruded tubes and one rod were studied, all fabricated from powder by the routes detailed in table 1. The tubes had thin walls (0.08–0.2 cm) so sections 0.5 cm wide by 2.5 cm. long were cut from the walls and up to five of these sections glued together to provide a blank sufficiently thick to be machined to a cylinder 0.38 cm diameter. After polishing, these cylinders were indented at intervals up to 30° around the circumference and this was repeated after

removal of $80\ \mu$ and $200\ \mu$. from the surface by electrolytic etching. Indentation at 10° intervals about a direction at right angles to the extrusion direction was carried out on the extruded rod.

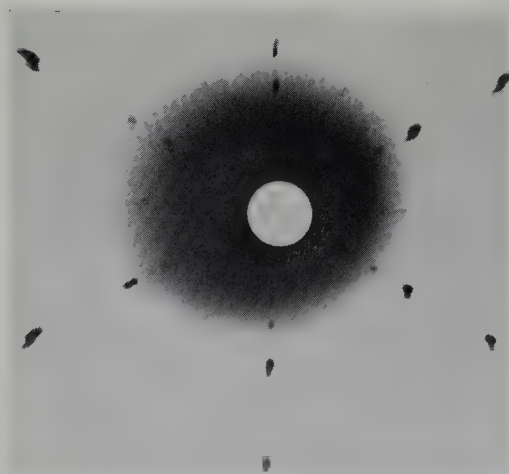
Textures in the beryllium sheets, rod and tubes examined were determined using a modified Norton Scan⁶) technique. The combined scans from a number of specimens cut at different angles enabled complete (0001) and



a. Machined cylinder



c. Machined cylinder, $50\ \mu$ removed from surface



b. Cleavage fragment



d. Machined cylinder, $250\ \mu$ removed from surface

Fig. 2. Laue X-ray photographs along [0001] axis.

$\{10\bar{1}0\}$ pole figures to be plotted for sheet. For tubes, cylindrical specimens could only be taken with axes parallel to the extrusion direction, consequently information on tubes was restricted to variations in the basal plane texture about the direction of extrusion.

3. Results

The hardness values are quoted as Diamond Pyramid Numbers for ease of comparison with other work. The Knoop hardness value for each impression was first calculated from the measured length of the longer diagonal, using the formula:

$$I = \frac{L}{l^2 C_P}$$

I = Knoop hardness number

L = Load in kg

l = Length of the long diagonal of the impression in mm

C_P = a constant = 7.028×10^{-2} .

This Knoop hardness number was then converted to Diamond Pyramid Hardness ⁷⁾. The conversion factor was checked by testing the same beryllium surface using the two indenters each under 200 g load (table 2).

3.1. SINGLE CRYSTAL BERYLLIUM

The variation in hardness values with indentation angle α relative to the basal plane is shown in figs. 1a-d for a beryllium cylinder machined from the single crystal so that the cylinder axis was parallel to a $[10\bar{1}0]$ direction. Figs. 1a-d are plotted in both cartesian and polar co-ordinates since the cylindrical specimens facilitate plotting on the polar system. The location of the basal plane was checked by the Laue X-ray reflection pattern.

Fig. 1a shows the hardness values obtained from the polished cylinder. The corresponding Laue photograph (fig. 2a) taken with the X-ray beam along the $[0001]$ axis reveals considerable asterism compared with a similar photograph (fig. 2b) taken from a cleaved basal surface. Removal of 50 μ of surface by electrolytic etching reduced the asterism in the Laue pattern (fig. 2c) and the corresponding hardness variations are shown in fig. 1b. Removal of 130 μ from the surface of the cylinder gave the hardness pattern shown in fig. 1c while removal of a total of 250 μ of metal from the surface by electrolytic etching gave the hardness variations shown in fig. 1d and the corresponding Laue pattern in fig. 2d which is similar to the pattern from a cleaved surface (fig. 2b). The progressive effect of etching upon the hardness values for the (0001) basal plane and a $(11\bar{2}0)$ prism plane is shown in fig. 4.

The variations of hardness with the direction of the longer diagonal for surfaces parallel to the (0001) basal, $(10\bar{1}0)$ prism and $(11\bar{2}0)$ prism planes, which had been polished and electrolytically etched to remove 250 μ of metal from the surface, are given in fig. 5.

Indentation of the basal (0001) plane caused twinning (fig. 3a) while the prism plane indentations were accommodated by deformation which manifested itself as wavy lines (fig. 3b). The macro-hardness (2 kg load) of the basal (0001) , and prism $(10\bar{1}0)$, planes given in table 3.

3.2. POLYCRYSTALLINE BERYLLIUM

The hardness values obtained from cylinders of sintered beryllium, as polished, and after removal by electrolytic etching of 25 μ and

TABLE 2
Conversion of Knoop results to Diamond Pyramid Hardness

Knoop result converted ⁷⁾ to DPN			Measured 136° Diamond Hardness
Indentation into a $(10\bar{1}0)$ prism crystal plane	(a) parallel to $[11\bar{2}0]$ direction	88-91	92
	(b) right angles to (a)	73-82	86

TABLE 3
Hardness Values using a load of 2000 g

Single Crystal: Basal (0001) plane – 184 DPN (230) †
Prism (10 $\bar{1}$ 0) plane – 82 DPN (90) †
(impression in [11 $\bar{2}$ 0] direction)

Sheet 1 (table 1) Surface – 300 DPN (300) †
Section through the sheet (rolling direction) – 180 DPN
(160) † indenter perpendicular to the sheet surface

† The figures in brackets are the values for a load of 200 g.

200 μ of metal from the surface, are plotted in fig. 6.

The results for cylinders taken from beryllium sheet, after removal of up to 200 μ . from the surface, are plotted in figs. 7 and 8. Each graph of hardness values is accompanied by the relevant plot of basal plane distributions and the complete sheet pole figures are also plotted in fig. 12. Fig. 8e shows the results from the highly oriented sheet obtained by rotation of the indenter both in the sheet plane and in a plane at right angles to it. The macro-hardness (2 kg load) of the sheet surface, and of a section through the sheet, are given in table 3.

The results for beryllium cylinders made from tubes are shown in fig. 9; the specimens were indented after electrolytic removal of 200 μ of metal surface. The appropriate Norton scan of basal plane intensities is recorded with the indentation hardness results.

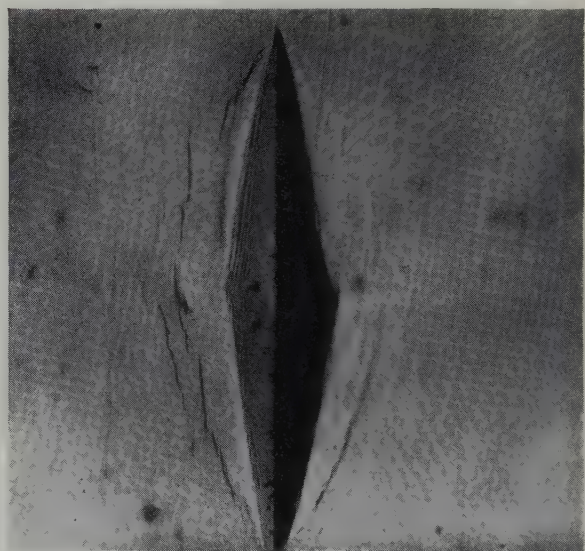
The results for the cylinder machined from an extruded rod (No. 3, table 1) are plotted in fig. 10 together with the Norton scan results.

4. Discussion

The indentation of a metal surface is a complex deformation process which entails a combination of both compressive and shear strain. Tabor²⁰) states that the indentation of an ideal plastic solid by a pyramidal indenter involves theoretical problems which have not yet been satisfactorily resolved. The hardness numbers from a Knoop or 136° pyramid impression are obtained by measurement of the diagonals of



a. Basal plane indentation, showing extensive twinning



b. Prism plane indentation

Fig. 3. Knoop impressions in a beryllium crystal.

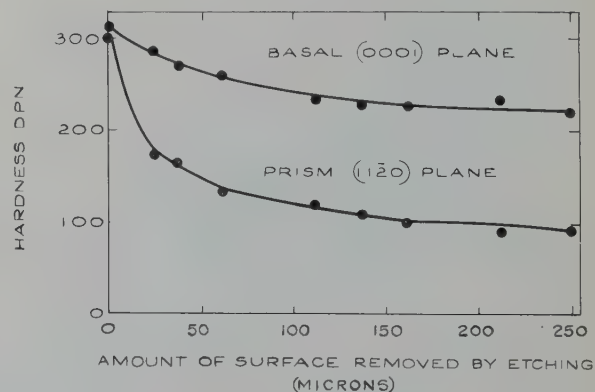


Fig. 4. Hardness variation on etching a single crystal.

the impression after removal of the load. The projected area of the impression is calculated from this measured length and the shape of the diamond indenter, and corresponds to the area of metal surface which is in contact with the indenter during indentation⁴). The hardness number, obtained by dividing the applied load

by this projected area, is thus a measure of the pressure needed to deform the metal. Using the solution proposed by Hill, Lee and Tupper²¹) for an infinite wedge pressing into a material which does not work harden, Tabor²⁰) has shown that this pressure is approximately three times the yield stress of the metal. This is borne

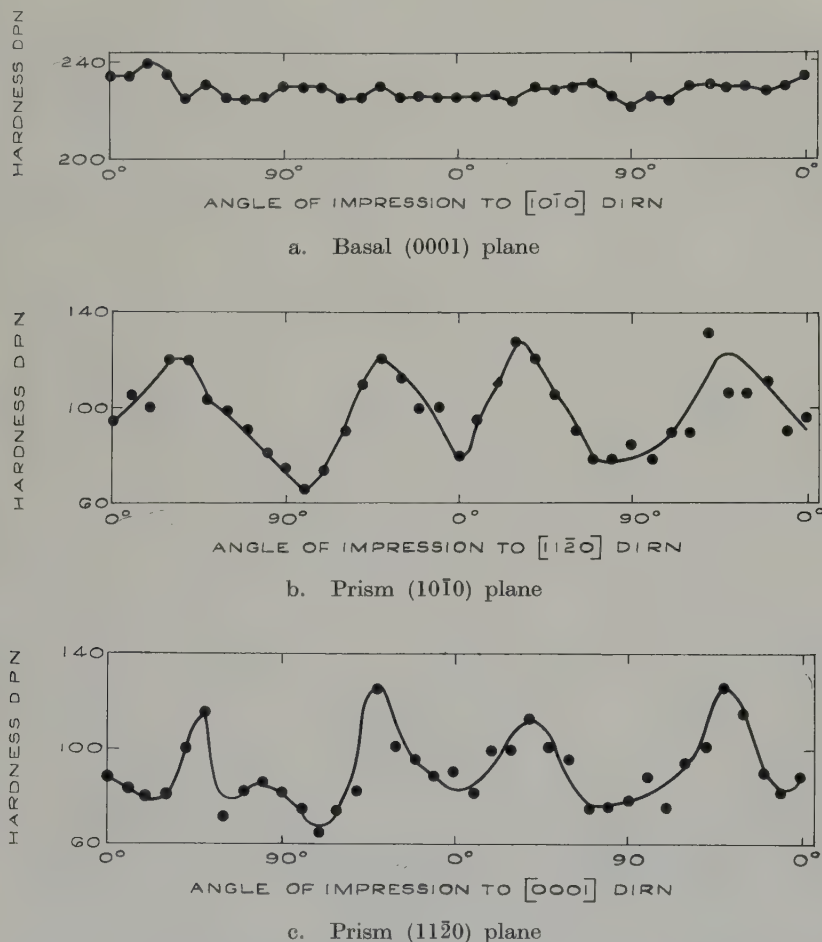


Fig. 5. Hardness variation on rotation of indenter in a crystal plane.

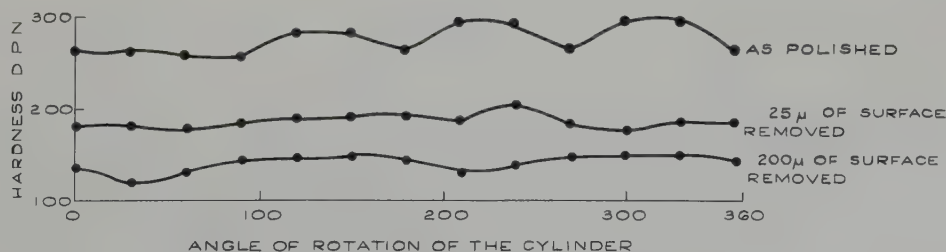
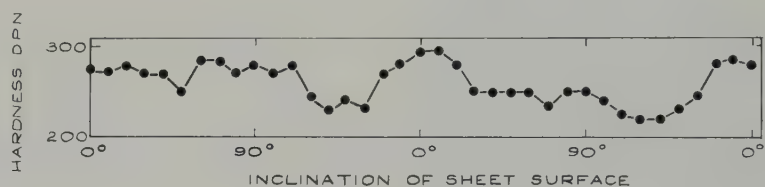


Fig. 6. Hardness variation round a sintered bar.

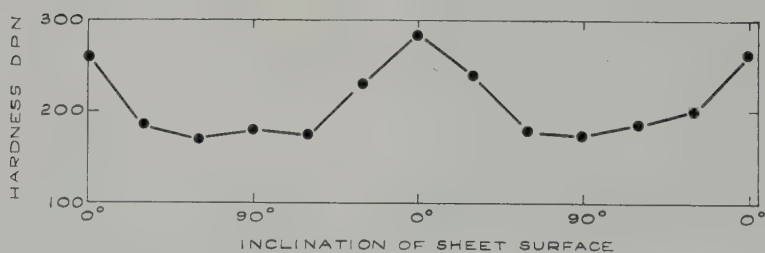
out by his macro-hardness measurements on both annealed and fully work-hardened materials.

As an alternative approach, the resistance of metal to deformation may be considered to depend on the deformation modes available, their yield stresses, the rate of strain hardening and the amount of strain present in the metal surface initially. Any surface strain increases the resistance of the metal to deformation and thus reduces the volume displaced by a given load. Hence, it is to be expected that work hardening would affect the crystallographic dependence of the indentation hardness. Figs. 1 and 4 show that a heavily work-hardened single crystal surface was virtually isotropic, the

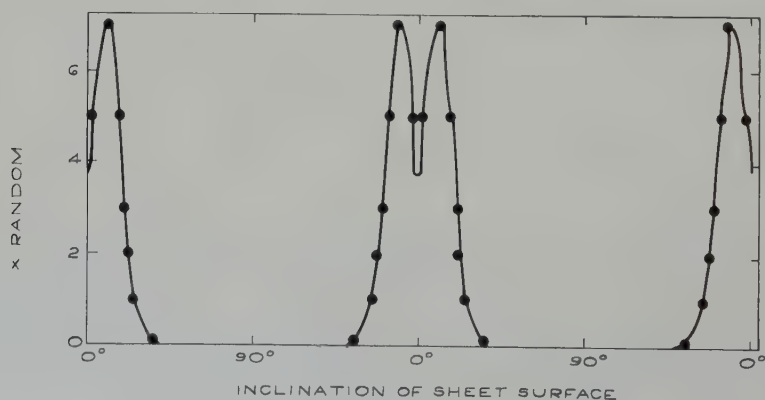
removal of $25\ \mu$ of surface was sufficient to indicate a difference in hardness dependent on the plane of indentation, but at least $200\ \mu$ of metal had to be removed before maximum variation was obtained. The cylindrical specimen had been machined using a carbide tipped tool with very light cuts, but the work hardening induced by this treatment (fig. 4) had been sufficient to increase the basal plane hardness by 70 DPN and the prism plane hardness by 210 DPN to give a surface layer which completely masked any crystallographic variations. Similar effects have been reported⁴) for other metals but normally the maximum depth of the work hardened layers was from 25 – $130\ \mu$, so



a. Hardness as polished.

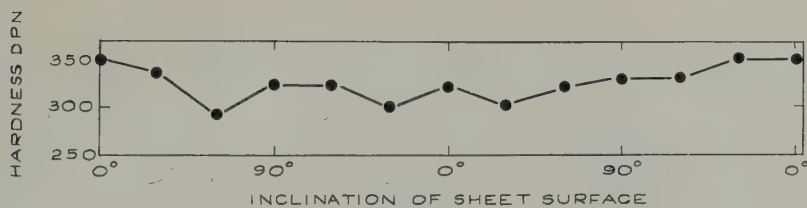


b. Hardness after removal of $130\ \mu$ of surface by etching.

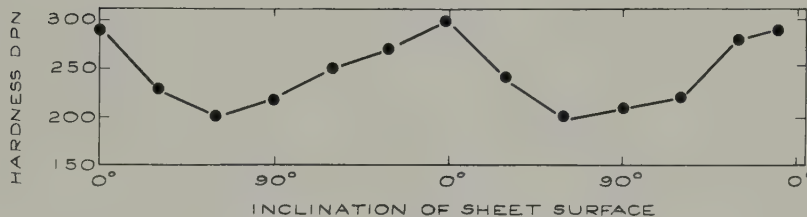


c. Intensity of X-rays diffracted from basal planes.

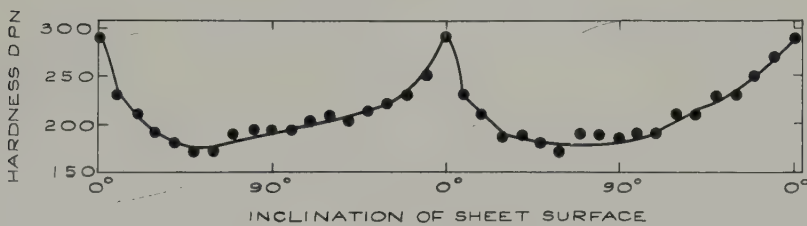
Fig. 7. Variations in hardness and preferred orientation on rotation of a cylinder with axis at right angles to the rolling direction in sheet 2 (table 1).



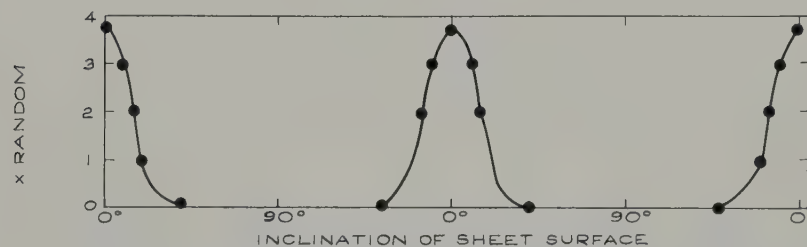
a. Hardness after etching off 25 μ of surface



b. Hardness after etching off 125 μ of surface



c. Hardness after etching off 200 μ of surface



d. Intensity of basal plane X-ray diffraction signal

Figs. 8a-d. Show rotation of a cylinder with axis parallel to the extrusion direction.

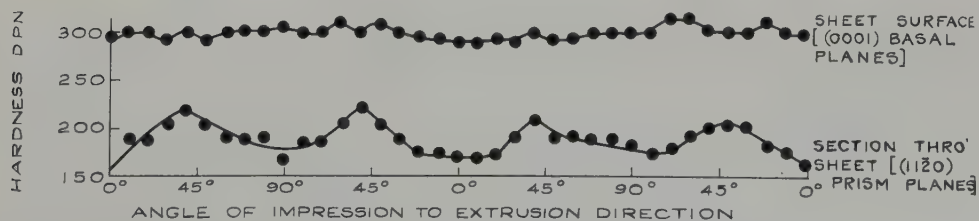
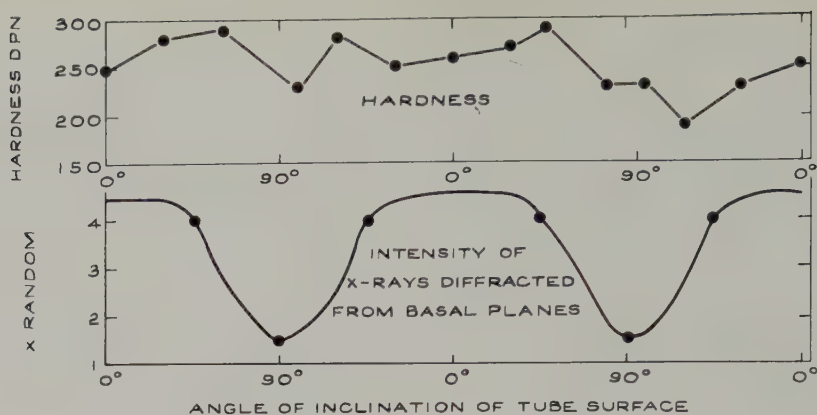
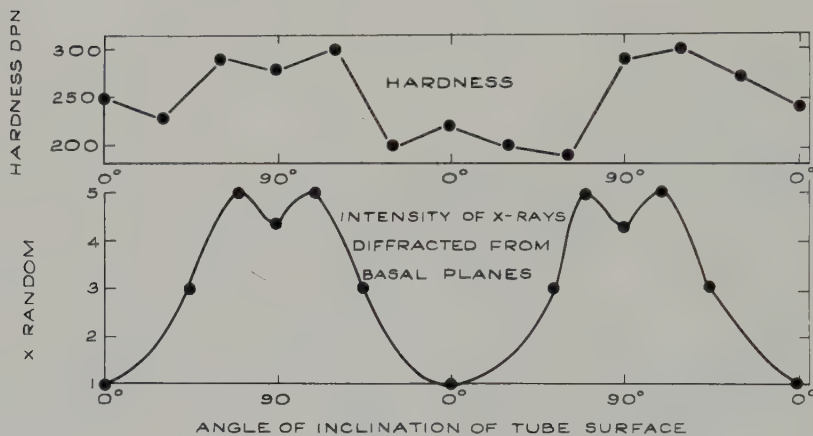


Fig. 8e. Hardness variation on rotation in sheet 1 (table 1)

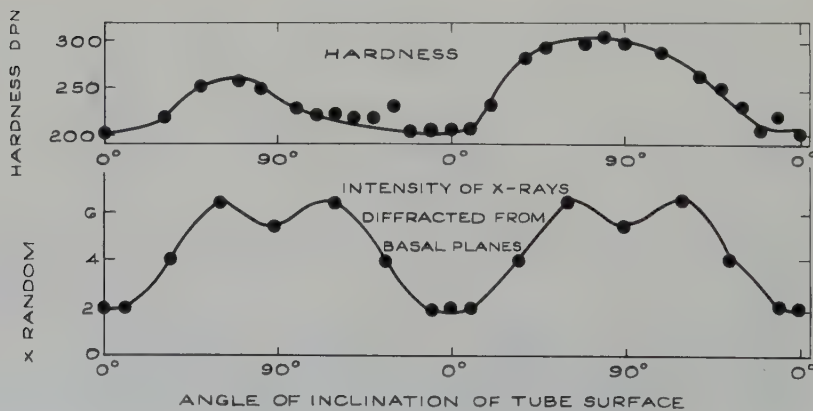
Fig. 8. Variations in hardness and preferred orientation in sheet 1 (table 1).



a. Tube 4 (table 1) 6:1 redn.

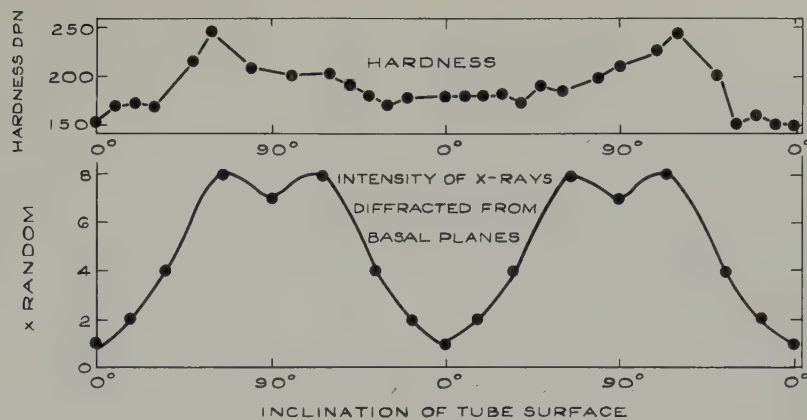


b. Tube 5 (table 1) 12:1 redn.

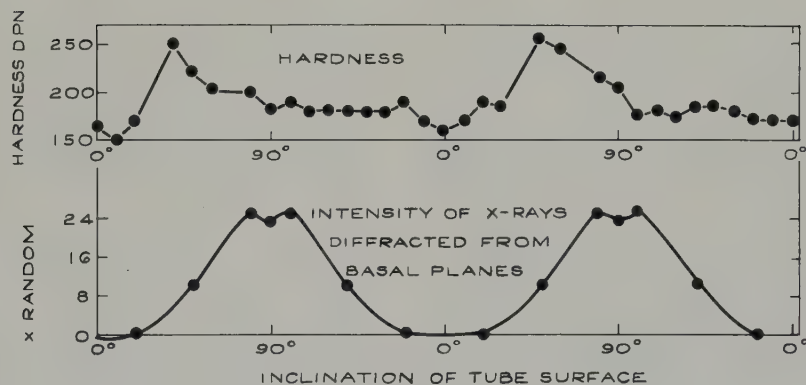


c. Tube 6 (table 1) 25:1 redn.

Fig. 9. Variations in hardness and preferred orientation on rotation of cylinders with axes parallel to the extrusion direction of tubes (after etching away 200 μ of surface).



d. Tube 7 (table 1) "double extruded".



e. Tube 8 (table 1) 50:1 redn.

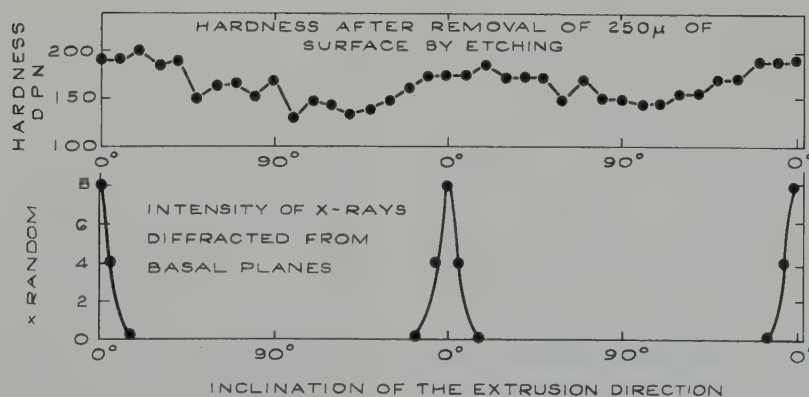
Fig. 9. Variations in hardness and preferred orientation on rotation of cylinders with axis parallel to the extrusion direction of tubes (after etching away 200 μ of surface).

Fig. 10. Variations in hardness and preferred orientation in an extruded rod [rotation of a cylinder cut with axis perpendicular to the direction of extrusion from rod 3 (table 1)].

that beryllium is unusual in work hardening to a depth of 200 μ . The disturbances of the diffraction pattern obtained in the Laue photographs (fig. 2) show that the work hardening has caused lattice distortion.

Once the masking effect of work hardening had been removed, the hardness variation with crystal planes in beryllium was very apparent. Indentation into the (0001) basal plane gave a hardness of 230 DPN whilst a (1120) prism plane gave 90 DPN.

The results of other investigations⁸⁾ suggest that the average hardness value for body centred cubic metals may be independent of the plane tested; whereas in hexagonal metals there is strong evidence of hardness variations due to the orientation. Perhaps the most conclusive work on hardness variation with orientation was that carried out by Daniels and Dunn⁹⁾. They deeply etched single crystals of zinc and carried out hardness tests using a Knoop indenter. The hardness values varied from 32.9 on a (1450) face to 16.7 on a (0001) face.

The curve plotted in fig. 1d shows the variation in hardness with inclination of the basal (0001) plane in a beryllium crystal about a $[10\bar{1}0]$ direction. There is very little fall in hardness from the maximum of 220 DPN for indentation of the basal (0001) plane until the indenter is inclined at more than 20° to the $[0001]$ direction; greater inclination causes a very rapid fall (~ 3 DPN/degree of inclination) until the inclination of the indenter is only 20° to the $[11\bar{2}0]$ direction, when there is very little further fall to the minimum of 90 DPN corresponding to indentation into the (1120) plane.

This wide variation in hardness is a manifestation of the extreme anisotropy in plastic properties of the beryllium single crystal. At room temperature only three deformation mechanisms have been found in the beryllium crystal¹⁰⁾; slip on $\{10\bar{1}0\}$ planes in $\langle 11\bar{2}0 \rangle$ directions in either tension or compression, slip on (0001) planes in $\langle 11\bar{2}0 \rangle$ directions in compression only (tensile slip leads to immediate fracture) and $\{10\bar{1}2\}$ twinning along $\langle 10\bar{1}1 \rangle$ shear directions. The deformation consequent

upon indentation must therefore be accommodated by these mechanisms.

The variation in hardness with angle of indentation α relative to the $[0001]$ basal pole should be related to the operation of the possible modes of deformation. It is likely that the twinning (fig. 3a) by which indentation into the (0001) basal plane is accommodated involves block movement of metal which may partly account for the smaller impression compared with the (1120) prism plane impression which appears to be formed by slip (fig. 3b).

Indentation by a Knoop indenter involves complex stress and strain systems and it does not seem possible to analyse the process in any detail; however a simplified approach can explain quantitatively some of the variation in hardness encountered in beryllium. The only forces acting are assumed to be a compressive force perpendicular to each facet of the indenter. The work hardening of the metal during indentation is ignored together with frictional effects. For slip on $\{10\bar{1}0\}$ prism planes, the angles between the normal to the indenter facet and the slip planes, (χ_1, χ_2, χ_3) , and the appropriate slip directions; $(\lambda_1, \lambda_2, \lambda_3)$, were measured from polar diagrams for each of the four indenter facets. This was repeated for different values of α from 0°–90° corresponding to rotation of the direction of indentation about a $[10\bar{1}0]$ direction in the single crystal.

The shear stress S on a given crystal plane was obtained from the formula¹³⁾.

$$S = \sigma \sin \chi \cos \bar{\lambda}$$

where σ is the applied stress. Following Le Chatelier's principle it was assumed that the (1010) plane on which slip actually occurs would be the one for which the value for $\sin \chi \cos \bar{\lambda}$ was a maximum. Using this selective principle for each facet of the indenter and combining the four results for each value of α , the values for the $\sin \chi \cos \bar{\lambda}$ factor were plotted in fig. 11 together with the corresponding values for the squares of the indentation lengths.

For values of α from 30° to 90° to the $[0001]$ direction the shapes of the two curves agree,

but for values smaller than 30° the indentation size is greater than predicted. The probable reason for this is that $\{10\bar{1}0\}$ slip is not the predominant deformation mechanism at angles of less than 30° but a combination of (0001) basal slip and $\{10\bar{1}2\}$ twinning has occurred to permit greater deformation. Microscopical examination of the impressions revealed twinning as in fig. 3a occurring at angles up to 30° .

Thus the hardness variation is apparently largely dependent on the variations in resolved shear stresses on the operative slip planes.

The above treatment, however, is only comparative. Calculation of the actual value of S , the applied shear stress on the $\{10\bar{1}0\}$ planes, was made from the equation, σ (the average normal stress on each facet of the indenter) being calculated from the applied load and the inclination of the indenter facet and using the value of $\sin \chi \cos \bar{\lambda}$ obtained from fig. 11. For indentation into the $(11\bar{2}0)$ prism plane ($\alpha = 90^\circ$ in fig. 11) this calculation gave

$$S = 37 \text{ kg/sq mm.}$$

Measurements by Tuer and Kaufmann¹⁰⁾ of the critical resolved shear stress for the onset of $\{10\bar{1}0\}$ slip gave a value of 6.6 kg/sq mm, i.e. approximately $1/6$ of the stress actually applied. The curves in fig. 11 show a good correlation for the variation in hardness with the resolved shear stress, but the actual value of applied stress is six times the critical shear stress.

Work by Arbtin and Murphy¹⁹⁾ shows that the 0.2 % proof stress ranges from a quarter to a sixth of the Vickers Hardness Number depending on test conditions, for a variety of metals. This indicates that the resolved shear stresses calculated for beryllium are related to the critical resolved shear stress for $\{10\bar{1}0\}$ slip by a factor which is commonly found to relate the applied stress on polycrystalline metal in macro-hardness testing with the critical stress for the onset of plastic deformation in tension. This supports the hypothesis that $\{10\bar{1}0\}$ slip is the operative deformation mechanism.

In considering the case of indentation into the basal (0001) plane of a single crystal from

which the work-hardened surface has been removed, it has to be borne in mind that direct compression of a beryllium cylinder parallel to the (0001) plane is impossible at room temperature. Loads up to 100 tons/in² are resisted elastically, whilst the application of considerably higher load causes explosive disintegration of the specimen into small fragments¹¹⁾. Thus the hardness indentation in the (0001) basal plane must be accommodated by movements of the metal in directions other than that of indentation. Two likely deformation mechanisms are (0001) basal slip in any $\langle 11\bar{2}0 \rangle$ direction and $\{10\bar{1}2\}$ twinning. The change in dimensions on twinning may be calculated by the following formula quoted from Schmidt and Boas¹²⁾.

$$l_1 l_0 = \sqrt{(1 + 2s \sin \chi^* \cos \bar{\lambda}^* + s^2 \sin^2 \chi^*)},$$

where s is the twinning shear and $\chi^* \bar{\lambda}^*$ are the angles between the stress direction and the twinning plane and shear vector respectively. For beryllium,

$$s = 0.186, \quad \chi^* = 47^\circ 53', \quad \bar{\lambda}^* = 29^\circ 19'$$

and we have $l_1 l_0 = 1.12$.

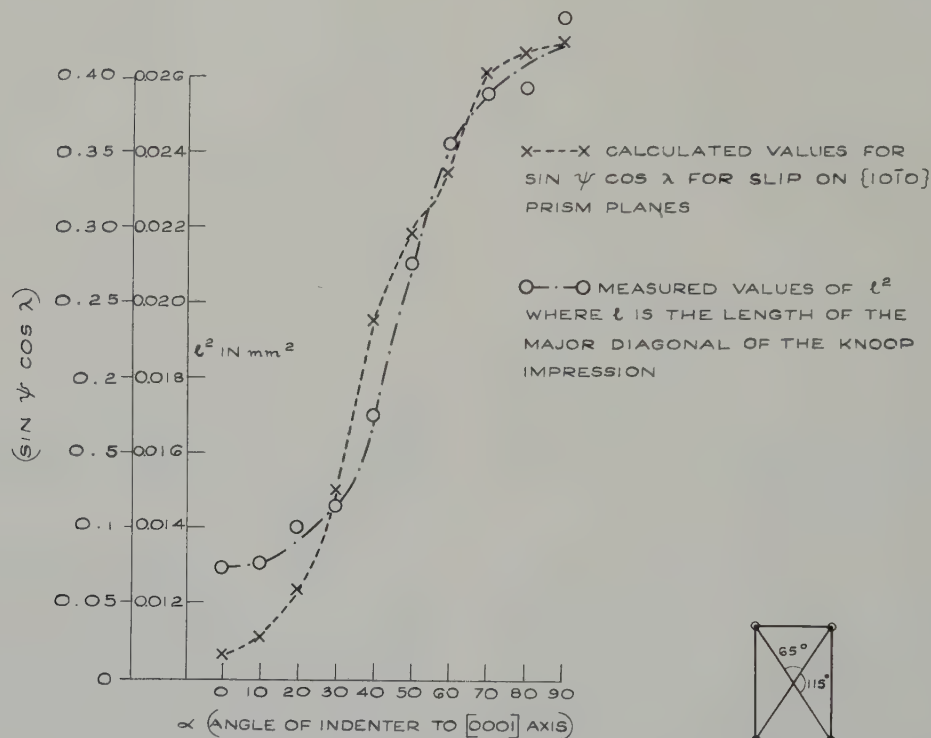
Thus the maximum expansion in the [0001] direction is 12 % by $\{10\bar{1}2\}$ twinning, while in the $\langle 10\bar{1}0 \rangle$ directions a contraction occurs. Indentation could therefore occur by a combination of (0001) slip to move the metal parallel to the surface and $\{10\bar{1}2\}$ twinning which raises the surface to accommodate the slipped metal. This hypothesis is supported by the appearance of twins around the indentation (fig. 3a).

The rotation of the indenter in a given crystal plane has been used by a number of investigators to establish hardness variations with the direction of the diagonals of the indenter; the results have been conflicting. Early work by Meincke¹⁴⁾ showed considerable differences in scratch hardnesses in copper (2.0–5.0), aluminium (1.0–2.0) and zinc (1.5–3.75). Mott and Ford¹⁵⁾ obtained large differences (650–1280 units) from rotation of a Knoop indenter in single grains of annealed magnesium but relatively small variations of hardness from similar rotation in zinc and aluminium. Daniels and

Dunn⁹⁾ investigated the faces of silicon ferrite crystals using a Knoop indenter and found that the number of hardness maxima per rotation was related to the crystallographic symmetry of the plane indented. Vacher¹⁶⁾ and Grodzinsky¹⁷⁾ obtained comparable results from single crystals

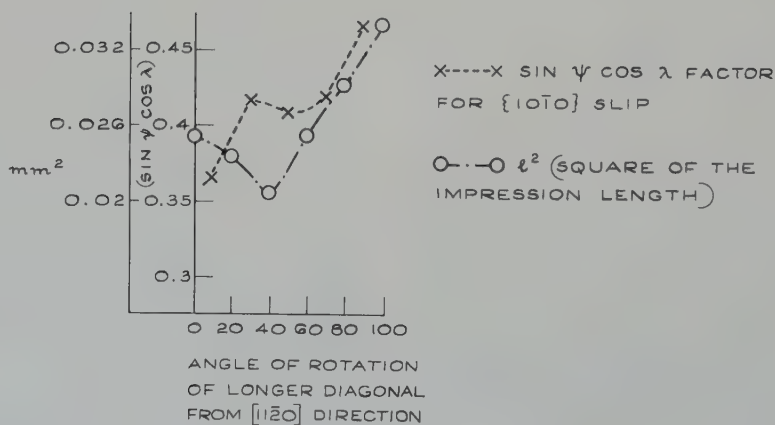
of copper using Knoop and double cone indenters respectively. Winton¹⁸⁾ using a Knoop indenter on cadmium and titanium found that the minimum hardness on a $(10\bar{1}0)$ plane was related to the available glide directions.

The graphs in fig. 5 show the effects of



a. Effect of rotation of the Basal plane about a $[10\bar{1}0]$ axes

b. The $(10\bar{1}0)$ plane in beryllium (schematic)



c. Rotation of the $(10\bar{1}0)$ plane

Fig. 11. Comparison of impression size with resolved shear stress factor.

rotation on beryllium surfaces from which the work-hardened layer had been removed corresponding to the (0001) basal plane (fig. 5a), and $\{10\bar{1}0\}$ prism plane (fig. 5b) and a $\{11\bar{2}0\}$ prism plane (fig. 5c). The effect of direction of the indenter in the (0001) basal plane on the indentation hardness value (fig. 5a) is negligible. This may be due to the occurrence of twinning (fig. 3a), since twinning is dependent only upon the energy dissipated during indentation. Also, if the four faces of the Knoop indenter are regarded as separate compression platens inclined at the appropriate angle to the surface of the metal, the resolved shear stresses for $\{10\bar{1}0\}$ slip will vary very little with the direction of the longer diagonal.

The variation of the resolved shear stress factor (i.e. $\sin \chi \cos \bar{\lambda}$) on the $\{10\bar{1}0\}$ planes is considerable and this is plotted together with the variations in the square of the indentation length in fig. 11c for rotation of the indenter in the $\{10\bar{1}0\}$ prism plane, the agreement between the two curves is only approximate, indicating that other factors such as friction and strain hardening may also cause variations. In fig. 5b, the irregular dispersion of the peaks in the $\{10\bar{1}0\}$ plane is probably due to the axial ratio of 1.56 which gives angles between the unit cell diagonals (see fig. 11b) on a $\{10\bar{1}0\}$ plane of 65° and 115° , the measured dispersions of maxima are $70^\circ \pm 5^\circ$ and $110^\circ \pm 5^\circ$ in fig. 5b, while for the $\{11\bar{2}0\}$ planes the angles between the unit cell diagonals are 85° and 95° corresponding to a measured peak dispersion of $90^\circ \pm 5^\circ$ in fig. 5c. Hence the hardness peaks can be related to the lines of closest atomic packing in a given crystal plane.

In the polycrystalline specimens tested, the hardness variation was dependent on the degree of perfection of the preferred orientation. For the sintered cylinder there was very little preferred orientation and the slight variations in hardness shown in fig. 6 are probably just scatter of results. The effect of work hardening is shown in fig. 6, etching reducing the average hardness from 270 to 130 DPN by the removal of 200μ of surface.

The pole figures (fig. 12) for sheet No. 1 (table 1), made by cross rolling extruded flat beryllium, reveal a very strong texture so that the properties of this sheet may be expected to be analogous to that of a single crystal of beryllium in which the basal plane is the sheet surface and a $[10\bar{1}0]$ direction corresponds to the direction of extrusion. After machining and slight etching, cylinders with axes parallel to concentrations of $[10\bar{1}0]$ and $[11\bar{2}0]$ directions gave hardness values ranging from 290–230 DPN (fig. 8a) but without any regular variations. Thus the effect of work hardening on polycrystalline beryllium is to produce an almost uniform surface with some scatter of hardness about a mean of 300 DPN i.e. almost identical with the single crystal results. Etching of the surface reveals the crystallographic dependence of the hardness but this does not appear until 130μ of surface have been removed showing that the completely work hardened surface

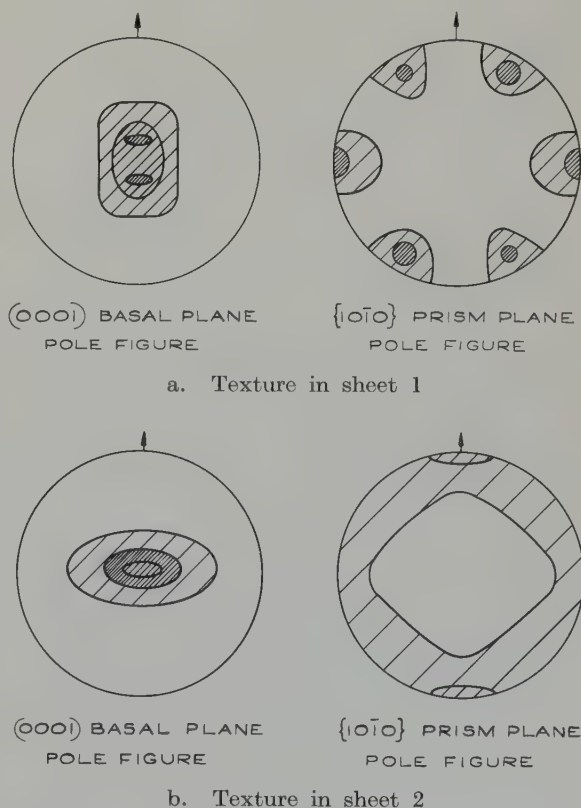


Fig. 12. Pole figures for beryllium sheets 1 and 2.

extends to a greater depth in a highly oriented beryllium sheet than in a single crystal. Removal of 200 μ of metal is necessary to achieve the maximum difference from 170 DPN for indentation into a (10 $\bar{1}$ 0) prism plane (with the longer diagonal of the indenter parallel to a [11 $\bar{2}$ 0] direction) to 290 DPN for the (0001) basal plane; this compares with 100 DPN \rightarrow 230 DPN for a single crystal. Thus the hardness *difference* of 120 DPN is almost identical with the difference of 130 DPN for the single crystal. The presence of the grain boundaries in a highly oriented sheet merely serves to raise the hardness figures on the basal and prism planes; the difference in hardness between the planes in this sheet is identical with the difference in a single crystal. Fig. 8c indicates that other characteristics may also be different in the case of polycrystalline material since the form of these curves differs appreciably from those in fig. 1d.

The rotation of the indenter in the surface of sheet No. 1 (table 1) gave very little variation in hardness (fig. 8e), in accord with the findings for the single crystal basal plane (fig. 5a). Indentation of a plane at right angles to the sheet surface into a high concentration of (11 $\bar{2}$ 0) prism planes gave a result similar on rotation of the indenter (fig. 8e) to that obtained from a (11 $\bar{2}$ 0) plane in a single crystal (fig. 5c); with the difference that the sheet hardness ranges from 160–220 DPN, compared with 70–120 DPN for the single crystal. As far as hardness variations are concerned, the highly oriented sheet No. 1 (table 1) therefore can accurately be called a "pseudo single crystal".

The results for tube in fig. 9 show that, for finding variations in basal plane texture in beryllium, the low load indentation hardness test is somewhat less sensitive than X-ray diffraction. In the case of a warm extruded tube (No. 4, table 1), the removal of 200 μ of surface only gives a drop from 230 DPN to 190 DPN for the minimum hardness figures recorded, the maximum remaining at 290 DPN, and no clear pattern of hardness variation is visible. With greater reduction (Tubes 5 and 6, table 1) at higher temperatures, the basal plane texture

is more marked (figs. 9b and c). This causes more distinct hardness variations, from maxima of 300 DPN to minima of 200 DPN; however the change in the basal plane texture from tube 5 (12:1 reduction) to tube 6 (25:1 reduction) has not materially affected the shape of the hardness curves. Thus the indentation hardness is not sensitive to small variations in texture.

In the case of tubes 7 and 8 (figs. 9d and e) which have each had greater reductions in extrusion (table 1) the texture peaks are well defined. The peaks in hardness values do not correspond exactly although there is a general similarity. In the case of tube 8 where there is a marked texture (fig. 9e) the hardness difference is from 250 DPN tangentially (corresponding to indentation into a high concentration of basal planes) to 160 DPN radially (prism plane concentration); approaching the differences found in single crystal and highly oriented sheet beryllium.

The results given in table 3 for an applied load of 2 kg are very similar to the low load (200 g) results obtained on the same specimens indicating that the applied load has little effect on the crystallographic dependence of hardness.

5. Conclusions

There is considerable variation in the low load indentation hardness depending both on the residual strain and the direction of indentation in both single crystal and oriented polycrystalline beryllium.

The effect of machining on the surface was sufficient to impart an isotropic hard surface (approximately 300 DPN) to both single and polycrystal beryllium which extends to a depth of up to 200 μ ; however the removal of 50–130 μ of surface was sufficient to indicate a variation with the direction of indentation.

The greatest variation in hardness of a single crystal was from a maximum of 230 DPN for indentation into a basal plane to a minimum of 70–80 DPN for indentation into a (10 $\bar{1}$ 0) prism plane with the longer diagonal in the [0001] direction. The rotation of the indenter in the basal plane of a single crystal gave no

systematic variation in hardness, but rotation in a prism plane gave considerable variations from minima of 70 DPN to maxima of 120 DPN.

In polycrystalline beryllium tube and sheet prepared from powder, any marked preferred orientation was revealed by low load indentation hardness measurements after removal of the surface work hardening.

With highly oriented cross-rolled sheet, marked variation in hardness was found after removal of the work hardened surface. The values ranged from 300 DPN for indentation into the sheet surface (i.e. into a concentration of (0001) basal planes) to 170 DPN for indentation into a cross-section of the sheet (i.e. into a concentration of (11 $\bar{2}$ 0) prism planes).

Rotation of the indenter in the sheet surface (high concentration of basal planes) produced no systematic hardness variation but rotation in a concentration of (11 $\bar{2}$ 0) prism planes produced a variation from 220 DPN to 170 DPN with peaks at approximately 90° intervals. The behaviour of this sheet was thus analogous to that of a single crystal.

In sheet and tube beryllium fabricated to give a variety of textures, without exception the greatest concentration of basal planes gave the highest hardness value and the lowest hardness value corresponded to the greatest concentration of prism planes. The more marked the texture under examination, the sharper the hardness peaks appeared and the greater the difference between maximum and minimum values.

Similar effects have been found with a limited number of macro-hardness tests (2 kg load) indicating that the load does not affect the crystallographic dependence.

A detailed explanation of the exact mechanism and reason for the observed relationship of crystallography and hardness in beryllium will not be possible until the deformation modes under conditions of complex stress have been fully explained. The hardness variation with

angle of inclination to the (0001) basal plane in an etched single crystal has been successfully correlated with the variation of the resolved shear stresses on the {10 $\bar{1}$ 0} prismatic slip planes.

Acknowledgements

The authors are indebted to Mr. J. Williams for suggestions and criticisms during the course of this work.

References

- 1) A. R. Kaufmann, P. Gordon and D. W. Lillie, *Trans. ASM* **42** (1950) 785
- 2) J. Greenspan, *Trans. AIME* **215** (1959) 153
- 3) N. A. Hill and J. Williams, AERE, Harwell (UK) Report, M/R 2652 (1958)
- 4) H. Bückle, *Metallurgical Reviews* **4** (1959) 49
- 5) F. Knoop, G. C. Peters and W. B. Emerson, *J. Res. Nat. Bur. Stand.* **23** (1939) 39
- 6) J. T. Norton, *J. Appl. Phys.* **19** (1948) 1176
- 7) Metal Progress Data Sheet, *Metal Progress* **74** (Dec. 1958)
- 8) B. W. Mott, *Micro-Indentation Hardness Testing* (Butterworths, London, 1956) pp. 77-79
- 9) F. W. Daniels and C. G. Dunn, *Trans. ASM* **41** (1949) 419
- 10) G. L. Tuer and A. R. Kaufmann, in *The Metal Beryllium* (Ed. D. W. White Jr. and J. E. Burke, ASM, 1955) 372 *et seq.*
- 11) H. T. Lee and R. M. Brick, *Trans. ASM* **48** (1956) 1003
- 12) E. Schmid and W. Boas, *Plasticity of Crystals* (Hughes, London, 1950) p. 72
- 13) *Ibid.*, p. 105
- 14) H. Meincke, *Z. Metallk.* **41** (1950) 344
- 15) B. W. Mott and S. D. Ford, AERE (Harwell), Memorandum M/M-70 (1954)
- 16) H. C. Vacher, *Trans. ASM* **41** (1949) 438
- 17) P. Grodzinski, *Sheet Metal Ind.* **29** (1952) 908
- 18) Work by Winton, reported by B. W. Mott, *Micro Indentation Hardness Testing* (Butterworths, London, 1956) p. 82
- 19) E. Arbtin and G. Murphy, Iowa State College Report, ISC-356 (1953)
- 20) D. Tabor, *The Hardness of Metals* (Clarendon Press, Oxford, 1951) Ch. VII
- 21) R. Hill, E. H. Lee and S. J. Tupper, *Proc. Roy. Soc. A* **188** (1947) 273

THE EFFECT OF INCLUSIONS ON THE FRACTURE OF URANIUM

D. M. DAVIES and J. W. MARTIN

Department of Metallurgy, University of Oxford, UK

Received 15 July 1960

A metallographic study has been made of the nucleation and propagation of tensile fracture in the α -range of commercially pure uranium. The crack nucleus appears to be associated with the inclusions present, and the effect of prior annealing in the γ -range upon the size-distribution of these inclusions has also been studied semi-quantitatively.

On a étudié, par métallographie, la nucléation et la propagation d'une rupture par traction dans le domaine α sur de l'uranium de pureté commerciale. L'origine de la rupture semble associée aux inclusions

présentes et l'on étudie également "semi-quantitativement" l'influence d'un recuit préalable dans le domaine γ sur la taille et la répartition des inclusions.

Über den Beginn und das Fortschreiten eines Bruches bei Zugbeanspruchung wurde im α -Bereich von handelsüblichem Uran eine metallographische Untersuchung angestellt. Der Beginn des Bruches scheint mit den vorhandenen Einschlüssen zusammenzuhängen. Der Einfluss einer vorausgehenden Glühung im γ -Zustand auf die Grösse dieser Einschlüsse wurde halbquantitativ untersucht.

1. Introduction

Grainger¹⁾ and Foote²⁾ have reviewed most of the early work on the mechanical properties of uranium, including tensile data by Chiswick and Mayfield³⁾ and a study by Marsh, Muehlenkamp and Manning⁴⁾ on the effect of hydrogen on the brittle/ductile transition in alpha-uranium. Recent work by Sergeyev *et al.*⁵⁾, McIntosh and Heal⁶⁾ as well as Chiswick *et al.*⁷⁾ has further expanded the study of the mechanical properties of commercially pure uranium at ordinary temperatures and at elevated temperatures.

In the above work hardly any metallographic examination of the test specimens has been carried out. It was therefore decided to study the microstructural changes occurring in commercially pure uranium during tensile testing in the alpha range and to attempt to correlate these changes with changes in mechanical properties. The work described forms part of these studies, and is particularly concerned with the nucleation and propagation of the tensile fracture.

2. Experimental

2.1. MATERIAL

The metal employed was magnesium-reduced uranium. A typical analysis is: oxygen 90 ppm, hydrogen 5 ppm, carbon 600 ppm, iron 60 ppm, aluminium 240 ppm and silicon 75 ppm.

The specimens were in the form of round tensile test-pieces, 0.16 cm² cross-sectional area and 1.60 cm gauge length. The grain-size of the material as provided is discussed later.

2.2. METALLOGRAPHY

The polishing technique adopted is that proposed by Mott and Haines⁸⁾, namely, primary grinding on silicon carbide papers under water, followed by diamond polishing and finally attack polishing with a mixture of 40 parts (by vol.) CrO₃, 10 parts HNO₃, 40 parts water containing a suspension of gamma-alumina. The attack polishing is carried out on a "Terylene" cloth mounted in a polythene bowl, as described by Haddrell, Sykes and Mott⁹⁾.

Fractured specimens are sectioned and mounted in plastic for metallographic examination, the fracture edge having previously been nickelplated, employing a very low current-density to ensure a deposit free from porosity. The plating is not attacked by the attack polishing solution.

Bierlein^{10,11}) used "Faxfilm" to replicate fracture surfaces of uranium, thereby obtaining two-stage silicon monoxide replicas for electron microscopy. In order to examine the fractured uranium surface itself, two stage carbon replication has been adopted using 0.75 mm (0.030") thick cellulose acetate strip as the intermediate stage. The acetate strip is softened in acetone before being placed on the freshly fractured surface, allowed to harden, and mechanically stripped. After shadowing with gold/palladium, carbon is deposited while the plastic replica is rotated in its own plane, so that an even deposition on the irregular surface is achieved. The acetate is dissolved in acetone, leaving the shadowed carbon replica for electron microscopy.

2.3. HEAT-TREATMENT

In the metal provided, the most prolific inclusions are of a cuboid variety, described by Meredith and Waldron¹²) and by Kehl *et al.*¹³) as complexes of uranium with oxygen, carbon and nitrogen. Inclusions of compounds of uranium with iron, aluminium and silicon have also been identified, as well as inclusions of uranium oxide. The "carbide" inclusions are darkened by etching in 1/1 nitric acid for 30 seconds (fig. 1).

The effect of isothermal annealing in vacuo upon the microstructure has been studied, and an interesting effect has been observed. Whereas the carbide inclusions are unaffected by heat-treatment in the β -range (668–774°C), on annealing in the (bcc) γ -range (774–1132°C) a series of changes takes place. The cuboid inclusions first become spheroidised (fig. 2), a further annealing causing a progressive coagulation. The change in particle-size distribution of these inclusions during an isothermal anneal in vacuo at 1010°C has been assessed by examin-

ing photomicrographs of polished sections, using a method employed by Hyam and Nutting¹⁴). Using their statistical treatment to calculate the actual particle-size distribution from measurements upon polished sections, a series of histograms was assembled illustrating the sequence of changes occurring (fig. 3). After long anneals in the gamma region, very large clusters of inclusions are observed (fig. 2). These, although included in the above analysis to demonstrate the trend of these changes, will certainly introduce statistical errors.

Before testing, all specimens were further oil-quenched from the beta-range, so that the grain-size distribution was always approximately the same. Grain-size assessment is

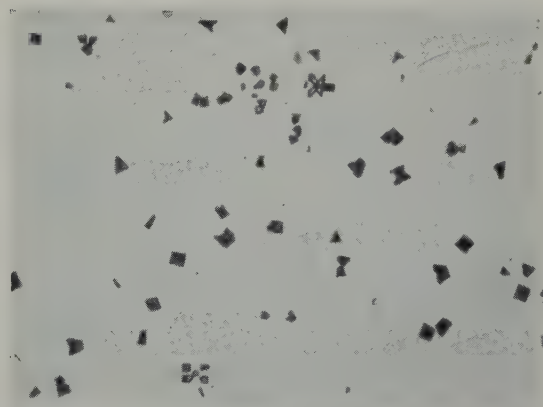


Fig. 1. As cast uranium. Etched 30 sec 1/1 HNO_3 .
 $\times 500$.

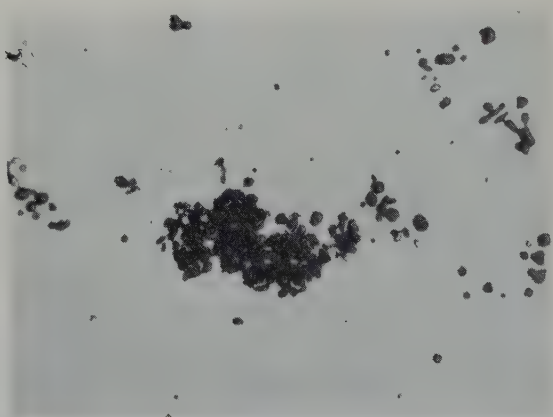


Fig. 2. Uranium heat-treated at 925°C in vacuo for 5 hours. Oil-quenched. Etched 30 sec 1/1 HNO_3 .
 $\times 350$.

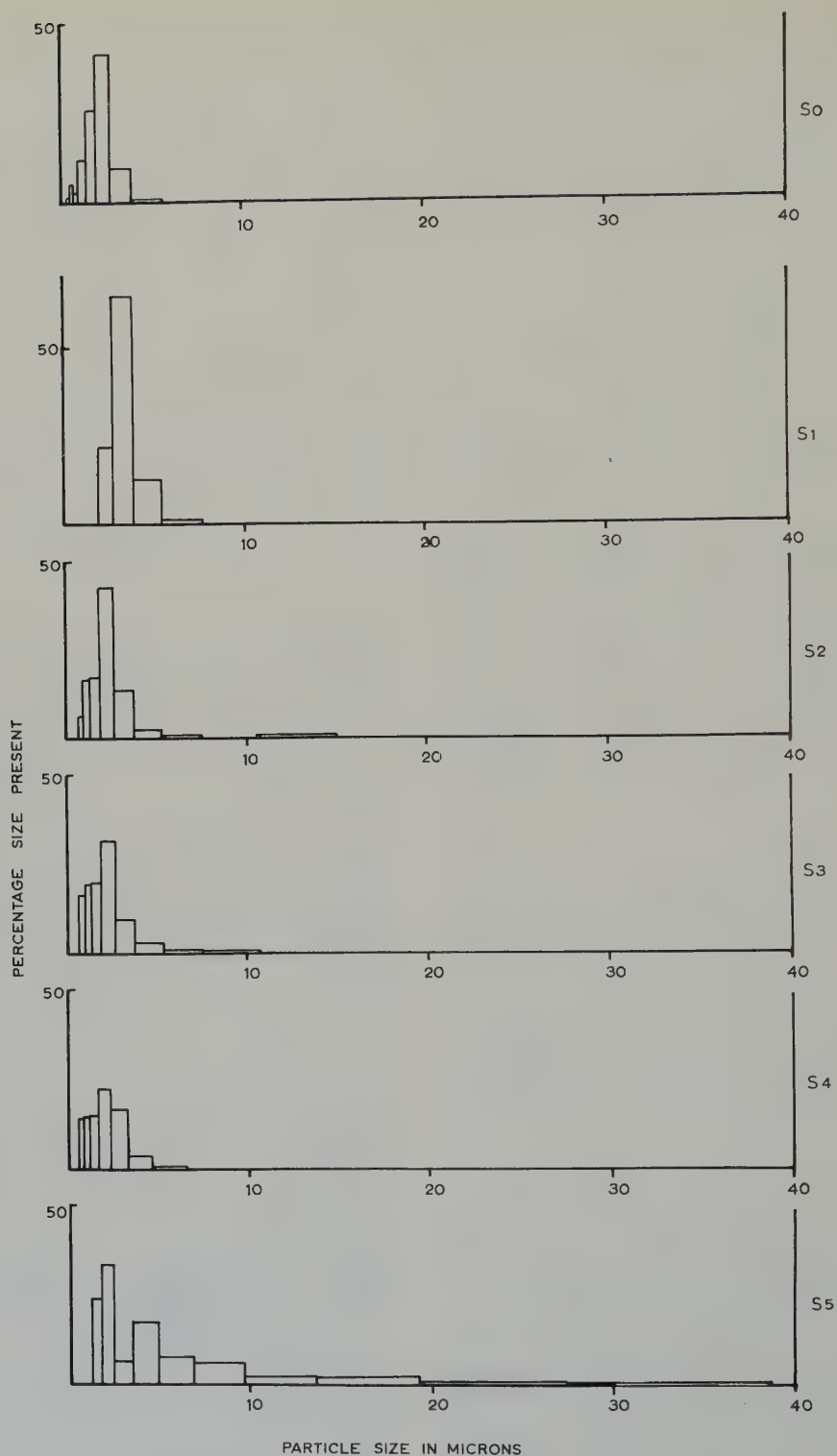


Fig. 3. Particle-size distributions in uranium after isothermal anneal at 1010°C and oil-quenching. S₀ - As provided. S₁ - 30 minutes. S₂ - 1 hour. S₃ - 1.5 hours. S₄ - 2 hours. S₅ - 120 hours. The ordinate represents the number of particles of each size-group present expressed as a percentage of the total number of particles counted.

difficult, as there is a wide scatter of grain-sizes within a specimen; the following are the approximate values obtained: As received (as-cast), 0.04 mm; 2 hours at 694° C and oil-quenched (i.e. beta-quenched), 0.02 mm; 45 hours at 907° C and oil quenched (i.e. gamma-quenched), followed by 2 hours at 694° C and oil quenched, 0.02 mm.

2.4. TENSILE TESTS

2.4.1. Room temperature tests

At these temperatures uranium fractures in a brittle manner, giving a fracture of fibrous appearance. The tensile specimens were pulled to fracture in a Hounsfield "Tensometer", at a cross-head speed of 0.20 mm/min, replicas were taken of the fracture surface, and the specimens themselves were then sectioned and examined as described above, together with several specimens pulled nearly to fracture.

The characteristic metallographic feature that was observed in these studies is that the inclusions apparently play a part in the initiation of fracture. Figs. 4-6 show the effect of the cuboid inclusions, and fig. 7 that of the "clusters". The cracking of the *dispersed* rounded inclusions in these annealed specimens was noticeably less widespread than in the as-cast material.

2.4.2. High temperature tests

These were carried out in an argon atmosphere with a modified Hounsfield "Tensometer". Replicas taken from the surface of the fracture still revealed inclusions on the fracture surface at testing temperatures up to 380° C. Optical microscopy confirmed that inclusions take part in the initiation of fracture up to this temperature.

Between 500° C and 660° C, the uranium undergoes a marked increase in ductility with extensive necking, resulting in a ductile fracture. The fracture surfaces are oxidised and so replication for these high test temperatures was not attempted. Metallographic sections of specimens deformed in this temperature range reveal, within the necked volume, holes opening

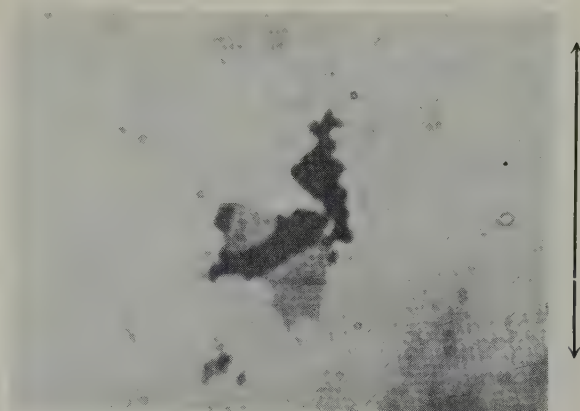


Fig. 4. As-cast uranium. Fractured specimen, area near fracture edge. Unetched. Arrow shows direction of tensile strain. $\times 2040$.

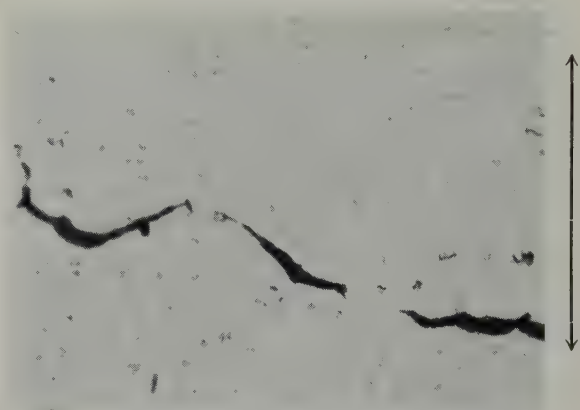


Fig. 5. As-cast uranium. Crack within the gauge-length of a tensile specimen fractured at room temperature. Unetched. $\times 350$.

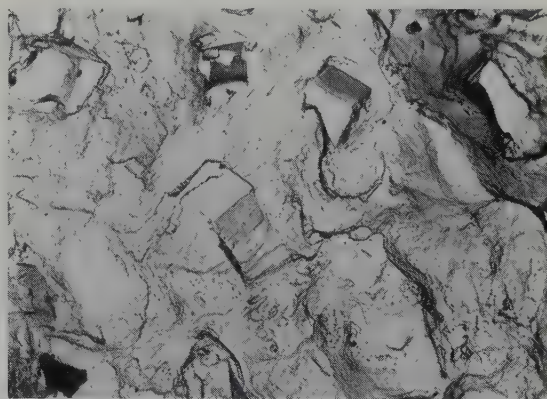


Fig. 6. Electron micrograph. Two-stage carbon replica, gold-palladium shadowed of a room temperature fracture surface. Specimen as-cast. $\times 1400$.

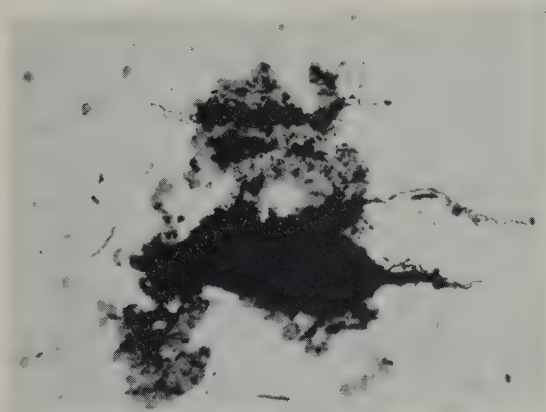


Fig. 7. Uranium annealed 6 hours 1000° C, oil quenched, then annealed 2 hours 694° C, oil quenched. 10 % room temperature tensile elongation. Unetched. $\times 350$.

out which are associated with the inclusions (fig. 8). The annealed specimens and the as-cast material both behave in the same manner. The large "cluster-like" groups of coagulated inclusions found in the annealed specimens provide most of the nuclei for the holes and these eventually coalesce to form the ductile fracture edge.

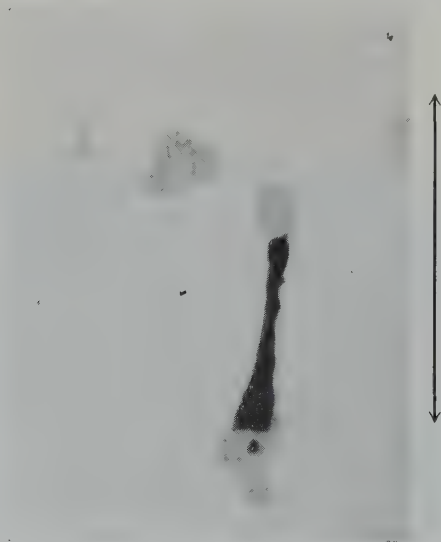


Fig. 8. Uranium heated 2 hours 694° C, oil quenched. Specimen fractured at 590° C. Region near fracture-edge, unetched. $\times 1425$.

3. Discussion

3.1. COAGULATION OF INCLUSIONS

Annealing at 1010° C leads to an increase in the number of large particles, as is clear from histogram S_5 in fig. 3. In the calculation, the assumption that the particles are spherical prevents too much weight being given to the curves representing the growth of the larger particles and the clusters referred to above. Although some of the histograms show an increase in the number of smaller particles with increasing time of anneal, it can be readily established that there is a decrease in the *volume* of inclusions less than (say) 3.0 μ diameter, per unit volume of metal.

Thus we can infer that the larger particles tend to grow at the expense of the smaller — a common phenomenon which can be explained by surface energy considerations.

3.2. FRACTURE AT ROOM TEMPERATURE

It has been demonstrated metallographically that tensile failure in uranium is initiated by the prior cracking of the inclusions or by the parting of an inclusion matrix interface at right-angles to the applied tensile strain. Fig. 4 shows a cuboid inclusion which has cracked, and the crack is beginning to propagate into the surrounding matrix. Fig. 5 shows a series of inclusions which have cracked or separated, and the resulting cracks are joining up to form the fracture edge. The electron micrograph of a replica of the fracture surface (fig. 6) shows these cuboid inclusions lying on the surface. Examination of the fracture surface of annealed specimens reveals that the cracks originate from the large "clusters" formed during the heat-treatment (fig. 7).

The effect of hydride distribution on the tensile properties of uranium has been studied by Gardner and Riches¹⁵). They included no fractography, although the hydride did seem to affect fracture. A photomicrograph in their paper includes a crack associated with a cuboid inclusion, but no comment was made.

The general observations made in the present

work on the effect of deformation upon inclusions is in general agreement with work on other systems. For example, inclusions in steels have been known to crack during mechanical working¹⁶⁾, and Frith¹⁷⁾ and Cummings *et al.*¹⁸⁾ have found that fatigue failure in certain steels is associated with inclusions. Nishimatsu and Gurland¹⁹⁾ studying the fracture path of the two-phase alloy system wolfram carbide/cobalt, have found that the cracks originate at the hard but brittle wolfram carbide phase.

3.3. FRACTURE AT HIGH TEMPERATURE

Up to 380° C the fracture is still associated with the inclusions in the above-mentioned brittle manner. A transition occurs between 380° C and 450° C, over which range the specimens are observed to become increasingly more ductile. At temperatures above 450° C, the inclusions are not sources of sharp cracks, but void formation takes place in their vicinity (fig. 8). This type of ductile failure has been observed by Puttick²⁰⁾ in copper, the voids forming at oxide inclusions. A similar explanation may be advanced in the present case, of the inclusions acting as vacancy sinks.

It may be stated in conclusion, therefore, that further study of the role played by the inclusions present in commercial uranium in the deformation and fracture of this material would be very rewarding.

Acknowledgements

The authors are grateful to Professor W. Hume-Rothery, O.B.E., F.R.S., Isaac Wolfson Professor of Metallurgy at Oxford, for his encouragement, and for the laboratory facilities made available, to many members of the staff of the Metallurgy Division, AERE, Harwell, for valuable discussions, and to Dr. S. L. Altmann for advice on the statistical analysis. One

of them (D.M.D.) is indebted to the United Kingdom Atomic Energy Authority for a Research Bursary, during the tenure of which the work was carried out.

References

- 1) L. Grainger, Uranium and Thorium (London, Newnes, 1958)
- 2) F. G. Foote, Progress in Nuclear Energy (1956) 148
- 3) H. H. Chiswick and R. M. Mayfield, Argonne National Laboratory (USA) Report, ANL-5296 (1956)
- 4) L. L. Marsh, C. T. Muehlenkamp and G. K. Manning, Battelle Memorial Institute (USA) Report, BMI-980 (1955)
- 5) G. Y. Sergeyev, V. V. Titova, Z. P. Nikolaeva, A. M. Kapeltsev and L. I. Kolobneva, Proc. 2nd. Geneva Conference, (1958) 25
- 6) A. B. McIntosh and T. J. Heal, *ibid* 413
- 7) H. H. Chiswick, A. E. Dwight, L. T. Lloyd, M. V. Nevitt and S. T. Zegler, *ibid* 394
- 8) B. W. Mott and H. R. Haines, J. Inst. Metals 80 (1951-52) 621
- 9) V. J. Haddrell, E. C. Sykes and B. W. Mott, *ibid* 84 (1956) 112
- 10) T. K. Bierlein and B. Mastel, Proc. Second Geneva Conference (1958), A/Conf. 15/P/1855
- 11) T. K. Bierlein, J. R. Morgan and G. R. Mallet, Hanford (USA) Report, HW-42184 REV (1956)
- 12) K. E. G. Meredith and M. B. Waldron, J. Inst. Metals 87 (1959) 311
- 13) G. L. Kehl, E. Mendel, E. Jaraiz and M. H. Mueller, Trans. ASM 51 (1959) 717
- 14) E. D. Hyam and J. Nutting, J. Iron and Steel Inst. 184 (1956) 148
- 15) H. R. Gardner and J. W. Riches, Trans. ASM 52 (1960) 728
- 16) F. B. Pickering, J. Iron and Steel Inst. 189 (1958) 148
- 17) P. H. Frith, Fatigue tests on rolled alloy steels, Iron and Steel Inst., Special Report No. 50
- 18) H. H. Cummings, F. B. Stulen and W. C. Schulte, Trans. ASM 49 (1957) 482
- 19) C. Nishimatsu and J. Gurland, Trans. ASM 52 (1960) 469
- 20) K. E. Puttick, Phil. Mag. 4 (1959) 964

CONTRIBUTION A L'ETUDE DE L'OXYDATION DE L'URANIUM DANS L'ANHYDRIDE CARBONIQUE AUX TEMPERATURES ELEVEES

J. PAÏDASSI, M. L. POINTUD, R. CAILLAT et R. DARRAS

*Centre d'Etudes Nucléaires de Saclay, Département de Métallurgie, Service de Chimie des Solides,
Gif-sur-Yvette (S. & O.) France*

Reçu le 20 juillet 1960

Des échantillons d'uranium de pureté nucléaire polis mécaniquement ont été soumis, dans l'intervalle 100-700° C, à l'action de l'anhydride carbonique très soigneusement purifié en oxygène et en vapeur d'eau, et leur oxydation a été suivie à la fois par voie gravimétrique à l'aide d'une thermobalance Eyraud et par voie micrographique.

Les points suivants ont pu être dégagés:

1) Les courbes d'augmentation de poids en fonction du temps sont sensiblement linéaires, mais dans l'intervalle 550-700° C, elles présentent une ou plusieurs brisures, ce qui s'explique en partie par l'agrandissement des échantillons au cours de l'oxydation.

Les augmentations de poids trouvées sont d'ailleurs nettement plus faibles que celles publiées jusqu'à ce jour, ce qu'il faut attribuer très vraisemblablement à une pureté plus grande de l'anhydride carbonique mis en oeuvre.

2) Dans l'intervalle 200-400° C, on observe la formation, sur un film d'oxyde très mince et continu, de "germes" d'oxyde grossièrement circulaires et d'épaisseur nettement plus grande que celle du film, germes qui se transforment en véritables pustules entre 400 et 500° C; ces germes ou ces pustules se forment préférentiellement sur les rayures de polissage et sur certaines inclusions, probablement des carbures.

3) Au voisinage des pustules, le métal subit une déformation plastique importante qui s'accompagne de la fissuration du film mince continu.

4) Aux températures d'oxydation supérieures à 600° C, les pustules rétrogradent fortement, mais il apparaît une déformation générale de l'échantillon qui s'agrandit considérablement, ce qui entraîne une fissuration importante de la pellicule.

Specimens of mechanically polished reactor grade uranium were treated at 100-700° C in carbon dioxide, very carefully purified from oxygen and water vapour, and their oxidation was followed simultaneously by

gravimetry (using an Eyraud thermobalance) and by micrography. The following observations were made:

1) The plots of weight gain as a function of time are sensibly linear, but in the range 550-700° C they have some breaks, which is partly attributable to the enlargement of the samples during oxidation. The weight gains found are moreover distinctly smaller than those hitherto reported, which is very probably due to the greater purity of the carbon dioxide used.

2) In the range 200-400° C, roughly circular oxide "nuclei" form upon a very thin, continuous oxide film. These nuclei are distinctly thicker than the film, and between 400 and 500° C they turn into blisters. Nuclei and blisters form preferentially on polishing scratches and on certain inclusions, probably carbides.

3) Near the blisters, the metal undergoes pronounced plastic deformation which results in cracking of the previously continuous thin film.

4) When the oxidation temperature exceeds 600° C, the blisters retreat considerably, but the whole specimen now deforms and grows, which leads to pronounced cracking of the scale.

Mechanisch polierte Uranproben von nuklearer Reinheit wurden zwischen 100 und 700° C der Einwirkung von Kohlendioxyd unterworfen. Das verwendete Kohlendioxyd war mit Sauerstoff und Wasserdampf sorgfältig vorgereinigt worden. Die Oxydation wurde gravimetrisch mit einer Eyraud-Thermowaage und mikroskopisch verfolgt.

Folgende Feststellungen liessen sich treffen:

1) Die Gewichtszunahme erfolgt streng linear mit der Zeit. Im Temperaturbereich von 550 bis 700° C treten ein oder mehrere Knicke im linearen Verlauf auf, die teilweise mit einer Volumenzunahme der Probe während der Oxydation zu erklären sind.

Die hier beobachteten Gewichtszunahmen sind übrigens deutlich geringer als die bislang veröffentlichten Werte. Dies ist sehr wahrscheinlich der

wesentlich grösseren Reinheit des hier verwendeten Kohlendioxyds zuzuschreiben.

2) Zwischen 200 und 400° C beobachtet man die Bildung ungefähr kreisrunder "Oxydkeime", die sich mit merklich grösserer Dicke auf dem schwachen, kontinuierlichen Oxydfilm aufbauen. Diese Keime wachsen bei 400 bis 500° C zu wirklichen Ausblühungen aus. Sie entstehen vornehmlich an Schleifkratzern und an bestimmten Einschlüssen, die vermutlich aus Karbid bestehen.

1. Introduction

La réaction de l'uranium avec l'anhydride carbonique a déjà fait l'objet de plusieurs recherches¹⁻⁵), qui ont été motivées surtout par des raisons d'ordre technologique. Effectivement, la connaissance de la cinétique de cette réaction est importante dans le cas d'une rupture de gaine dans les réacteurs atomiques dont le combustible est l'uranium métallique et dont le refroidissement est assuré par du gaz carbonique.

La première étude sur la réaction de l'uranium avec l'anhydride carbonique a été effectuée en 1947 au National Physical Laboratory¹⁾ et l'intervalle 250–700° C a été exploré. Huddle²⁾ a étudié la même réaction dans l'intervalle 175–500° C et Sylvester³⁾ à la température de 500° C. Champeix et Darras⁴⁾ ont étudié la réaction dans les intervalles 400–700° et 300–600° C, sous une pression d'anhydride carbonique de respectivement 1 et 15 atmosphères, dans des conditions statiques dans le premier cas et avec un débit gazeux de 5 m³/h dans le deuxième. Enfin, récemment, Antill et ses collaborateurs⁵⁾ ont étendu l'étude à l'intervalle 500–1000° C. L'oxyde formé est toujours UO₂.

Les données recueillies au cours de ces recherches paraissent suffisantes pour prévoir l'ordre de grandeur de la vitesse de la réaction entre l'uranium et l'anhydride carbonique en cas de rupture de gaine. Cependant, au point de vue fondamental, elles sont insuffisantes, puisqu'elles ont été obtenues en mettant en oeuvre un anhydride carbonique impur, contenant en particulier environ 600 ppm d'oxygène^{4,5)}.

3) In der Nachbarschaft der Ausblühungen unterliegt das Metall einer beträchtlichen plastischen Verformung, die mit einem Aufreissen des dünnen, kontinuierlichen Oxydfilms verbunden ist.

4) Bei Oxydationstemperaturen über 600° C werden die Ausblühungen stark rückgebildet. Dafür wird eine allgemeine Deformation der Proben zusammen mit einer beträchtlichen Volumenvergrösserung festgestellt, unter deren Auswirkungen die Oberfläche merklich aufreisst.

Compte tenu de ce fait et des divergences entre les résultats obtenus par les différents auteurs, nous avons jugé désirable de reprendre l'ensemble de la question dans un ample intervalle de températures (100–1000° C). Dans cette publication, nous nous proposons d'exposer nos résultats dans l'intervalle 100–700° C.

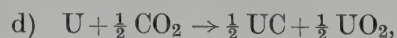
2. Réactions possibles

On peut envisager les réactions suivantes entre l'uranium et l'anhydride carbonique; les changements d'énergie libre ΔF ont été formulés entre 25 et 665° C par Kubaschewski et Evans⁶⁾, rapportés à un atome-gramme de métal:

- a) $U + 2 CO_2 \rightarrow UO_2 + 2 CO$, avec:
 $\Delta F = -125\,000 - 6,2 T \log T + 18,95 T$
 soit $\Delta F_{500^\circ C} = -124\,200$ cal.
 Le CO formé peut être réduit à son tour:
- b) $U + 2 CO \rightarrow UO_2 + 2 C$, avec:
 $\Delta F = -206\,600 - 6,2 T \log T + 102,35 T$.
 Ce qui conduit à la réaction:
- c) $U + CO_2 \rightarrow UO_2 + C$, avec:
 $\Delta F = -165\,800 - 6,2 T \log T + 60,65 T$
 soit $\Delta F_{500^\circ C} = -132\,700$ cal.

Comme on le voit, ces variations d'énergie libre sont considérables, tant pour la réaction a) que pour la réaction c). Cependant, l'importance relative des deux réactions n'est pas connue.

D'après Katz et Rabinowitch⁷⁾, le carbone libéré dans la réaction c) réagirait à 750° C sur l'uranium, de sorte que, finalement, il se formerait simultanément du carbure d'uranium et du bioxyde suivant la réaction:



En adoptant pour expression de la variation d'énergie libre de formation de UC en fonction de la température celle établie par ⁸⁾, nous obtenons:

$$\Delta F = 185\,090 - 6,45 T \log T + 61,0 T,$$

soit $\Delta F_{500^\circ\text{C}} = -76\,100 \text{ cal.}$

Champeix et Darras ⁴⁾ ont également mis en évidence du carbure UC dans les produits de réaction à 600 et à 700° C.

3. Techniques opératoires

L'uranium utilisé avait été élaboré à l'usine du Bouchet (réduction du fluorure d'uranium UF₄ par le calcium), qui fournit de l'uranium ayant pour analyse type:

Ag	< 0,5 ppm	Li	< 2 ppm
Al	120 ppm	Mg	≤ 50 ppm
B	0,1 ppm	Mn	8 ppm
C	130 ppm	Mo	< 20 ppm
Cd	< 0,5 ppm	Na	< 5 ppm
Cr	14 ppm	Ni	11 ppm
Cu	23 ppm	P	≤ 50 ppm
Fe	68 ppm	Pb	5 ppm
K	< 50 ppm	Si	50 ppm

Les échantillons, de dimensions 15×11 mm, furent découpés dans une bande laminée de 1 mm d'épaisseur présentant une texture d'orientation partielle, les plans (021) tendant à se placer parallèlement à la surface de l'échantillon. Leur préparation ne comportait qu'un polissage mécanique jusqu'au papier émeri 4/0, parachevé éventuellement par un polissage à la poudre de diamant (4–8 microns), et un lavage soigné au toluène. Pour préciser l'influence des impuretés du gaz sur la cinétique de l'oxydation, les échantillons ont été soumis dans l'intervalle 100–700° C à l'action d'anhydrides carboniques présentant trois teneurs différentes en oxygène, et en vapeur d'eau. Ces dernières d'ailleurs, faute d'analyseur suffisamment précis, n'étaient pas déterminées, sauf exception, mais simplement caractérisées par la technique de purification adoptée pour le gaz. Les trois qualités de gaz carbonique mises en oeuvre dans les trois séries successives d'expériences sont définies ci-dessous:

1ère série: CO₂ "technique", contenant 600 ppm d'oxygène, desséché à travers une colonne de perchlorate de magnésium.

2ème série: CO₂ "spécial", contenant moins de 50 ppm d'oxygène à la sortie du tube commercial, purifié ensuite au moyen d'une colonne de cuivre réduit, chauffé à 400° C, et d'une colonne de perchlorate.

3ème série: CO₂ "très pur", primitivement identique à celui utilisé dans la 2ème série, mais purifié au moyen de deux colonnes de perchlorate, une colonne de P₂O₅ et 2 colonnes de cuivre placées en série †.

L'oxydation des échantillons était effectuée dans une thermobalance à enregistrement électronique Eyraud, sensible au $\frac{1}{10}$ de milligramme. On prenait la précaution de préchauffer préalablement les échantillons sous vide poussé (<10⁻⁴ mm Hg) jusqu'à la température de l'expérience, après quoi l'anhydride carbonique était introduit dans le tube laboratoire sous un débit de 300 cm³/minute.

Après oxydation, l'augmentation totale de poids de chaque échantillon était déterminée à l'aide d'une balance analytique (sensibilité $\frac{1}{20}$ mg) et ce dernier était soumis à un examen micrographique approfondi.

4. Résultats

4.1. CINÉTIQUE DE L'OXYDATION

Les diagrammes des figures 1 à 3 résument les résultats obtenus. Quelle que soit la pureté de l'anhydride carbonique utilisé, on constate que la pellicule formée n'est pas protectrice, puisque les courbes d'augmentation de poids en fonction de la durée d'oxydation sont sensiblement linéaires ou à allure accélérée. Cependant, pour une même température, la pente de la droite ou la pente moyenne de la courbe diminue fortement quand on passe de l'anhydride carbonique "technique" (fig. 1) à celui "très pur" (fig. 3).

† Aux laboratoires de Culcheth, où la technique de purification de l'anhydride carbonique était analogue à celle-ci, des mesures précises ont montré que le gaz purifié contenait moins de 5 ppm d'oxygène et moins de 5 ppm de vapeur d'eau ⁹⁾.

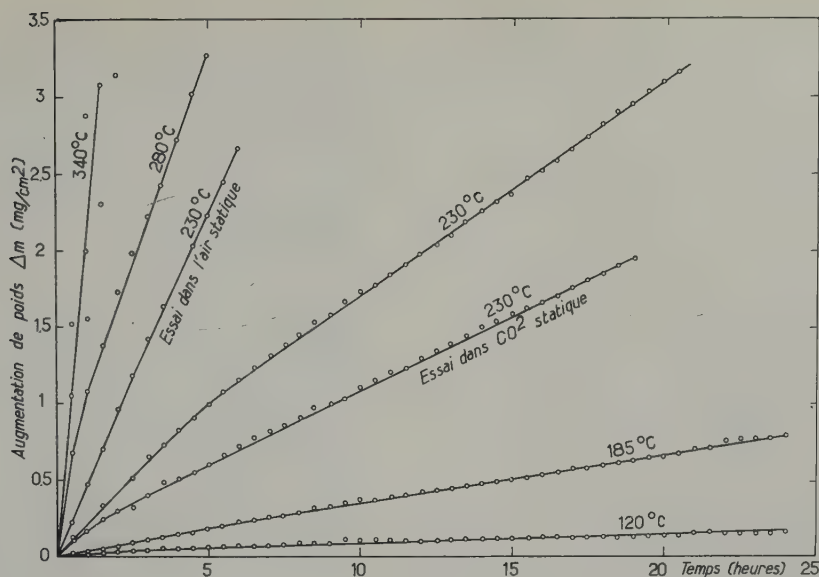


Fig. 1. Oxydation de l'uranium dans l'anhydride carbonique "technique", contenant 600 ppm d'oxygène (1ère série). Débit gazeux: $300 \text{ cm}^3/\text{min}$ (sauf pour l'essai "statique"). A titre de comparaison, la courbe d'oxydation dans l'air à 230°C a été tracée également.

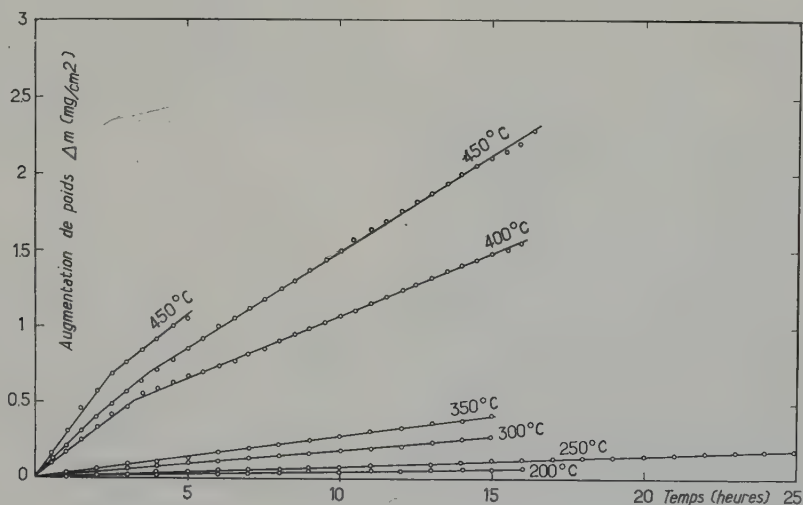


Fig. 2. Oxydation de l'uranium dans CO_2 "spécial" (2ème série).

Ceci montre l'influence primordiale des traces d'oxygène et de vapeur d'eau sur la vitesse d'oxydation de l'uranium dans ce gaz et rend indispensable sa purification très efficace si on veut atteindre la cinétique véritable du phénomène.

En outre, il y a lieu de remarquer que les augmentations de poids relatives à la 3ème série d'expériences sont nettement plus faibles que toutes celles publiées jusqu'à ce jour (fig. 4),

ce qu'il faut très vraisemblablement attribuer à une pureté plus grande de l'anhydride carbonique mis en oeuvre. Il n'est pas exclu toutefois que certaines impuretés contenues dans le métal, notamment le carbone, puissent également contribuer à augmenter l'oxydabilité de l'uranium.

D'ailleurs, les augmentations de poids mesurées dans le gaz carbonique "très pur" sont si faibles que seules les courbes isothermes pour

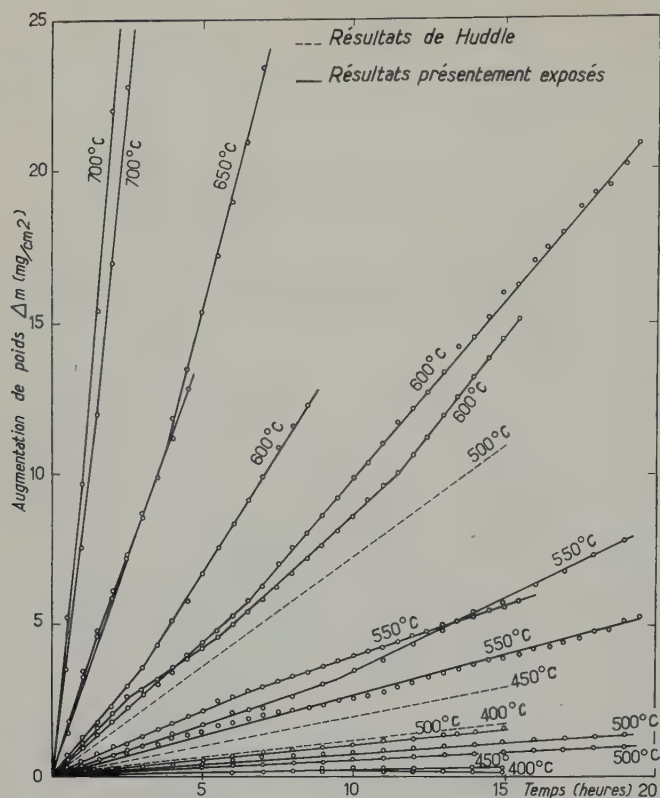


Fig. 3. Oxydation de l'uranium dans CO_2 "très pur" (3ème série).

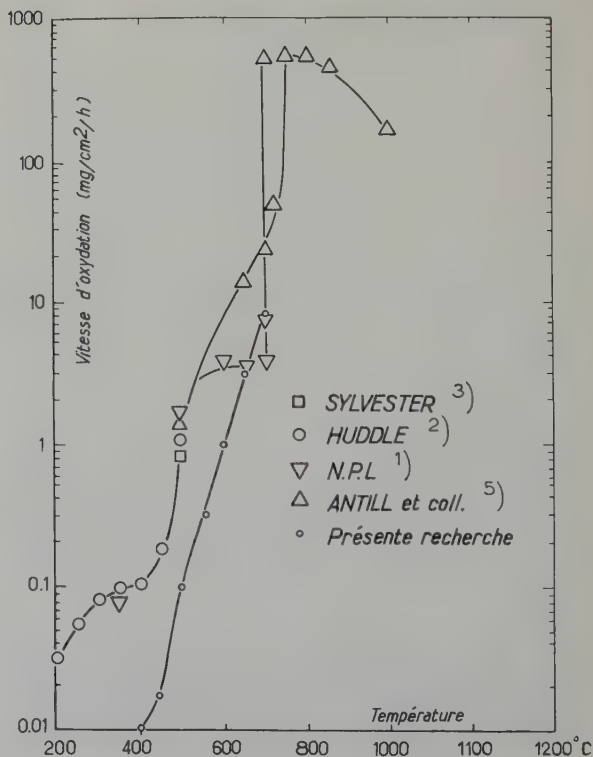
les températures égales ou supérieures à 400° C ont pu être tracées.

La purification poussée de l'anhydride carbonique entraîne une autre conséquence. Alors que la pellicule obtenue par oxydation de l'uranium dans le gaz "technique" se présente sous forme pulvérulente, celle formée dans le gaz "très pur" est au contraire compacte à l'examen visuel et parfaitement adhérente au support métallique. Cela explique qu'il y ait concordance parfaite, dans ce dernier cas, entre les augmentations de poids obtenues sur les courbes enregistrées à la thermobalance, et celles mesurées par pesée directe des échantillons oxydés, le refroidissement des échantillons et leur manipulation n'entraînant aucun détachement appréciable d'oxyde.

4.2. MORPHOLOGIE DES PELLICULES

Nous nous référerons surtout ici à la morphologie des pellicules obtenues dans l'anhydride carbonique "très pur". Cependant, la morphologie des pellicules relatives au gaz "spécial" est

Fig. 4. Comparaison des résultats relatifs à la période initiale de l'oxydation avec ceux des publications précédentes.



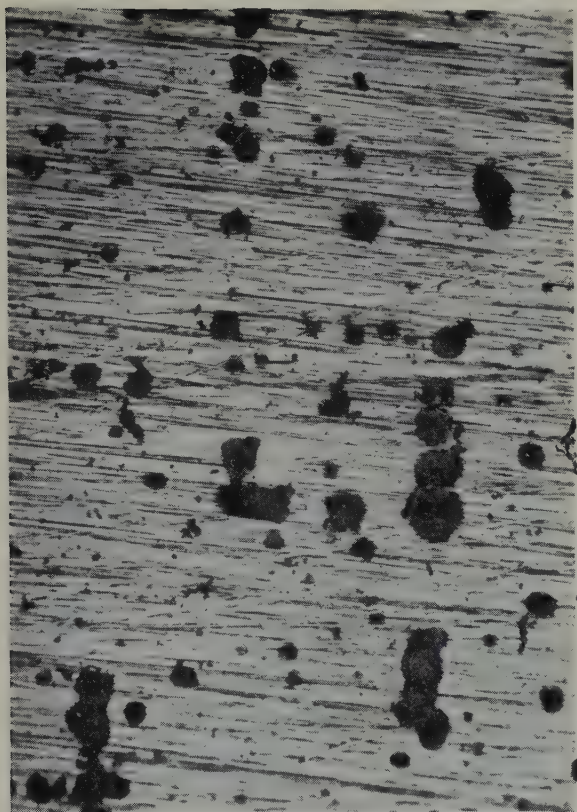


Fig. 5. Surface d'uranium oxydé dans CO_2 "spécial" à 300°C pendant 15 heures. $\times 575$.

sensiblement analogue à la précédente, si ce n'est que, toutes choses égales par ailleurs, les pellicules sont plus épaisses. Quant aux pellicules formées dans l'anhydride carbonique "technique", comme nous l'avons déjà dit, elles sont très différentes, puisqu'au lieu d'être compactes et adhérentes à leur support métallique, elles sont souvent pulvérulentes et n'ont en tout cas aucune consistance.

Précisément, dans le gaz carbonique "très pur", et entre 400 et 500°C , l'oxydation de l'uranium conduit à la formation d'un film d'oxyde très mince et continu, sur lequel on observe de place en place un "germe" d'oxyde, de forme grossièrement circulaire et d'épaisseur nettement plus grande que celle du film superficiel (fig. 5). Cela met en évidence la généralité du phénomène découvert par Bénard et Bardolle¹⁰) dans des conditions opératoires très différentes. Les germes se forment préférentielle-

ment sur les rayures de polissage (fig. 6), les bords de l'échantillon et certaines inclusions qui sont probablement des carbures (fig. 7). En outre, pour une durée d'oxydation donnée (15 heures), à mesure que la température s'élève, les germes deviennent de plus en plus volumineux; à 500°C , ils constituent de véritables pustules dont le faite est en relief de 10 à 30 microns par rapport à la surface de la pellicule continue (fig. 8). Au voisinage de ces pustules, le métal subit alors une déformation plastique importante, le mettant en relief par rapport à la surface des zones plus éloignées, déformation plastique qui s'accompagne de la fissuration du film mince continu (fig. 9). Dans la région déformée, il arrive d'ailleurs que le métal recristallise au cours de l'essai d'oxydation (fig. 10).

Aux températures d'oxydation supérieures à 500°C , les pustules rétrogradent fortement, mais il apparaît une déformation générale de

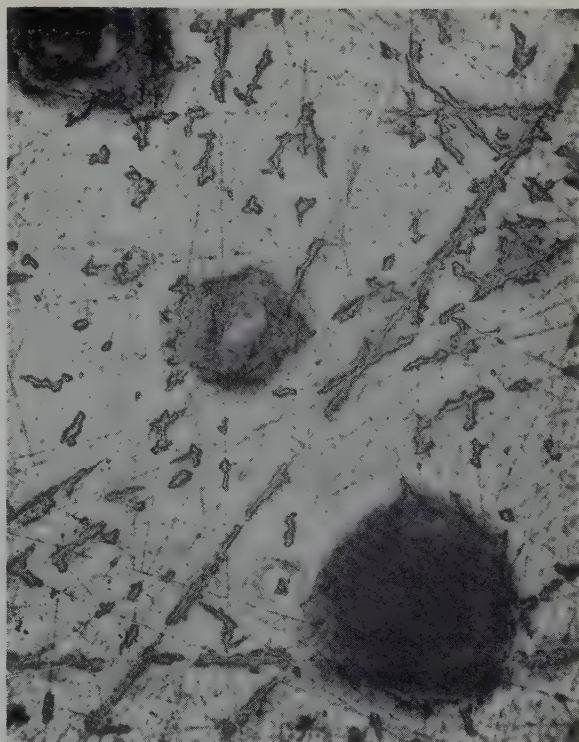


Fig. 6. Influence des rayures de polissage sur la formation des germes d'oxyde (CO_2 "très pur"). Oxydation de 15 heures à 500°C . $\times 285$.

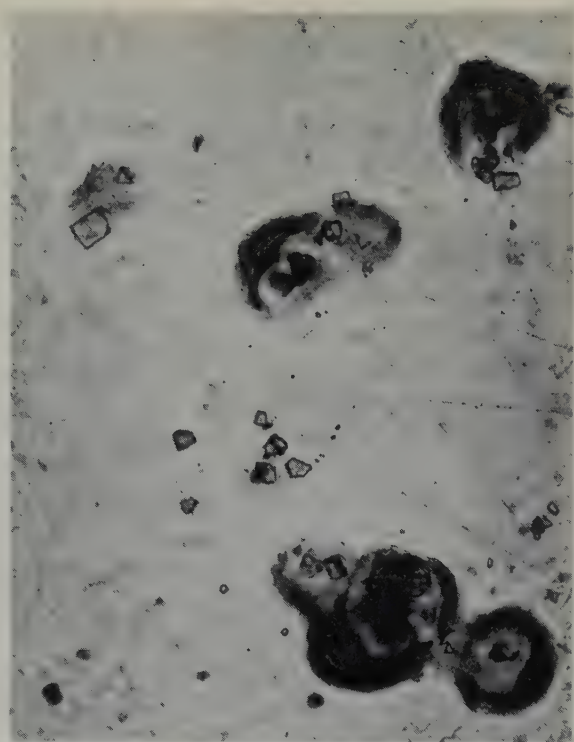


Fig. 7. Influence des inclusions sur la formation des pustules d'oxyde (CO_2 "très pur"). Oxydation de 15 heures à 450°C . $\times 285$.



Fig. 9. Aspect d'une pustule. $\times 575$.

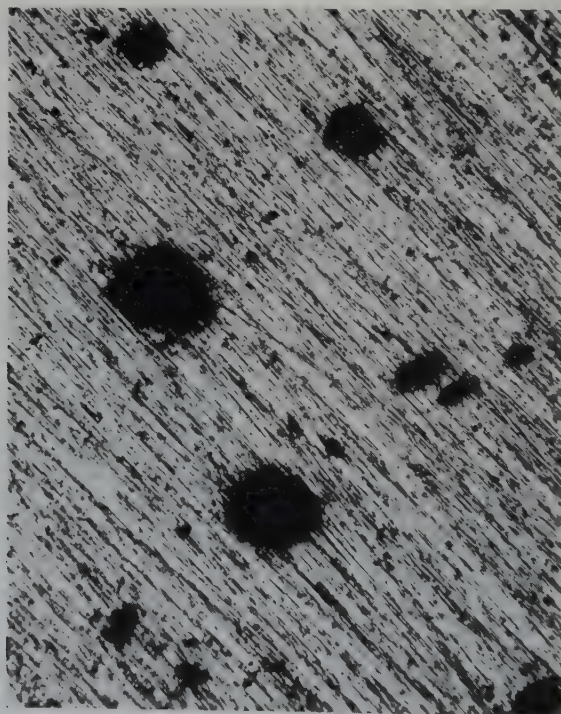


Fig. 8. Surface d'uranium après oxydation dans l'anhydride carbonique "spécial", pendant 15 heures à 450°C . Les taches sombres sont des pustules d'oxyde, dont le faite est en relief de 10 à 30 microns par rapport à la surface environnante. $\times 145$.

l'échantillon. Celui-ci prend souvent une courbure accentuée; de plus, il s'agrandit considérablement tant en longueur qu'en largeur. Par exemple, après une oxydation à 650°C pendant 15 heures, l'agrandissement de la surface de la plaquette d'uranium est d'environ 20 %, comme on peut le constater sur la macrographie de la figure 11 où les 4 échantillons avaient avant oxydation les mêmes dimensions, celles de l'échantillon 1. Cet agrandissement du support métallique entraîne à son tour une fissuration spectaculaire de la pellicule, comme on peut s'en rendre compte par l'examen des macrographies des figures 11 et 12 et des micrographies des figures 13 et 14.



Fig. 10. Aspect d'une autre pustule. Il est vraisemblable que la zone en forme de croissant qui appartenait à la région déformée du métal, a recristallisé au cours de l'essai d'oxydation, ce qui explique qu'elle ne soit plus traversée par les rayures de polissage. $\times 575$.

4.3. CONSTITUTION DES PELLICULES

Comme l'analyse aux rayons X a permis de le montrer †, quelles que soient la température et la durée d'oxydation dans l'anhydride carbonique "très pur", la pellicule était constituée d'oxyde UO_2 bien cristallisé, sensiblement stoechiométrique, avec une texture d'orientation partielle, les plans (220) de l'oxyde tendant à se placer parallèlement à la surface externe de l'échantillon. (Rappelons que l'uranium de départ avait lui-même une texture d'orientation partielle, les plans (021) tendant à se placer parallèlement à la surface de l'échantillon.)

† Spectres de diffraction aux rayons X effectués sous la direction de MM. Frisby et Portneuf.

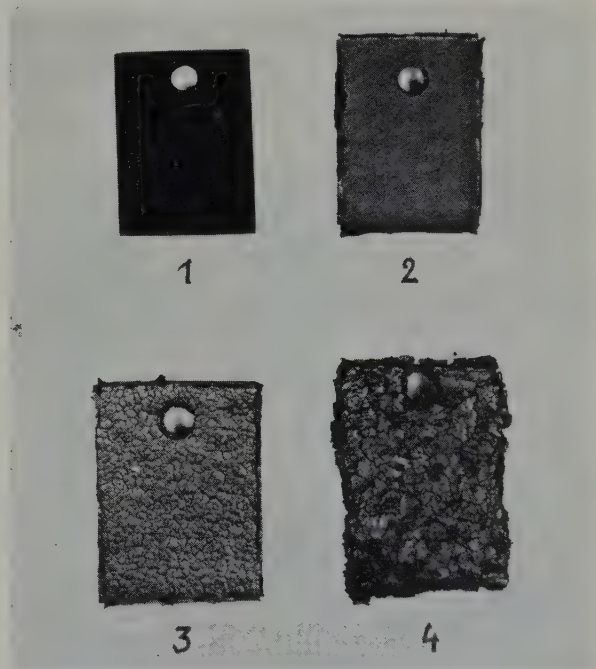


Fig. 11. Surfaces de 4 échantillons d'uranium ayant comme dimensions initiales $11 \times 15 \times 1$ mm oxydés dans l'anhydride carbonique "très pur", dans les conditions suivantes:

1. 450°C ; 15 h
2. 500°C ; 5 jours
3. 650°C ; 15 h
4. 700°C ; 3 h.

Seul l'échantillon 1 a conservé les dimensions originales, les autres se sont agrandis considérablement. $\times 1,6$.

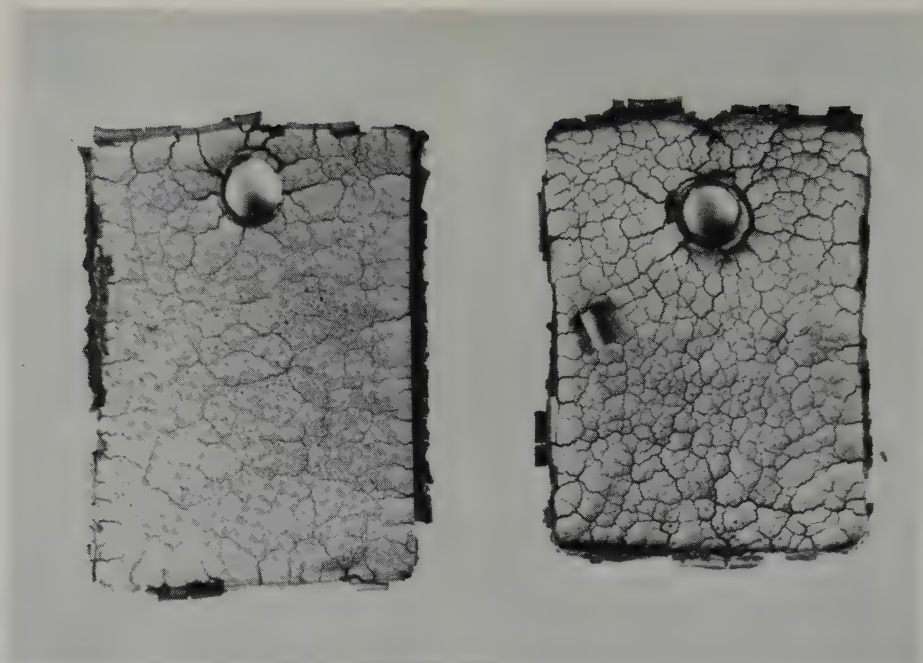


Fig. 12. Surfaces fissurées de deux échantillons d'uranium oxydés à 600° C pendant 15 h. $\times 3,2$.

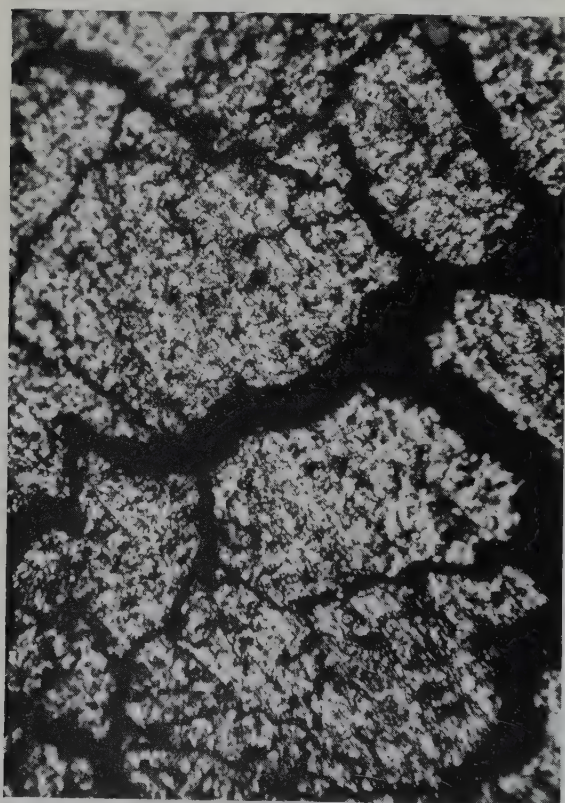


Fig. 13

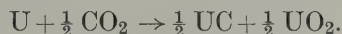


Fig. 14

Figs. 13 et 14. Surface externe d'une pellicule très fissurée, après oxydation dans CO_2 "très pur" pendant 15 heures à 650° C. (fig. 11: $\times 285$; fig. 12: $\times 575$).

De plus, dans certains cas, il a été décelé du carbure UC très finement cristallisé et représentant quelques pour cent seulement du poids de UO_2 .

La présence de carbure dans la pellicule, qui confirme les observations de Champeix et Darras ⁶⁾, ne peut s'expliquer que si l'oxydation de l'uranium par l'anhydride carbonique s'effectue en partie suivant la réaction :



Soulignons cependant que la détermination précise des conditions d'apparition de la phase UC dans la pellicule, ainsi que de sa proportion et de sa morphologie exigerait d'entreprendre une recherche complémentaire qui entre d'ailleurs dans nos projets.

5. Discussion

Etant donné que l'oxydation suit une loi linéaire, on est conduit à penser que la pellicule est, dès le début de l'oxydation, perméable à l'oxygène par suite de fissurations qui pourraient être la conséquence d'un rapport volumétrique $\frac{\text{oxyde}}{\text{métal}}$ élevé (1,94), conjointement à une plasticité insuffisante de l'oxyde UO_2 .

Mais une question se pose : la fissuration de la pellicule s'étend-elle jusqu'à l'interface métal-oxyde, ou bien existe-t-il au contact du métal un film d'oxyde mince, compact et adhérent, à travers lequel s'effectuerait la diffusion des ions. L'existence d'un tel film avait été suggérée par Loriers ¹¹⁾ pour expliquer les particularités de l'oxydation du cérium dans l'oxygène, et surtout récemment par Gregg et Jepson ¹²⁾ pour expliquer l'allure des courbes d'augmentation de poids dans le cas de l'oxydation du magnésium sous oxygène sec ou humide.

Une preuve micrographique directe de l'existence d'un tel film est très difficile à fournir, vu sa faible épaisseur et la quasi-impossibilité de distinguer les zones de la pellicule, fissurées ou non, quand les fissures sont submicroscopiques. Il faut d'ailleurs noter que les auteurs précédents observaient, aussi bien pour le cérium que pour le magnésium, une période initiale à cinétique d'oxydation parabolique ; dans le cas du magnésium, sa durée était très courte (2 heures au maximum) et les augmentations de poids étaient très faibles (de l'ordre du $\mu\text{g}/\text{cm}^2$). Dans le cas présent de l'uranium, cette période initiale apparaît encore plus courte, bien qu'elle

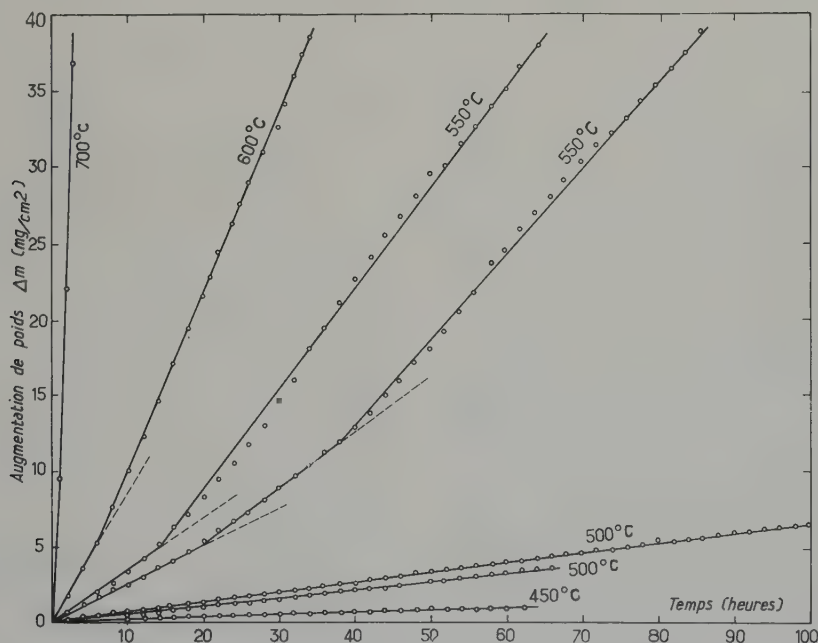


Fig. 15. Oxydation de l'uranium dans CO_2 "très pur".

n'ait pas été étudiée en détail, et dans ce qui suit, elle sera négligée, vu l'échelle des courbes représentées.

Quoi qu'il en soit, l'examen des figures 3 et 15 montre que, jusqu'à 500° C, chaque courbe d'oxydation est constituée par une seule droite passant par l'origine, alors qu'au-dessus de 500° C, plusieurs segments de droites apparaissent, dont les pentes sont d'autant plus prononcées qu'ils sont plus éloignés de l'origine. D'ailleurs, la durée d'oxydation qui correspond à la première brisure diminue en même temps que la température d'essai augmente: de 14 à 20 heures à 550° C, elle n'est plus que de 3 à 7 heures à 600° C. Cette constatation laisserait effectivement supposer la présence d'un film très mince, compact et adhérent sur le métal, sous-jacent à la couche d'oxyde épaisse extérieure. Il suffirait en effet d'admettre, conformément aux conceptions de Gregg et Jepson ¹²⁾, que l'oxydation linéaire initiale correspond à un état stationnaire où les vitesses de croissance et de fissuration du film sont égales; une augmentation de la vitesse d'oxydation correspondrait alors à un état où les fissurations s'étendraient plus profondément dans le film, et, dans le cas d'une vitesse d'oxydation finale stable, à un état où ces fissures atteindraient l'interface métal-oxyde lui-même.

Cependant, au-dessus de 550° C, un autre phénomène est susceptible d'intervenir: il s'agit de l'agrandissement général de l'échantillon métallique, décrit précédemment. D'où une accélération de la vitesse d'oxydation, comme simple conséquence de l'accroissement progressif de la surface de l'échantillon.

Finalement, il semble bien que, dans le cas le plus général, les deux phénomènes se combinent, le second prenant évidemment plus d'importance lorsque la température s'élève. Ils ne sont d'ailleurs pas indépendants l'un de l'autre, puisqu'au moins aux températures élevées, l'agrandissement peut être une cause de fissurations: cela expliquerait l'absence de brisures sur les courbes correspondant aux températures inférieures à 550° C, puisqu'alors le fluage est négligeable. La succession des phénomènes

serait donc la suivante: dans une période initiale, l'échantillon se recouvre d'une pellicule qui se fissure rapidement, à l'exception d'un film mince et compact adhérent au métal, et dont l'épaisseur e_0 (qui correspond à un état stationnaire où les vitesses de croissance et de fissuration du film sont égales) est indépendante du temps. Ajoutons que ce film est le siège de contraintes de compression importantes, du fait d'un rapport des volumes spécifiques $\frac{\text{oxyde}}{\text{métal}}$ voisin de 2. A un certain moment, l'âme métallique soumise, elle, à des contraintes de traction, et dont la résistance mécanique diminue en même temps que son épaisseur, commence à fluer, avec une vitesse sensiblement constante, ce qui a pour résultat de réduire l'épaisseur du film mince compact jusqu'à un nouvel état stationnaire e_1 (correspondant à une vitesse d'oxydation plus forte) et de fissurer de façon spectaculaire la pellicule (fig. 13 et 14).

Ensuite, il est probable que le fluage s'accélère progressivement, du fait de la diminution

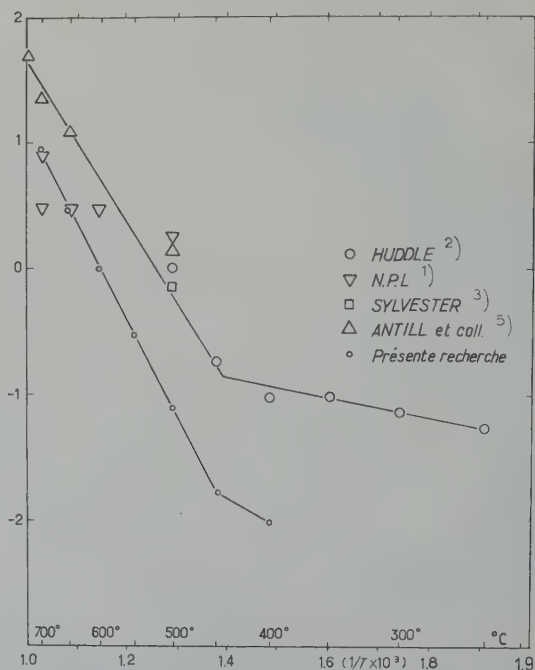


Fig. 16. Influence de la température sur la vitesse d'oxydation de l'uranium dans CO₂ "très pur" (3ème série). Représentation d'Arrhénius.

lente de l'épaisseur de l'âme métallique de l'échantillon. En tout cas, à un certain moment, le film compact devient de nouveau instable et son épaisseur e_1 devient e_2 (avec $e_2 < e_1$), d'où un nouvel accroissement de la vitesse de réaction. Finalement, les fissurations s'étendent jusqu'au métal lui-même ($e=0$) et la vitesse linéaire d'oxydation se stabilise à sa valeur maximale.

Il est d'ailleurs à remarquer que les diverses courbes d'oxydation obtenues à la suite de divers essais à une même température présentent une dispersion notable, qui doit être imputable aux caractéristiques différentes de la période initiale perturbée, notamment par suite d'un état de surface d'échantillon non rigoureusement reproductible; mais en tout cas, à une température donnée (par exemple 550°C), tous les derniers segments de droite ont une pente sensiblement égale, ce qui est bien en accord avec l'interprétation précédente (fig. 15).

Enfin, dans le cas du gaz carbonique "très pur", si on considère les courbes d'oxydation (fig. 3) avant la première brisure, c'est-à-dire lorsque l'agrandissement est encore négligeable, la variation de la constante d'oxydation k_1 en fonction de l'inverse de la température absolue $1/T$ est donnée par la figure 16. La courbe correspondante implique une énergie d'activation de $34\,400$ cal/mole dans l'intervalle $450\text{--}700^\circ\text{C}$. Cette énergie d'activation est très voisine de la valeur $29\,700 \pm 2300$ cal/mole qui, d'après Auskern et Belle¹³⁾, caractérise la diffusion de l'oxygène dans le bioxyde d'uranium. Cette concordance suggère que, parmi les quatre phénomènes intervenant dans l'oxydation de l'uranium: accès du gaz jusqu'au film mince compact et adhérent de bioxyde d'uranium par les fissures de la couche externe, dissociation de l'anhydride carbonique, diffusion de l'oxygène dans le film précédent, et enfin sa réaction à l'interface métal-oxyde, c'est bien l'avant-dernier qui détermine la vitesse de la réaction.

6. Conclusion

Compte tenu de la purification poussée de

l'anhydride carbonique et de la pureté du métal mis en oeuvre, est-il possible de conclure que les lois d'oxydation de l'uranium pur dans l'anhydride carbonique pur ont été réellement déterminées? Il en est sans doute bien ainsi aux températures supérieures à 450°C , où l'augmentation de poids qui résulterait de la fixation de la totalité de l'oxygène contenu à l'état d'impureté dans l'anhydride carbonique ayant traversé le four resterait négligeable, par rapport à l'augmentation de poids mesurée. Par contre, ce n'est pas certain dans l'intervalle $400\text{--}450^\circ\text{C}$ et *a fortiori* pour les températures inférieures à 400°C , où une purification complémentaire de l'anhydride carbonique serait indispensable, de manière à ramener sa teneur en oxygène et en vapeur d'eau à des valeurs très basses, si possible inférieures au ppm.

Quant à la cause de la formation des germes et des pustules, il apparaît prématuré de la formuler avec sûreté dans l'état d'avancement actuel de cette recherche. En effet, il est difficile de trancher si l'apparition des germes et des pustules est spécifique de la réaction de l'anhydride carbonique avec l'uranium, ou si elle est au contraire le résultat de la réaction des ultimes traces d'impuretés gazeuses de l'anhydride carbonique avec le métal ou de celle des impuretés de l'uranium avec ce gaz.

La mise en évidence au cours de cette recherche de l'agrandissement des échantillons d'uranium oxydés dans l'anhydride carbonique spécial et très pur, mérite d'être soulignée.

Cet exemple d'agrandissement vient s'ajouter à divers autres. Parmi ceux-ci il faudrait en particulier citer:

- 1) l'agrandissement du zirconium oxydé dans l'air, étudié par Baldwin *et al.*¹⁴⁾ et par Hérenguel *et al.*¹⁵⁾;
- 2) l'agrandissement de l'aluminium oxydé dans l'eau, mis en évidence par Coriou *et al.*¹⁶⁾ et étudié en détail par Hérenguel *et al.*¹⁷⁾;
- 3) l'agrandissement du manganèse oxydé dans l'air, constaté par Païdassi¹⁸⁾.

Ces exemples dont le nombre pourra être vraisemblablement augmenté dans les années qui viennent, montrent que le phénomène de

l'agrandissement des échantillons métalliques oxydés aux températures élevées présente un certain caractère de généralité, à condition que l'on prenne la précaution de se placer dans des conditions d'oxydation convenables.

Remerciements

Nous tenons à remercier MM. Frisby et Portneuf, du Service de Chimie des Solides, Département de Métallurgie, pour le concours qu'ils nous ont apporté dans la détermination, par diffraction de rayons X, de la nature des phases présentes dans les pellicules formées ainsi que de leurs textures d'orientation.

Bibliographie

- ¹⁾ N.P.L., BR 779 (1947)
- ²⁾ R. A. U. Huddle, TRDC P 36
- ³⁾ D. R. Sylvester, AERE (Harwell) Report M/R 2437
- ⁴⁾ L. Champeix et R. Darras, Commissariat à l'Energie Atomique (France) Rapport DM n° 310 (1956)
- ⁵⁾ J. E. Antill, K. A. Peakall, J. Crick et M. Gardner, AERE (Harwell) Report, M/R/2524 (1958)
- ⁶⁾ O. Kubaschewski et E. Evans, LL., Metallurgical Thermochemistry (Pergamon Press, 1958)
- ⁷⁾ J. J. Katz et E. Rabinowitch, The Chemistry of Uranium (McGraw Hill, 1951) p. 151
- ⁸⁾ A. B. Tripler, M. J. Snyder et W. H. Duckworth, Battelle Memorial Institute (USA) Report BMI-1313 (1959)
- ⁹⁾ J. Waddams, UKAEA (UK), Communication privée
- ¹⁰⁾ J. Bénard et J. Bardolle, C.R. Acad. Sci., **232** (1951) 2317
- ¹¹⁾ J. Lories, C.R. Acad. Sci. **229** (1949) 547; Thèse, Paris, 1952
- ¹²⁾ S. J. Gregg et W. B. Jepson, J. Inst. Metals **87** (1958-1959) 187
- ¹³⁾ A. B. Auskern et J. Belle, J. of Chem. Phys. **28** (1958) 1, 171
- ¹⁴⁾ C. A. Phalnikar et W. M. Baldwin, Proc. Amer. Soc. Testing Mater. **51** (1951) 1038
- ¹⁵⁾ J. Herenguel, D. Whitwham et J. Boghen, C.R. Acad. Sci., **243** (1956) 2060
- ¹⁶⁾ H. Coriou, L. Grall et J. Huré, Rev. de Métallurgie **53** (1953) 775
- ¹⁷⁾ P. Lelong et J. Hérenghuel, J. Nucl. Mat. **1** (1959)
- ¹⁸⁾ 58 J. Païdassi, 3ème colloque de Métallurgie, Centre d'Etudes Nucléaires de Saclay (France) 29-30 juin et 1er juillet 1959, (North-Holland Publishing Co, Amsterdam, 1960) p. 95

THE HIGH TEMPERATURE OXIDATION OF BERYLLIUM

PART III

IN CARBON DIOXIDE, CARBON MONOXIDE AND CARBON MONOXIDE-CARBON DIOXIDE MIXTURES

S. J. GREGG, R. J. HUSSEY and W. B. JEPSON[†]*Department of Chemistry, University of Exeter, Exeter, UK*

Received 22 July 1960

The kinetics of the oxidation of electrolytic flake beryllium in carbon dioxide, in carbon monoxide and in carbon monoxide-carbon dioxide mixtures have been measured at temperatures from 500° to 750° C. In carbon dioxide, at temperatures up to 700° C, the rate of oxidation continuously decreases with time to reach a very small value (e.g. at 700° C, 0.13 $\mu\text{g}/\text{cm}^2 \text{ h}$ after 300 h) whilst at 750° C the rate first decreases and then increases, indicating breakaway. If the carbon dioxide is admitted to the preheated sample the oxidation is very rapid at first and most of the carbon deposition occurs over this initial period. In carbon monoxide, the oxidation is non-protective above 550° C, the rate of oxidation being considerably greater than in carbon dioxide.

When beryllium is heated at 650° C in carbon monoxide-carbon dioxide mixtures containing up to 7.5 % of carbon monoxide, the kinetics are the same as in pure carbon dioxide.

La cinétique de l'oxydation de paillettes de beryllium électrolytique dans le gaz carbonique, dans l'oxyde de carbone et dans un mélange de gaz carbonique et d'oxyde de carbone a été mesurée pour des températures allant de 500° à 750° C. Dans le gaz carbonique, pour des températures allant jusqu'à 700° C, la vitesse d'oxydation décroît continuellement avec le temps pour atteindre une très petite valeur (c'est-à-dire 0.13 $\mu\text{g}/\text{cm}^2 \text{ h}$ à 700° C après 300 heures) tandis qu'à 750° C, la vitesse décroît d'abord puis croît, ce qui est l'indice d'un "breakaway". Si le gaz carbonique est admis sur l'échantillon chauffé au préalable,

l'oxydation se produit très rapidement d'abord et le carbone se déposera presque en totalité pendant cette période initiale. Dans le gaz carbonique, l'oxydation n'est pas protectrice au-dessus de 550° C, la vitesse d'oxydation étant considérablement plus grande que dans le gaz carbonique.

Quant le beryllium est chauffé à 650° C dans le mélange oxyde de carbone-gaz carbonique contenant jusqu'à 7.5 % d'oxyde de carbone, les cinétiques sont les mêmes que dans le gaz carbonique pur.

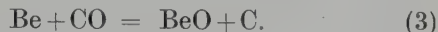
Es wurde die Oxydationskinetik von elektrolytisch hergestelltem Beryllium in Kohlendioxyd, Kohlenmonoxyd und in Mischungen beider Gase bei 500 bis 750° C untersucht. In Kohlendioxyd nimmt die Oxydationsgeschwindigkeit bei Temperaturen bis 700° C mit wachsender Versuchsdauer kontinuierlich ab und erreicht sehr kleine Werte (z.B. 0,13 $\mu\text{g}/\text{cm}^2 \text{ h}$ nach 300 Std. bei 700° C). Dagegen wird bei 750° C die Geschwindigkeit zuerst kleiner, wächst dann aber wieder an, was auf ein Aufplatzen der Oxydschicht hinweist. Wird Kohlendioxyd zu der vorgeheizten Probe zugelassen, so ist die Oxydation anfänglich sehr heftig. Dabei findet der größte Teil der Kohlenstoffablagerung während dieses ersten Zeitabschnitts statt. In Kohlenmonoxyd bilden sich oberhalb 550° C keine schützenden Deckschichten aus. Die Oxydationsgeschwindigkeit ist hier beträchtlich größer als in Kohlendioxyd.

In Mischungen von Kohlendioxyd mit 7,5 % Kohlenmonoxyd wird bei 650° C die gleiche Kinetik wie in reinem Kohlendioxyd gefunden.

1. Introduction

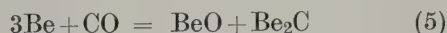
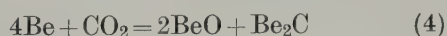
In Part II¹⁾, the chemistry of the reactions of beryllium with carbon dioxide and with carbon monoxide at temperatures of 500° C and above was elucidated, and it was demonstrated

that the following reactions occur:



[†] Now at Atomic Energy Research Establishment, Harwell, Didcot, Berks., UK.

In addition, beryllium carbide was shown to be present in the reaction product, but it was not possible to decide unequivocally whether this was formed directly by the reactions



or indirectly by reaction of beryllium with carbon deposited in (2) or (3)



The rate of carbon deposition during oxidation of beryllium in carbon dioxide at a number of temperatures was measured, and the results showed that reaction (2) only occurs to a small extent, at the beginning of the run. Accordingly, the important reaction, from the corrosion aspect, is (1).

In the present Part, the oxidation of beryllium in carbon dioxide at temperatures in the range 500°–750° C has been investigated with the vacuum microbalance. Since the method was gravimetric, the results provide information about the overall rate of oxidation [the contributions of both (1) and (2) to the total weight gain] and are thus complementary to those described in Part II. Results are also presented for the kinetics of the reactions in carbon monoxide at 500°–750° C and in three carbon monoxide–carbon dioxide mixtures at one temperature, 650° C.

2. Experimental

The electrolytic flake beryllium was of the same batch as that used in the earlier studies^{1,2}) and each sample was chemically polished³) before use in a solution of phosphoric, chromic and sulphuric acids for 30 sec at 100° C.

2.1. CARBON DIOXIDE

For oxidation in carbon dioxide, the weight gain of the sample was determined on a vacuum microbalance which had a range of 1700 μg and a sensitivity such that with a sample size of 4 cm \times 1.5 cm, a weight gain of 0.14 $\mu\text{g}/\text{cm}^2$ could be detected. Except for a few runs (which will be specifically referred to), the procedure

was much the same as that for oxidation in oxygen²), the sample being outgassed at reaction temperature before the carbon dioxide was admitted to the balance case. All the runs were carried out at a pressure of 10 cm and the carbon dioxide was either spectroscopically pure or was isotopically labelled with C^{14} ; no attempt was made to oxidise the carbon monoxide generated in reaction (1) back to carbon dioxide since the volume of the balance case was such that the maximum concentration of carbon monoxide (weight gain of 100 $\mu\text{g}/\text{cm}^2$) at the end of a run was only 0.5 %.

2.2. CARBON MONOXIDE

The course of the oxidation in carbon monoxide at approximately 10 cm pressure was followed by measuring the change of count rate and hence the decrease in pressure of carbon monoxide contained in the volumetric apparatus; the latter was similar to that described in Part II except that a ballast volume of 100 cc was attached to increase the range. A weight gain of 2 $\mu\text{g}/\text{cm}^2$ could be detected with a sample measuring 4 cm \times 1.5 cm; the radioactive carbon monoxide was prepared, as before¹), by diluting the highly active gas with spectroscopically pure inactive carbon monoxide.

3. Oxidation in Carbon Dioxide

3.1. CARBON DIOXIDE ADMITTED TO PRE-HEATED SAMPLE

Runs were carried out at temperatures in the range 500° to 750° C and at 10 cm pressure, at least one run at each temperature being continued for 300 h or longer; at 600° and 750° C, three long runs were carried out.

The reproducibility of the curves of weight gain against time was rather poor, whether the sample was "as-received" or was chemically polished. As will be seen (figs. 1 and 2), the weight gain after 70 h varied from 17 $\mu\text{g}/\text{cm}^2$ to 28 $\mu\text{g}/\text{cm}^2$ for the "as-received" samples at 550° C and from 24 $\mu\text{g}/\text{cm}^2$ to 52 $\mu\text{g}/\text{cm}^2$ for chemically polished samples at 600° C,

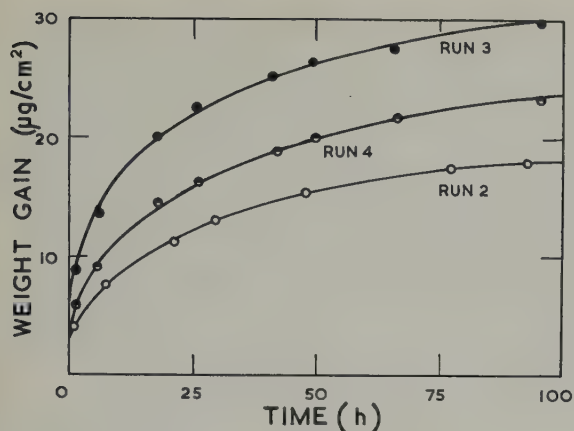


Fig. 1. Oxidation of beryllium at 550°C in carbon dioxide at 10 cm pressure; the samples were "as-received".

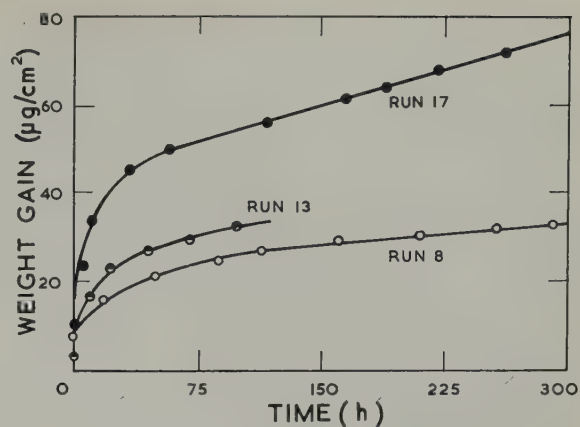


Fig. 2. Oxidation of beryllium at 600°C in carbon dioxide at 10 cm pressure; the samples were chemically polished.

The curves of weight gain against time are summarised in fig. 3 (500° to 750° C) and fig. 4 (750° C) and shown in greater detail in fig. 5 (500°, 550° and 600° C). Apart from the curve for 650° C which crosses that for 600° C, the curves fall into a regular sequence, the weight gain after 300 h increasing fairly uniformly with temperature. At temperatures in the range 500° to 700° C the rate of oxidation decreases continuously with time (fig. 3), whilst at 750° C the

rate decreases and then increases with time (runs 15 and 16, fig. 4), i.e. breakaway occurs.

All the curves show the unusual feature of a rapid weight gain over the first few minutes. At 500° and 550° C this initial weight gain was followed by a period of several hours over which the weight of the sample remained sensibly constant (fig. 6); but at higher temperatures (compare run 17 at 600° C, fig. 6) this period of constancy was not observed (except

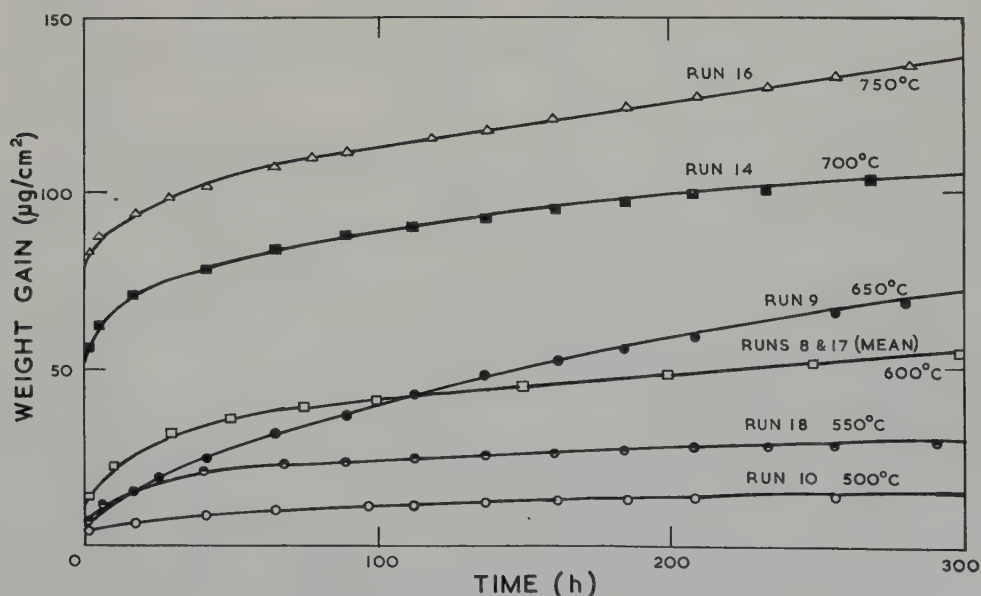


Fig. 3. Oxidation of beryllium at 500°, 550°, 600°, 650°, 700° and 750° C in carbon dioxide at 10 cm pressure. The curve for 600° C is the average of runs 8 and 17 shown in fig. 2.

perhaps in one or two cases), the oxide layer continuing to thicken, though at a reduced rate, throughout the run. The initial weight gain comprised a large percentage of the total measured weight gain (representing, for example at 750° C, about 60 % of the weight gain after 300 h, fig. 4); it was not due to instrumental

error, for at the end of each run the total weight gain checked on an analytical balance agreed well (often within $\pm 3\%$) with that registered on the microbalance; and in one test run, deliberately stopped after 30 min, the weight gains were $460 \pm 10 \mu\text{g}$ (analytical balance) and $442 \mu\text{g}$ (microbalance) respectively.

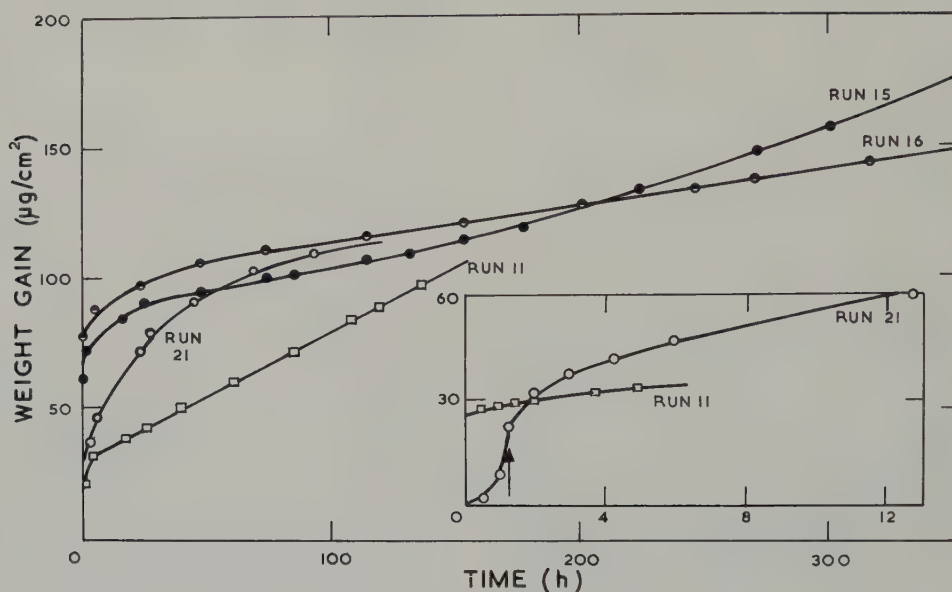


Fig. 4. Oxidation of beryllium at 750° C in carbon dioxide at 10 cm pressure. The arrow \uparrow indicates the time at which the sample in run 21 reached 750° C.

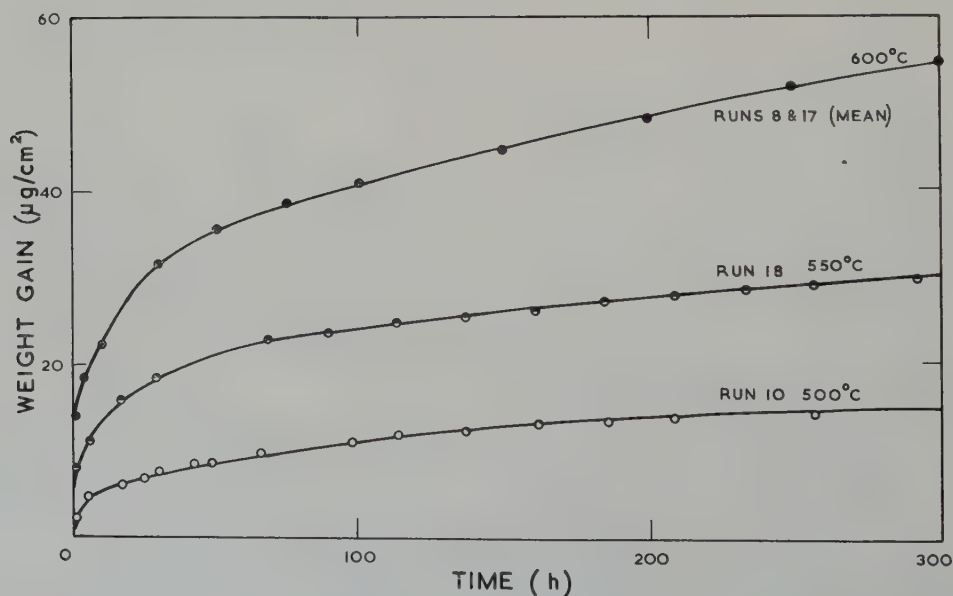


Fig. 5. Oxidation of beryllium at 500°, 550° and 600° C in carbon dioxide at 10 cm pressure.

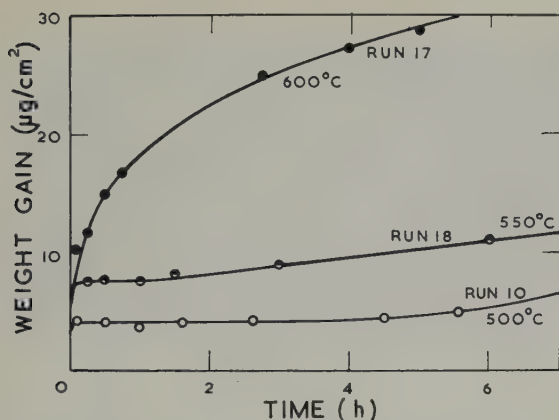


Fig. 6. The early stages of the oxidation of beryllium at 500°, 550° and 600° C in carbon dioxide at 10 cm pressure.

Along the flatter portion of the graphs the data fitted (within experimental error) the empirical equation

$$aw^2 + bw = t \quad (7)$$

where w is the weight gain at time t and a and b are constants (see fig. 7). The values of a and b , along with the time range over which the equation was found to be valid are given in table 2, together with the rate at 300 h calculated by eq. (7). The rates do not vary entirely regularly with temperature (the rate at 700° C

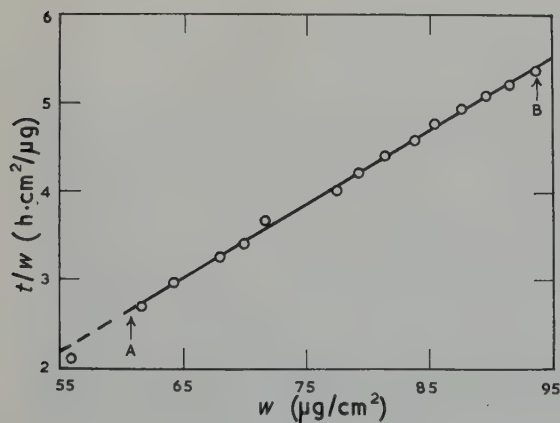


Fig. 7. Oxidation of beryllium at 600° C in carbon dioxide at 10 cm pressure. The data of run 17 are plotted as t/w against w (eq. (7)). Note that the curve is linear over the interval A (100 h) to B (500 h).

is anomalous) and at a given temperature (600° C) the duplicate values differ widely. All the rates are however relatively small and from the nature of eq. (7) they should tend to zero—unless a breakaway intervenes, as in fact happens at 750° C.

In at least one run at each temperature, the gas in the balance case was isotopically labelled with C^{14} and the amount of carbon deposited on the sample was estimated at the end of the run by direct counting using a Geiger-Müller tube with an end window 2.4 cm in diameter; counts were taken with the window placed over successive areas of the specimen (the edges being disregarded) and the reproducibility of the assay for a given sample was about 1 %. The counter was "calibrated" using a series of beryllium samples which had been oxidised on the volumetric apparatus¹).

The results for the amount of carbon deposited (w_C) on each sample are given in table 1, together with the corresponding weight (w_O) of oxygen taken up as beryllium carbide; as is seen, both w_C and the ratio $w_C:w_O$ vary somewhat erratically from specimen to specimen with perhaps a slight tendency to greater values of both w_C and the ratio $w_C:w_O$ with increasing temperature of oxidation. Although the values of w_C are expressed for convenience in terms of unit area of surface, the density of deposited carbon was by no means uniform, as can be seen from fig. 8, which shows a number of typical autoradiographs, obtained by placing each sample in contact with X-ray film (Ilford Industrial G) for a time depending upon the amount of carbon actually present (e.g. 350 h for 6 $\mu\text{g}/\text{cm}^2$).

The specimens oxidised at the lower temperatures showed interference colours which varied from one part of the surface to another, indicating non-uniformity of thickness of the oxide layer; it is believed that with the more highly oxidised samples a high surface density of carbon is associated with a correspondingly greater amount of combined oxygen. Both factors illustrate that the beryllium surface is by no means homogeneous.

TABLE 1

Summary of data for the oxidation of beryllium in carbon dioxide (at 10 cm pressure)

Run No.	Length of run (h)	Temperature (°C)	w_c ($\mu\text{g}/\text{cm}^2$) ^a	w_o ($\mu\text{g}/\text{cm}^2$) ^a	w_c/w_o (per cent)
10	305	500	not detd.	14.7 ^b	—
18	306	550	1.4	28.9	4.8
13	99	600	0.8	31.2	2.6
17	502	600	6.0	87.5	6.9
20	325	650	1.2	84.1	1.4
14	307	700	5.6	100.1	5.6
12	0.5	750	4.5	33.2	14
11	143	750	1.7	95.8	1.8
15	312	750	6.6	150.6	4.4
16	330	750	10.4	133.6	7.8

^a w_c is the weight of deposited carbon and w_o the weight of oxygen taken up as beryllium oxide.^b This value also includes the weight of deposited carbon.

TABLE 2

Oxidation of beryllium in carbon dioxide at 10 cm pressure. Values of the coefficients a and b corresponding to eq. (7) and the calculated rate of oxidation is after 300 h. Values for the rate of oxidation in oxygen at 300 h are included for comparison

Run No.	Temp. (°C)	a ($\text{cm}^4 \text{ h}/\mu\text{g}^2$)	b ($\text{cm}^2 \text{ h}/\mu\text{g}$)	Range of validity of eq. (7) (h)	Rate at 300 h ($\mu\text{g}/\text{cm}^2$)	
					in carbon dioxide	in oxygen
10	500	5.71	—63.2	185–305	0.0096	0.02
18	550	0.972	—19.5	69–306	0.026	0.04
8	600	1.30	—34.0	138–281	0.019	0.04
17		0.0821	— 2.30	120–500	0.098	
9	650	0.0519	0.40	42–305	0.126	0.04
14	700	0.120	— 9.90	209–307	0.065	0.13
16	750	0.0523	— 4.50	50—	^a	^a

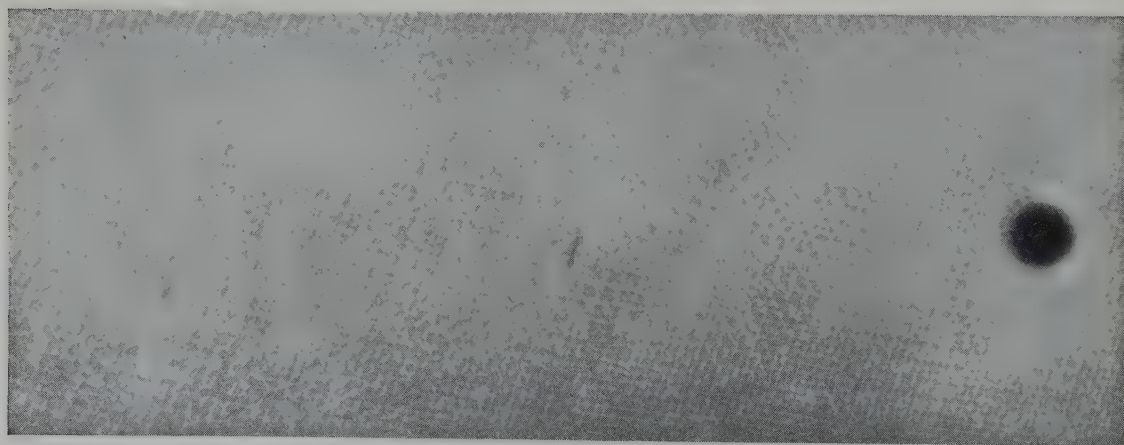
^a Breakaway occurs both in carbon dioxide and oxygen at 750° C.

Fig. 8a

(For caption of fig. 8 see next page)

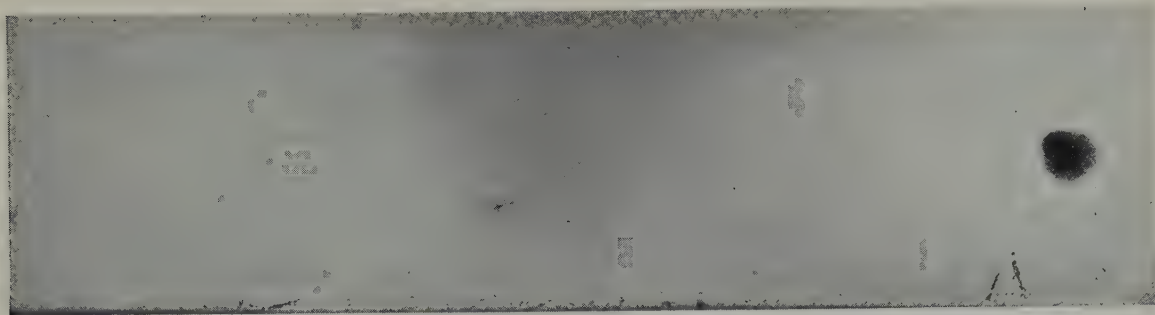


Fig. 8b

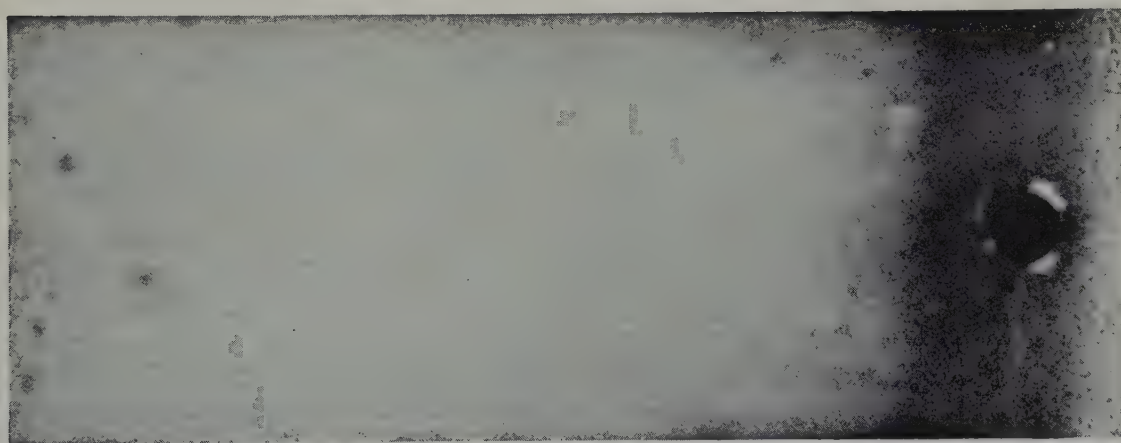


Fig. 8c

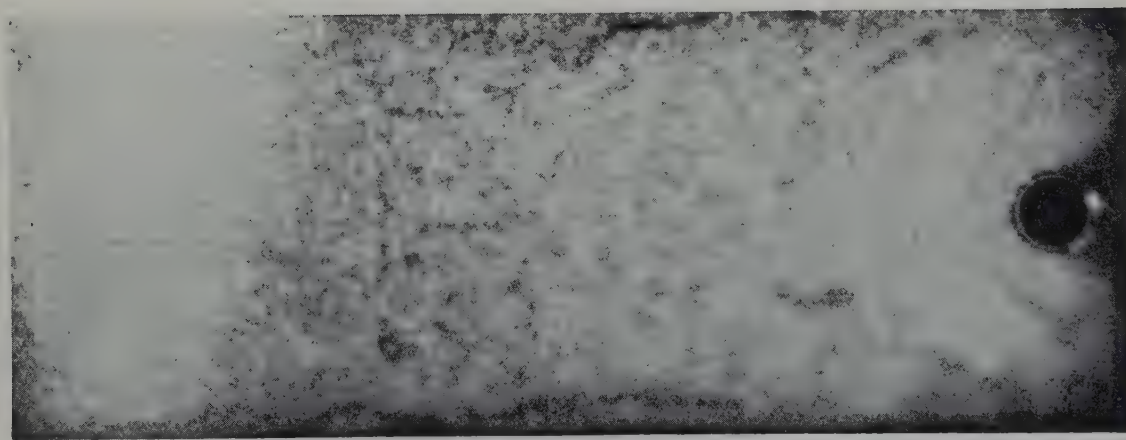


Fig. 8d

Fig. 8. Autoradiographs showing the variation in the distribution of carbon (elementary and combined) over the specimen surface: (a) run 14; (b) run 15; (c) run 17 and (d) run 18 (see table 1). $\times 4$.

3.2. SAMPLES HEATED TO REACTION TEMPERATURE IN CARBON DIOXIDE

A few additional runs were carried out, both on the microbalance and on the volumetric apparatus, in which the sample was heated to reaction temperature in carbon dioxide, outgassing being confined to room temperature.

A typical run, at 750° C, on the microbalance is shown in fig. 4 (run 21); the initial rapid weight gain is now absent and the rate of oxidation decreases uniformly from the start of the run. From the general appearance of the curve it would seem that had the run been continued for a long enough time, the latter stages of the curve would have conformed broadly to those of runs 15 and 16 obtained with the standard procedure of admitting the gas to the heated sample. The amount of deposited carbon was however significantly less than the mean of the values for runs 11, 15 and 16 ($0.7 \mu\text{g}/\text{cm}^2$ as compared with $6.2 \mu\text{g}/\text{cm}^2$).

Two runs were also carried out, at 650° and 750° C respectively, on the volumetric apparatus ¹) to study the rate of deposition of carbon directly; the generated carbon monoxide was re-oxidised to carbon dioxide by means of heated cupric oxide (cf. Part II). At 650° C (fig. 9) the amount of deposited carbon steadily

increased over the first 150 h, levelling off at a value about half that obtained when the gas was admitted to the pre-heated sample [line AB,¹]. In the run at 750° C, however, the amount of deposited carbon steadily increased to reach a value significantly greater than that obtained when the standard procedure was used [line CD,¹]. Since, however, the total weight gain of $500 \mu\text{g}/\text{cm}^2$ (found by direct weighing at the end of the run) was considerably greater than in the runs at 750° C referred to in fig. 4, the present run is probably not typical.

The effect of heating the metal to reaction temperature in carbon dioxide rather than admitting the gas to the heated sample is thus to eliminate the initial rapid weight gain and probably also to reduce the amount of carbon deposited without significantly altering the total weight gain after a period of 100 h or more.

4. Oxidation in Carbon Monoxide

Runs were carried out at temperatures in the range 500° to 750° C for times extending up to 150 h; the initial pressure of carbon monoxide was 10 cm and the run normally terminated either before or when the pressure had fallen to 5 cm; evidence presented below will show that the rate of oxidation is essentially independent of pressure over this range.

4.1. KINETIC RESULTS

The data (now expressed as mg/cm^2) are summarised in fig. 10 and their course over the first 12 h is shown in greater detail in fig. 11. As is seen from fig. 10, the agreement between duplicate runs is considerably better than that obtained with oxidation in carbon dioxide.

All the curves again show a rapid initial weight gain which varied from $0.1 \text{ mg}/\text{cm}^2$ for 500° C to $0.5 \text{ mg}/\text{cm}^2$ for 700° C (fig. 11). At the former temperature there is little reaction after the initial weight gain (slope of curve is $0.4 \mu\text{g}/\text{cm}^2 \text{ h}$) so that the oxidation would seem to be protective; whereas at 550° C and above, the metal continues to oxidise at an appreciable rate. At 550° C the rate reached a constant value ($4.5 \mu\text{g}/\text{cm}^2 \text{ h}$) after about 50 h and it is

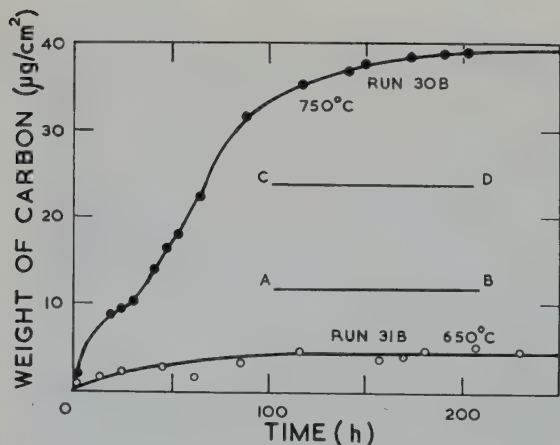


Fig. 9. Oxidation of beryllium at 650° C and 750° C showing the rate of carbon deposition. The samples were heated from room to reaction temperature in carbon dioxide. The lines AB and CD are referred to in the text.

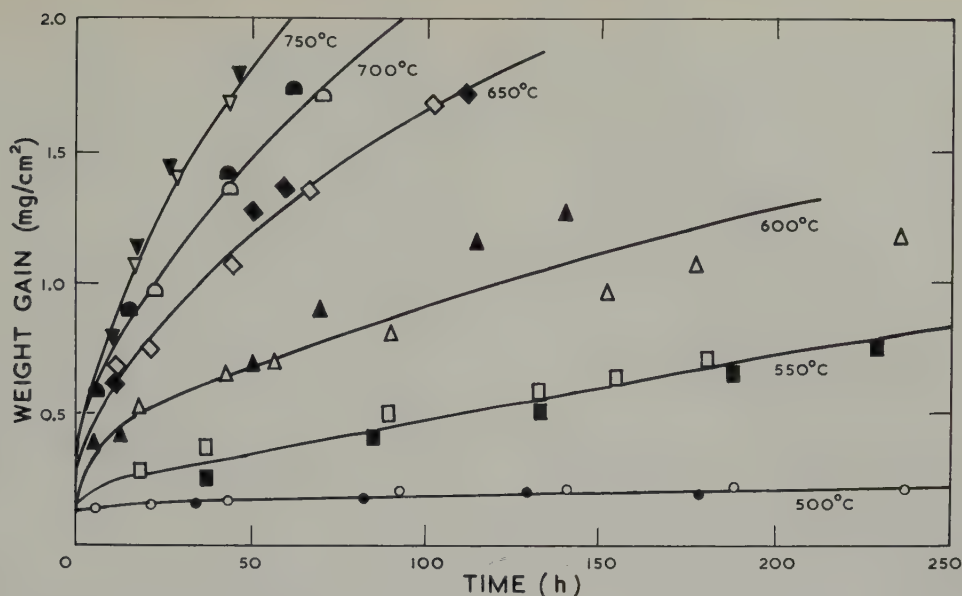


Fig. 10. Oxidation of beryllium in carbon monoxide at 500°, 550°, 600°, 650°, 700° and 750° C. The initial pressure was 10 cm and the runs terminated before the pressure had decreased to 5 cm.

likely that the curves at the higher temperatures might similarly have reached a constant rate had the runs been continued for a sufficiently long period. Thus the oxidation is almost certainly non-protective at 550° C and above, a conclusion supported by the fact that the reaction product spalled as a black powder from the specimen during the course of the run; moreover, in some of the runs, particularly those at 600° and 650° C, the rapid initial

weight gain was followed by a period of time over which the rate decreased and then abruptly increased (fig. 11), indicating breakaway.

At 500° and 650° C runs were also carried out in which the sample was heated from room to reaction temperature in carbon monoxide (cf. Section 3.2). As in the corresponding experiments with carbon dioxide, the initial rapid weight gain was absent (e.g. at 500° C after 50 h, the weight gain was only 0.5 $\mu\text{g}/\text{cm}^2$) but the subsequent rate of oxidation, judging from the run 39A at 650° C, was approximately the same as if the gas had been admitted to the pre-heated sample (fig. 12).

In one run at 600° C a further charge of carbon monoxide was admitted (at A, fig. 13) when the pressure had fallen from 10 cm to 5 cm; no change in the rate of oxidation was noted, thus disproving the possibility that the decrease in rate is due to a reduction in the pressure of carbon monoxide.

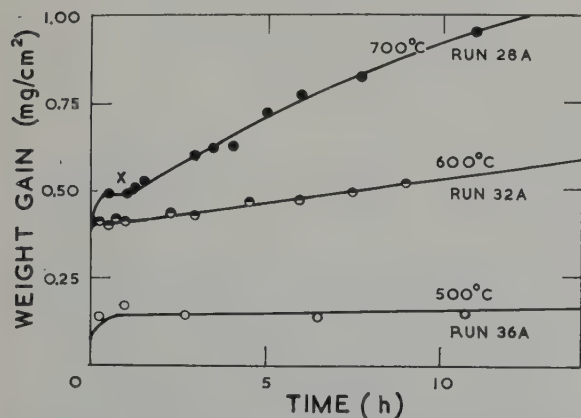


Fig. 11. Early stages of the oxidation of beryllium at 500°, 600° and 700° C in carbon monoxide at 10 cm pressure.

4.2. COMPARISON WITH CARBON DIOXIDE

A comparison of the data for carbon monoxide with those of Section 3.1 shows that both the total weight gain and the rate of oxidation are

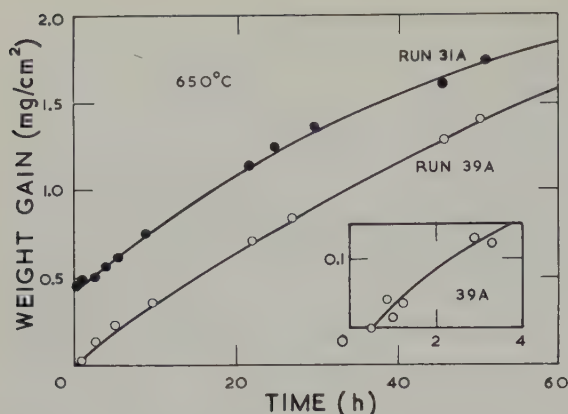


Fig. 12. Oxidation of beryllium at 650° C in carbon monoxide at 10 cm pressure. The sample of 39A was heated in carbon monoxide from room to reaction temperature; the curve is displaced from that of 31A, where the gas was admitted to the pre-heated sample, by an amount equivalent to the rapid initial weight gain.

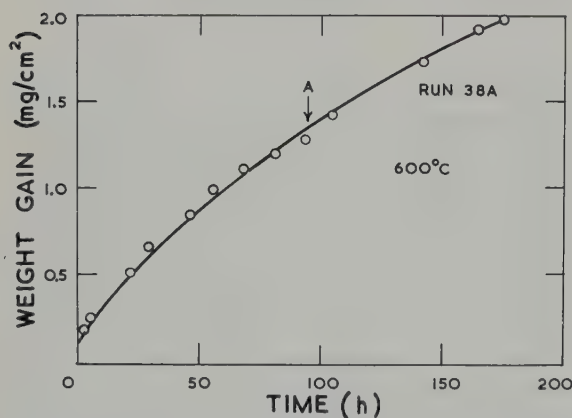


Fig. 13. Oxidation of beryllium in carbon monoxide at 600° C. At A, more carbon monoxide was admitted to restore the pressure to 10 cm; that the rate is unaffected shows that the reaction is independent of pressure over the range 5 to 10 cm.

considerably greater in carbon monoxide than in carbon dioxide for a given time and temperature; thus at 550° C the weight gain is some twenty times larger after a period of 50 h, while the rate at 300 h is two hundred times greater. A second and more important difference is that the oxidation in carbon dioxide is protective at temperatures up to 700° C whereas in carbon monoxide it ceases to be protective at a temperature between 500° and 550° C.

5. Oxidation in Carbon Monoxide-Carbon Dioxide Mixtures

Since the oxidation of beryllium in a mixture containing relatively small concentrations of carbon monoxide is of some technological importance, the reaction at 650° C was studied in each of three gas mixtures containing respectively 2.5, 5 and 7.5 % of carbon monoxide by volume and with a total gas pressure of 10 cm.

Except for one run, the method of continuous weighing was abandoned; separate samples were oxidised, the weight gain of each sample being determined by direct weighing and the amount of deposited carbon by the direct "counting" procedure described in Section 3.1. The gas mixture contained both radioactive carbon monoxide and radioactive carbon dioxide, the specific activities of the two gases being approximately the same; analysis of the mixture at the end of the oxidation run showed that any change in composition during the run was less than 1 %.

Samples were oxidised for 50, 100, 200 and 300 h and from the results (fig. 14) it is clear, taking into account the fact that each experimental point was determined using a separate sample, that there is little increase in weight

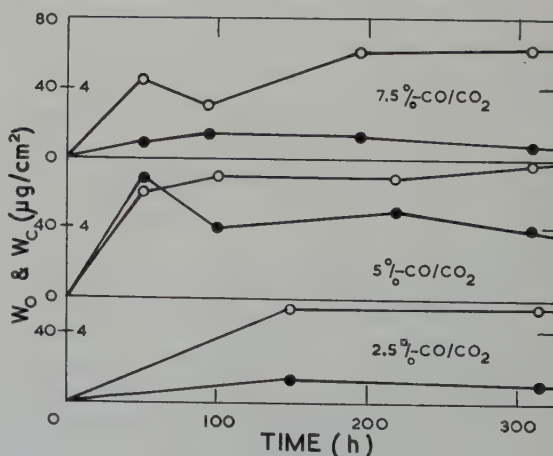


Fig. 14. Oxidation of beryllium at 650° C in three carbon monoxide-carbon dioxide mixtures at a total pressure of 10 cm. The weights of combined oxygen (w_o) and of combined carbon (w_c) are shown by the left-hand and right-hand scales or ordinates respectively.

over the last 100 to 200 h of each of the three composite runs. This conclusion was confirmed by a single run on the microbalance in a mixture containing 5 % carbon monoxide, when, as is seen (run 19, fig. 15), the rate continuously decreased to reach a value of $0.05 \mu\text{g}/\text{cm}^2 \text{ h}$ at 300 h. Little significance is attached to the fact that the curve for the mixture crosses and falls below that for carbon dioxide (run 9), since the latter curve is anomalous—it does not fall into the regular family of curves for the lower temperatures (fig. 3).

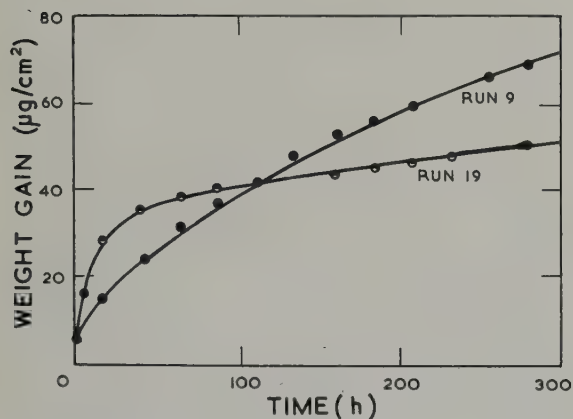


Fig. 15. Comparison of the oxidation of beryllium at 650°C in carbon dioxide at 10 cm pressure (run 9) with that in a 5 % carbon monoxide-carbon dioxide mixture (run 19).

If the weight (w_0) of combined oxygen after 300 h is taken as a standard of comparison, there is no significant increase in the amount of oxidation with increasing concentration of carbon monoxide (fig. 14); w_0 varies in a somewhat erratic manner from $73 \mu\text{g}/\text{cm}^2$ for the mixture containing 0 % carbon monoxide to $62 \mu\text{g}/\text{cm}^2$ for that containing 7.5 % carbon monoxide. Similarly, the amount of deposited carbon (w_c) shows no significant trend with increasing carbon monoxide concentration, and varies from $1.2 \mu\text{g}/\text{cm}^2$ for 0 % carbon monoxide to $0.6 \mu\text{g}/\text{cm}^2$ for 7.5 % carbon monoxide.

The above results indicate that when beryllium is oxidised in mixtures containing up to 7.5 % carbon monoxide, the oxidation follows the same course as in carbon dioxide alone.

That the carbon monoxide in a mixture containing 5 % carbon monoxide and 95 % carbon dioxide does not react to a significant extent with beryllium, is proved in an experiment in which a sample of the metal was oxidised for 90 h in a mixture containing isotopically labelled carbon monoxide; the amount of radioactive carbon deposited on the sample was $0.2 \mu\text{g}/\text{cm}^2$ so that the weight gain due to reaction with carbon monoxide was only $0.4 \mu\text{g}/\text{cm}^2$ ($0.2 \times \frac{28}{12}$) as compared with a total weight gain of $60 \mu\text{g}/\text{cm}^2$.

6. Discussion

6.1. OXIDATION IN CARBON DIOXIDE

By analogy with the oxidation of beryllium in oxygen²⁾, the thickening of the film in carbon dioxide is likely to proceed by the outward diffusion of Be^{++} ions and their electrons from the metal to react with chemisorbed carbon dioxide at the gas/oxide interface. In principle, there are two different ways in which carbon dioxide⁴⁾ could be chemisorbed; it could either be associated with a lattice O^{--} ion to form a CO_3^{--} ion (fig. 16a), or it could be dissociated (fig. 16b) into a CO^+ ion and an O^- ion, the

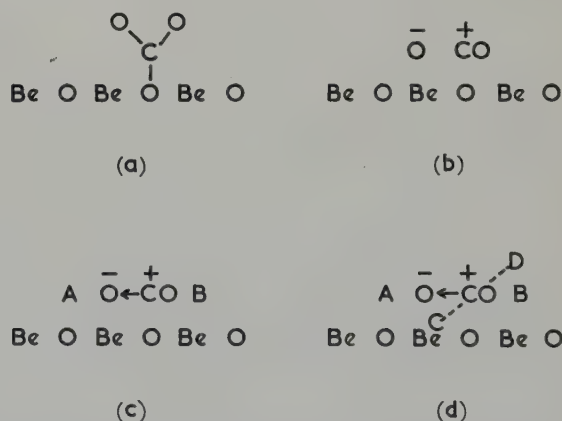
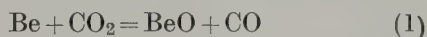


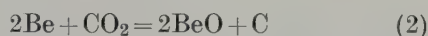
Fig. 16. Illustrating the chemisorption of carbon dioxide on the oxide surface: (a) interaction of CO_2 with a lattice O^{--} ion to form a CO_3^{--} ion; (b) dissociation of CO_2 into a CO^+ ion and an O^- ion; (c) the probable state of the chemisorbed CO_2 molecule; the positions A and B are referred to in the text; (d) as for (c), the positions A, B, C and D are referred to in the text.

former taking up a position over an O^{--} ion and the latter over a Be^{++} ion; the O^- ion may capture an electron from the metal to become doubly charged. The actual condition of the chemisorbed carbon dioxide is likely to be intermediate between the two, and for convenience one might regard it as that of a polarised carbon dioxide molecule oriented in such a way that the negative end is close to a lattice Be^{++} ion and the positive end close to a lattice O^{--} ion (fig. 16c).

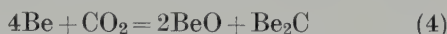
On the basis of this model it is possible to give a qualitative interpretation of the reaction between beryllium and carbon dioxide in terms of the number of Be^{++} ions diffusing through the film and thus available to form a transition complex with the chemisorbed carbon dioxide molecule. Thus the reaction:



is seen to correspond to a Be^{++} ion being present at position A of fig. 16c and reacting to form one BeO and discharging a CO molecule. If, on the other hand, two Be^{++} ions were to be present simultaneously in each of positions A and B of fig. 16c, the carbon dioxide molecule would be so strained as to produce two BeO and release a carbon atom:



stated in other terms, an activated complex would be set up and would decompose to form $2BeO + C$. It is easy to see that if the reaction



were to occur, this would require four Be^{++} ions to be present simultaneously in the positions A, B, C and D of fig. 16d, and since the probability of such a conformation must be extremely small, it is likely that the beryllium carbide present in the oxide layer is formed by reaction of beryllium with carbon after the latter has been deposited:



If, then, reaction (4) is excluded so that deposition of carbon only proceeds by reaction (2),

it is easy to calculate (by comparing w_0 and w_c for run 17 at $750^\circ C$, table 1) that over the period of the rapid initial weight gain, one out of every six carbon dioxide molecules reacts with two Be^{++} ions as in (2) and five out of every six carbon dioxide molecules react with only one Be^{++} ion as in (1).

Now reaction (2) should be favoured relative to reaction (1) when the diffusion flux of Be^{++} ions through the film is relatively large; and this is found in practice for those runs where the carbon dioxide was admitted to the pre-heated sample; almost all the carbon deposition occurred over the period of the rapid initial weight gain whereas along the flatter part of the oxidation curve beryllium oxide was the only solid product.

This picture explains why the initial weight gain (when it occurs) is associated with a relatively large amount of carbon deposition but it does not explain why the rapid initial oxidation should occur at all; for as the film thickens the number of Be^{++} ions diffusing through the film would be expected to correspondingly decrease. It must however be realised that the film formed over the period of the initial weight gain contains a relatively large amount of carbon (e.g., at $750^\circ C$ the film contains 8 % by weight of carbon) which will give rise to a highly imperfect lattice; the resultant imperfections will promote the diffusion of Be^{++} ions. In time the lattice would become more regular, probably as a result of one or both of two processes: (a) the carbon atoms may react with the Be^{++} ions and electrons diffusing through the film to form beryllium carbide (reaction 4); the resultant carbide ions could then diffuse through the oxide lattice to form a nucleus of beryllium carbide which grows into discrete particles⁵), (b) the carbon atoms themselves may migrate in atomic form to produce discrete crystallites (while carbon atoms are not mobile in a carbon lattice at these temperatures, they could well be mobile in a distorted beryllium oxide lattice). The mechanism (a) would explain why, at the lower temperatures (fig. 6), the initial weight

gain is sometimes followed by a period of little further oxidation; presumably only a few Be^{++} ions reach the gas/oxide interface, and a majority of those entering the film react there with the carbon already present to form beryllium carbide, a process involving no weight gain.

It might be thought that the initial weight gain arises because the heat generated by the reaction raises the temperature of the sample significantly above that of the furnace, but even for the runs at 750°C the calculated maximum value of the temperature rise⁶⁾ would only be 6°C . Further, it is particularly significant that the rapid initial weight gain was not obtained with the runs in oxygen, yet the molar heat of reaction is actually greater than that in carbon dioxide.

Apart from the initial weight gain, perhaps the most striking feature of the curves is their general similarity to those for oxidation in oxygen: for temperatures up to and including 700°C the weight gains at 300 h are about the same as in oxygen and the rates of oxidation after 300 h in the two gases are of the same order (see table 2); a further point of similarity is that at 750°C breakaway occurs in both gases. This suggests that when, after the period of initial weight gain, the lattice has become more ordered, the rate of diffusion of Be^{++} ions across the oxide film is the same for oxidation in carbon dioxide as for oxidation in oxygen. There is however one difference between oxidation in oxygen and in carbon dioxide: the intermittent or "jerky" oxidation found with the former is absent in carbon dioxide, pointing to some difference in the mechanical properties of the film (see Part I).

The data, after the initial weight gain at all temperatures even for the 500 h run at 650°C , conform closely to the empirical equation

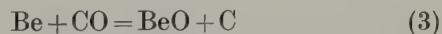
$$aw^2 + bw = t \quad (7)$$

but since this contains two disposable constants and because the conformity is restricted to the flat part of the curves, the agreement does not in itself constitute a proof that the rate of

oxidation is controlled by the rate of diffusion of Be^{++} ions across the film⁷⁾.

6.2. OXIDATION IN CARBON MONOXIDE

When beryllium is oxidised in carbon monoxide, only the two reactions:



are possible on thermodynamic grounds and this gives rise to an important difference between oxidation in carbon dioxide and in carbon monoxide. In carbon dioxide the amount of carbon deposition can in principle vary from zero to a maximum value of 27 % of the total weight gain, whereas in carbon monoxide the carbon deposition must of necessity be accompanied by oxide formation and so is fixed at 43 % of the total weight gain.

The carbon monoxide molecule is probably weakly chemisorbed on the beryllium oxide surface⁸⁾ and by arguments similar to those developed in the preceding section for carbon dioxide it is likely that reaction (3) corresponds to the formation of a transition complex of the form $(\text{Be}^{++} \dots \text{OC})$ on the oxide surface, which decomposes to form one BeO and one carbon atom. Since reaction (5) would necessitate the formation of the rather unlikely transition complex involving three Be^{++} ions, it would seem that most if not all of the beryllium carbide (comprising 30 % by weight of the reaction product) is formed by reaction between beryllium and carbon already deposited.

The oxidation curves again show a rapid initial weight gain whose magnitude, for a given temperature, is greater than that obtained in carbon dioxide ($259 \mu\text{g}/\text{cm}^2$ as compared with $61.5 \mu\text{g}/\text{cm}^2$ at 750°C). This is readily explained along the lines of Section 6.1: since the amount of carbon in the film is greater, the lattice is correspondingly larger until, in the region of X (fig. 11), the film crystallises.

If the sample is heated to reaction temperature in carbon monoxide the rapid initial weight gain is no longer obtained. Indeed at 500°C

there was little reaction and the film hardly thickened above its room temperature value whilst at 650° C the metal oxidised non-protectively and the curve was approximately parallel to that obtained using the standard procedure (fig. 12). It would thus appear that for runs where the gas is admitted to the heated sample the carbon deposition, in addition to giving rise to a distorted lattice in the newly created film, also causes imperfections in the underlying room temperature film, for otherwise the period of rapid initial weight gain would not have been obtained at 500° C (fig. 11).

6.3. OXIDATION IN CARBON MONOXIDE-CARBON DIOXIDE MIXTURES

When beryllium is heated in a mixture of carbon monoxide and carbon dioxide, it will react with each component to an extent depending upon the relative number of adsorption sites which each gas occupies at the gas/oxide interface. This in turn will depend upon the composition of the gas mixture. The graphs of fig. 14 show that for mixtures containing up to 7.5 % of carbon monoxide, the oxidation follows the same course as in carbon dioxide alone; and the experiment with isotopically labelled carbon monoxide and inactive carbon dioxide would seem to demonstrate conclusively that for a mixture containing 5 % of carbon monoxide, reaction at 650° C between beryllium and carbon monoxide is almost negligible.

An interesting question is whether beryllium, when heated in various carbon monoxide-carbon dioxide mixtures, will continue to react essentially with carbon dioxide alone until some critical composition of carbon monoxide is reached or whether the reaction will gradually change from one with carbon dioxide alone to one with both carbon monoxide and carbon dioxide. In Part II it was suggested (from kinetic measurements at 700° C) that there exists a minimal concentration of carbon monoxide (greater than 90 %) below which beryllium reacts with carbon dioxide alone. This inference has been confirmed in part by a test experiment on the volumetric tracer

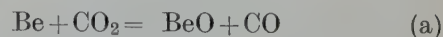
apparatus in which a sample was heated at 700° C for 140 h in a mixture containing equal molar concentrations of carbon monoxide and carbon dioxide: the rate of carbon deposition was just detectable (0.18 $\mu\text{g}/\text{cm}^2 \text{ h}$) so that even for a mixture of this composition the reaction is still essentially one with carbon dioxide alone (the rate of carbon deposition in pure carbon monoxide at 700° C is about 7 $\mu\text{g}/\text{cm}^2 \text{ h}$ and in pure carbon dioxide almost zero).

Conclusions

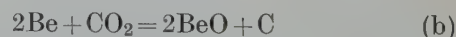
When electrolytic flake beryllium is heated in carbon dioxide at temperatures up to and including 700° C, the rate of oxidation continuously decreases with time to reach a very small value after 300 h, varying from 0.01 $\mu\text{g}/\text{cm}^2 \text{ h}$ at 500° C to 0.07 $\mu\text{g}/\text{cm}^2 \text{ h}$ at 700° C. An experiment at 600° C, which was continued for 500 h, showed that the rate at 300 h is not a limiting value. At 750° C the rate of oxidation first decreases and then increases with time, indicating breakaway.

When the carbon dioxide is admitted to the sample pre-heated to reaction temperature, there first occurs a period of rapid weight gain after which the rate of oxidation decreases; most of the carbon deposition occurs over this initial period. If, however, the sample is heated in carbon dioxide from room to reaction temperature, the initial weight gain is no longer obtained and carbon deposition occurs over a longer period and the amount deposited is less. An experiment at 750° C indicates that after about 100 h the total weight gain and the rate of oxidation are about the same for each of the two starting procedures. A striking feature of the oxidation curves in carbon dioxide is their general similarity, apart from the initial weight gain, to those in oxygen for any given temperature.

In carbon dioxide the reactions are



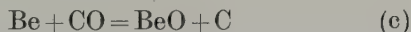
and



with (a) predominating. Whilst (a) corresponds

to the formation of a transition complex on the oxide surface involving one Be^{++} ion and one CO_2 molecule, (b) requires a transition complex with two Be^{++} ions so that this reaction will only proceed to an appreciable extent when the flux of Be^{++} ions through the film is relatively large. This is the case over the period of the rapid initial weight gain; after the film crystallises and the rate of oxidation decreases, reaction (b) only proceeds to a negligible extent and the metal thus oxidises almost exclusively by (a). Since the direct formation of beryllium carbide would require the unlikely transition complex of four Be^{++} ions and one CO_2 molecule, it is concluded that beryllium carbide is formed indirectly by reaction of some of the carbon already deposited in (b).

The rate of oxidation of beryllium in carbon monoxide is considerably greater than in carbon dioxide, and at 550°C and above, the oxidation is non-protective and the reaction product spalls from the sample during the run. Because there is only the one reaction



carbon deposition must of necessity accompany oxide formation and it is the former which, by distorting the lattice, increases the diffusion flux (the rapid initial weight gain is considerably greater in carbon monoxide than in carbon dioxide) and ultimately causes the film to crack.

The kinetics of the oxidation at 650°C in carbon monoxide-carbon dioxide mixtures

containing up to 7.5 % of carbon monoxide, and at 700°C in a mixture containing 50 % of carbon monoxide, have been shown to be the same as in pure carbon dioxide. (In Part II other evidence was adduced that the kinetics only change when the percentage of carbon monoxide is in excess of 90 %.) That the reaction remains essentially one with carbon dioxide is attributed to preferential adsorption of carbon dioxide on the oxide surface.

Acknowledgements

It is a pleasure to thank Dr. J. E. Antill for his interest in this work and Mr. C. P. Lloyd-Jones for advice on autoradiography. We are also grateful to the UK Atomic Energy Authority for financial support.

References

- 1) S. J. Gregg, R. J. Hussey and W. B. Jepson, *J. Nucl. Mat.* **2** (1960) 225
- 2) D. W. Aylmore, S. J. Gregg and W. B. Jepson, *J. Nucl. Mat.* **2** (1960) 169
- 3) J. E. Antill, private communication
- 4) For general references, see E. R. S. Winter, *Advances in Catalysis* **10** (Academic Press, London, 1958) pp. 196-239
- 5) V. D. Scott, *Nature* **186** (1960) 466
- 6) O. Kubaschewski and E. L. Evans, *Metallurgical Thermochemistry* (Pergamon Press, London, 1956)
- 7) N. F. Mott and N. Cabrera, *Rept. Prog. Phys.* **12** (1949) 163
- 8) K. Hauffe, in *Semi-Conductor Surface Physics*, Ed. by R. H. Kingston (University of Philadelphia, Philadelphia 1957) pp. 259-281

THE HIGH TEMPERATURE OXIDATION OF BERYLLIUM

PART IV

IN WATER VAPOUR AND IN MOIST OXYGEN

D. W. AYLMOORE, S. J. GREGG and W. B. JEPSON †

Department of Chemistry, University of Exeter, Exeter, UK

Received 17 September 1960

The kinetics of the oxidation of electrolytic flake beryllium both in water vapour (1.2 cm pressure) and in moist oxygen (10 cm total pressure; partial pressure of water, 1.2 cm) have been investigated at temperatures in the range 500°–750° C; there was no significant difference between oxidation in these two gases. At temperatures up to and including 600° C the oxidation follows the same course as in dry oxygen, the rate continuously decreasing with time to reach a very small value after about 100 h. At 650° C and above, the oxidation is no longer protective and breakaway takes place, both the weight gain and the time at which breakaway occurs becoming less with increasing temperature. Metallographic examination of partially oxidised samples shows that the reaction after breakaway takes the form of attack down the particle boundaries giving rise to an interpenetrating network of oxide and metal. The effect of an oxide layer pre-formed in dry oxygen is shown to retard but not prevent breakaway on subsequent exposure to water vapour.

La cinétique de l'oxydation de paillettes de béryllium électrolytique à la fois dans la vapeur d'eau (1.2 cm de pression) et dans l'oxygène humide (pression totale 10 cm; pression partielle de l'eau, 1.2 cm) a été étudiée pour des températures dans le domaine 500°–750° C; il n'y avait pas de différence notable d'oxydation dans ces deux gaz. Pour des températures allant jusqu'à 600° C inclus, l'oxydation suit exactement la même loi que dans l'oxygène sec, la vitesse décroît continuellement avec le temps pour atteindre une très petite valeur après 100 heures environ. A 650° C et au-dessus, l'oxydation n'est plus protectrice et un "breakaway" se produit, le gain de poids et le

temps auquel se produit le "breakaway" diminuant avec la température croissante. Un examen métallographique d'éprouvettes partiellement oxydées révèle qu'après le "breakaway", la réaction a lieu sous forme d'attaque sous les limites des particules, ce qui donne lieu à un réseau où s'interpénètrent oxyde et métal. Une couche d'oxyde préformée dans l'oxygène sec aurait pour effet de retarder, mais non d'empêcher le "breakaway" au cours d'une exposition ultérieure à la vapeur d'eau.

Es wurde die Kinetik der Oxydation von elektrolytisch hergestelltem Beryllium im Wasserdampf (12 mm Druck) und in feuchtem Sauerstoff (100 mm Totaldruck, 12 mm Partialdruck des Wassers) zwischen 500 und 750° C untersucht. Die Oxydation war in den beiden Gasen nur unwesentlich verschieden. Bis zu 600° C nimmt die Oxydation den gleichen Verlauf wie in trockenem Sauerstoff. Die Geschwindigkeit fällt hierbei mit steigender Versuchsdauer stetig ab und erreicht nach etwa 100 Stdn. einen sehr kleinen Wert. Bei 650° C und darüber werden keine schützenden Deckschichten mehr gebildet. Die Oxydschichten platzen auf, wobei die Zeit bis zum Aufplatzen und die bis dahin erreichte Gewichtszunahme mit wachsender Temperatur abnimmt. An teilweise oxydierten Proben ließ sich mikroskopisch zeigen, daß nach dem Aufplatzen ein Angriff vornehmlich entlang der Teilchengrenze stattfindet, wodurch sich gegenseitig durchdringende Netze aus Oxyd und Metall entstehen. In trockenem Sauerstoff vorgebildete Oxydschichten verzögern beim nachfolgenden Angriff durch Wasserdampf das Aufplatzen der Deckschichten, vermögen dies aber nicht völlig zu verhindern.

1. Introduction

Earlier Parts ^{1,2,3}) of the series have dealt with the oxidation of electrolytic flake beryllium in oxygen, carbon monoxide and carbon dioxide

at temperatures between 500° and 750° C. The present Part is concerned with the kinetics of the isothermal oxidation in water vapour at 1.2 cm pressure (equivalent to the saturation

† Now at Atomic Energy Research Establishment, Harwell, Didcot, Berks., UK.

vapour pressure of water at 18° C) and in moist oxygen at a total pressure of 10 cm and a partial pressure of water of 1.2 cm. A number of temperatures in the range 500° to 750° C were studied and at one temperature, 700° C, the oxidation was also carried out in water vapour at two pressures below 1.2 cm.

The results strongly suggest that the course of the oxidation in moist oxygen is essentially as in water vapour alone. A striking feature of the results is that breakaway occurs at 650° C and above in both media; metallographic examination shows that after breakaway, oxidation is accompanied by marked intergranular penetration of the metal.

2. Experimental

The electrolytic flake beryllium was of the same batch as that used in Parts I–III and, as before, each sample was chemically polished in a mixture of phosphoric, chromic and sulphuric acids (at 100° C for 30 sec) prior to oxidation.

The course of the oxidation was followed by measuring the weight gain of the beryllium specimen on a vacuum microbalance similar to that used in Part I¹). Because of the larger weight gains to be expected, the range of the balance was increased to 4 mg and the sensitivity correspondingly reduced to 4 μg (equivalent to 0.6 $\mu\text{g}/\text{cm}^2$ for a sample measuring 3.5 cm \times 1 cm). Two of the runs (those in moist oxygen at 500° and 550° C) were however carried out on a balance sensitive to 1 μg .

For oxidation in water vapour the procedure was similar to that for dry oxygen¹); the sample was outgassed at reaction temperature and the required pressure of water vapour (1.2 cm) was then produced by opening the balance case to a bulb containing a saturated aqueous solution of ammonium nitrate, thermostated at 22.5° C. For the runs in moist oxygen, the sample was first outgassed as before, oxygen then admitted to a pressure of 8.8 cm and water vapour admitted (by breaking open a sealed bulb containing the requisite quantity of liquid water) to give a total pressure of 10 cm; this meant that for the first few minutes of each

run the beryllium was exposed to dry oxygen alone. As distinct from the runs in water vapour where the pressure was kept constant throughout the run, the water consumed during oxidation in moist oxygen could not be replaced; but even for a weight gain of 4 mg, the partial pressure of water would only decrease by 10 %. (Volume of balance case was 2 litres.)

3. Results

3.1. OXIDATION IN WATER VAPOUR

The curves for oxidation in water vapour (1.2 cm) at temperatures from 550° to 750° C are shown in figs. 1 to 4. At 550° C (fig. 1) oxidation effectively ceased after about 100 h, since after a further 200 h the additional weight gain was only 0.7 $\mu\text{g}/\text{cm}^2$ corresponding to the addition of about 10 atomic layers. At 600° C the rate of oxidation was again comparatively large at first but it progressively decreased to a constant, and relatively small, value of 0.06 $\mu\text{g}/\text{cm}^2$ h after about 80 h.

The curves at 650° C and above (figs. 2 to 4) are distinguished from those at the lower temperatures by the fact that the oxidation is no longer protective: the rate first decreases and then increases, indicating breakaway and subsequent non-protective oxidation. At 650° and 700° C the rate of oxidation was apparently still increasing when the runs were stopped, whereas at 750° C a constant rate (700 $\mu\text{g}/\text{cm}^2$ h) was reached after about 2 h. Reference to figs. 2 and 4 will show that the time and the weight gain at which breakaway occurred both diminished with increasing temperature; thus at 650° C breakaway intervened after about 35 h (weight gain, 65 $\mu\text{g}/\text{cm}^2$) while at 750° C breakaway occurred after only 1 h (weight gain, 5 $\mu\text{g}/\text{cm}^2$). Since breakaway takes the form of localised intergranular penetration of the metal (Section 3.3), the weight gain per cm^2 of geometrical area is of formal significance only. The discontinuities in the curve at 650° C (run A36, fig. 2) are also explicable in terms of localised intergranular oxidation.

At 700° C runs were also carried out with two smaller pressures of water vapour, 0.058 cm

and 0.000 05 cm (corresponding to the saturation vapour pressure of water at -23°C and -78°C respectively) and, as is seen (fig. 5), the oxidation rate is pressure dependent. In run B41 (0.000 05 cm) breakaway did not occur in the 75 h period

of the run, but the calculated pressure of corrosion product, hydrogen, in the balance case was then about 0.13 cm, so that the rate of diffusion of water vapour to the sample may have been rate-controlling. Run B41 showed

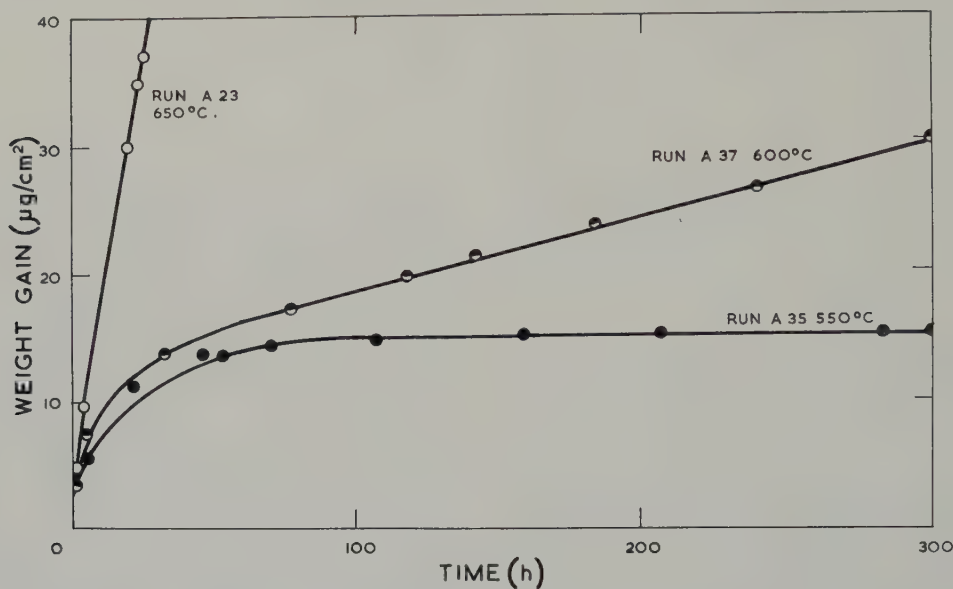


Fig. 1. Oxidation of beryllium at 550°, 600° and 650° C in water vapour at a pressure of 1.2 cm.

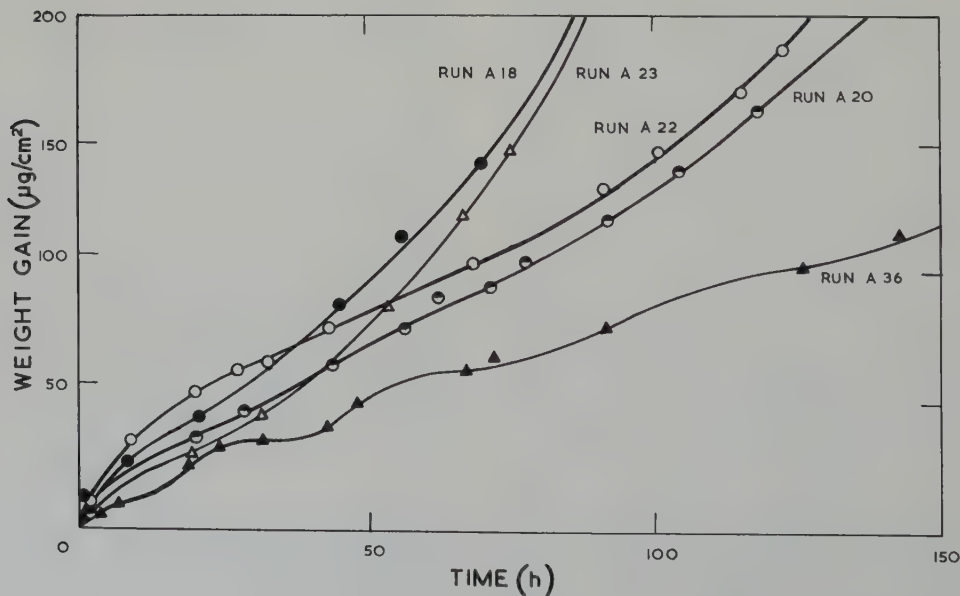


Fig. 2. Oxidation of beryllium at 650° C. Comparison of the oxidation in water vapour at a pressure of 1.2 cm (runs A22, A23 and A36) with that in moist oxygen at 10 cm with 1.2 cm partial pressure of water (runs A18 and A20).

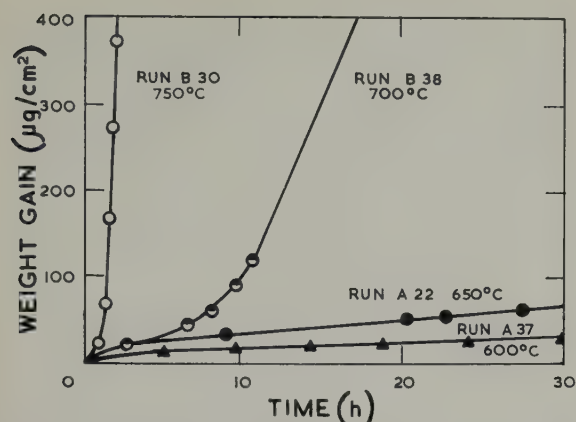


Fig. 3. Oxidation of beryllium at 600°, 650°, 700° and 750° C in water vapour at a pressure of 1.2 cm.

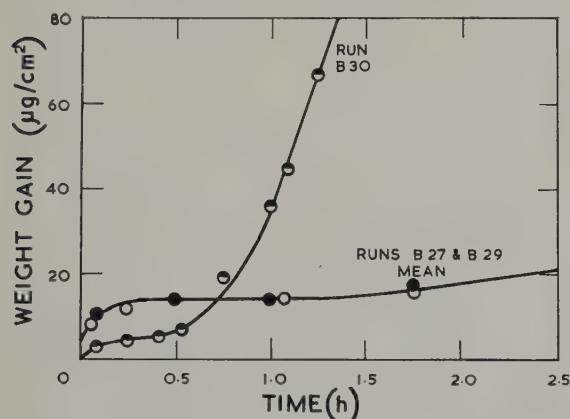


Fig. 4. Oxidation of beryllium at 750° C. Comparison of the oxidation in water vapour at a pressure of 1.2 cm (run B30) with that in moist oxygen at 10 cm total pressure with 1.2 cm partial pressure of water (runs B27 and B29).

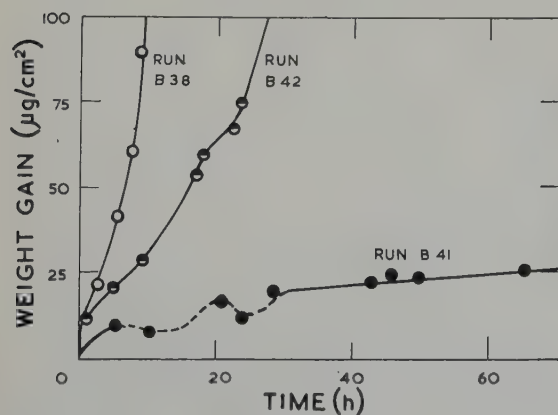


Fig. 5. Oxidation of beryllium in water vapour at 700° C showing the effect of pressure (run B41, 0.000 05 cm; run B42, 0.058 cm; run B38, 1.2 cm).

also the unusual feature of an actual loss in weight after ca 10 and ca 45 h, for reasons as yet unexplained. The run at a pressure of 0.058 cm (B42) falls below that at 1.2 cm (B38) and the discontinuous weight changes associated with localised penetration into the metal are again clearly evident. For technical reasons the pressure of water vapour unavoidably diminished by about 17 % overnight, but since the dependence of rate on pressure is likely to be logarithmic, this decrease should not have significantly altered the kinetics.

3.2. OXIDATION IN MOIST OXYGEN

Curves for the oxidation in moist oxygen (partial pressure of water vapour, 1.2 cm) are shown in fig. 6; at temperatures up to and including 600° C the oxidation is protective, for at 550° C there is little further oxidation after about 60 h, and at 600° C the rate decreases to a constant value of $0.07 \mu\text{g}/\text{cm}^2 \text{ h}$ as compared with $0.06 \mu\text{g}/\text{cm}^2 \text{ h}$ for pure water vapour. The course of the oxidation in moist oxygen is thus very similar to that in water vapour, and reference to table 1 will show that the weight gains in moist oxygen are slightly but not significantly greater than the corresponding values in water vapour. An interesting feature of the curve at 500° C (fig. 6) is the discontinuity at 180 h, which causes the weight gain after 300 h to be greater at 500° C than at 550° C. Analogous discontinuities were found when electrolytic flake beryllium was oxidised in dry oxygen (Part I).

At 650° C and above, the rate of oxidation first decreased and then increased, indicating breakaway (figs. 2 and 7); and both the weight gain and the time at which breakaway occurred diminished with increasing temperature (compare B27 and B29 at 750° C with B31 at 700° C, fig. 7). Further, breakaway occurred earlier in water vapour than in moist oxygen at both 700° and 750° C (fig. 4); the probable reason is that in the runs in moist oxygen several minutes elapsed before water vapour could be admitted to the balance case, so that a "dry" oxide film which might be expected to retard breakaway

was inevitably formed. The ability of such a film to retard breakaway was demonstrated by a further experiment at 700° C (B39, fig. 8) in which a "dry" film was deliberately pre-formed by first exposing a sample to dry oxygen for 113 h, yielding a weight gain of 90 $\mu\text{g}/\text{cm}^2$ (4600 Å); on pumping out the oxygen and admitting water vapour to 1.2 cm pressure,

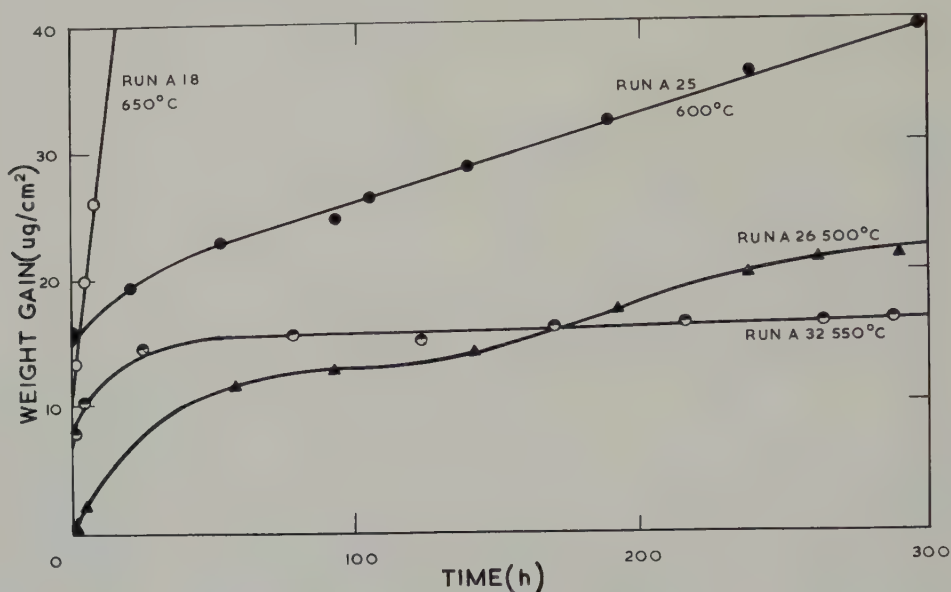


Fig. 6. Oxidation of beryllium at 500°, 550°, 600° and 650° C in moist oxygen at a total pressure of 10 cm with 1.2 cm partial pressure of water.

TABLE 1

Summary of the weight gains obtained in water vapour, moist oxygen and dry oxygen¹⁾

Temp. (°C)	Water vapour			Moist oxygen			Dry oxygen		
	Run ^{a, b}	Time (h)	Wt. gain ($\mu\text{g}/\text{cm}^2$)	Run	Time (h)	Wt. gain ($\mu\text{g}/\text{cm}^2$)	Run	Time (h)	Wt. gain ($\mu\text{g}/\text{cm}^2$)
500	—	—	—	A26	290	22.0	A 9	313	20.8
550	A35	300	15.4	A32	289	16.6	A 3	300	36.3
600	A37	300	30.5	A25*	309	41.2	A 7	308	42.0
650	A22*	163	298	A18	70	144	A10	290	60.7
	A23	93	220	A20*	165	276	—	—	—
	A36	185	144	—	—	—	—	—	—
700	B38*	26	815	B31	31	429	B13	300	70.9
	B33*	11.3	98.1	—	—	—	—	—	—
750	B30	2.3	543	B27*	12	556	B14	50	210
	—	—	—	B29*	9.6	547	B15	107	226
	—	—	—	—	—	—	B16	166	226

^a The letters A and B before the run number indicate sample sizes of 4 cm × 1.5 cm and 3.5 cm × 1 cm respectively.

^b The asterisk * denotes those samples which were sectioned and examined metallographically.

12 h elapsed before breakaway occurred as compared with 5 h for moist oxygen and 3 h for pure water vapour; moreover the rate of oxidation after breakaway was less (fig. 9).

For oxidation in dry oxygen 750°C was the lowest temperature at which breakaway was detected. It was therefore considered of interest to find whether the relatively rapid rate of attack after breakaway at 700°C in water vapour could be arrested by changing the oxidising gas to dry oxygen; but as is seen (B33, fig. 8), though the rate of reaction did at

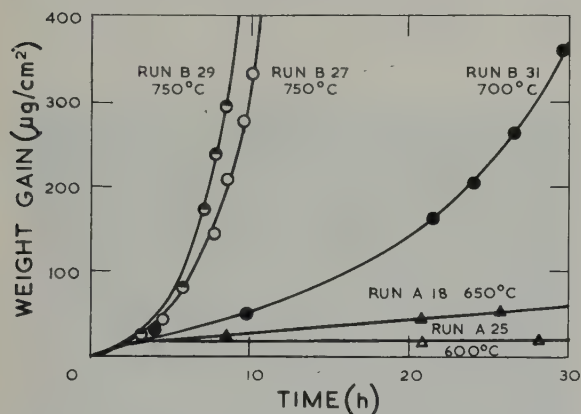


Fig. 7. Oxidation of beryllium at 600°, 650°, 700° and 750°C in moist oxygen at a total pressure of 10 cm with 1.2 cm partial pressure of water.

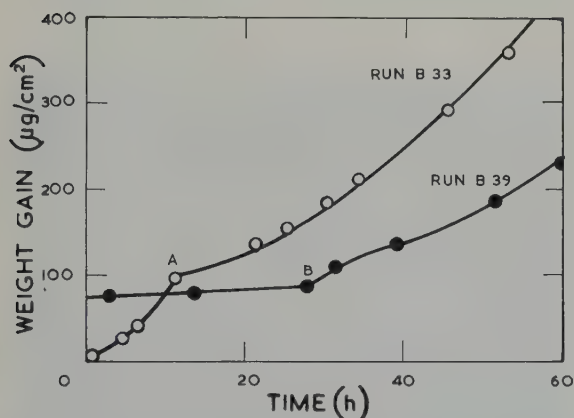


Fig. 8. Oxidation of beryllium at 700°C. In run B33 the oxidising gas was changed at A from water (1.2 cm) to dry oxygen (10 cm) and in run B39 from dry oxygen (10 cm) to water vapour (1.2 cm) at B. The part of the curve of run B39 corresponding to oxidation in water vapour is shown in fig. 9. For run B39, add 90 h to the time axis.

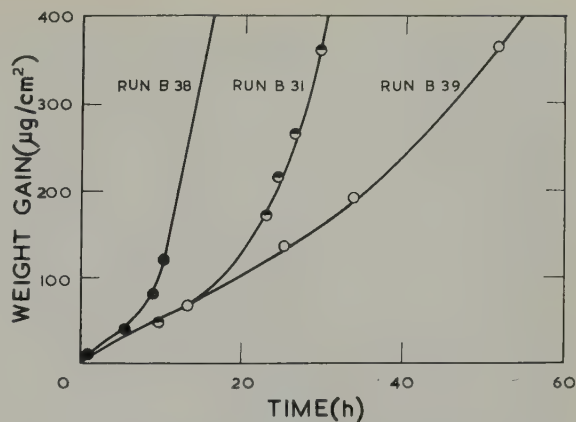


Fig. 9. Oxidation of beryllium at 700°. Run B38, water vapour (1.2 cm); run B31, moist oxygen (10 cm total pressure, partial pressure of water 1.2 cm); run B39 (pre-oxidised in dry oxygen for 113 h) in water vapour (1.2 cm).

first abruptly decrease, it subsequently increased again, and after 50 h was much greater than if dry oxygen had been used from the start of the run ($8 \mu\text{g}/\text{cm}^2 \text{ h}$ compared with $0.2 \mu\text{g}/\text{cm}^2 \text{ h}$).

3.3. METALLOGRAPHIC EXAMINATION OF OXIDISED SAMPLES (with J. K. Higgins †)

A number of the oxidised samples (those denoted by an asterisk in table 1) were examined metallographically, each sample being sectioned (see fig. 10) and one half being mounted in Perspex. After grinding on emery paper, lubricated with paraffin, down to Grade 600, the metal cross-section was successively polished with grades of "Hyprez" diamond dust of increasing fineness, the final polish being carried

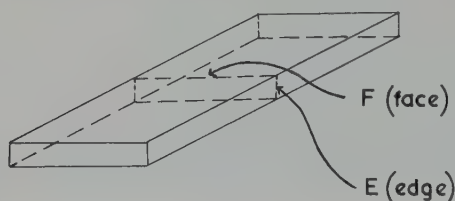


Fig. 10. Cross-section of beryllium specimen illustrating the edge "E" and face "F" used to describe the micrographs in fig. 11.

† Metallurgy Division, AERE, Harwell.

out on No. 1 grade and paraffin. Finally the metal was given a light etch in 10 % oxalic acid solution and dried in air after rinsing with ethyl alcohol.

Each of the sectioned samples was carefully examined under the microscope at a magnification of about 250, and no differences could be detected in the appearance of samples oxidised at a given temperature whether the gas was moist oxygen, water vapour, or dry oxygen followed by water vapour. From the typical micrographs shown in fig. 11 it is evident that in those samples which had undergone breakaway, there is extensive attack down the grains

of the metal, so that instead of a distinct metal/oxide interface, there is an interpenetrating network of oxide and unattacked metal; but in the sample which had been oxidised at 600° C (A25) in moist oxygen for 300 h without breakaway (fig. 11a), the metal surface is well defined and there is no indication of intergranular attack.

The thickness of the interpenetrating zone of metal and oxide was by no means constant in a particular sample, as shown by comparing figs. 11b and 11c which represent different regions of the sample (B27 at 750° C). In all the micrographs the edges and face of the sample

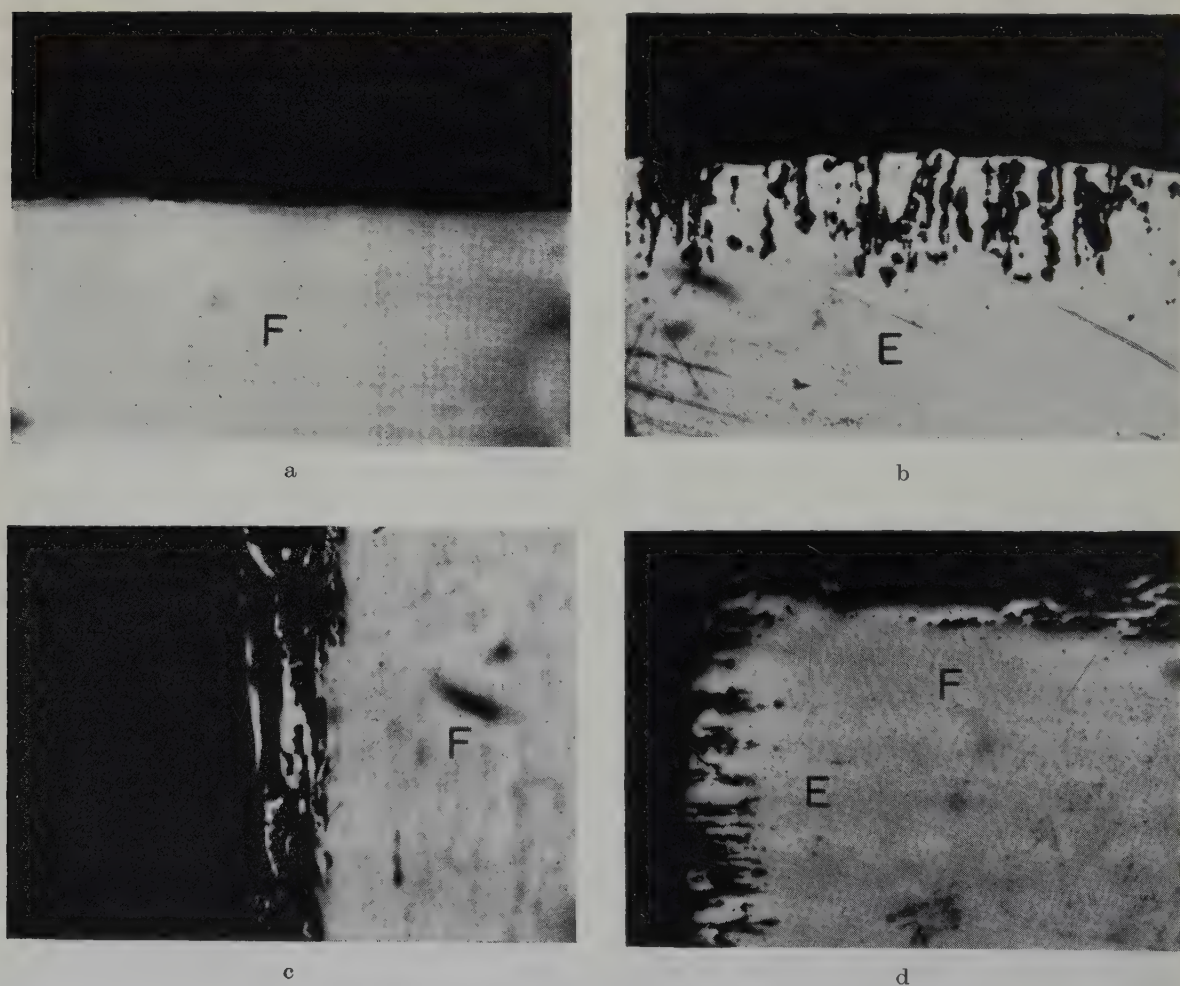


Fig. 11. Micrographs of oxidised beryllium specimens showing the intergranular penetration of oxide into the metal. (a) run A25; (b) run B27; (c) run B27; and (d) run B29. The weight gains and oxidising conditions are recorded in table 1. $\times 150$.

before sectioning are indicated by the letters "E" and "F" respectively (see fig. 10) and reference to fig. 11d will show that penetration occurs to a greater extent at the edge than the face—in other words parallel rather than perpendicular to the direction of rolling of the powdered material. Since with rolled specimens of beryllium, the basal planes of the crystals usually lie parallel to the surface, the more extensive penetration at the edge may reflect a greater rate of oxidation along the basal planes rather than perpendicular to them.

4. Discussion

4.1. GENERAL

The oxidation graphs, whether in water vapour or in moist oxygen, fall into two groups according as breakaway does or does not occur.

At temperatures in the range 500°–600° C there is no breakaway (at any rate within the 300 h duration of the experiments); and the graphs at any one temperature are broadly similar whether the oxidation was carried out in moist oxygen or in pure water vapour (cf. figs. 1 and 6) or in dry oxygen (Part I). Accurate comparison of graphs is hampered by the poor reproducibility, but the weight gains at 300 h in the three gases agree reasonably closely at a given temperature (table 1).

At temperatures between 650° and 750° C there is a contrast between the results in moist oxygen and pure water vapour on the one hand, and in dry oxygen on the other; breakaway occurs in the two former media but is absent in dry oxygen except at 750° C, and even then it occurred only after 60 h. The curves for moist oxygen and for water vapour are broadly similar, as can be seen by reference to fig. 2 for 650° C. Such differences as do exist can be reasonably attributed to the poor reproducibility already referred to, and more particularly to the experimental procedure, inasmuch as oxidation proceeded initially in dry oxygen; the oxide film thus formed before exposure to water vapour commenced would retard breakaway (cf. figs. 8 and 9).

Thus it seems that when beryllium is oxidised in moist oxygen at 650° C and above, it reacts only with the water vapour—a conclusion supported by the experiments at 700° C when on changing the gas from water vapour to dry oxygen, or vice versa, the rate of oxidation altered suddenly (fig. 8).

4.2. MECHANISM OF FILM GROWTH

The essential similarity between the curves for oxidation in dry oxygen (Part I) and in water vapour (no distinction will be made between oxidation in water vapour and in moist oxygen) at temperatures up to and including 600° C suggests that the rate controlling step is the same in the two gases.

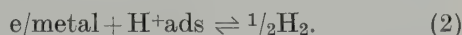
The curves for dry oxygen fall within what is generally termed the "thin film" region of oxidation⁴⁾ and according to the accepted model, the metal ions and their electrons diffuse across the oxide layer under the influence of an electrostatic field F resulting from the electrostatic potential V across the film. This potential arises because the faster moving electrons ionize the oxygen which is adsorbed at the gas/oxide interface and the equilibrium



is set up. In the original theory of Mott and Cabrera⁴⁾, V was assumed to be independent of film thickness X , so that $F = V/X$; it was shown that the metal (n-type oxide) should then thicken according to a parabolic rate law (not to be confused with the earlier parabolic law of Wagner⁵⁾ which refers to much greater values of X). More recently, Cabrera⁶⁾ has suggested that V is not constant but instead diminishes as X increases because the equilibrium (1) is never reached; the rate of oxidation should therefore decrease with increasing time in a complicated manner, and the curve of X against time should accordingly fall below that predicted by the original theory. The marked deviations from the parabolic rate law which occur when beryllium is oxidised in dry oxygen (Part I) are probably to be explained largely along these lines, rather than by compositional changes in

the oxide film which probably constitute at most a secondary factor, and no longer the primary factor as was envisaged in Part I.

In water vapour the surface will be covered, though almost certainly incompletely, with chemisorbed water molecules; it is reasonable to suppose that this water is present as an OH^- ion located close to a lattice Be^{++} ion and an H^+ ion close to a lattice O^{--} ion (fig. 12a). For the metal to oxidise in water vapour, Be^{++} ions must diffuse across the oxide layer and this can only occur under the influence of an electrostatic field; such a field could be set up if a proportion of the H^+ ions was to capture electrons from the metal and discharge (fig. 12b) as hydrogen gas.



The exact mechanism by which the hydrogen atoms combine to form H_2 molecules is uncertain, but it would seem likely that surface diffusion plays some part.

Each outward diffusing Be^{++} ion on reaching the gas/oxide interface can in principle take up a position alongside one OH^- ion (as in B of fig. 12b) or more probably a position between

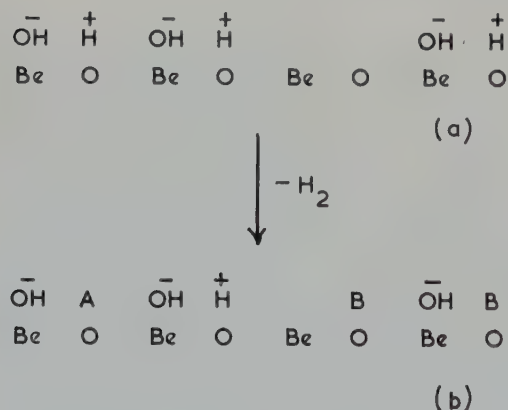


Fig. 12. Diagram illustrating (a) the chemisorption and dissociation of water on the oxide surface and (b) the loss of protons (as hydrogen gas) in order that an electrostatic field may be set up across the oxide layer. The positions A and B are referred to in the text (Section 4.3).

two OH^- ions (as in A of fig. 12b). Since beryllium hydroxide is unstable⁷⁾ in the bulk form at the temperature and pressures of the present work, presumably either the transition complex $[\text{HO} \cdot \text{Be} \cdot \text{OH}]$ decomposes to evolve water, or alternatively a two-dimensional nucleus grows until it reaches a critical size when it decomposes into oxide and water.

4.3. BREAKAWAY

The generally accepted mechanism of breakaway^{8,9)} is that a continuous oxide layer grows on the metal surface until the stresses in the oxide, whether compressional or tensional, cause it to crack; the attacking gas then penetrates these cracks so that the rate of oxidation is controlled by the rate of diffusion of reactant through a very thin layer (barrier film) adhering to the metal. The weight gain at which breakaway occurs differs widely from metal to metal, being about $50 \mu\text{g}/\text{cm}^2$ for niobium^{9,10,11)} and magnesium⁸⁾ and from 2 to $3 \text{ mg}/\text{cm}^2$ for zirconium and some of its alloys^{12,13,14)}.

The fact that beryllium undergoes breakaway during oxidation in moist oxygen or water vapour at a lower temperature than in dry oxygen is not in itself surprising, for the effect of water in promoting film breakdown on metals is well recognised^{8,15,16)}. There are, however, several curious features associated with the breakaway oxidation of beryllium in water vapour: (a) the weight gain at which breakaway occurs markedly decreases with increasing temperature of oxidation so that at 750°C the value is only $5 \mu\text{g}/\text{cm}^2$ corresponding to a film thickness of about 350 \AA (allowing 100 \AA for the thickness of the "room temperature" film); (b) the attack after breakaway takes the form of penetration between the grains of the metal, whereas with other metals (tungsten¹⁷⁾, niobium⁹⁾) the metal/oxide interface, although irregular, remains reasonably well defined. It is not certain how far this uneven attack results from the mode of fabrication of the beryllium. The two features (a) and (b) will now be discussed in turn.

(a) *Mechanism of Breakaway*

As already discussed, the rates of oxidation in dry oxygen and in water vapour are not greatly different (at 600° C for times up to 300 h and at 650° C and above, up to the time at which breakaway occurs) so that it would seem reasonable to suppose that the compositions of the films formed in these gases are similar. On the other hand, the film formed in dry oxygen at 750° C grows to a thickness of 5000 Å before breakaway occurs, whereas that in water vapour only reaches 350 Å in thickness. This suggests that in water vapour some additional factor is operating to promote breakaway; and it is tentatively suggested that (as is believed to occur with certain other metals¹⁸), an inward flow of protons accompanies the outward diffusion of Be⁺⁺ ions and their electrons †. The diffusion of protons might consist in jumps from one interstitial position to the next, or from one O⁻⁻ ion (which would thus be temporarily converted to an OH⁻ ion) to the next O⁻⁻ ion. Since the solubility of hydrogen in beryllium is probably extremely small (beryllium has been heated in hydrogen at temperatures up to 882° C without any reaction²⁰), the protons would not enter the metal when they reached the beryllium/oxide interface, but would be discharged as hydrogen gas. As Draley and Ruther¹⁸) have commented, a small amount of hydrogen might be sufficient to rupture the oxide film. The pronounced decrease in the film thickness at which breakaway occurs may be interpreted in terms of the relative temperature coefficients of the rates of diffusion of Be⁺⁺ ions and of protons.

Although there is no direct evidence for the above model, it is easy to see why a pre-formed oxide film is able to retard breakaway: the diffusion path across the oxide layer will be greater, and the time which elapses before sufficient hydrogen is able to diffuse through the film and so disrupt the oxide layer will be larger.

† The inward diffusion of OH⁻ ions is considered to be unlikely because of the large size of the OH⁻ ion (1.7 Å as compared with 1.4 Å for the O⁻⁻ ion¹⁹).

(b) *Postbreakaway Oxidation*

It is not clear why, after breakaway, oxidation takes place preferentially along the particle boundaries; it may be that the film first cracks along the lines where the particle boundaries emerge or alternatively these places may only be attacked when the film has undergone a general cracking. It is clear that once intergranular oxidation begins, the process will be favoured by the fact that the oxide-to-metal volume ratio for beryllium is 1.7:1, so that the compressive stresses resulting from the conversion of metal to oxide will tend to force the grains apart. Furthermore, one infers that the oxide must be porous to gaseous water; this porosity was proved by an experiment in which the surface area of a sample oxidised in water vapour at 750° C for 2.3 h (B30) was measured by the method of krypton sorption²¹). The resultant value of 0.135 m² corresponds to a specific surface of 23 m² per gram of oxide, so that the latter is penetrated by cracks of molecular dimensions which permit the ready passage of krypton and therefore of water molecules.

(c) *Discontinuous Oxidation*

It finally remains to discuss the discontinuous weight changes obtained in some of the runs. It would seem fairly clear that those obtained at 650° C and 700° C (figs. 2 and 5) represent what may be termed localised breakaway; indeed, the curve after breakaway can be regarded as resulting from individual breakaway processes which take place over a large number of isolated areas, and blend to give a smooth oxidation curve. The discontinuity found in the run at 500° C in moist oxygen (fig. 6) was similar to those found in a number of runs during oxidation in dry oxygen at temperatures between 500° C and 600° C (Part I). This raises the interesting question of whether the discontinuities in dry oxygen are also associated with localised penetration of oxide into the metal; unfortunately no metallographic investigation of the specimens in Part I was undertaken and would in any case be difficult

because the associated weight changes were very small (equivalent to $1 \mu\text{g}/\text{cm}^2$).

5. Conclusions

When electrolytic flake beryllium is oxidised at temperatures from 500° to 750°C , the oxidation follows essentially the same course in water vapour as in moist oxygen (10 cm total pressure) for the same pressure of water vapour (1.2 cm). At temperatures up to and including 600°C , the rate of oxidation continuously decreases with time to reach a very small value (e.g. $0.06 \mu\text{g}/\text{cm}^2 \text{ h}$) after about 100 h so that the oxidation is protective; the weight gains in this temperature range are essentially the same as in dry oxygen for a given temperature and time of oxidation.

At 650°C and above, the rate of oxidation first decreases and then increases with time, indicating breakaway and subsequent non-protective oxidation; the weight gain at which breakaway occurs decreases with increasing temperature of oxidation: at 750°C breakaway occurs when the film is only 350 \AA thick. Experiments at 700°C show that if an oxide layer is first pre-formed in dry oxygen, breakaway is retarded but not prevented on subsequent exposure to water vapour; conversely, non-protective oxidation produced by oxidation in water vapour cannot be arrested by continuing the oxidation in dry oxygen. Metallographic examination of a number of samples indicates that after breakaway, oxidation proceeds preferentially at the particle boundaries giving rise to an interpenetrating zone of oxide and unattacked metal.

The mechanism of the reaction of beryllium with water vapour is discussed and it is suggested that an inward diffusion of protons may accompany the outward diffusion of Be^{++} ions through the film and cause the film to crack.

Acknowledgements

It is a pleasure to thank Dr. J. K. Higgins for carrying out the metallographic work, and Dr. J. E. Antill for his continued interest. We are also grateful to the UK Atomic Energy Authority who supported this work.

References

- ¹) D. W. Aylmore, S. J. Gregg and W. B. Jepson, *J. Nucl. Mat.* **2** (1960) 169
- ²) S. J. Gregg, R. J. Hussey and W. B. Jepson, *J. Nucl. Mat.* **2** (1960) 225
- ³) S. J. Gregg, R. J. Hussey and W. B. Jepson, *J. Nucl. Mat.* **3** (1961) 225
- ⁴) N. Cabrera and N. F. Mott, *Rep. Progr. Phys.* **12** (1948) 163
- ⁵) C. Wagner, *Z. physikal. Chem.* **21B** (1933) 25
- ⁶) N. Cabrera in *Semiconductor Surface Physics*, Ed. by R. H. Kingston (University of Pennsylvania Press, Philadelphia, 1957)
- ⁷) P. Murray and R. W. Thackray, AERE (Harwell) Report M/R 1410 (1954)
- ⁸) S. J. Gregg and W. B. Jepson, *J. Inst. Metals* **87** (1958-59) 187
- ⁹) J. V. Cathcart, J. J. Campbell and G. P. Smith, *J. Electrochem. Soc.*, **105** (1958) 442
- ¹⁰) D. W. Aylmore, S. J. Gregg and W. B. Jepson, *J. Electrochem. Soc.* **107** (1960) 495
- ¹¹) E. A. Gulbransen and K. F. Andrew, *J. Electrochem. Soc.*, **105** (1958) 4
- ¹²) L. F. Kendall, R. G. Wheeler and S. H. Bush, *Nuclear Science and Eng.* **3** (1958) 171
- ¹³) E. A. Gulbransen and K. F. Andrew, *Trans. AIME* **212** (1958) 281
- ¹⁴) E. A. Gulbransen and K. F. Andrew, *Corrosion* **14** (1958) 50
- ¹⁵) H. J. Svec and C. Apel, *J. Electrochem. Soc.* **104** (1957) 346
- ¹⁶) S. J. Gregg and W. B. Jepson, to be published
- ¹⁷) W. W. Webb, J. T. Norton and C. Wagner, *J. Electrochem. Soc.* **103** (1956) 107
- ¹⁸) J. E. Draley and W. E. Ruther, *J. Electrochem. Soc.* **104** (1957) 329
- ¹⁹) see however T. P. Hoar and N. F. Mott, *J. Phys. Chem. Solids* **9** (1959) 97
- ²⁰) E. A. Gulbransen and K. F. Andrew, *J. Electrochem. Soc.* **97** (1950) 383
- ²¹) D. W. Aylmore and W. B. Jepson, to be published

ATMOSPHERIC CORROSION TESTS OF SEVERAL DELTA-PHASE ALLOYS OF PLUTONIUM

J. T. WABER, W. M. OLSON and R. B. ROOF, Jr.

Los Alamos Scientific Laboratory, University of California, New Mexico, USA

Received 22 July 1960

A study of the oxidation of delta-phase, binary plutonium alloys containing small additions of aluminum, cerium, hafnium, zinc and zirconium has been conducted. The oxidation rates at 75° C in moist air are all lower than the oxidation rate of unalloyed plutonium under the same conditions. The results do not appear to be in accord with the simple theory of the influence of solute additions on the oxidation rate as proposed by Wagner and Hauffe. A size rule was suggested for deciding *a priori* whether a solid-solution miscibility gap between oxide phases might occur. This rule was only partially successful in predicting which oxide phases would be observed to form separate layers.

It is interesting that the zirconium and hafnium alloys were found to form ZrO_2 and HfO_2 as separate phases in the oxide layer. These separate oxide phases are to be expected on the basis of the size-factor rule discussed above. There is no evidence, however, that Al_2O_3 or ZnO , in which smaller metal-oxygen distances occur, were present as separate phases in the oxidation products. For thermodynamic reasons, ZnO should not appear in the products. The special reasons that Ce_2O_3 and Al_2O_3 might not be detected have been discussed.

The analyses of Wagner concerned with the formation of single or duplex oxide films have been discussed and it is shown that the formation of HfO_2 and ZrO_2 as well as Al_2O_3 and Ce_2O_3 should occur. The apparent reduction in rates can be rationally interpreted on this basis.

L'oxydation en phase delta d'alliages binaires de plutonium contenant de faibles additions d'aluminium, cérium, hafnium, zinc et zirconium, a été étudiée. Les vitesses d'oxydation à 75° C dans l'air humide ont été trouvées toutes plus faibles que celle du plutonium non allié, oxydé dans les mêmes conditions. Les résultats ne semblent pas être en accord avec la théorie simple de Wagner et Hauffe qui traite de l'influence des additions de soluté sur la vitesse d'oxydation. Une règle faisant intervenir la taille des

ions a été suggérée pour prévoir *a priori* si une lacune de miscibilité entre les solutions solides des phases d'oxydes pouvait se produire. Le succès obtenu par cette règle dans la prévision des phases d'oxydes qui devaient être observées à l'état de couches séparées, n'a été que partiel.

Il est intéressant de noter que les alliages de zirconium et de hafnium donnaient lieu à la formation de ZrO_2 et HfO_2 respectivement à l'état de phases séparées dans la pellicule d'oxydation. En se basant sur la règle du facteur de taille, discutée plus haut, on devait bien s'attendre à l'apparition des phases séparées de ces oxydes. Par contre Al_2O_3 ou ZnO , dans lesquels on trouve des distances métal-oxygène plus faibles, n'ont pas été mis en évidence à l'état de phases séparées dans les produits d'oxydation. Pour des raisons d'ordre thermodynamique, ZnO ne devrait pas apparaître dans les produits de réaction. Les raisons particulières pour lesquelles Ce_2O_3 et Al_2O_3 ne peuvent être décelés sont discutées.

Les analyses de Wagner ayant trait à la formation d'oxydes simples ou doubles ont été discutées et il a été montré que la formation de HfO_2 et de ZrO_2 , de même que celle de Al_2O_3 et de Ce_2O_3 devrait avoir lieu. La réduction constatée des vitesses peut être interprétée de façon rationnelle sur cette base.

Die Oxydation binärer δ -Legierungen von Plutonium mit geringen Zusätzen an Aluminium, Cer, Hafnium, Zink und Zirkonium wurde untersucht. Bei 75° C ergaben sich in feuchter Luft durchweg kleinere Oxydationsgeschwindigkeiten als bei unlegiertem Plutonium. Die Ergebnisse scheinen nicht übereinzustimmen mit der einfachen Theorie von Wagner und Hauffe über den Einfluss kleiner, gelöster Beimengungen auf die Oxydationsgeschwindigkeit. Es wurde eine die Atomgrösse berücksichtigende Regel vorgeschlagen, die vorherzusagen gestattet, ob eine Mischungslücke im Oxydsystem auftritt. Diese Regel war für die Voraussage, ob ein bestimmtes Oxyd als separate Schicht zu beobachten ist, nur teilweise geeignet.

Von Interesse ist, dass bei Legierungen von Zirkonium und Hafnium ZrO_2 und HfO_2 als getrennte Phase in der Oxydschicht erscheinen. Auf Grund der oben erwähnten Regel war dies zu erwarten. Dagegen waren keine Hinweise dafür vorhanden, dass Al_2O_3 oder ZnO , bei denen kleinere Metall-Sauerstoff-Abstände vorliegen, als separate Phase im Oxydationsprodukt auftreten. ZnO sollte aus thermodynamischen Gründen in den Reaktionsprodukten nicht vorkommen.

1. Introduction

The corrosion behavior of unalloyed plutonium was discussed several years ago ¹⁾ and the corrosion resistance of three dilute alloys was briefly reported at the Second Geneva Conference ²⁾. The results of high-temperature oxidation runs have been presented by Dempsey and Kay ³⁾ as well as by Waber ¹⁾.

It was noted that small additions of thorium were not very beneficial, whereas similar additions of aluminum afforded some protection against oxidation by moisture. Additional experiments with alloys containing small amounts of aluminum and zirconium were performed by Waber ²⁾. Recently Sackman ⁴⁾ also compared the atmospheric corrosion resistance of 3.5 at % aluminum alloy with that of unalloyed plutonium in dry and in moist air. The present report deals with the results of further tests that were conducted in an effort to elucidate the mechanism of protection conferred by the alloying addition in delta-phase alloys.

2. Influence of Alloying Elements

Wagner, Hauffe and their colleagues ⁵⁾ have shown that the rates of oxidation and corrosion processes can be significantly influenced by changing the concentration of either lattice imperfections or of mobile carriers of electronic current in the oxide film by means of solute additions to the film; either approach can limit the rate of attack. While many of the theoretical and practical ramifications of such an approach cannot conveniently be discussed here, the situation as it pertains to plutonium will be briefly reviewed.

Plutonium dioxide, which has the fluorite

Die spezielle Ursache dafür, dass Ce_2O_3 und Al_2O_3 nicht gefunden werden, wurde besprochen.

Die Analyse von Wagner, welche sich auf die Bildung von einfachen Oxyden oder Doppeloxyden bezieht, wurde diskutiert. Es wurde gezeigt, dass HfO_2 und ZrO_2 ebenso wie Al_2O_3 und Ce_2O_3 gebildet werden sollten. Die offensichtliche Abnahme der Reaktionsgeschwindigkeit kann auf dieser Basis in vernünftiger Weise erklärt werden.

(CaF_2) type structure, is the major product observed in various oxidation experiments. The other stable oxides, Pu_2O_3 and Pu_4O_7 , are characterized by anion vacancies, and their lattice arrangements are closely related to the fluorite lattice, as Holley *et al.* ⁶⁾ report. Attempts to prepare compositions of the type PuO_{2+x} have been unsuccessful ⁶⁾. Thus it is likely that random anion vacancies will occur in oxides having the compositions PuO_{2-x} (where x is small) and that the interstitial anions will be only those arising from Anti-Frenkel defects. The best analysis of the contribution of these three types of imperfections, namely, anion vacancies, interstitial anions and Anti-Frenkel defects to diffusion processes in fluorite lattices is the work of Ure ⁷⁾ which dealt with doped CaF_2 .

The nature of the conduction mechanism in PuO_2 is not known but can be inferred by analogy to UO_2 and CeO_2 . Willardson, Moody, and Goering ⁸⁾ showed that UO_{2+x} (where x is small) is a p-type semiconductor. The positive holes in the conduction band are in keeping with the enhanced valence of 5 or 6 which the uranium atom can acquire. In contrast, the plutonium atom apparently can only acquire a valence lower than or equal to 4 in its solid oxides. Thus one would anticipate that PuO_2 would have a more negative character as a semiconductor than urania would.

In further contrast to uranium, the sesquioxides of plutonium and cerium are apparently more stable than the dioxides, as will be discussed below. Czanderna and Honig ⁹⁾ have shown that during vacuum treatment CeO_2 will lose oxygen from its fluorite lattice and become an n-type semiconductor with decreased ohmic

resistance. Thus a change in PuO_2 from a p-type to an n-type semiconductor would be expected as the net oxygen content in the oxide decreased. At small defect concentrations, the electron hole conductivity would be very reduced or nil. When the x in PuO_{2-x} becomes large enough, quasi-free electrons would be the majority carriers.

In general, the dissolution in PuO_2 of cations having a valence lower than 4 will increase the concentration of anion vacancies, and as a consequence, the diffusion of anions through the oxide will be increased. In a narrow range of x values in the metal-to-oxygen ratio (near $2-x$), where the concentrations of both the quasi-free electrons and positive holes are very low, the electrical conductivity of the oxide may significantly reduce the oxidation rate, despite the adequate diffusion rate. This is one way in which a soluble alloying element B , whose cations are also soluble in the oxide, may influence the oxidation rate.

As a first step toward establishing the suitability of this approach, one must determine that a potential alloying element will dissolve in both the metal and the oxide. Other treatments of the oxidation process may be applied in case these criteria are not fulfilled.

The following alloying elements are known to be soluble in delta plutonium: aluminum, cerium, hafnium, zinc, and zirconium. They offer an interesting opportunity to apply Wagner's concept of alloy oxidation, inasmuch as zinc has the valence 2 and aluminum 3, whereas cerium, hafnium and zirconium are quadrivalent and thus should exert little influence on the vacancy concentration in PuO_2 and hence on the corrosion rate.

Unfortunately, little information is available on the solubility of oxides mixed with plutonia. Mulford and Ellinger^{10,11} have found that complete solid miscibility exists in the systems $\text{PuO}_2 + \text{UO}_2$, $\text{PuO}_2 + \text{CeO}_2$ and $\text{PuO}_2 + \text{ThO}_2$. In the absence of further information, one may predict the solubility of oxides in plutonium dioxide by analogy to mixed oxide systems involving uranium dioxide and thorium dioxide.

Examination of the phase equilibria diagrams for various mixed oxide systems suggests that cations which differ greatly in size do not form oxide solutions having extensive solubility ranges. An effective working rule is discussed below.

While the influence of alloying additions on the defect concentration is well understood, there are at least two other manners by which oxidation can be retarded. If the solute B is more noble than plutonium, with respect to oxidation, a depleted zone (rich in B) may develop beneath the oxide and thus reduce the rate of arrival of plutonium atoms at the oxide-metal interface. Alternatively, a thin layer of an oxide of B designated BO may form during the initial stages of oxidation and thus limit the oxidation of the plutonium alloy by reducing the diffusion of ions through it to the outer surface of the oxide layer.

Some attention is given below to interpreting the corrosion results from these different viewpoints. The separation of oxide phases apparently does have an important influence on the oxidation of plutonium alloys.

3. Experimental Procedure

Binary plutonium alloys were made with aluminum, cerium, hafnium, zinc, and zirconium by induction melting and casting into MgO slab molds. Chemical analyses for impurities contained in these alloys are presented in table 1. The original 0.6 cm ($\frac{1}{4}$ in.) thickness of each coupon was reduced by successively cold rolling (about 50 % reduction) and annealing at 420°C for $\frac{1}{2}$ h or more. Both sides of the resulting 20 mil sheet were then metallographically polished through 600 grit paper without using a lubricant. Specimens approximately one inch square were cut, weighed and placed in weighed and numbered beakers, which were then placed in desiccators containing a saturated solution of NaBr . This solution was selected because, over a range of temperatures, the activity of water in it yielded approximately 50 % relative humidity in the air of the desiccators. The desiccators were kept in thermostatted

TABLE I

Chemical analyses of the delta-phase alloys used in the corrosion experiments

Alloying element	Composition (at %) Nominal	Vacuum fusion (ppm)		Spectroscopic analysis (ppm)							
		C	O	Na	Mg	Al	Si	Fe	Ni	Cr	La
Al	6	135	65	< 100	< 50	—	200	100	< 100	< 50	< 100
	6	140	15	< 100	< 50	—	300	100	< 100	< 50	< 100
	12	130	75	< 100	< 50	—	200	100	< 100	< 50	< 100
Ce	6	85	460	< 100	< 50	< 50	< 100	200	< 100	< 50	< 100
	9	35	90	< 100	< 50	< 50	< 100	200	< 100	< 50	< 100
	12	50	50	< 100	< 50	< 50	< 100	200	< 100	< 50	< 100
Hf	6	40	65	< 10	< 5	30	3500	< 100	< 100	< 50	< 10
	9	15	60	< 10	< 5	40	100	< 100	< 100	< 50	< 10
	12	20	85	< 10	< 5	40	20	< 100	< 100	< 50	< 10
Zn	6	130	70(250) †	< 100	< 50	100	400	600	150	100	< 100
	9	65	65(135) †	< 100	< 50	150	400	600	150	100	< 100
	12	80	275(360) †	< 100	< 50	150	200	400	150	< 50	< 100
Zr	4.3	15	50	< 10	< 5	20	< 100	200	< 400	< 50	< 10
	8.9	70	100	< 10	10	75	< 100	200	100	< 50	< 10

† Duplicate values indicating segregation.

ovens. After a suitably long exposure to moist air, the beakers and specimens were removed from each desiccator (after it had been permitted to cool to room temperature) and weighed on a Mettler Gramatic type microbalance. Then the beakers and specimens were returned to the desiccators for further exposure.

Each oxidized specimen was wrapped with a thin Mylar film to prevent the spread of radioactive contamination, and the identity of the oxide was established by X-ray diffraction analysis with a Norelco Diffractometer. The bulk of the oxide was then removed by polishing. The polished specimens, which were covered with a thin, almost transparent oxide layer, were then re-examined to determine whether changes in the oxide or the underlying alloy had occurred. In addition, specimens were examined after electropolishing and after subsequent mechanical polishing. The latter samples were oxidized for only 24 hours in the desiccators containing 50 % relative humidity at 75° C

and re-examined. The X-ray diffraction results on oxidized specimens, as well as on the unoxidized annealed alloy specimens, will be discussed below.

Plutonium specimens, although covered with a loosely adherent oxide, were handled safely in the open laboratory (without spreading radioactive contamination) when wrapped in Mylar foil. This experience in handling plutonium in the open laboratory is similar to that reported by Cramer and Schonfeld¹²).

3.1. RESULTS OF EXPOSURE TESTS

The principal results of this investigation, namely, the corrosion rates, are presented in figs. 1, 2, 3, 4 and 5. It will be seen that, with the exception of cerium, the alloying elements impart substantial protection to plutonium. The mechanism by which the corrosion rate is reduced contrary to the Wagner-Hauffe prediction is apparently complex and will be discussed below.

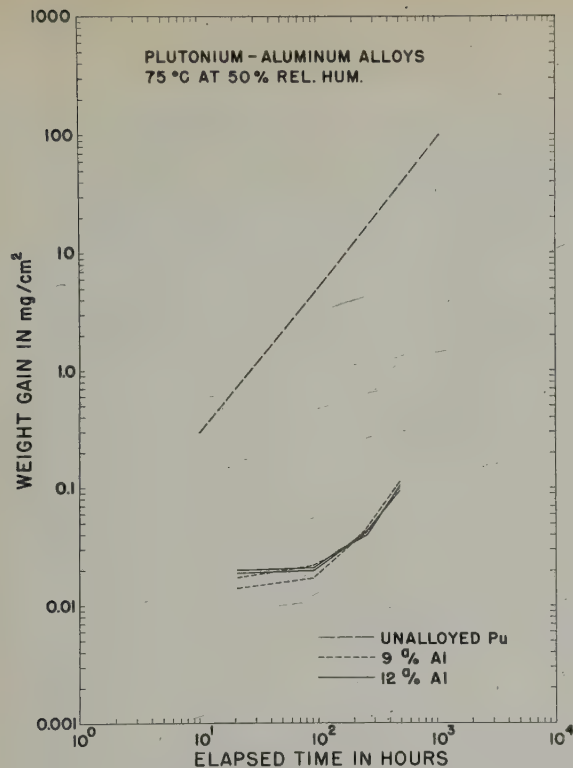


Fig. 1. Comparison of the corrosion behaviors of plutonium-aluminum alloys and unalloyed plutonium exposed to air at 75° C and 50 % relative humidity.

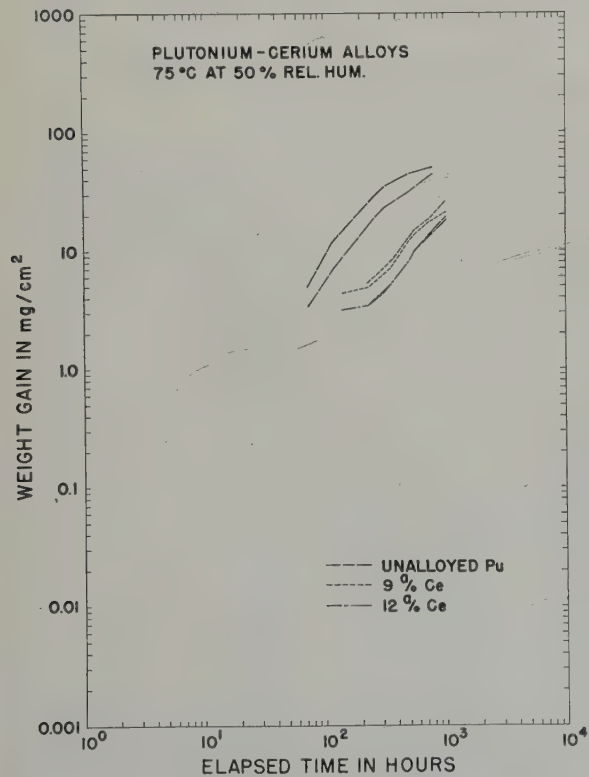


Fig. 2. Comparison of the corrosion behaviors of plutonium-cerium alloys and unalloyed plutonium exposed to air at 75° C and 50 % relative humidity.

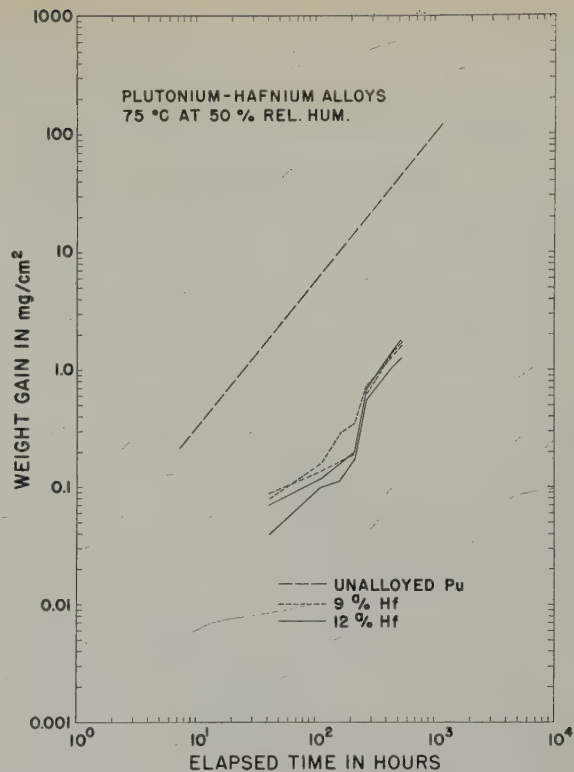


Fig. 3. Comparison of the corrosion behaviors of plutonium-hafnium alloys and unalloyed plutonium exposed to air at 75° C and 50 % relative humidity.

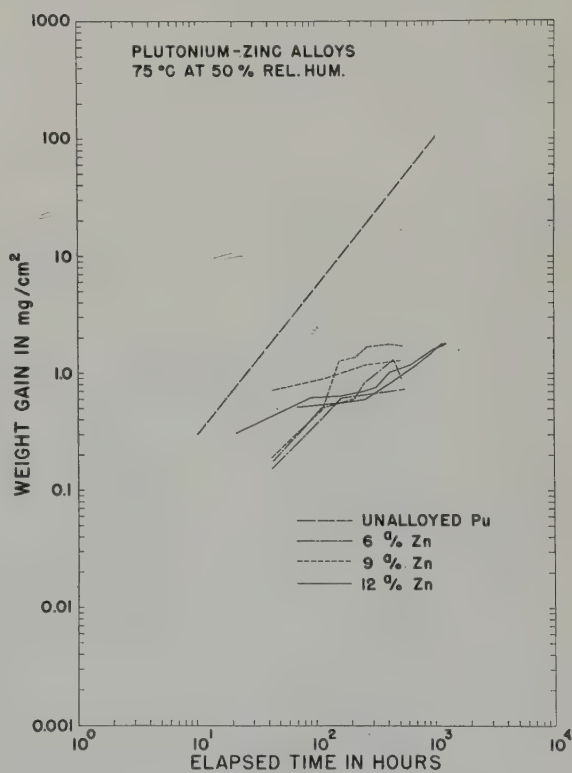


Fig. 4. Comparison of the corrosion behaviors of plutonium-zinc alloys and unalloyed plutonium exposed to air at 75° C and 50 % relative humidity.

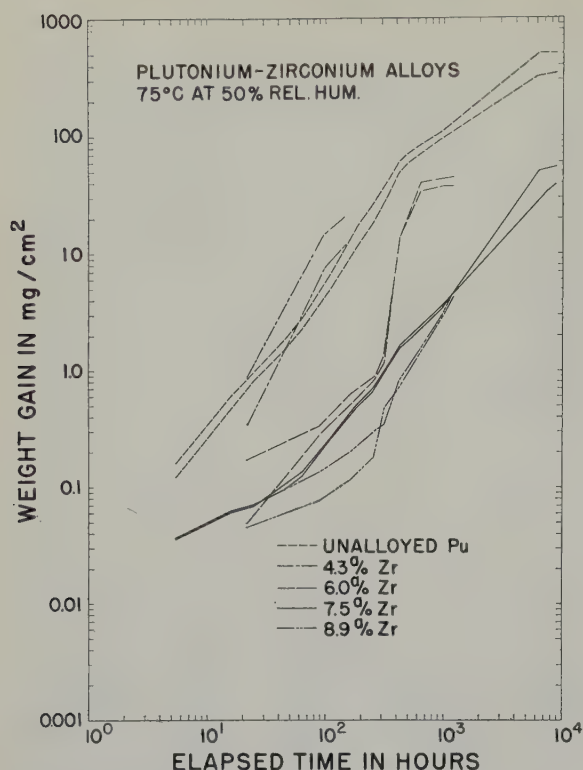


Fig. 5. Comparison of the corrosion behaviors of plutonium-zirconium alloys and unalloyed plutonium exposed to air at 75°C and 50% relative humidity.

One reasonable way to compare the effect of different alloying elements on corrosion behavior is to compare the merit ratios of the alloys at equivalent times. This quantity is defined as the weight gain of unalloyed plutonium divided by the weight gain of the alloy at a given time. If the time dependence is not the same for an alloy as it is for the unalloyed metal (and Waber²) notes that this frequently occurs) the merit ratio will, of course, change with time. The data of the present investigation for 500 and 1000 h exposures are thus conveniently summarized in table 2. Weight gains for the unalloyed plutonium specimens exposed in the same desiccator with the alloyed specimens are also presented in table 2. It will be seen that there are fairly large variations among the alpha-plutonium specimens. Unfortunately, no explanation is available for this variability among specimens presumed to have been identically exposed.

3.2. X-RAY DIFFRACTION RESULTS

An effort was made to establish by X-ray diffraction whether the metal near the inner

TABLE 2

Merit ratios for delta-phase plutonium alloys exposed to air containing 50% relative humidity at 75°C

Alloy comp. (at %)		Merit ratio observed		mg/cm ² gained, alpha Pu	
		at 500 h	at 1000 h	at 500 h	at 1000 h
Aluminum	9	428	666	42.0	100.0
Aluminum	12	388	588	42.0	100.0
Cerium	9	2.69	2.19	33.0	46.0
Cerium	12	5.55	2.70	45.9	50.1
Hafnium	9	24.3	44.4	40.0	100.0
Hafnium	12	23.6, 33.5 †	43.4, 64.5	40.0	100.0
Zinc	6	34.0, 44.1 †	122	~ 34.0	100.0
Zinc	9	19.7, 26.1 †	80	~ 34.0	100.0
Zinc	12	31.1, 36.8 †	62.5t	~ 34.0	100.0
Zirconium	4.3	1.22	0.61	13.5	24.5
Zirconium	6.0	1.1	—	—	—
Zirconium	8.9	17.1	7.42	20.0	24.5

† Duplicate values of the merit ratio are listed where differences between duplicate values appeared to be significant.

interface became enriched or depleted in the added element or whether a separation of the oxide phases occurred. The dilute delta phase alloys are, in general, metastable and show a decided tendency to transform under pressure as Elliott and Gschneidner¹³⁾ have shown. The possibility that the surface of these alloys could contain the monoclinic alpha plutonium phase as a result of mechanical polishing, was also investigated. This was important since the occurrence of this phase at the end of the corrosion could equally be interpreted as evidence that an insufficient amount of the alloying element was present to retain the delta phase, i.e., that depletion had occurred, or as evidence that mechanically induced transformation had occurred.

The results of the X-ray diffraction examination of the unoxidized alloys are presented in table 3. The observed lattice parameter of the delta phase is also given although, in general, this quantity is not a sufficiently smooth function of the alloy composition to permit a

determination of whether enrichment occurred or not.

The zinc alloys provide the only clear-cut case of transformation induced by mechanical polishing. The maximum solubility of zinc in the delta phase at high temperatures is 4.2 at. % as determined by Cramer, Ellinger and Land⁴⁾. Thus it is not surprising that neither the lattice parameter of the delta phase nor the corrosion resistance changed significantly on increasing the zinc content of the alloy. Evidently the alloys with higher zinc concentration contained a sufficient amount of the compound PuZn_2 to be detected by X-ray diffraction methods.

Transformation occurs to a lesser extent in the cerium specimens than in the zinc alloys. That is, the relative amount of the alpha phase increased on polishing. If the removal of metal by electropolishing had been more extensive, all of the alpha formed during the initial surface preparation might have been removed. Perhaps then the case for transformation of the cerium

TABLE 3
Summary of X-ray diffraction results on the unoxidized specimens

Alloying element	Nominal comp. (at %)	Lattice parameter (Å)	Phases observed †	
			Electropolished	Following abrasion
Aluminum	6	4.612	delta	delta + trace PuO_2
Aluminum	9	4.577	delta	delta + trace PuO_2
Aluminum	12	4.545	delta	delta + trace PuO_2
Cerium	6	4.656	delta + alpha + PuO_2	delta + alpha + PuO_2
Cerium	9	4.690	delta + alpha + PuO_2	delta + alpha + PuO_2
Cerium	12	4.670	delta + alpha + PuO_2	delta + alpha + PuO_2
Hafnium	6	4.661	delta + trace HfO_2	HfO_2 + delta + PuO_2
Hafnium	9	4.643	delta + trace HfO_2	HfO_2 + delta + PuO_2
Hafnium	12	4.653	delta + trace HfO_2	HfO_2 + delta + PuO_2
Zinc	6	4.621	delta	delta + alpha + PuO_2
Zinc	9	4.624	delta	delta + alpha + PuO_2
Zinc	12	4.617	delta + PuZn_2	delta + alpha + PuO_2
Zirconium	4.3	4.665	delta	delta + ZrO_2 + PuO_2
Zirconium	6.0	4.665	delta + $\text{Pu}_x\text{Zr}(?)$	delta + ZrO_2 + PuO_2
Zirconium	7.5	—	delta	delta + ZrO_2 + PuO_2
Zirconium	8.9	4.6145	delta + $\text{Pu}_x\text{Zr}(?)$	delta + ZrO_2 + PuO_2

† Arranged in the order of decreasing line intensity.

TABLE 4

Oxidation products of alloy plutonium specimens exposed to air containing 50 percent relative humidity at 75° C

Alloying element	Nominal comp.	Oxidized (24 h)	Oxidized (1000 h)	Partial oxide removal after polishing
Aluminum	6	delta + trace PuO ₂	—	—
Aluminum	9	delta + trace PuO ₂	delta + weak PuO ₂	delta + weak PuO ₂
Aluminum	12	delta + trace PuO ₂	delta + weak PuO ₂	delta + weak PuO ₂
Cerium	6	—	—	—
Cerium	9	PuO ₂	—	—
Cerium	12	PuO ₂	—	—
Hafnium	6	PuO ₂	—	—
Hafnium	9	PuO ₂ + trace HfO ₂	PuO ₂	PuO ₂ + oriented HfO ₂ + trace alpha
Hafnium	12	PuO ₂ + trace HfO ₂	PuO ₂	PuO ₂ + oriented HfO ₂ + trace alpha
Zinc	6	PuO ₂ + delta + alpha	PuO ₂	delta + alpha + PuO ₂
Zinc	9	PuO ₂ + delta + alpha	PuO ₂	PuO ₂ + delta + alpha
Zinc	12	PuO ₂ + alpha + delta	—	—
Zirconium	4.3	PuO ₂	—	—
Zirconium	6.0	PuO ₂	monoclinic ZrO ₂ + PuO ₂	—
Zirconium	7.5	PuO ₂	—	—
Zirconium	8.9	PuO ₂ + ZrO ₂	—	—

Phases arranged in the order of decreasing line intensity.

alloys, induced by abrasion, would also have been clear-cut.

These data provide some evidence that abrasion of the zirconium and hafnium alloys promoted the formation of ZrO₂ and HfO₂. Apparently no such effect occurred with either the stable aluminum or with the zinc and cerium alloys. It is possible that the surface was heated sufficiently to cause surface oxidation.

The results of the X-ray diffraction examination of the oxidized specimens are presented in Table 4. The aluminum alloys were also the most resistant ones on the basis of these results as the diffraction lines of the base alloy were the major contribution to the patterns obtained with the specimens oxidized 1000 hours. In contrast, the cerium alloys were so thickly covered with loose, powdery oxide after a thousand hours that they were considered to be unsafe for handling in the open laboratory. Consequently no X-ray data were obtained for these samples in the oxidized or partially polished condition.

The zirconium and hafnium additions con-

ferred a little protection to the plutonium. Unfortunately the oxidation products on the zirconium specimens were not removed by abrasion following the 1000 hour exposure. Therefore, it is difficult to decide whether the monoclinic ZrO₂ would have been a major component in the oxide film adjacent to the alloy. Its presence in the few specimens examined suggests that the separate formation of ZrO₂ plays some role in the over-all oxidation process.

It is interesting that the cubic or fluorite form of HfO₂, rather than the low temperature monoclinic form, was observed in the products. The intensity of the (200) line of HfO₂ was strikingly larger than that of the adjacent (111) and (220) lines. This suggests a large degree of preferred orientation in that oxide, but at the present time there is insufficient information to establish the orientation relations.

In connection with the last column of table 4, the amount of PuO₂ present is strongly influenced by how thoroughly the oxide was removed by abrasion. Thus a detailed comparis-

on of the relative amounts of alloy and remaining oxide is not justified. The two zinc alloys provide an example of this statement; in one case, PuO_2 is the major contributor to the pattern whereas in the other PuO_2 is minor, although both alloy compositions have comparable resistances to corrosion.

On the basis of these data it is difficult to decide in which cases the separate oxide of the alloying element occurs at the outer or the inner interface. The significance of this decision will be discussed below.

TABLE 5

Merit ratios for a plutonium alloy containing 3.5 at % aluminum, under various exposure conditions (after Sackman ⁴⁾)

Temp. (° C)	Rel. humid.	Merit ratio observed at					
		12 h	24 h	50 h	250 h	500 h	1000 h
90	95	130	—	—	—	—	—
90	55	50	100	120	—	—	—
30	95	—	—	—	13	13	8
100	0	—	—	—	20	12	6

3.3. COMPARISON WITH PREVIOUS RESULTS

The data of Sackman ⁴⁾ cannot be compared directly either with the data previously obtained ^{1,2)} or with those of the present investigation, because his specimens were exposed at generally higher relative humidities and at different temperatures. However, the results of his investigation of a 3.5 at % aluminum alloy are summarized in terms of merit ratios in table 5. Earlier data of Waber ²⁾ relative to the corrosion resistance of alloys containing aluminum and zirconium, and exposed to air containing 50 % relative humidity at 75° C, are presented in table 6. While the present merit ratios for the aluminum alloys do not differ greatly from those previously obtained, the results for the 4 and 6 at % zirconium alloys are substantially lower than those observed earlier for alloys containing 7.5 and 10 at % zirconium. Inasmuch as the weight gains for the alpha-plutonium specimens exposed with

TABLE 6

Merit ratios for several plutonium alloys exposed to air containing 50 percent relative humidity at 75° C (after Waber ²⁾)

Alloy comp. (at %)	Merit ratio observed at			
	900 h	4300 h	8730 h	10 000 h
3.5 Al	—	—	—	17.4
8.0 Al	19	42.5	51	—
3.5 Th	—	—	—	3.1
7.5 Zr	22	152	226	—
10.0 Zr	22	133	197	—

the zirconium alloys are rather low, the merit ratios in table 3 for the zirconium alloys are very likely too low.

Sackman ⁴⁾ noted that his unalloyed plutonium specimens suffered an internal attack, similar to intergranular attack, and disintegrated within a relatively short time. An acceleration of the attack was observed. When corrosion occurs at an increasing rate, the slope on a log-log graph exceeds unity. Thus a progressive increase in merit ratio for the alloys would be expected. However the data in table 5 for the lower temperatures suggest that decreases in merit ratio occur. In the continuation of these tests ¹⁵⁾ the merit ratio did increase with time. For example, the value for 30° C and 95 % relative humidity became 23 at 2000 h. The merit ratio is, of course, sensitive to the behavior of the unalloyed material and in Sackman's case the temporary decrease in merit ratio was caused by the atypically low corrosion of the alpha specimen in the period 500 to 830 h.

Sackman ¹⁵⁾ has pointed out that the rapid deterioration of alpha was observed using specimens stored for several months prior to testing. However, with fresh cast specimens, which were much more resistant to corrosion, penetration and deterioration set in much later. The new merit ratios were substantially smaller than those in table 5; none of the values exceeded 5.5. Temporary decreases were also noted. These values could be misleading unless his graphs are considered in detail.

No cause of such grain boundary attack has

TABLE 7

Comparison of observed corrosion weight gains for alpha plutonium with calculated weight gains for two compositions of the products

Initial wt. metal (g)	Exposure Time (h)	Final weight (g)	Wt. PuO ₂ calc. (g)	Percent excess	x in formula †
1.548 748	3,360	1.779 133	1.756 114	1.310	0.188
1.716 152	2,832	1.969 484	1.945 929	1.210	0.173
1.063 517	2,832	1.220 691	1.205 912	1.226	0.175
2.213 135	2,712	2.541 928	2.509 454	1.294	0.186
2.022 589	2,352	2.309 693	2.293 955	0.710	0.101

† Value of x in the composition PuO₂· x H₂O.

been offered. However, it seems possible that small amounts of PuH _{x} may have formed or been precipitated at grain boundaries and that these acted as the foci for attack by moisture. This suggestion does not account for the source of the hydrogen. Unalloyed uranium has been observed by Waber¹⁶⁾ to develop needles of UH₃ buried below the oxide films after exposure for several months to moist helium. Plutonium may conceivably act similarly and form hydrides during atmospheric corrosion.

Sackman⁴⁾ observed that the weight increase for alpha-plutonium specimens oxidized to completion corresponded to the formula PuO_{2.1}, or to PuO₂·0.1 H₂O. He concluded that, inasmuch as a higher oxide of plutonium is not known, this excess increase in weight over that allowed by the stoichiometric composition of plutonium dioxide must be attributed to strongly adsorbed moisture. No information was presented by Sackman relative to whether an excess in weight gain occurs with the aluminum alloy. He apparently did not consider the possibility of a hydroxide.

The likelihood of hydroxides appearing in the corrosion products of uranium and plutonium has been discussed by Waber²⁾. To establish this hypothesis, several of the specimens used in the present investigation were withdrawn from test and were transferred in their beakers to a different desiccator where they were oxidized to completion under the same conditions that obtained during the test, namely,

in air containing 50 percent relative humidity at 75° C. The resulting data are summarized in table 7.

In table 7, the initial weights of five specimens of alpha plutonium are given, together with their final weights achieved after more than 2000 h of exposure. One sees that the observed final weight exceeds the computed weight, which was calculated on the assumption that all of the original specimen had been converted to plutonium dioxide. The average weight excess amounts to 1.15 %. If one makes the assumption, as Sackman did, that the composition of the corrosion products could be represented by the formula PuO₂· x H₂O, values for x can be computed from the excess in weight gain over that expected for forming stoichiometric PuO₂. Values for this quantity are listed in table 7 and the mean value is 0.165. This value for x is larger than the value 0.10 reported by Sackman⁴⁾.

It is further interesting that Sackman⁴⁾ observed that the delta-stabilized alloy, when kept at 30° C and 95 percent relative humidity, appeared to stop oxidizing after approximately 900 h, and that essentially no further increase in weight was observed during the next 600 h, at the end of which the corrosion test was terminated. Arrests of this nature observed in the course of experimental observations will be discussed in a forthcoming publication. It is regrettable that no explanation is known for this very interesting phenomenon.

3.4. DISCUSSION OF RESULTS

The influence of the valence of the solute atom is not clearly indicated in the results presented above. If the Wagner-Hauffe argument were applicable, one would anticipate that aluminum additions would substantially increase the number of anion vacancies, and consequently the rate of diffusion of oxygen through the film would be expected to increase. One finds, however, that the aluminum alloys are the best of the five types of alloys considered in the present work. Further in accordance with this discrepancy, the results on zinc alloys are even more striking, because in plutonia that contains any significant amount of zinc, presumably one oxygen should be missing for each zinc atom. There is no X-ray evidence that aluminum oxide forms as a separate phase and so one is led to attribute the retarding effect of aluminum to a reduced electronic conductivity. However, an amorphous Al_2O_3 is not excluded by the present experiments. ZnO will be discussed below.

Further, with the three quadrivalent elements, cerium, hafnium and zirconium, there should be little if any influence on the vacancy concentrations in the PuO_2 . One sees that the cerium additions do slightly reduce the oxidation. But while these results may be in keeping with expectation, one finds that hafnium and zirconium definitely reduce the corrosion rate. As indicated in table 3, the latter elements form separate dioxide phases. Thus the reduced rate is largely due to the initial presence (or the formation) of such films which then reduce the amount of PuO_2 that forms.

Thus, it is apparent that the simple concept of the alloys adding vacancies to the oxide film as suggested by Wagner and Hauffe cannot be applied to the oxidation of the delta-phase plutonium alloys. A more detailed examination of how these solute elements influence the oxidation rate must be made before the oxidation process can be fully understood. A knowledge of the influence of such solutes on the characteristics of PuO_2 as a semiconductor would also be helpful.

As noted above, a brief analysis of the data available on the behavior of mixed oxide systems suggests that a large disparity in cell size would limit solid solubility. Because of the relative complexity of the Al_2O_3 lattice, it is more convenient to use the cation radius or the metal-oxygen distance rather than the lattice parameter when discussing the influence of a size factor in oxide systems. It is interesting that, in a recent paper, Voronov *et al.*¹⁷⁾ regarded the separation of oxide phases in the systems $\text{UO}_2 + \text{ZrO}_2$ and $\text{ThO}_2 + \text{ZrO}_2$ to be a consequence of the disparity in the cation sizes.

With regard to specific phase diagrams, Hund and his collaborators have studied solid solutions of rare earth oxides with thorium^{18,19)} and urania²¹⁻²⁴⁾. Lambertson and Mueller²⁶⁻²⁷⁾ have studied the equilibrium between four oxides and UO_2 . A number of these systems have been reinvestigated by Budnikov *et al.*²⁹⁾. In addition, reference should be made in passing to the work of Anderson and Johnson³⁰⁾ on the magnesia-urania system. Waber^{16,31)} has described other studies involving urania with thorium and various oxides. No attempt has, however, been made in the present paper to discuss mixed oxide systems that do not involve one of the fluorite type oxides of the three actinide elements, uranium, thorium or plutonium.

Values of the ratios of the cation radii of various elements to the radii of three of the actinide ions are presented in table 8. From a consideration of the above information on phase equilibria, one may propose as a reasonable working rule, that the oxides of elements whose cation radii have a disparity greater than ± 14 percent will probably not form solid solutions having extensive ranges of concentration. The size factor value of 14 percent is the same as the criterion that Hume-Rothery used in determining the probable extent of solid solubility in metallic alloys.

The ratios between the metal-oxygen distance have also been examined, and as they lead to a similar rule there is no sufficient reason for selecting one form of this size factor rule over

TABLE 8

Ratios of cation Radii involved in mixed oxides

Cation considered	Cation radius (Å)	Plutonium	Uranium	Thorium
		$\frac{R(M)}{R(\text{Pu}^{+4})}$	$\frac{R(M)}{R(\text{U}^{+4})}$	$\frac{R(M)}{R(\text{Th}^{+4})}$
Al ⁺³	0.45	0.500	0.484	0.454
Ce ⁺³	1.02	1.132	1.096	1.030
Ce ⁺⁴	0.92	1.022	0.989	0.929
Hf ⁺⁴	0.77	0.885	0.828	0.778
Zn ⁺²	0.74	0.822	0.796	0.747
Zr ⁺⁴	0.77	0.855	0.828	0.778
Th ⁺⁴	0.99	1.10	1.064	1.000
U ⁺⁴	0.93	1.03	1.000	0.939
Pu ⁺⁴	0.90	1.000	0.968	0.909

 $R(M)$ represents the radius of the cation considered.

another on the basis of the present information.

On the basis of this size factor, the oxides of aluminum and zinc are not likely to form continuous solid solutions with PuO_2 . Since they are borderline cases, it is difficult to decide whether ZrO_2 and HfO_2 would be more than slightly soluble in plutonia. Extrapolation from the behavior of urania and thoria with ZrO_2 suggests that both HfO_2 and ZrO_2 would be relatively insoluble in PuO_2 . In the case of cerium, CeO_2 should be soluble in PuO_2 but the trivalent ion has a borderline ratio and some separation of Ce_2O_3 might be expected. It is reasonable to assume that the body-centered-cubic C-type sesquioxide (Mn_2O_3 type) would form. This lattice is closely related to the fluorite lattice and only a few weak lines (due to ordering of the anion vacancies) necessitate doubling the edge of the FCC pseudo-cell to form the BCC cell. The lattice parameter of the pseudo-FCC cell is closer to that of CeO_2 than the cation sizes would suggest. Thus probably the separation of Ce_2O_3 and PuO_2 could not be detected by X-ray diffraction even if it did occur.

The data on corrosion films are compatible with these deductions. ZrO_2 and HfO_2 do occur as separate phases. While Al_2O_3 and ZnO have not been observed there are other considerations. It is probable that so little oxide is formed on the aluminum specimens and the aluminum

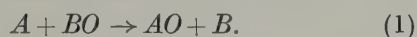
ion scatters so poorly in comparison with the plutonium atom and ion that it may be impossible to demonstrate the presence of corundum except by electron diffraction. Furthermore, an amorphous form of Al_2O_3 is usually observed during the oxidation of aluminum oxides at low temperatures³²⁾ and this form may be present in the case at hand. The formation of ZnO would not be anticipated on the basis of a thermodynamic argument which will be presented below.

Wagner^{33,34)} has also dealt with more complex cases which occur in the oxidation of alloys and apparently these theoretical discussions apply to plutonium alloys. He has shown that under specific experimental conditions and in certain composition ranges either one or both oxides will form. The three distinct composition ranges have been deduced from a mathematical analysis³³⁾ which involves firstly, the interrelations of the self-diffusion coefficient D_A of the solvent ion A (in this case, plutonium) as well as a similar quantity D_B for the solute ion, in their oxides to the interdiffusion coefficient D_{AB} in the alloy; secondly, the relative stability of the two oxides and thirdly, the relative oxidation rates of the two pure metals. It is generally observed that when a dilute A -base alloy containing x_B of the less noble addition B is oxidized, the outer portion of the film is largely AO , and BO is buried beneath it. Thus the volume fraction of BO is larger near the oxide-alloy interface. This structure of a composite scale is in accordance with Wagner's analysis. At larger concentrations of B in the alloy, the formation of AO may be stifled by the preponderance of BO near the interface since it is assumed that the solubility and the net transfer of A -ions through BO is low. At a somewhat higher critical concentration of B in the alloy, BO may be formed exclusively. In very dilute alloys, of course, only AO will be observed and the limiting concentration of B , namely, x_B^* at which only the oxide of the more noble metal A will occur, is generally quite low. This limit is proportional to the ratio (D_{AB}/D_A) and to the critical concentra-

tion x_B' which is defined as the concentration at which both AO and BO are in thermodynamic equilibrium with the alloy for the particular activity of the oxygen in the film near the interface.

At the present time, no information is available on the interdiffusion coefficient D_{AB} for plutonium alloys. Thus, although D_B is calculable for the five alloying elements considered in this investigation and D_A for plutonium can be obtained from the high temperature oxidation rates reported by Waber and Wright¹⁾ and by Dempsey and Kay³⁾, the foregoing analysis can not be applied and tested quantitatively.

The phrase "less noble" has been used to denote both a faster oxidation rate and a more stable oxide. However, if BO is less stable than AO , either BO may not form or it may be reduced near the interface according to the displacement reaction



Even in this case, a small amount of the alloying element B may reduce the overall oxidation rate. In the event that the ratio (D_A/D_{AB}) is low, an enriched zone of B will form in the alloy near the interface and limit the rate of arrival of A . This case has also been discussed by Wagner³⁴⁾. If the interfacial concentration of B becomes large in comparison to x_B' , some BO may occur. However, when the interdiffusion coefficient is large, back diffusion of B will permit the alloy to oxidize at a rate similar to that observed for the pure base metal A .

Although a quantitative check of the suitability of Wagner's analyses must await the determination of the interdiffusion coefficient in delta phase alloys, one qualitative feature of his analyses can be discussed. As he pointed out, a stable duplex structure of the oxide film depends on the relative stability of the two oxides in contact with the alloy.

The standard free energies of formation of several oxides are presented in table 9. Most of these data have been published by Coughlin³⁸⁾. The value reported for PuO_2 by Holley *et al.*⁶⁾ has been substituted for Coughlin's.

TABLE 9

Standard free energies of formation per oxygen atom

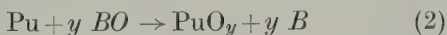
Oxide	298.1° K	600° K	Error
Al_2O_3 (corundum)	—125.8	—118.2	0.3
Ce_2O_3	—137.2	—129.2	8.3
CeO_2	—115.0	—107.2	6.2
HfO_2 (monoclinic)	—125.9	—118.8	0.2
Pu_2O_3	—128	—120	8
PuO_2	—120.2	—113.8	5.5
ZnO	—76.1	—69.0	0.2
ZrO_2 (α , β)	—123.9	—117.0	0.12

The value for Pu_2O_3 was estimated by Mulford³⁶⁾.

It will be seen that the sesquioxides of plutonium and cerium are more stable than their dioxides. Thus the latter should lose oxygen when heated in vacuum as has been noted by Czanderna and Honig⁹⁾ for ceria and by Mulford³⁷⁾ for plutonia. It will be seen that Al_2O_3 , HfO_2 and ZrO_2 are probably more stable than PuO_2 , whereas ZnO is significantly less stable. However, the differences between the ΔF values for each of the solute elements and that for PuO_2 are only a few kilocalories per mole. In view of the accuracy of this data as indicated by the tabulated values of the probable error, it is difficult to decide whether the displacement reaction will be spontaneous. It should be noted that standard free energies in table 9 are based on a unit activity of the solutes in the delta phase and it is not probable that the activity coefficients are large enough for the activities of Al, Hf and Zr to approach unity in alloys containing 12 at % or less. Assuming Henry's Law and unit values of the activity coefficients, the correction to ΔF for a 10 at % alloy would reduce the net ΔF values for reaction (1) by approximately 1.7 kcal at 75° C. Smaller values for the activity coefficient would further reduce the free energy change. As far as the authors are aware, the only information for plutonium alloys from which activity coefficients might be obtained is the excess relative heats of mixing published recently by Waber and Gschneider³⁾ and these values pertain only to epsilon alloys. The

accuracy of the data for pure plutonium in table 9 would appear to be too poor to justify any further analysis or firm statement.

The greater stability of Pu_2O_3 would apparently cause all of these oxides with the possible exception of Ce_2O_3 to be reducible by plutonium according to the reaction



where y is assumed to be equal to $\frac{3}{2}$. The possibility of y being $\frac{7}{4}$ as in the compound Pu_4O_7 reported by Holley *et al.*⁶⁾ will not be discussed in detail because of the poor knowledge of its free energy of formation. The large number of anion vacancies created at the alloy-oxide interface when y becomes less than two, by virtue of reaction (2) occurring, is compatible with the mechanisms of anion diffusion and electron hole migration assumed above.

Assuming that plutonium can be regarded as the more noble metal A in the case of the aluminum, hafnium and zirconium alloys, i.e. that it has a more positive value in table 9, then the formation of PuO_2 (or possibly PuO_2 mixed with either Al_2O_3 , HfO_2 or ZrO_2) would be anticipated depending on whether or not the alloy content exceeds the limiting concentration x_B^* established for exclusive formation of AO. Such duplex oxide films are observed with both the hafnium and zirconium alloys. In the case of the aluminum alloys, it is possible that $x_B = 12\%$ Al is less than x_B^* . However, it would appear more probable that it exceeds x_B^* and that Al_2O_3 would be present as a separate phase.

On the other hand, because of the stability of Ce_2O_3 , plutonium must be regarded as the more noble constituent in the cerium alloys. As discussed in connection with the size factor criterion, it is difficult to decide whether cerium sesquioxide will be detectable in the oxide film. Thermodynamically, it will be more stable than PuO_2 and thus any CeO_2 will yield its oxygen to the plutonium (which should have an activity approximately equal to unity by Raoult's law). Some separation of Ce_2O_3 may further be anticipated since the cation radius

ratio for Ce_2O_3 has a "borderline value". One may interpret the fact that the rates for cerium alloys are higher than those for the aluminum, zinc, hafnium or zirconium alloys, in the absence of any X-ray diffraction results to the contrary, as due to the formation of cerium sesquioxide or of a (cerium + plutonium) oxide film which contains many anion vacancies in the basic fluorite lattice.

The monoclinic α -Pu phase was observed for hafnium alloys as noted in the last column of table 4. This could be interpreted as evidence that the delta phase was being depleted of such an amount of its alloy content that it could not be retained at 75°C . The data in table 3 indicate that partial transformation of the delta phase did not result from mechanical abrasion of the hafnium alloys. Thus these X-ray diffraction results on hafnium alloys are consistent with Wagner's mechanism which involves local depletion of the less noble alloy element B, the formation of BO as a separate phase and consequently the reduction of the rate of forming the oxide of the more noble solvent metal as well as partial transformation of the metastable delta-plutonium phase. However, it is difficult to decide in the case of the zinc and other alloys, on the basis of the X-ray diffraction results obtained with the oxidized and partially polished samples, whether the alpha resulted from depletion near the interface or from the process of oxide removal.

It is interesting that in these runs at 75°C , the higher temperature or cubic form of HfO_2 was formed whereas the ZrO_2 was present in its monoclinic form. One might infer from this observation that plutonia has some ability to stabilize the cubic lattice of HfO_2 to room temperature. It might be interesting to investigate this inference.

It is the separate formation of HfO_2 , ZrO_2 and possibly of Al_2O_3 , which limits the oxidation rate. In the case of the zinc alloys, the slight reduction in rate may be attributed to the development of a zone, enriched in zinc, through which the plutonium must diffuse.

A further consideration, which should not be

overlooked, is that it is impossible to determine the oxidation rate of unalloyed delta-phase plutonium at or near atmospheric temperatures because the delta phases cannot be retained without alloying additions. Assuming, however, that the rate for unalloyed delta phase is comparable to (but probably not larger) the corrosion rate obtained for the cerium alloys, it is still clear, using the arguments of Wagner and Haufler, that the addition of zinc or aluminum should increase the oxidation rate. The experimental results contrast with this deduction.

Despite plausible arguments^{2,16} for the occurrence of hydroxides in the corrosion products formed on uranium and plutonium, it is difficult to distinguish such combined water from that tightly adsorbed on the corrosion product. Some method will have to be found to establish whether the hydroxide interpretation or the one being favored by Sackman is correct.

References

- 1) J. T. Waber and E. S. Wright, *The Metal Plutonium*, A. S. Coffinberry and W. N. Miner, Editors (American Society for Metals, Novelty, Ohio, 1960) Ch. XVIII
- 2) J. T. Waber, *Proceedings of the Second Geneva Conference* **6** (1958) 204
- 3) E. Dempsey and A. E. Kay, *J. Inst. Metals* **86** (1958) 379
- 4) J. F. Sackman, *Memoire No. 11, Conference Internationale sur la Metallurgie du Plutonium*, Grenoble (Cleaver-Hume Press, London, 1960)
- 5) K. Haufler, (see for example) *Prog. in Metal Physics* **4** (1953) 71
- 6) C. E. Holley, Jr., R. N. R. Mulford, E. L. Huber, E. E. Head, F. H. Ellinger and C. W. Bjorklund, *Proceedings of the Second Geneva Conference* **6** (1958) 215
- 7) R. W. Ure, Jr., *J. Chem. Phys.* **26** (1957) 1363
- 8) R. K. Willardson, J. W. Moody and R. L. Goering, *Battelle Memorial Institute (USA) Report*, BMI-1135 (1956)
- 9) A. W. Czanderna and J. M. Honig, *Purdue University (USA) Report*, AD-136, 591 (1957)
- 10) R. N. R. Mulford and F. H. Ellinger, *J. Am. Chem. Soc.* **80** (1958) 2023
- 11) R. N. R. Mulford and F. H. Ellinger, *J. Phys. Chem.* **63** (1958) 1466-7
- 12) E. M. Cramer and F. W. Schonfeld, *Proceedings of the Second Geneva Conference* **17** (1958) 668
- 13) R. O. Elliott and K. Gschneidner, in *Behavior of Some Delta Stabilized Plutonium Alloys at High Pressures*, Extractive and Physical Metallurgy of Plutonium and Its Alloys, W. D. Wilkinson, Editor (Interscience Publishers, Inc., New York) in press
- 14) E. M. Cramer, F. H. Ellinger and C. C. Land, "The Plutonium-Zinc Phase Diagram", in *Extractive and Physical Metallurgy of Plutonium and Its Alloys*, W. D. Wilkinson, editor (Interscience Publishers, Inc., New York) in press
- 15) J. F. Sackman, *Discussion of ref. 4*
- 16) J. T. Waber, *Los Alamos Scientific Laboratory (USA) Report*, LA-2035 (1956)
- 17) N. M. Voronov, A. E. Voltekhova and A. S. Danilin, *Proceedings of the Second Geneva Conference* **6** (1958) 221
- 18) F. Hund and G. Niessen, *Elektrochem.* **56** (1952) 972
- 19) F. Hund and R. Mezger, *Phys. Chem.* **201** (1952) 268
- 20) F. Hund, *Z. f. anorg. und allgem. Chem.* **274** (1953) 105
- 21) F. Hund and U. Peetz, *Z. f. anorg. und allgem. Chem.* **271** (1952) 6
- 22) F. Hund and U. Peetz, *Elektrochem.* **56** (1952) 223
- 23) F. Hund, U. Peetz and G. Kottenhahn, *Z. f. anorg. und allgem. Chem.* **278** (1955) 284
- 24) F. Hund and U. Peetz, *Z. f. anorg. und allgem. Chem.* **267** (1952) 189
- 25) W. H. Lambertson and M. H. Mueller, *J. Amer. Ceram. Soc.* **46** (1953) 329
- 26) W. H. Lambertson and M. H. Mueller, *J. Amer. Ceram. Soc.* **36** (1953) 365
- 27) W. H. Lambertson and M. H. Mueller, *J. Amer. Ceram. Soc.* **36** (1953) 397
- 28) W. H. Lambertson, M. H. Mueller and F. H. Gunzel, *J. Amer. Ceram. Soc.* **36** (1953) 307; See also L. Epstein and W. H. Howland, *ibid* **36** (1953) 334
- 29) P. P. Budnikov, S. G. Tresoyatsky and V. I. Kushakovsky, *Proceedings of the Second Geneva Conference* **6** (1958) 124
- 30) J. S. Anderson and K. D. H. Johnson, *J. Chem. Soc. (Lond.) Part II* (1953) 1731
- 31) J. T. Waber, *Los Alamos Scientific Laboratory (USA) Report*, LA-2035 (1956)
- 32) R. K. Hart, *Trans. Faraday Soc.* **53** (1957) 1020; see also M. S. Hunter and P. Fowle, *J. Electrochem. Soc.* **103** (1956) 482
- 33) C. Wagner, *J. Electrochem. Soc.* **103** (1956) 627
- 34) C. Wagner, *J. Electrochem. Soc.* **103** (1956) 571; see also, *ibid* **99** (1952) 369
- 35) J. P. Coughlin, *Bureau of Mines Bull.* **542** (1954)
- 36) R. N. R. Mulford, private communication
- 37) R. N. R. Mulford and L. E. Lamar, *The Volatility of Plutonium Oxide, Conference Internationale sur la Metallurgie du Plutonium*, Grenoble 1960 (Cleaver Hume Press, London)

CREEP PROPERTIES OF A ZIRCONIUM-HYDROGEN URANIUM ALLOY

J. C. BOKROS

General Atomic Division of General Dynamics Corporation, John Jay Hopkins Laboratory for Pure and Applied Science, San Diego, California, USA

Received 4 August 1960

The temperature and stress dependence of the steady-state creep rate of a zirconium-hydrogen-uranium alloy (atomic ratio of 1:1:0.03) has been determined in the temperature range of 500° to 600° C which includes an eutectoid transformation. The stress (σ) dependence of the creep rate ($\dot{\epsilon}$) can be represented by an equation of the form: $\dot{\epsilon} = k\sigma^n$, with $n = 4.1$ below the transformation temperature and $n = 4.7$ to 4.9 above the transformation temperature. An activation energy of 80 000 cal/g atom was observed below the transformation temperature, whereas values of 65 000 to 73 000 cal/g atom were observed above the transformation temperature.

On a déterminé l'influence de la température et de la tension sur le fluage à vitesse constante d'un alliage uranium-zirconium hydrogène (rapport des compositions en atomes de 1:1:0,03) pour un domaine de température allant de 500° à 600° C qui comprend une transformation eutectoïde. L'influence de la tension appliquée (σ) sur la vitesse du fluage ($\dot{\epsilon}$) peut être représentée par une équation de la forme $\dot{\epsilon} = k\sigma^n$ avec

$n = 4,1$ au-dessous de la température de transformation et $n = 4,7$ à 4,9 en-dessus de la température de transformation. L'énergie d'activation était de 80 000 cal/g atome au-dessous de la température de transformation tandis que des valeurs de 65 000 à 73 000 cal/g atome étaient observées au-dessus de la température de transformation.

Der Einfluß der Temperatur und der Spannung auf die Kriechgeschwindigkeit von einer Zr-H-U-Legierung (Atomverhältnis 1:1:0,3) wurde zwischen 500 und 600° C untersucht. Dieser Temperaturbereich enthält auch eine eutectoide Umwandlung. Die Abhängigkeit der Kriechgeschwindigkeit $\dot{\epsilon}$ von der Spannung σ kann durch die Gleichung $\dot{\epsilon} = k\sigma^n$ beschrieben werden. Dabei ist $n = 4,1$ unterhalb und $n = 4,7$ bis 4,9 oberhalb der Umwandlungstemperatur. Ferner wurde unterhalb des Umwandlungspunktes eine Aktivierungsenergie von 80 000 cal/g Atom bestimmt, während oberhalb Werte zwischen 65 000 und 73 000 cal/g Atom ermittelt wurden.

1. Introduction

Zirconium-hydrogen uranium alloys are being used extensively as combination fuel-moderator materials¹⁾. The work reported herein describes the creep properties of a zirconium-hydrogen uranium fuel alloy with an atom ratio of 1:1:0.03 in the temperature range of 500° to 600° C, which includes an eutectoid transformation. Above the transformation, the alloy consists of a mixture of beta (a body-centered-cubic solid solution of hydrogen in zirconium) and gamma zirconium hydride (a face-centered-cubic to face-centered-tetragonal modification of approximate composition $\text{ZrH}_{1.45}$ ²⁾) (see

fig. 1). In the range of 537° to 550° C, the beta solid solution in this mixture (roughly 2 parts gamma and 1 part beta) decomposes eutectoidally into a finely divided mechanical mixture of alpha zirconium (a hexagonal close-packed zirconium phase which can contain less than 1 wt % uranium in solid solution) and gamma hydride in a ratio of about 2 alpha to 3 gamma (see fig. 2). The continuous phase in the vicinity of the transformation temperature is gamma zirconium hydride. Because of the transformation, a discontinuous change is expected in the creep rate (at constant stress) in the temperature range of 537° to 550° C.

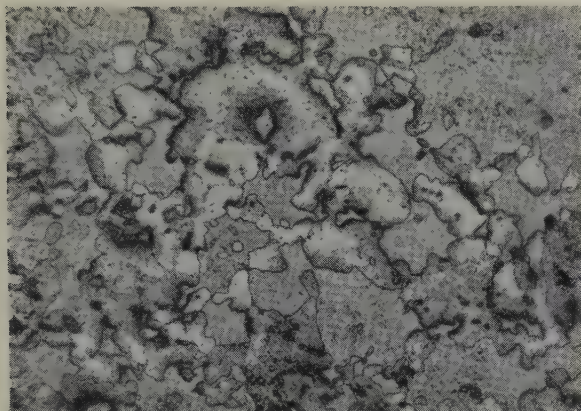


Fig. 1. Microstructure of Zr-H-U (atom ratio 1:1:0.03) annealed 900 h at 600° C (above transformation temperature) and quenched. Zirconium hydride (darker phase) plus alpha prime (transformed beta). $\times 175$.

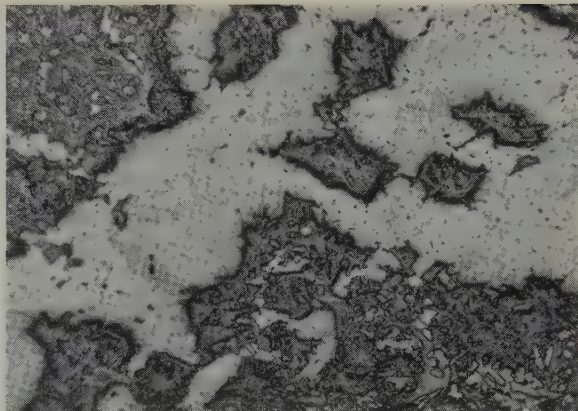


Fig. 2. Microstructure of Zr-H-U (atom ratio 1:1:0.03) annealed 900 h at 500° C (below transformation temperature) and quenched. Light phase is zirconium hydride; dark phase is alpha zirconium. $\times 175$.

2. Experimental

The zirconium-hydrogen uranium alloy was prepared by double vacuum arc-melting a compacted bar of zirconium sponge and uranium. The resulting 10 cm (4 in) billet was extruded to a 6 cm (1.50 in)-diameter rod and hydrided at 800° C to 1.0 wt % hydrogen. The final alloy composition is shown in table 1.

TABLE 1
Chemical analysis of Zr-H-U alloy

Element	wt %
U	8.03
H	1.07
O	0.0935
N	0.0017
Fe	0.1139
Si	0.0050
Cr	0.0050
Al	0.0055
Zr	Balance

Standard 0.505-in (1.26 cm)-diameter creep specimens with a 5 cm (2.0-in) gauge length were machined from the hydride rod. The specimens were creep tested in a helium atmosphere by using platinum strip-type extensometers and measuring the creep strain optically. The creep strain could be measured to 5 μ (2×10^{-4} in).

The helium atmosphere was purified by passing it through a molecular sieve, over titanium turnings at 553° C and over uranium turnings at 538° C. The purity of the gas was maintained at 99.999 % helium or better. The gas was analyzed periodically with a gas chromatograph in the helium system.

The furnace used for heating the creep specimens consisted of three windings which could be controlled separately. The temperature gradient along the gauge length of the specimen could be maintained at less than 1° C and the specimen temperature was controlled to within $\pm 1^\circ$ C of the set temperature.

The stress dependence of the creep rate at constant temperature was determined by (1) measuring a steady-state creep rate at a given stress, (2) changing the stress and establishing a new creep-rate characteristic of that stress level, and (3) returning to the original stress and re-establishing the original creep rate. The above procedure was used to ensure that significant structural changes had not taken place.

The temperature dependence of the creep rate at constant stress was established in a similar manner. A steady-state creep rate was established at a given temperature, the temperature was changed about 15° to 20° C (stress

remaining constant), and the new steady-state creep rate was established at the new temperature. The temperature change required about one-half hour. Subsequently, the initial temperature was re-established and the steady-state creep rate was measured. It is realized that any temperature change can result in changes in composition of the phases present as well as changes in their relative amounts; however, in all cases, after the initial temperature (or stress) was re-established, the creep rate did not deviate significantly from the previously measured creep rate.

Hydrogen analyses of the creep specimens

revealed no detectable hydrogen loss ($<5\%$) as a result of the tests.

3. Results and Discussion

The curve of creep-strain versus time at various stresses at 502°C (below the transformation) is shown in fig. 3. The steady-state creep rates at 4000, 5000, 6000, 7000, and 8000 psi were measured in that order (see fig. 4, circled points); the tests were repeated at 4000, 5000, and 6000 psi (boxed points). The logarithm of steady-state creep rates versus the logarithm of the stress indicate that the data can be represented by the usual relationship,

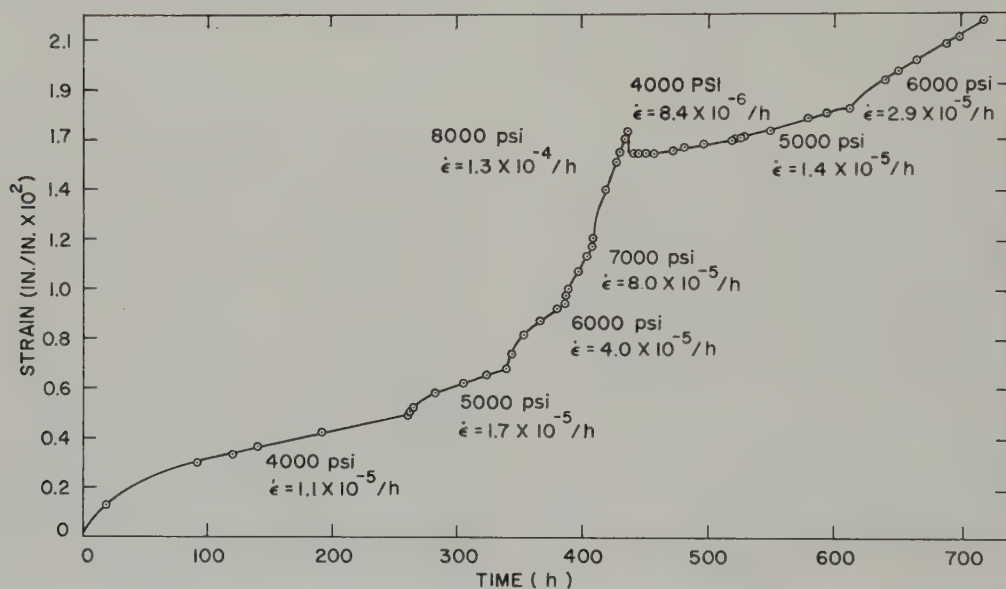


Fig. 3. Creep-strain at various stresses versus time for a zirconium-hydrogen-uranium (atom ratio 1:1:0.03) alloy tested at 502°C in helium.

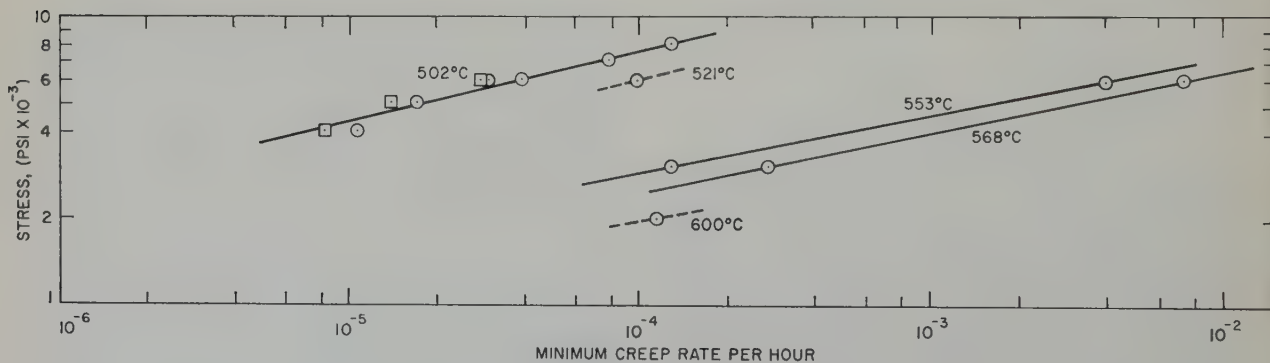


Fig. 4. Minimum creep rate versus stress at various temperatures for a zirconium-hydrogen-uranium (atom ratio 1:1:0.03) alloy.

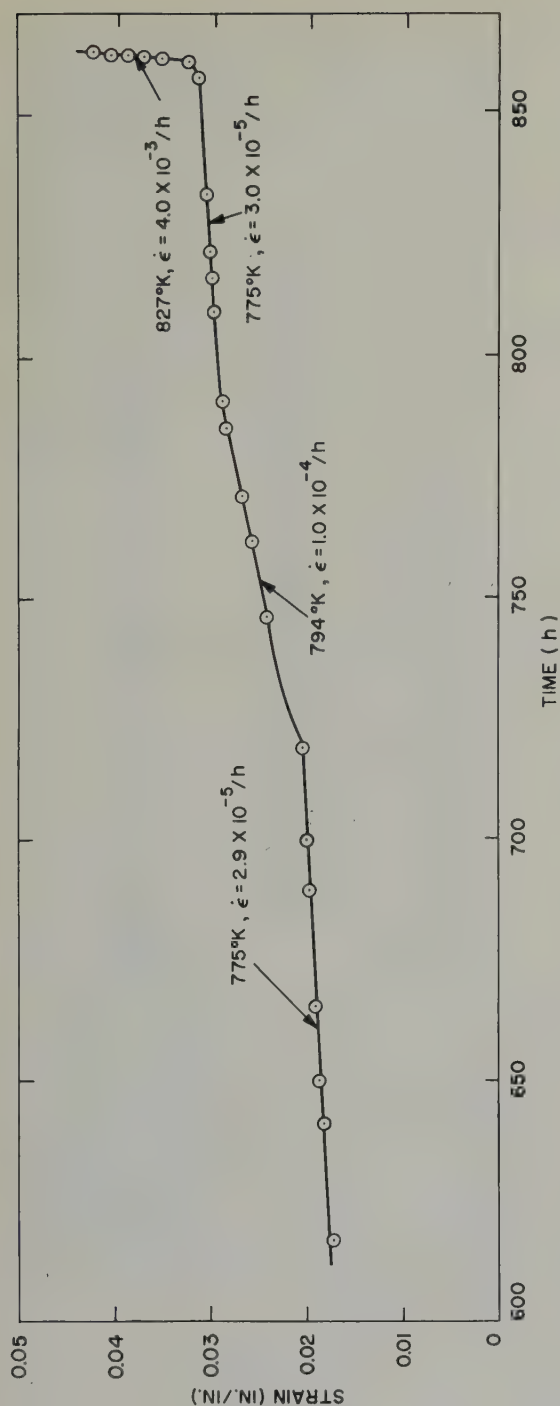


Fig. 5. Creep-stress versus time at various temperatures for a zirconium-hydrogen-uranium (atom ratio 1:1:0.03 alloy; stress constant at 6000 psi).

$\dot{\epsilon} = k\sigma^n$, where $\dot{\epsilon}$ is the steady-state creep rate per hour, k is a constant, σ is the stress, and n is a constant equal to 4.1. Above the transformation temperature (553° and 658° C), the data are limited, but they can be represented by a similar relationship with $n = 4.93$ at 553° C and $n = 4.71$ at 568° C.

The temperature dependence of the steady-state creep rate below the transformation temperature at a constant stress of 6000 psi was computed from the data shown in fig. 5. These results yield an activation energy of 80 000 cal/g atom. Above the transformation temperature, data obtained in a similar manner at a stress of 6000 psi yield an activation energy of 65 000 cal/g atom. A discontinuous increase in the steady-state creep rate occurred when the temperature was increased through the transformation temperature range. At a lower stress (3000 psi), an activation energy of 73 000 cal/g atom was computed from data obtained at 553° and 568° C (see fig. 6). The temperature dependence of the steady-state creep rate at 3000 and 6000 psi is summarized in fig. 7.

The activation energies for creep of this alloy are much higher than those reported for self-diffusion in alpha and beta zirconium; namely, 27 000 cal/g atom in beta and 22 000 cal/g atom in alpha zirconium³).

It is likely therefore that the rate-controlling step for creep in this zirconium-hydrogen-uranium alloy, above and below the transformation temperature, involves the diffusion of zirconium atoms in zirconium hydride (the continuous phase), and the large discontinuity at the transformation temperature is due to the transformation of the mixture of alpha zirconium and zirconium hydride to the much weaker BCC beta phase.

It is interesting to note that although this alloy is rather brittle at room temperature, it is quite ductile in the temperature range of 500° C and above. For example, fig. 8 illustrates a creep specimen tested to incipient failure at 568° C at a stress of 6000 psi—an elongation of 70 % took place.

4. Conclusions

The stress dependence of the steady-state creep rate of zirconium-hydrogen-uranium (atom ratio of 1:1:0.03) was determined at 502°C

over the range 4000 to 8000 psi. The data can be represented by the equation $\dot{\epsilon} = k\sigma^n$, where $n = 4.1$.

Above the transformation temperature (553°

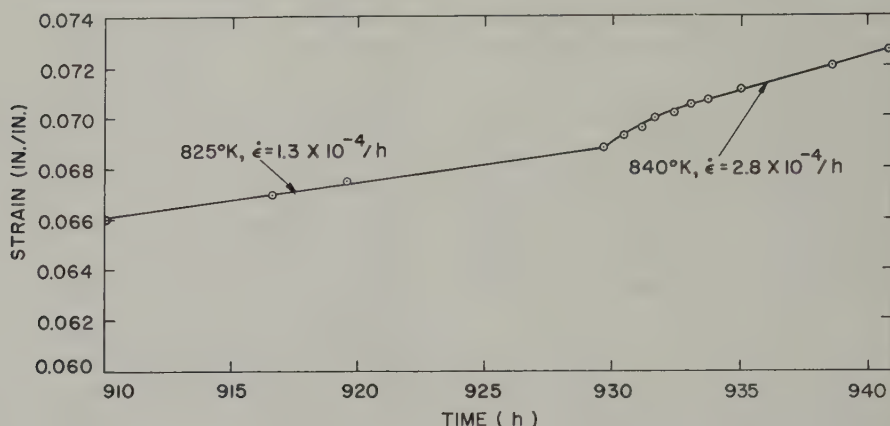


Fig. 6. Creep-strain versus time at 825° K and 840° K for a zirconium-hydrogen-uranium (atom ratio 1:1:0.03) alloy; stress constant at 3000 psi.

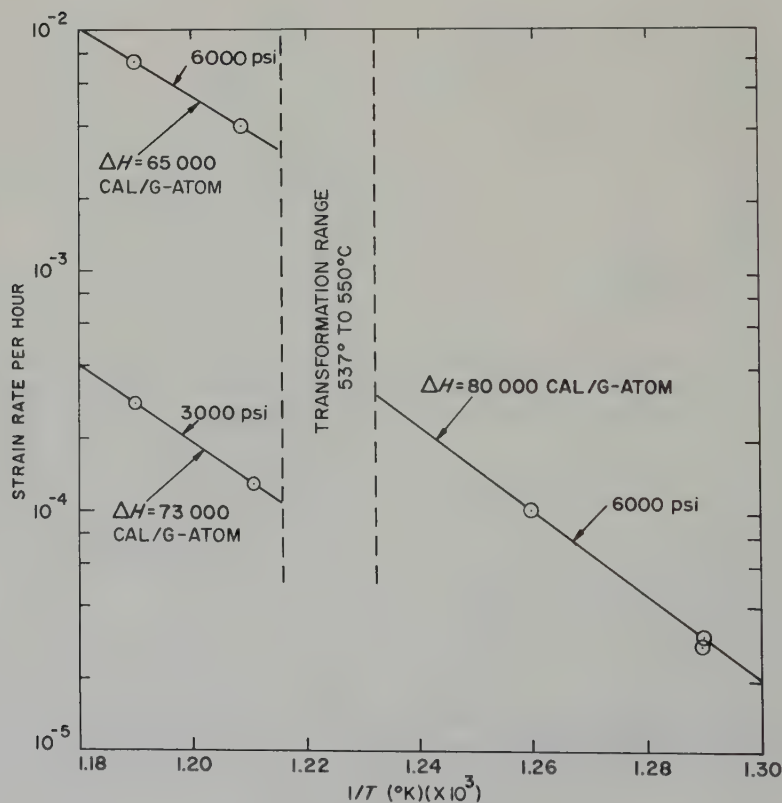


Fig. 7. Steady-state creep rate of a zirconium-hydrogen-uranium (atom ratio 1:1:0.03) alloy versus the reciprocal of the absolute temperature at 3000 and 6000 psi.

and 568° C), a similar relationship where $n = 4.7$ to 4.9 represents the data for a stress range of 3000 to 6000 psi.

The temperature dependence of the steady-state creep rate yields activation energies of 80 000 cal/g atom below the transformation temperature and 65 000 to 73 000 cal/g atom above the transformation temperature.

Acknowledgement

The author is indebted to Mr. D. Guggisberg who conducted the majority of the experimental work.

References

- 1) U. Merten, R. S. Stone and W. P. Wallace, Nuclear Fuel Elements (Reinhold Publishing Co., New York, 1959) p. 79
- 2) L. D. LaGrange *et al.*, J. Phys. Chem. 63 (1959) 1025
- 3) P. L. Gruzin, U. S. Emelayanov, G. G. Ryabova and G. B. Federov, Proc. Second Geneva Conference (1958) 19/P. 2526



Fig. 8. Creep specimen tested at 568° C under a nominal stress of 6000 psi. Specimen has elongated 70 %.

OBSERVATIONS MICROGRAPHIQUES SUR L'ALLIAGE Mg-Zr À 0,6 % EN POIDS, CHAUFFÉ DANS L'HYDROGENE

P. LELONG, J. DOSDAT, J. BOGHEN ET J. HÉRENGUEL

Centre de Recherches d'Antony de la Sté. des Tréfileries et Laminoirs du Havre, Antony (Seine), France

Reçu le 29 septembre 1960

La structure micrographique d'un alliage Mg-Zr à 0,6 % en poids, chauffé dans l'hydrogène, a été étudiée par microscopie optique et microscopie électronique. La diffusion de l'hydrogène dans l'alliage entraîne la formation d'un précipité d'hydrure de zirconium qui se sépare en plaquettes de symétrie hexagonale. Les conséquences métallurgiques de cette précipitation sont de deux types:

- 1°) Blocage du joint de grains qui conduit à une structure micrographique puissamment stabilisée, la formation de l'hydrure étant irréversible et sa vitesse de coalescence par chauffage extrêmement lente.
- 2°) Durcissement structural, lorsque les particules d'hydrure sont suffisamment fines.

Ces deux effets, en relation avec la répartition, le nombre et la dimension des précipités, dépendent des facteurs métallurgiques et des conditions de l'hydrogénation.

The structure of a Mg-0.6 % wt Zr alloy after heating in hydrogen was studied with the optical and with the electron microscopes. The diffusion of hydrogen in this alloy brings about a precipitation of zirconium hydride which separates in the form of flat hexagonal plates. The effects of such precipitation are principally of two types:

- 1) Anchoring of the grain boundaries leading to a "blocked" microstructure, the formation of hydride

1. Préambule

On sait que l'addition de zirconium au magnésium a pour effet d'inhiber le grossissement du grain sous l'action de chauffage à température élevée pendant des temps prolongés: cet effet particulièrement favorable a permis d'augmenter les températures de fonctionnement des cartouches des réacteurs français refroidis

being irreversible and the speed of coalescence extremely slow.

- 2) Precipitation hardening when the hydride particles are sufficiently fine.

These two effects related to the distribution, the number and size of the precipitates are dependent on various metallurgical factors and on the conditions of hydriding.

Das Gefüge einer Mg-Legierung mit 0.6 Gewicht % Zr wurde nach einer Wasserstoffglühung licht- und elektronenmikroskopisch untersucht. Das Eindiffundieren von Wasserstoff führt zur Ausscheidung von Zirkonhydrid in Form ebener Plättchen mit sechsfacher Symmetrie. Diese Ausscheidungen bewirken im wesentlichen folgendes:

- 1) Verankern der Korngrenzen, wodurch das Gefüge stabilisiert wird. Die Hydridbildung ist irreversibel, und die Geschwindigkeit der Teilchenvergrößerung ist beim Erwärmen nur sehr gering.
- 2) Aushärten, falls die Hydridpartikel genügend fein sind.

Diese beiden Erscheinungen, die mit der Verteilung, der Zahl und der Größe der Ausscheidungen zusammenhängen, werden von verschiedenen metallurgischen Maßnahmen und von den Hydrierbedingungen beeinflusst.

au gaz carbonique, qui utilisent ce matériau comme gaine. La stabilisation de la structure est en effet nécessaire pour éviter l'évolution défavorable des propriétés quand le grain grossit¹⁻⁵).

Les alliages magnésium-zirconium sont capables d'absorber de l'hydrogène à chaud. Celui-ci se fixe sur le zirconium et le phénomène

s'accompagne d'une augmentation de la résistance mécanique à froid et à chaud ^{6,7,8)} ainsi que d'une stabilisation supplémentaire de la grosseur du grain, plus efficace que celle qui résulte de la seule addition de zirconium. La figure 1 rappelle l'influence de cette absorption d'hydrogène à 500° C, sur les propriétés mécaniques et la taille du grain.

L'étude structurale des alliages hydrogénés a été reprise au microscope photonique et au

microscope électronique: on a pu voir l'hydruure de zirconium qui s'est séparé de la phase Mg α en petites plaquettes de symétrie de croissance hexagonale. Cet hydruure a le même aspect que celui qu'on voit par hydruuration ménagée du zirconium lui-même.

Sa répartition est en relation avec la texture d'hétérogénéité et d'orientation de l'alliage Mg-Zr. La dimension moyenne des plaquettes, imposée par les conditions de leur formation, semble jouer un rôle important pour les conséquences métallurgiques de l'hydrogénation.

2. Structure de l'alliage magnésium-zirconium avant hydrogénation

Les traitements dans l'hydrogène dont il sera fait mention ci-après ont été appliqués à un alliage Mg-Zr à 0,6 % brut de solidification. Dans cet état, on peut voir sur un même échantillon le comportement de solutions solides de titres en zirconium progressivement différents, grâce au vallonement ⁹⁾ qui résulte de la ségrégation mineure. L'alliage apparaît comme sur les figures 2 et 3. Sur la figure 3 en particulier, on voit un germe de solidification primaire, constitué par du zirconium d'après les diagrammes d'état ¹⁰⁾, et entouré d'une série d'auréoles concentriques. Ces dernières traduisent l'existence d'un gradient de concentration complexe dont la forme est schématisée sur la figure 4.

Ce phénomène résulte, comme l'ont indiqué H. Kostron et M. Schippers ¹¹⁾, d'une compétition de vitesse entre le déplacement du front de solidification et la diffusion des atomes d'addition dans le liquide, depuis la zone enrichie devant le front, vers le reste du liquide. De tels aspects sont fréquemment rencontrés, notamment avec les alliages d'aluminium, surtout lorsque ceux-ci contiennent du titane. Ils sont d'autant plus marqués que le front de solidification se déplace plus rapidement, ce qui est favorisé par l'existence d'un intervalle de solidification étroit. Un liquidus à faible pente, qui entraîne une ségrégation instantanée importante (différence de composition entre liquide et solide en équilibre), l'accentue égale-

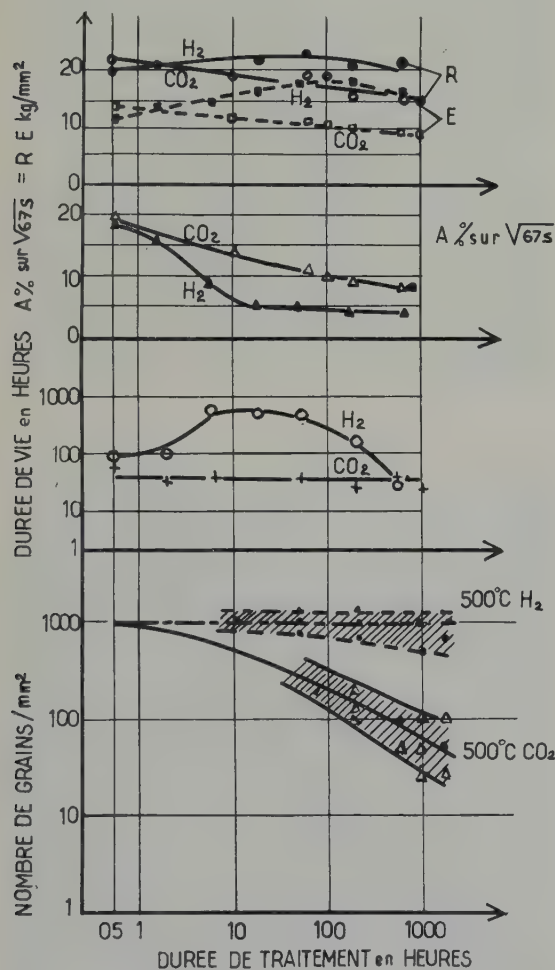


Fig. 1. Influence de la durée d'un chauffage préalable dans l'hydrogène à 500° C sur les caractéristiques d'un alliage Mg-Zr 0,6 % corroyé.

De haut en bas:

- Propriétés mécaniques à 20° C
- Durée de vie à 200° C sous une contrainte de 3,5 kg/mm²
- Nombre de grains par mm².

[Extrait de réf.⁸⁾.]

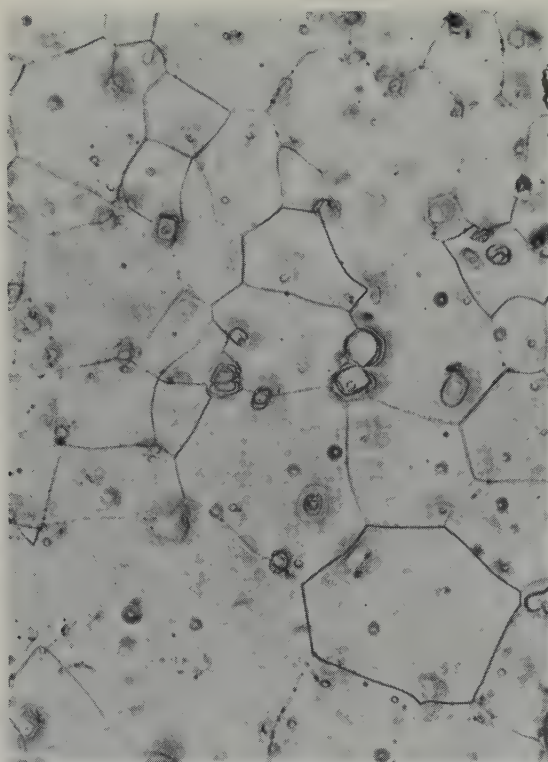


Fig. 2. Alliage Mg-Zr à 0,6 %. Etat brut de solidification. Polissage électrolytique. $\times 180$.

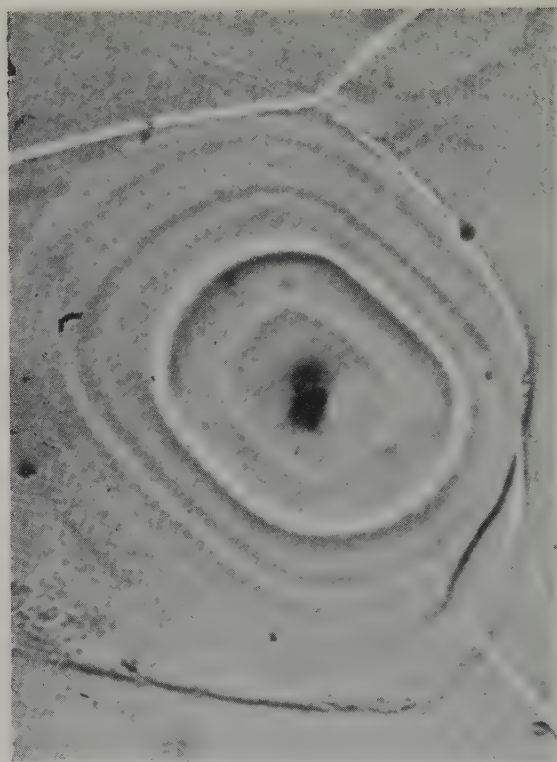


Fig. 3. Comme figure 2. $\times 1800$.

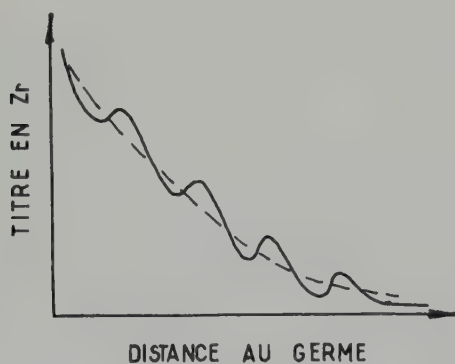


Fig. 4. Variation du titre en zirconium en fonction de la distance au germe de solidification.

ment. Ces conditions paraissent être particulièrement remplies avec les alliages Mg-Zr et Al-Ti.

Il est évident qu'un chauffage peut régulariser les gradients de titre, mais seul un corroyage suffisant peut les supprimer totalement.

3. Evolution de la structure de fonderie par chauffage prolongé dans l'hydrogène

Après 10 h dans l'hydrogène à 600° C, l'alliage se présente comme sur les figures 5 et 6, et après 100 h, comme sur les figures 7 et 8.

Les auréoles, un peu uniformisées par le chauffage, sont le siège d'une précipitation d'hydruure dont l'importance est en relation avec le titre local en zirconium. Des alignements préférentiels de précipités plus grossiers peuvent être observés:

- 1°. Suivant certains joints de grains, anciens ou actuels. On retrouve ainsi des aspects tout à fait analogues à ceux rencontrés par P. Lacombe¹²⁾ et par R. Segond et l'un d'entre nous⁹⁾ lors de la précipitation provoquée dans une solution solide Al-Mg de titre non uniforme.
- 2°. Suivant certains sous-joints de polygonisation, comme cela est particulièrement

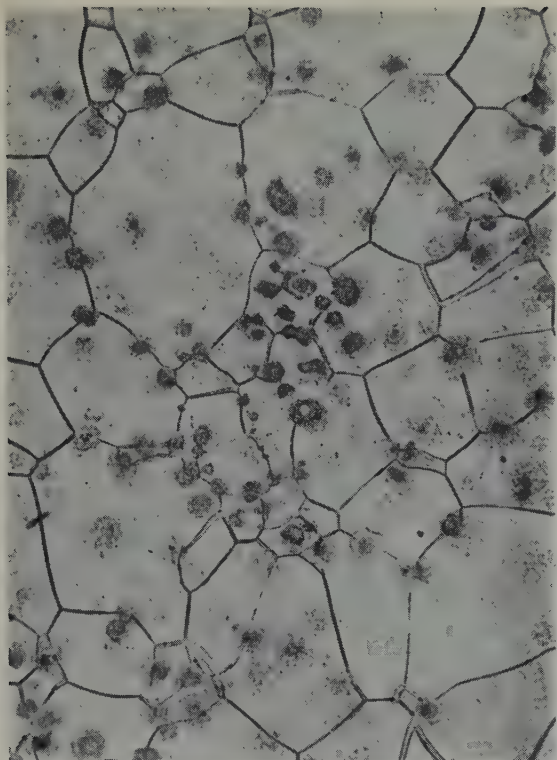


Fig. 5. Alliage Mg-Zr à 0,6 % en structure de fonderie. Effet d'un chauffage de 10 h dans l'hydrogène à 600° C. $\times 180$.

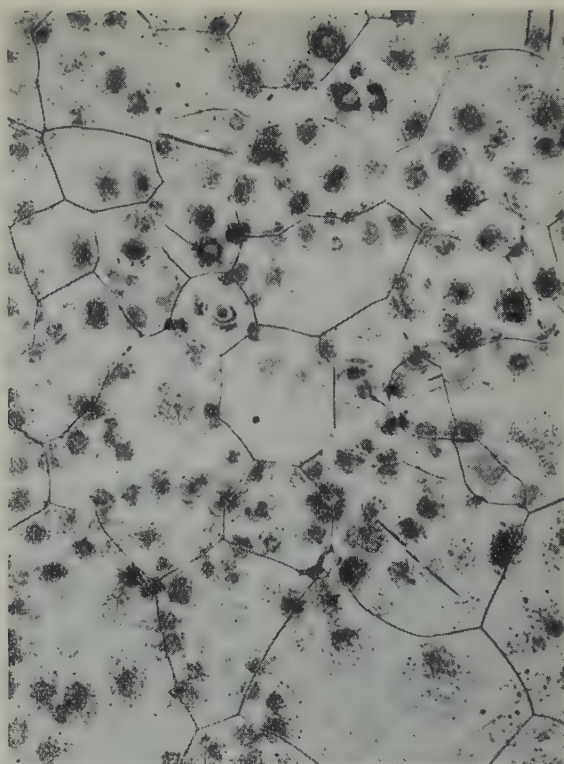


Fig. 7. Alliage Mg-Zr à 0,6 % en structure de fonderie. Effet d'un chauffage de 100 h dans l'hydrogène à 600° C. $\times 180$.

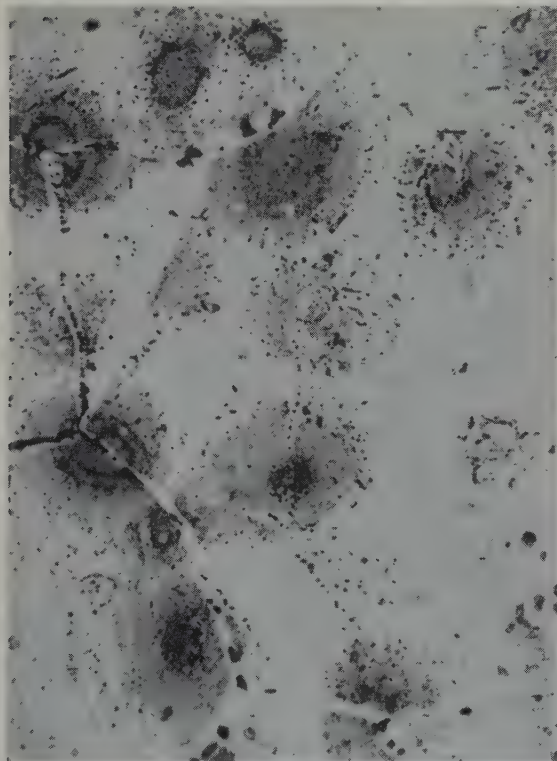


Fig. 6. Comme figure 5. $\times 900$.

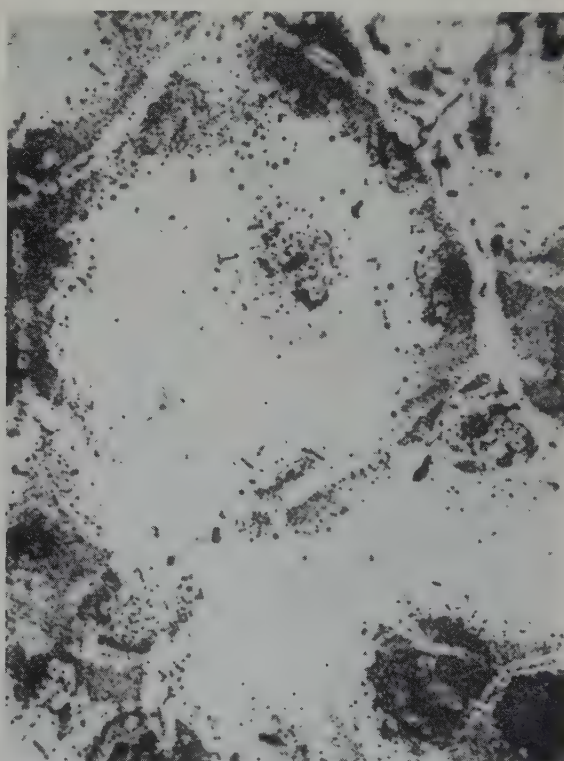


Fig. 8. Comme figure 7. $\times 900$.

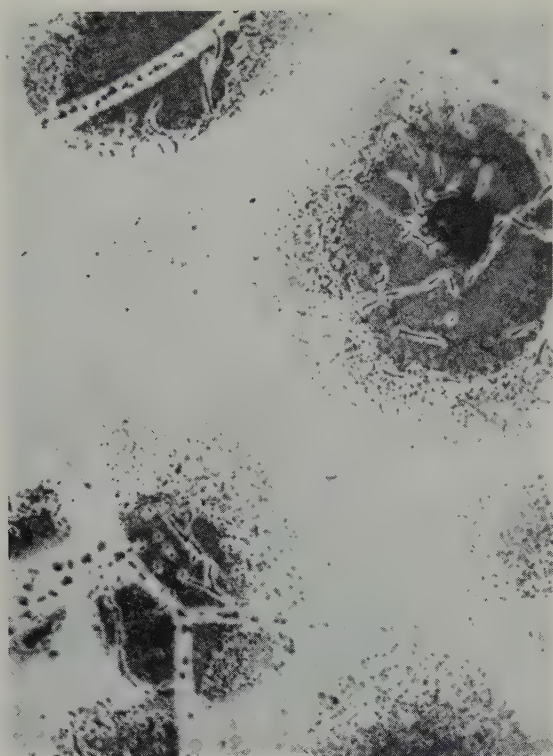


Fig. 9. Zone où les alignements d'hydrure coalescent dans les joints et les sous-joints sont particulièrement bien visibles. (Chauffage de 10 h dans l'hydrogène à 600° C.) $\times 900$.

bien visible sur la figure 9. De telles localisations préférentielles de la précipitation ont déjà été observées, notamment dans les alliages Al-Cu et Al-Zn¹³).

De part et d'autre des deux types d'alignements, on observe un liseré appauvri exactement comme dans le cas d'une précipitation classique à partir d'une solution solide sursaturée. Du point de vue micrographique, la précipitation d'hydrure, dont l'intensité est en relation directe avec le vallonement, présente tous les aspects du maillage classique^{9,12}.

4. Aspect des particules d'hydrure

L'existence de deux formes principales de particules, l'une régulière, l'autre allongée, peut déjà être discernée sur les micrographies photographiques précédentes. Au microscope électronique, ces aspects se précisent.

Au grossissement 4000, les auréoles de précipités se présentent comme sur les figures 10 et 11, par la méthode de réplique d'une part, et par la méthode d'examen direct sur prélèvement aminci d'autre part.

La méthode d'amincissement nous a conduit d'une façon générale à des images bien plus lisibles que les répliques. Cependant certains précipités sont entourés d'une zone grise qui peut être due, soit à une contamination dans le microscope résultant de la tension élevée (100 kV) nécessaire à l'examen direct, soit à un gradient de titre, soit à une variation locale d'épaisseur, associée ou non à un gradient de titre; l'hydrure étant très peu soluble dans les solutions d'amincissement (acide nitrique à 36° Bé et acide chlorhydrique à 22° Bé à 2 % dans l'éthanol), nous pensons que le relief doit être le principal responsable de ce phénomène. Sur les répliques, on voit les empreintes, ou les particules d'hydrure elles-mêmes qui ont été emportées: dans ce dernier cas, elles apparaissent en teinte foncée et, à quelques accidents près, à la place exacte qu'elles occupaient dans l'échantillon.

Les figures 12 et 13 représentent de telles répliques et le diagramme de diffraction électronique de la figure 14, effectué sur l'un des hexagones noirs, montre qu'il s'agit bien d'un monocristal du constituant lui-même. On sait que de tels reports peuvent être exploités systématiquement pour étudier la structure des composés^{14,15}.

Les différentes formes de l'hydrure peuvent être classées en trois types principaux, visibles sur les figures 12, 13 et 15 à 18

- 1) Hexagone presque régulier (fig. 12, 13, 15, 17, 18);
- 2) Lamelle hexagonale allongée (fig. 12, 17, 18);
- 3) Parallélogramme (fig. 16, 17).

Ces trois formes résultent en fait d'une symétrie de croissance unique, certains axes étant parfois privilégiés. Les schémas de la figure 19 montrent comment elles peuvent se déduire géométriquement les unes des autres.

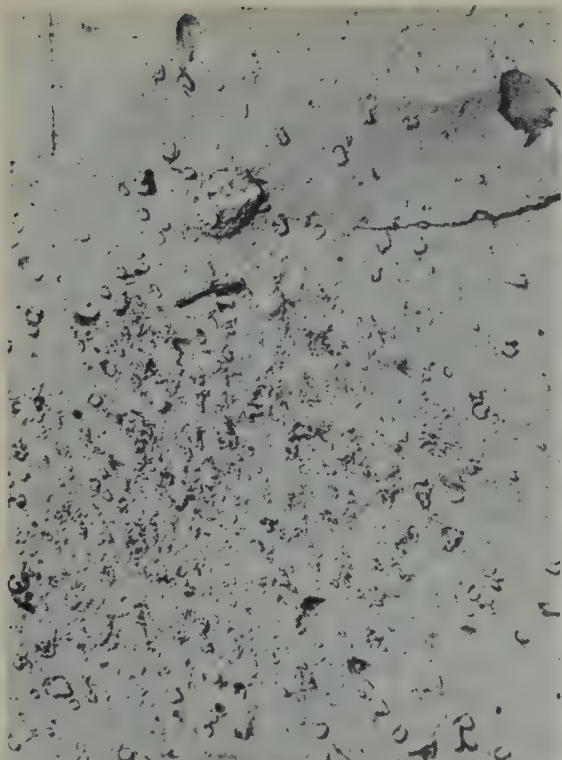


Fig. 10. $\times 4000$.

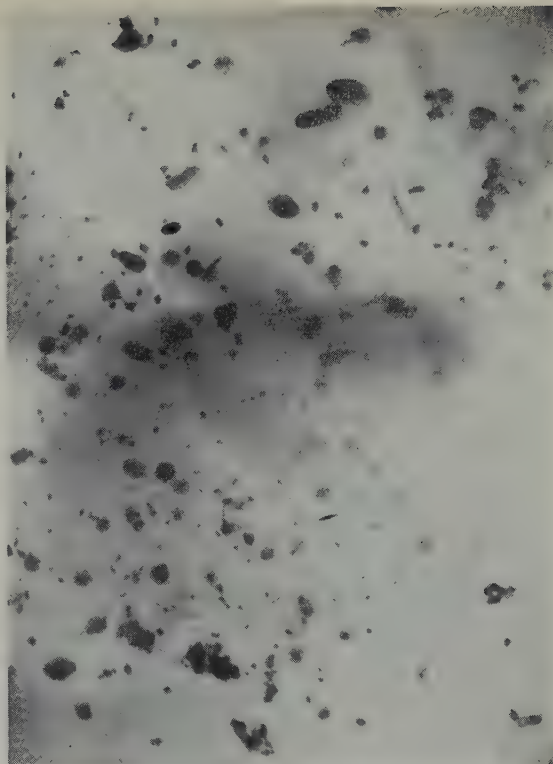


Fig. 11. $\times 4000$.

Fig. 10 et 11. Aspect au microscope électronique des auréoles d'hydruure précipité. (Chauffage de 100 h dans l'hydrogène à 600°C .) Comparaison entre la méthode des répliques (fig. 10) et celle d'amincissement (fig. 11).

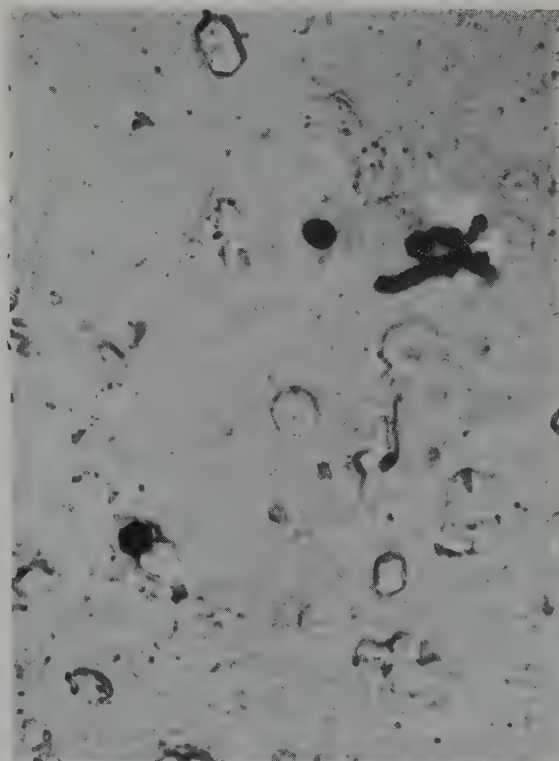
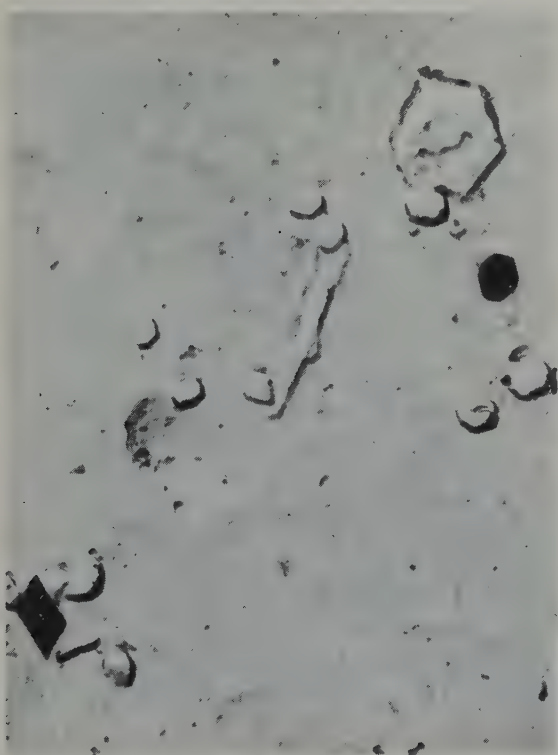


Fig. 12 et 13. Chauffage de 100 h dans l'hydrogène à 600°C . $\times 13\,500$.

Les figures 20 et 21 illustrent deux aspects successifs que peut prendre un hexagone de grande dimension en cours de croissance: la partie externe se forme d'abord, puis la zone centrale se complète tandis que les angles rentrants se remplissent, rendant le profil plus stable. Ce mécanisme de formation explique le trou semi-circulaire que l'on rencontre fréquemment au centre des plus grands cristaux (fig. 12, 13, 15).

C'est la seule structure interne que nous ayons pu mettre en évidence: les lignes sombres que l'on voit sur certaines micrographies sont des franges de diffraction et des franges d'interférences.

Des cristaux d'hydrure identiques à ceux qui viennent d'être décrits peuvent être rencontrés dans du zirconium hydrogéné (à faible teneur) et soumis à un revenu de précipitation.

On voit sur la figure 22 un alliage zirconium-

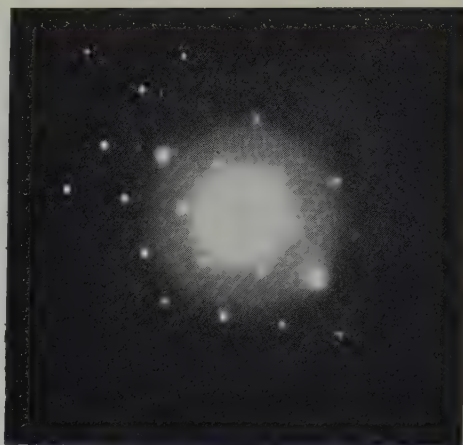


Fig. 14. Diagramme de diffraction d'un monocristal d'hydrure emporté sur une réplique.

hydrogène à 4 % en atomes d'hydrogène, dans lequel l'hydrure a été précipité par chauffage à 550° C et refroidissement lent. Les hexagones orientés sensiblement dans le plan d'examen ont été emportés sur la réplique. Presque tous les autres n'apparaissent que par leur empreinte:



Fig. 15.

(Pour légendes, voir p. 229).



Fig. 16.

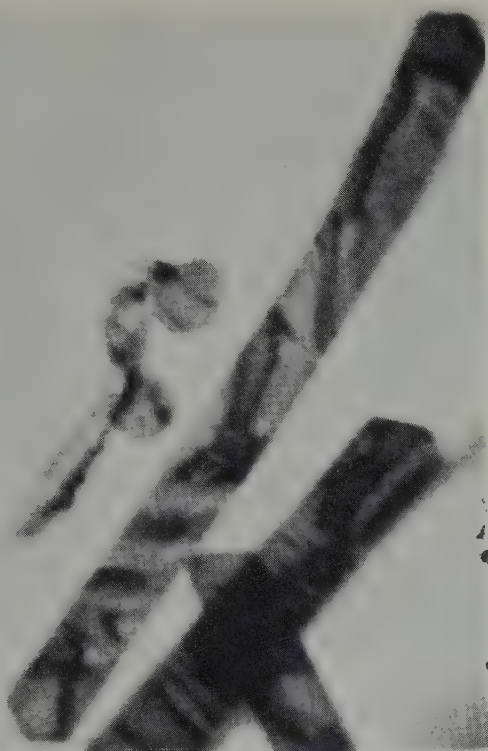


Fig. 17.

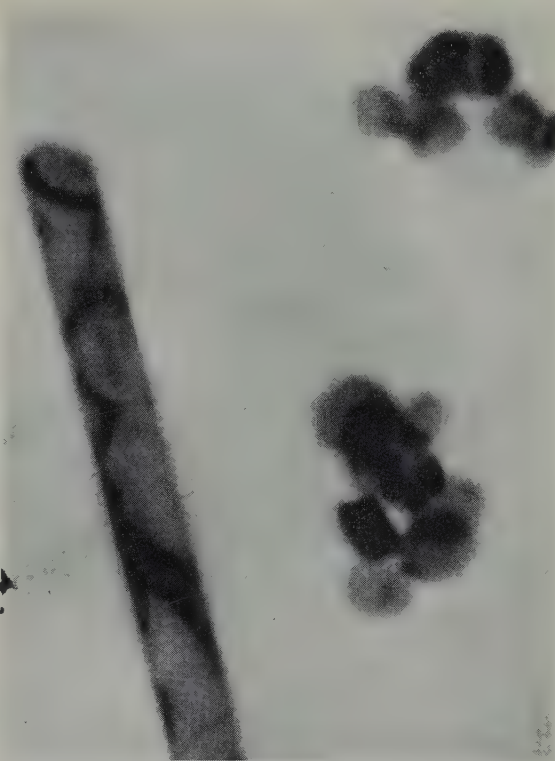


Fig. 18.

Fig. 15, 16, 17 et 18. Différentes formes de plaquettes d'hydrure rencontrées dans un alliage Mg-Zr à 0,6 % chauffé 100 h dans l'hydrogène à 600° C.

Fig. 15. $\times 120\,000$ et 16. $\times 72\,000$. Plaquettes emportées sur une réplique.

Fig. 17. $\times 80\,000$ et 18. $\times 80\,000$. Examen direct de prélèvement aminci.

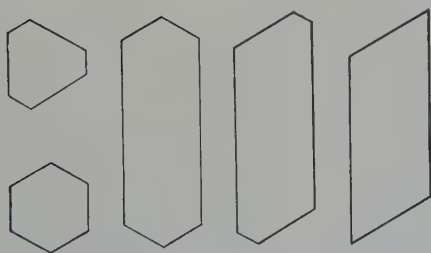


Fig. 19. Différents aspects que peuvent présenter des plaquettes dont la symétrie de croissance est hexagonale.

celle-ci, étroite et allongée, confirme bien la forme en plaquettes. On peut voir en outre que l'hydrure se sépare de façon préférentielle dans les sous-joints de polygonisation comme l'avait indiqué D. Whitwham ¹⁶⁾.

D'autres formes peuvent être également ren-

contrées dans le zirconium; les principales d'entr'elles sont représentées sur la figure 23.

La nature de l'hydrure qui se sépare sous ces différentes formes sera précisée dans nos études ultérieures. On peut déjà dire qu'il est peu probable que la symétrie de croissance hexagonale soit due à celle de la matrice environnante: en effet, on trouve dans un même grain des hexagones voisins orientés de diverses manières. Tout porte à penser, à moins qu'il ne s'agisse d'un hydrure inconnu, que nous sommes en présence de l'une des deux phases, cubique à faces centrées ou quadratique, identifiées par E. A. Gulbransen et K. F. Andrew ¹⁷⁾ et dont l'existence a été confirmée par D. Whitwham dans le travail déjà cité.

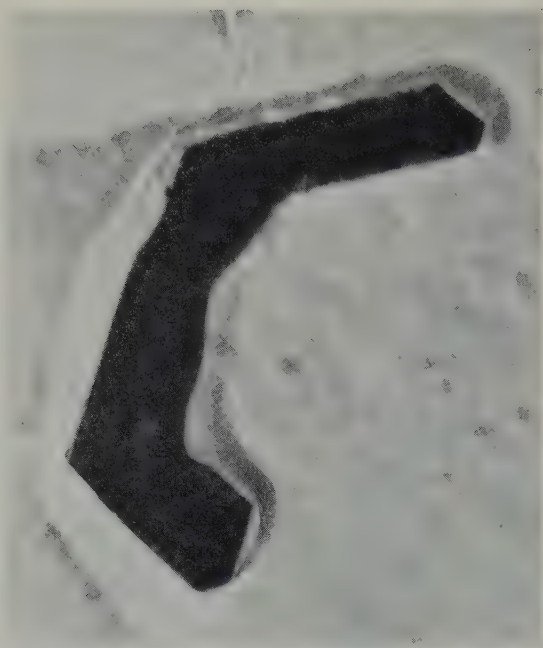


Fig. 20.



Fig. 21.

Fig. 20 et 21. Aspects successifs d'un hexagone de grande dimension en cours de croissance. $\times 60\,000$.

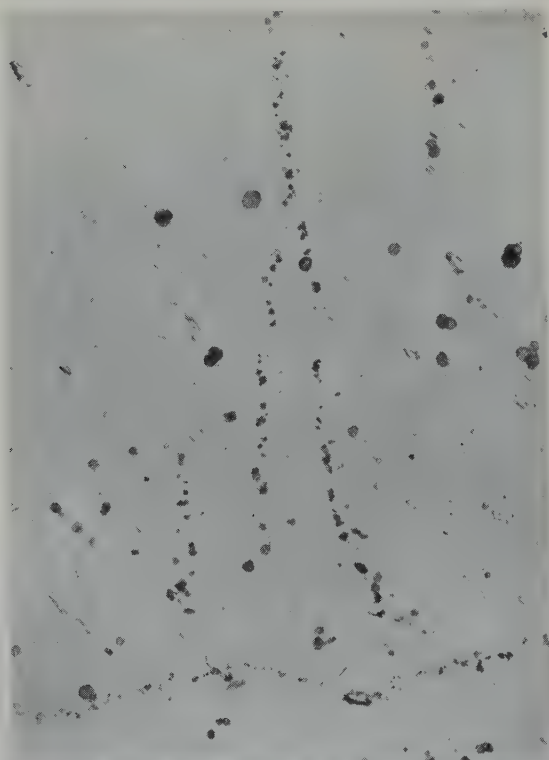


Fig. 22. Hydrure précipité dans un alliage Zr-H à 4 % at. d'hydrogène. Réplique. $\times 9\,000$.



Fig. 23. Différentes formes de l'hydrure précipité dans un alliage à 4 % at. d'hydrogène. $\times 13\,500$.

5. Influence des conditions du chauffage dans l'hydrogène

Le nombre, la dimension moyenne et le motif de répartition des précipités d'hydrure dépendent, pour une texture donnée, des principaux facteurs suivants:

- Titre en zirconium
- Durée du chauffage dans l'hydrogène
- Température du chauffage dans l'hydrogène.

L'influence du titre sera étudiée en détail par ailleurs. Il semble que pour un traitement donné, les particules soient plus grosses quand le titre est plus faible; en particulier, en texture de fonderie hydrogénée, les grands hexagones, autres que ceux alignés dans les joints et les sous-joints, sont le plus fréquemment rencontrés dans la partie externe des auréoles.

Le grossissement des particules en fonction

de la *durée du chauffage* sous hydrogène est certain: on peut le voir déjà au microscope photonique par comparaison des figures 5 et 6 avec les figures 7 et 8. Il s'agit d'un phénomène de coalescence pure, l'hydrogénation étant déjà totale bien avant la 10ème heure, comme le montre l'analyse chimique effectuée par ailleurs. Il s'agit cependant d'un type de coalescence un peu particulier puisque le zirconium et l'hydrogène se sont insolubilisés réciproquement dans le magnésium. Comme cela avait déjà été indiqué⁸⁾, cette coalescence ne se fait qu'à une vitesse très lente. Des essais de chauffage dans d'autres atmosphères, après hydrogénation, sont actuellement en cours pour préciser si un excès d'hydrogène est nécessaire pour permettre l'évolution structurale après insolubilisation du zirconium.

La *température de séjour* sous hydrogène joue un rôle déterminant sur la dimension des



Fig. 24. Alliage Mg-Zr à 0.6 % en structure de fonderie. Effet d'un chauffage de 10 h dans l'hydrogène à 500° C. Examen direct. $\times 80\,000$.

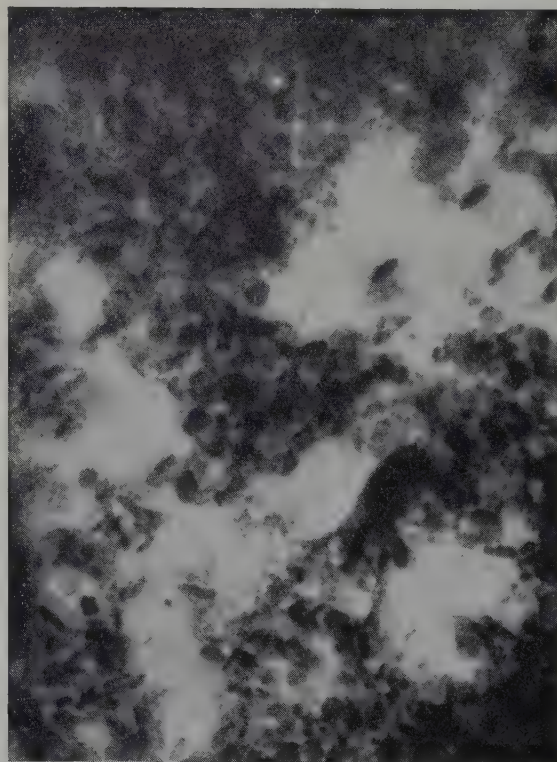


Fig. 25. Effet d'un chauffage de 20 h dans l'hydrogène à 450° C. Examen direct. $\times 125\,000$.

plaquettes. Les micrographies 24 et 25 montrent, par examen électronique direct, le résultat des chauffages de 10 h à 500° C (grossissement 80 000) et de 20 h à 450° C (grossissement 125 000) respectivement. Par effet de masque, provoqué par le feutrage des nombreuses petites particules inattaquées par la solution d'amin-cissement, la dernière préparation est relative-ment épaisse et son image de transmission plus confuse. On y distingue certaines de ces très petites plaquettes, orientées en biais ou per-pendiculairement au plan d'examen, d'où leur forme étroite. L'ordre de grandeur des dimen-sions moyennes peut en être déduit: la médiane de l'hexagone est de l'ordre de 300 à 400 Å et l'épaisseur des plaquettes de l'ordre d'une trentaine d'angströms.

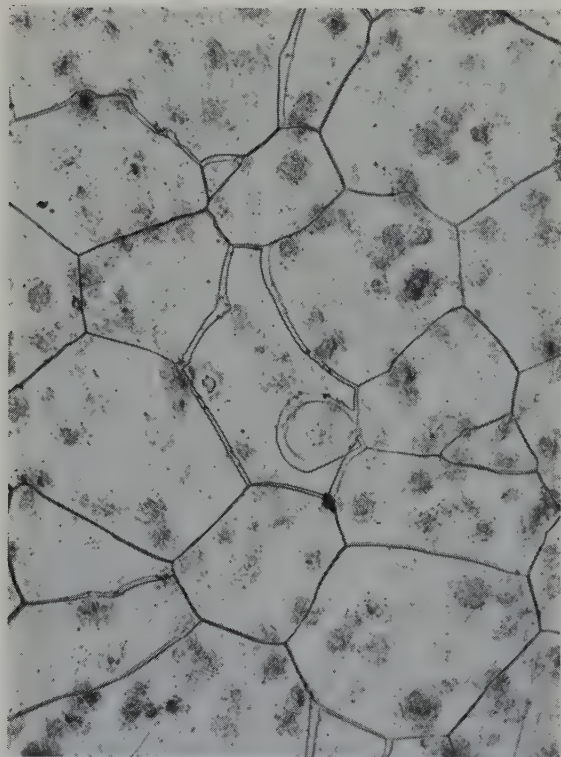


Fig. 26. Blocage des joints par les particules d'hydrure. Noter les irrégularités associées à la présence des nuages de fines particules ou à la présence de grosses particules individuelles. (Chauffage de 100 h à 600° C dans l'hydrogène.) $\times 180$.

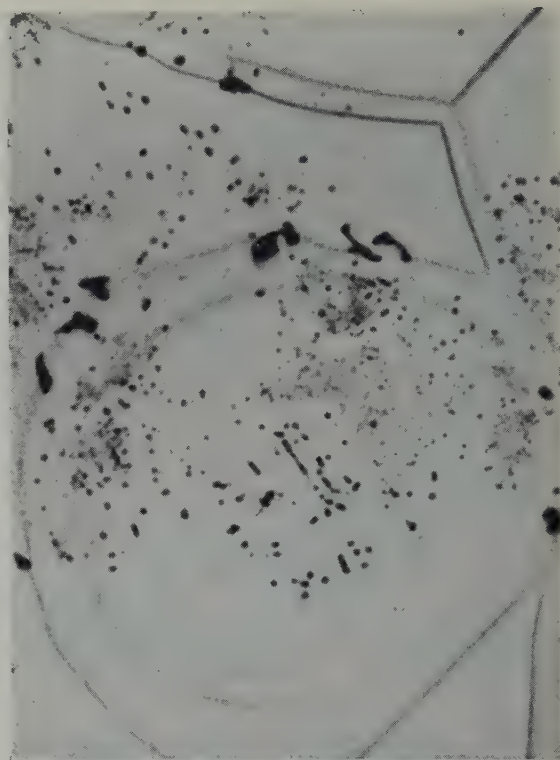


Fig. 27. Détail de la figure 26 montrant plusieurs ancrages de joints sur de grosses particules d'hydrure. $\times 1400$.

6. Conséquences métallurgiques

Suivant leurs dimensions moyennes, les plaquettes d'hydrure peuvent modifier différemment les propriétés de l'alliage.

Le *durcissement structural* qui peut résulter de l'hydrogénation s'obtient avec les plaquettes de plus petite dimension: c'est ainsi que le traitement prolongé à 450° C conduit à une résistance à la déformation à froid plus élevée que les traitements à 500° C ou à 600° C. Bien entendu, pour ces températures élevées, les temps courts doivent permettre l'obtention de petites plaquettes, mais de grandes différences peuvent alors être rencontrées entre les zones corticales et le centre des fortes sections.

Le *blocage du grain*, phénomène qui a déjà été rencontré dans de nombreux autres cas ^{18,19,20}), semble par contre être efficace dans un très large domaine de dimensions. La micrographie de la figure 26 montre plusieurs

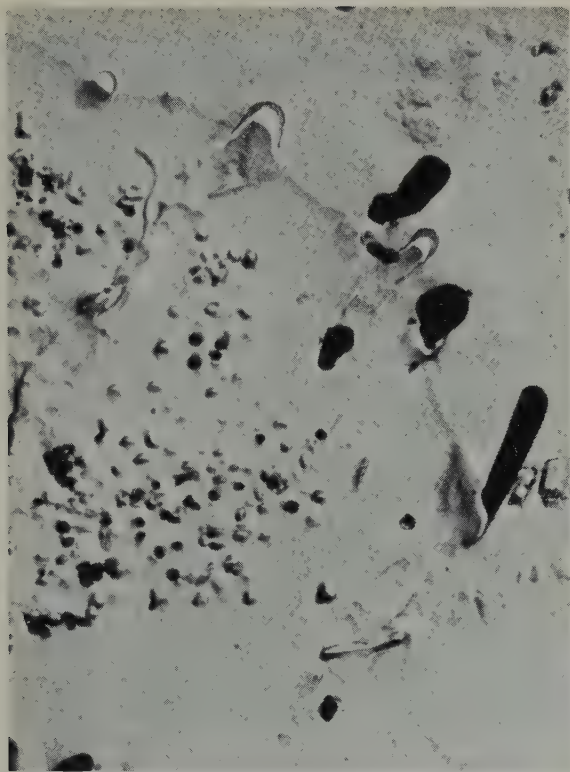


Fig. 28. Ancrages multiples sur plusieurs particules rapprochées. Réplique. $\times 13\,500$.

exemples où les joints de grains sont arrêtés avec des formes qui seraient absolument hors d'équilibre si elles n'étaient le résultat d'ancrages sur de gros précipités individuels ou sur les nuages de fins précipités que constituent les auréoles. A faible grossissement, l'ancrage sur de gros précipités se traduit par un angle assez prononcé comme on peut le voir sur la figure 27. Les nuages de fins précipités conduisent en général à des modifications de parcours du joint présentant des rayons de courbure apparents assez grands en première approximation; un examen à grossissement élevé montre que les fines particules agissent sensiblement comme les grosses (figure 28), les courbures étant la résultante de petits ancres très voisins les uns des autres.

Il faut noter enfin que la distance moyenne des particules est plus déterminante, vis-à-vis de l'efficacité de l'ancrage, que leur dimension.

La dégradation lente du blocage du joint

s'entretient par elle-même. En effet, le joint est un lieu de coalescence privilégiée et cette coalescence s'accompagne d'un appauvrissement de part et d'autre du joint. Sous l'effet du chauffage, les ancres tendent à s'éloigner les uns des autres et finissent par libérer le joint qui peut alors se déplacer d'autant plus loin que le liseré est plus large.

Le blocage suivant se dégradera progressivement de la même manière, et ainsi de suite, mais en pratique le déplacement du joint restera assez lent tant que les vitesses de diffusion qui contrôlent les phénomènes de dégradation seront faibles. C'est bien ce qui paraît être le cas pour le système Zr-H dans le magnésium.

7. Conclusions

Par des examens micrographiques photoniques et électroniques, on a identifié dans les alliages magnésium-zirconium hydrogénés un hydrure de zirconium de forme identique à l'un de ceux observés dans le zirconium faiblement chargé en hydrogène. Cet hydrure, dont la symétrie de croissance est hexagonale, est probablement la phase cubique qui a été identifiée par d'autres auteurs.

Le précipité d'hydrure présente de nombreuses analogies avec les précipités traditionnels qui se séparent des solutions solides sursaturées: en particulier il forme des alignements préférentiels suivant les joints de grains et les sous-joints de polygonisation avec appauvrissement de part et d'autre de ceux-ci.

Mais le précipité d'hydrure jouit toutefois d'une précieuse propriété que n'ont pas les précipités métallurgiques résultant de la sursaturation des solutions solides: sa formation est irréversible et les chauffages ne peuvent que le coalescer. De plus, par rapport aux phases intermétalliques de sursaturation à toutes températures (réseau de réticulation ou d'hypercorroyage), la dispersion d'hydrure jouit d'un autre avantage aussi précieux: sa coalescence est très lente. Pour ces deux raisons, la structure micrographique est puissamment stabilisée.

Les plaquettes d'hydrure, quand elles sont

suffisamment rapprochées, ancrent les joints de grains, les amas denses de plaquettes paraissant plus efficaces que les plaquettes plus dispersées. Le titre de l'alliage, et par ailleurs l'hérédité de la texture d'hétérogénéité de solidification et tout mécanisme modifiant la répartition du zirconium, sont des facteurs influant sur l'efficacité de l'inhibition.

Le durcissement structural déjà observé se produit par formation des plaquettes les plus fines, et s'atténue par leur coalescence lente.

Remerciements

Cette étude a été faite au Centre de Recherches d'Antony de la Société des Tréfileries et Laminoirs du Havre, en contribution à des recherches sous contrat avec le Commissariat à l'Energie Atomique. Nous remercions ici M. Salesse, Chef du Département de Métallurgie du Centre d'Etudes Nucléaires de Saclay, avec qui ces recherches ont été coordonnées et qui a bien voulu autoriser notre publication.

Nous remercions par ailleurs Melle Lebrun pour sa contribution personnelle aux examens de microscopie électronique.

Bibliographie

- 1) J. Hérenghuel, Thèse, Lille 1936 (Publ. Scient. Techn. Minist. Air n°. 93)
- 2) J. Hérenghuel, J. Boghen et M. Cerclet, CDRA-2001 du 5.12.1955. (Travail remis au C.E.A. dans le cadre d'un contrat d'études)
- 3) J. Hérenghuel, J. Boghen et M. Cerclet, CDRA-2011 du 26.4.56 (*ibid*)
- 4) J. Boghen et J. Hérenghuel, CDRA-2027 du 26.6.1957 (*ibid*)
- 5) B. Boudouresques, Symposium de Métallurgie Spéciale organisé à Saclay les 27 et 28 Juin 1957 par le Département de Métallurgie et de Chimie Appliquée (Presses universitaires de France, 1958) pp. 57-72
- 6) J. Boghen et J. Hérenghuel, CDRA-2029 du 5.12.1957. (Travail remis au C.E.A. dans le cadre d'un contrat d'études)
- 7) J. Hérenghuel, J. Boghen et P. Lelong, Comptes Rendus Acad. Sci. (Paris) **245** (1957) 2272
- 8) J. Hérenghuel et J. Boghen, Mém. Scient. Rev. Métall. **56** (1959) 371
- 9) J. Hérenghuel et R. Segond, Rev. Métall. **46** (1949) 377
- 10) M. Hansen, Constitution of Binary Alloys (Mc. Graw Hill, New-York, 1958) p. 932
- 11) H. Kostron et M. Schippers, Z.f. Metallkde **44** (1953) 477
- 12) P. Lacombe et P. Morize, Métaux **19** (1944) 30
- 13) A. Berghezan, Thèse, Paris 1952 (Publ. Scient. Techn. Minist. Air, n°. 385) p. 67
- 14) E. Smith et J. Nutting, Brit. J. Appl. Physics **7** (1956) 214
- 15) G. Henry, J. Plateau et J. Philibert, C.R. Acad. Sci. (Paris) **246** (1958) 2753
- 16) D. Whitwham, Mém. Scient. Rev. Métall. **57** (1960) 2
- 17) E. A. Gulbransen et K. F. Andrew, J. Electrochem. Soc. **101** (1954) 474
- 18) P. A. Beck, M. L. Holzworth et P. R. Sperry, Trans. AIME **180** (1949) 163
- 19) F. Haessner, G. Masing et H. P. Stüwe, Z.f. Metallkde **47** (1956) 743
- 20) J. Hérenghuel, P. Lelong et J. Moisan, C.R. Acad. Sci. (Paris) **250** (1960) 2200

LETTERS TO THE EDITORS – LETTRES AUX REDACTEURS

ELEKTRONENBEUGUNGS-UNTERSUCHUNG AN EINKRISTALLINEN SCHICHTEN
VON URANOXYDEN IM BEREICH VON UO_2 BIS U_4O_9

S. STEEB

Max-Planck-Institut für Metallforschung, Abteilung für Sondermetalle, Stuttgart, Deutsche Bundesrepublik

Eingegangen am 17. November 1960

Im Zusammenhang mit einem kürzlich in dieser Zeitschrift erschienenen Beitrag¹⁾ sind folgende Abschnitte bemerkenswert:

Werden dünne, durch Aufdampfen von Uran bei 10^{-5} Torr[†] auf heiße Steinsalzspaltflächen (400°C) erhaltene orientierte Schichten in einem Elektronendiffraktograph²⁾ mit 50 kV Elektronen durchstrahlt, so erhält man die Abb. 1.

Die Auswertung derartiger Aufnahmen ergibt unter Verwendung von MgO als Eichsubstanz das kubisch flächenzentrierte Gitter von $\text{UO}_2(\text{CaF}_2\text{-Typ})$ mit Gitterkonstanten von 5,45 bis 5,458 Å.

In³⁾ wurden die Gitterkonstantenbestim-

mungen mehrerer Autoren kritisch betrachtet und die gemessenen Werte a der Gitterkonstanten über O/U aufgetragen. Man leitet aus der so erhaltenen Geraden leicht die Beziehung ab:

$$\text{O/U} = \frac{5,667 - a}{0,1066} \quad (1,75 \leq \text{O/U} \leq 2,35).$$

Danach hatten unsere Ausgangspräparate eine zwischen $\text{O/U} = 2,04$ und $1,96$ schwankende Zusammensetzung.

Um nun das in Fig. 2 gezeigte Überstrukturdiagramm zu erhalten, wurde obiges Präparat im Diffraktograph auf Temperaturen zwischen 250°C und 550°C erhitzt und dann Sauerstoff bis zu einem Druck von 10^{-3} Torr eingeleitet. Schon nach wenigen Minuten erschienen zahl-

[†] 1 Torr = 1 mm Quecksilbersäule.

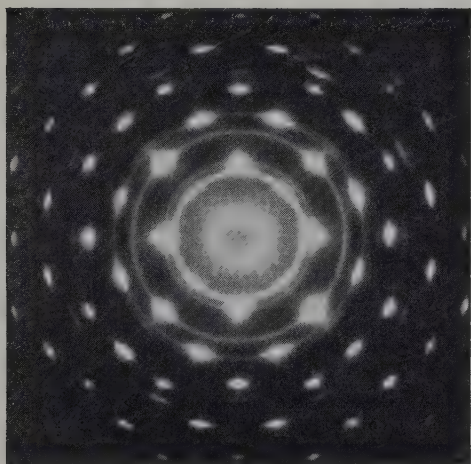


Abb. 1. Elektronenbeugungsaufnahme von UO_2 .

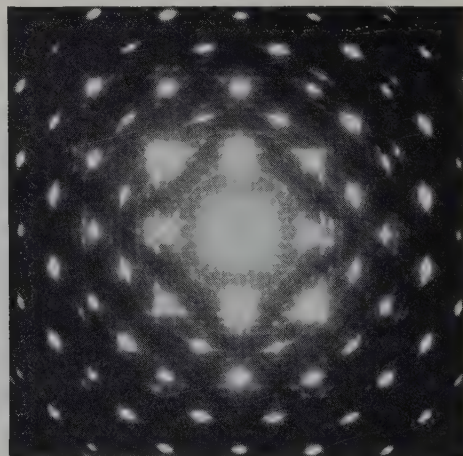


Abb. 2. Überstrukturdiagramm (Aus Abb. 1 nach 12 min bei 500°C und 10^{-3} Torr erhalten).

reiche neue Punkte in der Grundmatrix, deren Gitterkonstante sich nur wenig bis auf ca. $5,43 \text{ \AA}$ verringert hatte, was nach obiger Gleichung etwa der Zusammensetzung U_4O_9 entspricht.

Die „Überstrukturpunkte“ sind auf einem quadratischen Netz angeordnet, dessen Kantenlänge sich zur ursprünglichen wie 1:8 verhält, d.h., im zugehörigen Kristallgitter sind Überstrukturzellen mit einer Kantenlänge von $8 \times 5,43 \text{ \AA} = 43,44 \text{ \AA}$ entstanden.

Wird der Sauerstoff abgepumpt, so verschwinden die Überstrukturpunkte; sie treten aber kurze Zeit nach dem erneuten Zuleiten von Sauerstoff wieder auf. Die Ausbildung der Überstruktur ist also reversibel.

Bei Überschreitung einer vom Sauerstoffpartialdruck abhängigen kritischen Temperatur T_c verschwinden die Überstrukturpunkte.

($T_c = 580^\circ \text{C}$ für 10^{-3} Torr O_2 und

$T_c = 415^\circ \text{C}$ für 10^{-4} Torr O_2).

Die Gitterkonstante in den Diagrammen wurde jeweils bei Zimmertemperatur nach Aufrauchen von MgO vermessen.

Die Druckmessung erfolgte mit einem auf Sauerstoff geeichten Ionisationsmanometer, die Temperaturmessung mit einem Pt-Pt/Rh-Thermoelement.

Die orientierten Uranoxydschichten verändern sich nach Bildung der Überstruktur bei 400°C und 10^{-3} Torr O_2 im Zeitraum von 11 h nicht weiter. Höhere Oxyde treten bei diesem Druck erst nach Erhöhung der Temperatur auf ca. 500°C auf.

Unter der Annahme, dass die Überstrukturbildung in allen drei Koordinatenrichtungen in gleicher Weise erfolgt, müssen zu ihrer Beschreibung $8^3 = 512$ UO_2 -Zellen mit zusammen 2048 Uran- und 4096 O-Atomen zu einer Überzelle zusammengefasst werden.

In 2048 zur Verfügung stehende Zwischen-gitterplätze sind dann 512 weitere Sauerstoffatome einzubauen.

Somit können aus der endgültigen Auswertung der Abb. 2 interessante Hinweise auf den Einlagerungsmechanismus der Sauerstoffatome im UO_2 -Gitter erwartet werden.

Eine ausführliche Darstellung folgt demnächst.

Literatur

- 1) B. E. Schaner, J. Nucl. Mat. 2 (1960) 110
- 2) KD3 der Fa. Trüb-Täuber, Zürich
- 3) K. Q. Bagley und D. S. Oliver, UKAEA (Culcheth) Report, R & DB (C) TN-41 (1953)

RESTAURATION THERMIQUE DU PARAMETRE DE L'UO₂ FAIBLEMENT IRRADIE

Mme J. BLOCH

Centre d'Etudes Nucléaires de Saclay, France

Reçu le 17 décembre 1960

Le bioxyde d'uranium, de structure cristalline cubique type fluorure de calcium, présente une augmentation appréciable des dimensions de sa maille après irradiation par les neutrons thermiques.

Ce changement de paramètre atteint rapidement une valeur maximum lorsque la dose d'irradiation est telle que chaque fission recuise autant de défauts qu'elle en produit. Cela est réalisé pour un flux intégré voisin de 2×10^{17} neutrons/cm² 1).

Nous avons étudié la restauration du paramètre cristallin par des recuits isochrones d'un échantillon pour lequel la variation relative de paramètre avait atteint sa valeur maximum égale à $8,6 \times 10^{-4}$. L'irradiation a été faite dans la pile EL2 sous un flux de $2,5 \times 10^{12}$ neutrons/

cm².sec pendant une durée de 7 jours, soit un flux intégré de $1,48 \times 10^{18}$ neutrons/cm². La température d'irradiation est restée inférieure à 62° C. Le contrôle de la température maximum de l'échantillon au cours de l'irradiation est réalisé en plaçant contre lui un fil de paraffine et en nous assurant que celui-ci n'a pas fondu (température de fusion 62° C).

Le matériau que nous avons utilisé sous forme massive a été fritté sous hydrogène à 1650° C.

La valeur du paramètre de l'échantillon non irradié, $a_0 = 5,4690$ Å peut être attribuée à un UO₂ stoechiométrique pour autant que l'on connaisse cette valeur avec une erreur absolue inférieure à 0,001 Å, c'est-à-dire avec une dispersion suivant le mode de préparation

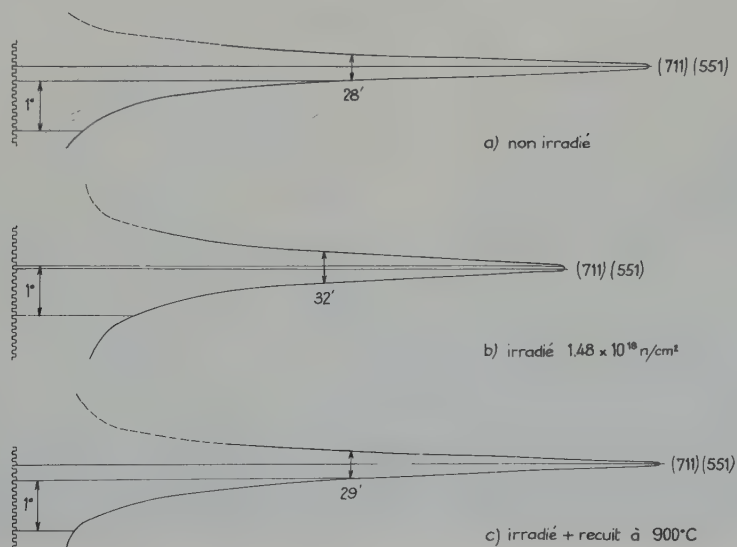


Fig. 1. Profil de la raie résultant de la superposition des réflexions (551) (711) dans les cas de: a) l'échantillon non irradié; b) l'échantillon irradié $1,48 \times 10^{18}$ neutrons/cm²; c) l'échantillon irradié et recuit à 900° C.

des échantillons correspondant à $\pm 5 \times 10^{-4}$ Å.

Les recuits ont été faits sous une pression inférieure à 5×10^{-6} mm Hg, leur durée a été choisie de 10 heures et les températures espacées de 100° C.

Les mesures de paramètre ont été faites sur l'appareil de radiocristallographie pour matériaux irradiés décrit dans la référence ²⁾. La raie étudiée qui résulte de la superposition des réflexions (551) et (711) étant située aux grands angles (θ voisin de 75°), la précision relative obtenue sur le paramètre est égale à 0.8×10^{-4} .

La raie de diffraction est très peu modifiée par l'irradiation: nous constatons une légère diminution d'intensité et un très faible élargissement de la raie aux plus grands angles dans l'échantillon irradié. Après recuit à 900° C la raie a repris son aspect initial (fig. 1).

Les résultats des mesures de paramètre sont indiqués sur la courbe de la figure 2. La restauration se fait en deux stades principaux: l'un à partir de 200° C, l'autre à partir de 500° C. Ces résultats sont en très bon accord avec ceux obtenus par E. Wait par des méthodes un peu différentes ³⁾.

A 900° C la restauration est presque complète.

Nous avons fait subir dans le même four la série des recuits successifs à un échantillon d' UO_2 identique et non irradié. Le diagramme est resté inchangé et le paramètre constant.

Le changement de paramètre produit par l'irradiation est en sens contraire de celui que provoquerait une oxydation. D'autre part, du fait que l' UO_2 a été préalablement recuit sous atmosphère d'hydrogène, il ne peut s'agir d'une

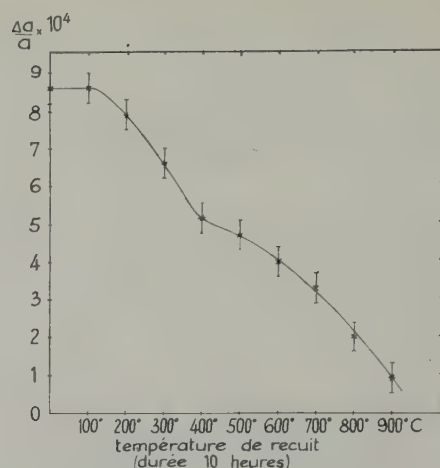


Fig. 2. Courbe de variation relative du paramètre d' UO_2 irradié en fonction de la température des recuits isochrones.

perte d'oxygène ultérieure au cours de l'irradiation.

Les produits de fission, dont la concentration est très faible (environ 20 ppm) ne pourraient être la cause que d'un changement de paramètre bien inférieur à 2×10^{-5} .

La seule explication possible de la variation de paramètre reste la création de défauts ponctuels au cours de l'irradiation, défauts qui disparaîtront au cours de recuits après irradiation.

Bibliographie

- ¹⁾ Y. Quéré et F. Nakache, J. Nucl. Mat. 2 (1959) 203
- ²⁾ J. Bloch, Rapport CEA, No. 1499 (Mai 1960)
- ³⁾ E. Wait, AERE (Harwell), Communication personnelle

THE COMPATIBILITY OF BERYLLIUM AND URANIUM DIOXIDE

A. G. KNAPTON and K. B. C. WEST

Research Laboratory, Associated Electrical Industries, Aldermaston Court, Aldermaston, Berks., UK

Received 5 August 1960

The economic advantages to be gained by raising the coolant temperature in gas cooled graphite moderated reactors has focused considerable attention on the possibility of beryllium as a canning material. Consequently, it is of considerable importance to establish the temperature at which reaction between beryllium and uranium dioxide or other possible reactor materials becomes appreciable. The preliminary results described cover a temperature range of 500° to 800° C.

Baird and West ¹⁾ showed that mixed powders of uranium dioxide (5μ particle size) and

beryllium reacted completely to UBe_{13} after 28 days at 700° C. Considerable UBe_{13} was also detected in X-ray powder photographs after the same period at 600° C.

Tests have now been made on stoichiometric uranium dioxide pellets (95 % theoretical density) clamped ²⁾ in contact with hot rolled beryllium sheet. The reaction product was identified metallographically and by micro-hardness measurements. In the clamped specimens, reaction was restricted to small areas (fig. 1), but resulted in appreciable penetration of the beryllium. The maximum thickness of

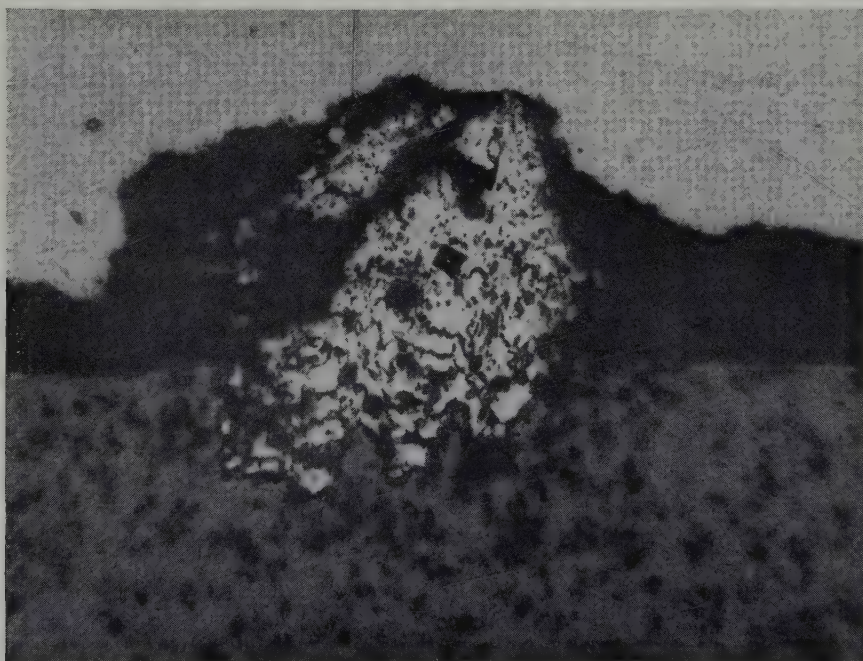


Fig. 1. Beryllium-uranium dioxide couple heated 1000° C seven days, showing localised UBe_{13} formation. Beryllium at top. $\times 200$.

reaction product was measured at right angles to the original interface in samples heated at temperatures between 600° and 800° C for times up to 224 days. The results are given in table 1 and shown plotted in fig. 2. Due to the limited number of areas of contact between the materials, the scatter of results is large, and fig. 2 should only be taken to indicate the general trend of reaction thicknesses.

TABLE 1
Reaction rate studies of beryllium with other materials

	Time (days)	Reaction layer thickness (μ)		
		500° C	600° C	700° C
Beryllium- iron	7	None observed	10	48
	14	8	10	80
	28	12	30	228
	56	24	40	240
	112	24	80	312
Beryllium- nickel	7	64	44	256
	14	120	60	350
	28	206	84	802
	56	210	124	1120
	112	180	280	1260
Beryllium- stainless steel	7	None observed	12	70
	14	14	35	90
	28	21	50	140
	56	30	66	184
	112	56	92	288
Beryllium- uranium	14	—	5	12
	28	4	10	—
	56	2	10	32
	112	4	14	40
	224	—	—	60
	254	—	20	—
Beryllium-† UO ₂		600° C	700° C	800° C
	14	None observed	4	20
	28	2	8	20
	56	2	10	80
	112	None observed	80	90
	224	36	110	140

† Also 7 days, 1000° C; 160 μ .

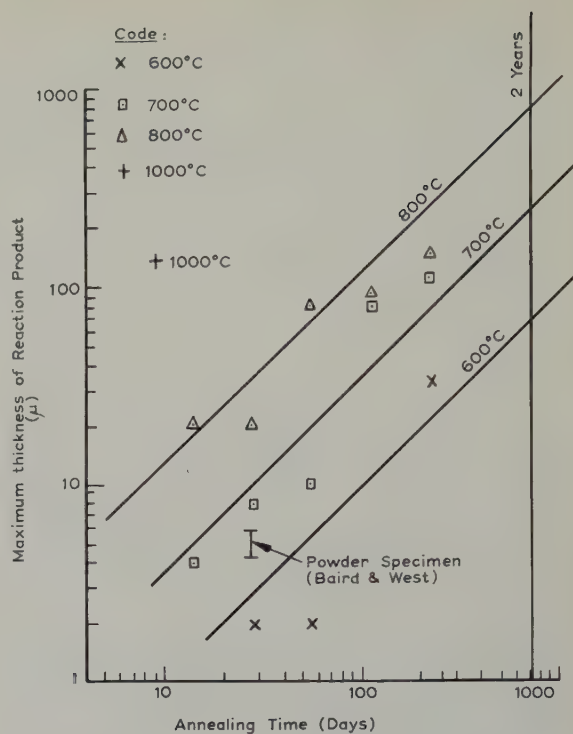


Fig. 2. Beryllium-uranium-dioxide reaction.

However, it may be concluded that in localised areas, appreciable reaction between uranium dioxide and beryllium has been observed, even at 600° C. Further work is required to confirm this trend and to establish what this means in terms of beryllium can performance under reactor conditions.

Simultaneously with the work on beryllium-uranium dioxide compatibility, the interaction of beryllium with several metallic materials has been studied by similar techniques. Results from these studies are also included in Table 1.

Acknowledgements

The authors wish to thank Dr. G. A. Geach for his encouragement and interest in the work, and Dr. T. E. Allibone, F.R.S., Director of the Laboratory, for permission to publish this note.

References

- 1) J. D. Baird and K. B. C. West, Confidential A.E.I. Research Report A. 862 (November, 1958)
- 2) J. D. Baird, G. A. Geach, A. G. Knapton and K. B. C. West, Second Geneva Conference, 1958, A/Conf. 15/P/24

TEMPERATURE DEPENDENCE OF THE SLIP DIRECTION FOR $\{110\}$ SLIP IN α -URANIUM

L. T. LLOYD

Argonne National Laboratory, Argonne, Ill. USA [†]

and

P. LACOMBE, D. CALAIS and Mrs. N. SIMENEL

Centre de Recherches Métallurgiques de l'Ecole des Mines de Paris, France ^{††}

Received 4 November 1960

Slip on $\{110\}$ planes of orthorhombic alpha-uranium was first reported by Cahn¹⁾. This type of deformation was not found by Lloyd and Chiswick²⁾ for single crystals compressed at room temperature; whereas it was observed in similar studies by Teeg³⁾ at -196°C and by Lloyd⁴⁾ at 600°C . More recently Calais, Lacombe and Simenel⁵⁾ have obtained $\{110\}$ slip upon room temperature tensile deformation of crystals grown by $\beta \rightarrow \alpha$ transformation. Thus, the occurrence of $\{110\}$ slip over a wide temperature range is well established, although the literature records different active slip directions.

As Cahn pointed out, the closest-packed directions in $\{110\}$ planes are $\langle 112 \rangle$ and $\langle 110 \rangle$ with atom spacings of approximately 3.00 and 3.26 Å, respectively (fig. 1). The atoms in the $\langle 110 \rangle$ are in a straight line, while those in $\langle 112 \rangle$ are alternately displaced 0.29 Å from the direction. Based on spacing alone, the $\langle 112 \rangle$ is the most probable slip direction, but if straightness of the rows is important, the $\langle 110 \rangle$ would be preferred.

[†] A portion of the work reported in this letter was performed under the auspices of the U.S. Atomic Energy Commission.

^{††} Work performed under contract between the "Commissariat à l'Energie Atomique" and the "Centre de Recherches Métallurgiques de l'Ecole des Mines de Paris".

Cahn was not able to positively identify the slip direction experimentally; however, from stereographic analyses he tentatively concluded that it was $\langle 110 \rangle$. By the metallographic technique of preparing surfaces which contained the

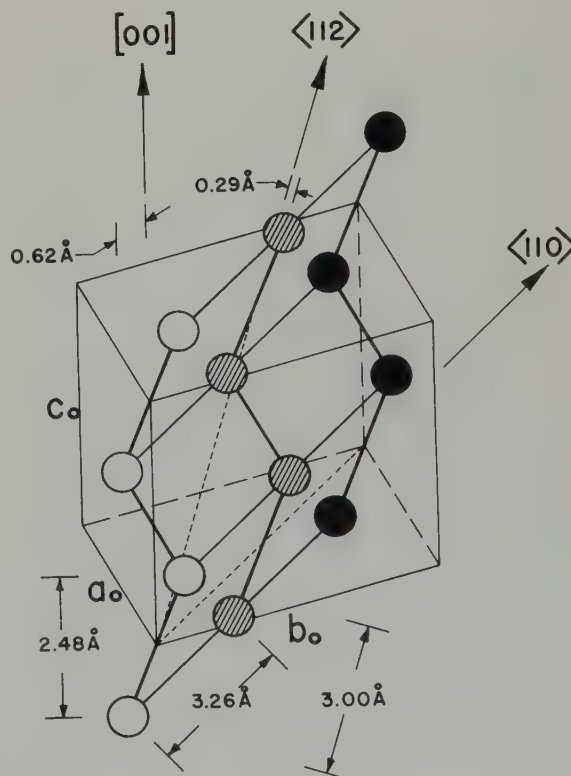


Fig. 1. Comparison between principal interatomic distances in α -uranium

slip direction but which did not reveal traces upon deformation of the crystal by $\{110\}$ slip, Teeg proposed the $[001]$ direction as operative at -196°C . The in-line spacing of the atoms in the $[001]$ direction is rather large, 4.96 \AA ; however, if it is considered zigzag, the atoms are separated by 2.48 \AA parallel and alternately displaced 0.62 \AA from the direction. The rotational asterism of Laue back-reflection photograms of Teeg's samples did not conclusively identify the slip direction. In many cases the asterism appeared consistent with duplex slip in $\langle 112 \rangle$ directions, and the author concluded that the observed $[001]$ might be the result of such cooperative slip.

The operative direction at 600°C has been identified experimentally by Lloyd from rotational asterism observed in a Laue photogram for a crystal deformed by slip on one set of $\{110\}$ planes (fig. 2). Since the rotation was about the (001) pole (or $[001]$ axis), the slip

direction was unequivocally identified as the $\langle 110 \rangle$ direction lying in the slip plane and perpendicular to the rotation axis. Geometrical analyses of dimensional changes found for other crystals deformed by $\{110\}$ slip and agreement of calculated critical resolved shear stress, when the slip elements were considered as $\{110\}-\langle 110 \rangle$, substantiated this identification.

In the tensile deformation experiments of Calais *et al.* at room temperature, the $[001]$ slip direction was identified by metallographic examination. Confirmation of this result from the asterism of Laue back-reflection spots was not easy, however, due to the inherent imperfection of the initial crystals, prepared by the phase-change growth method. On the other hand, it is in principle possible, using the Boas-Schmid critical shear stress relation,

$$\frac{E}{A} = \frac{\sigma}{\sin \chi \cos \lambda}$$

to calculate the shear stress required to initiate slip, either on the $\{110\}-\langle 110 \rangle$, the $\{110\}-[001]$ or the $\{110\}-\langle 112 \rangle$ systems, depending on the crystal orientation. Figs. 3, 4, 5 and 6 show the curves, or contours, corresponding to given shear stress values, on the assumption that the critical shear stress is equal to unity for the possible slip systems, both in tension and compression.

In figs. 3 and 4 are plotted the orientations of the crystals for which Calais, Lacombe and Simenel found $\{110\}$ slip after tensile deformation at 20°C . On the first hypothesis of $\{110\}-\langle 110 \rangle$ system (fig. 3), it may be noted that the tensile stress must attain a value of 8 times the critical shear stress (for orientations very close to (001)). In contrast, the second hypothesis of $\{110\}-[001]$ slip requires a tensile stress of only twice the critical shear stress. The $\{110\}-[001]$ slip mechanism therefore seems much more likely on a dynamic basis.

Moreover, the crystals for which Lloyd found $\{110\}$ slip after compression at 600°C , possess orientations which are very different from those found by Calais *et al.* to show the same $\{110\}$ slip after tensile deformation at 20°C . The

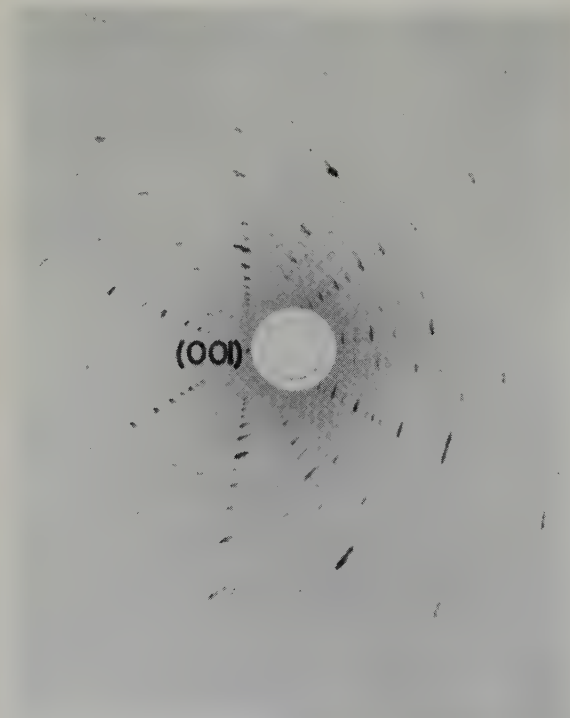


Fig. 2. Rotational asterism about (001) plane pole for a crystal deformed by slip on one set of $\{110\}$ planes (after Lloyd)

orientations of Lloyd's crystals are concentrated in the (100)–(010) zone, for which $\{110\}$ – $[001]$ slip would require very large values of shear stress. Fig. 5 shows that, for the same crystals, the $\{110\}$ – $\langle 110 \rangle$ slip hypothesis leads to values of tensile stress equal to at most 1.5 times the critical shear stress.

If one adopts the $\{110\}$ – $\langle 112 \rangle$ slip mechanism proposed by Teeg for compression at -196°C , then fig. 6, showing a plot of both Teeg's results at -196°C and those of Calais at 20°C , illustrates that the $\langle 112 \rangle$ direction is not incompatible on this dynamic approach.

It also becomes possible to explain why the

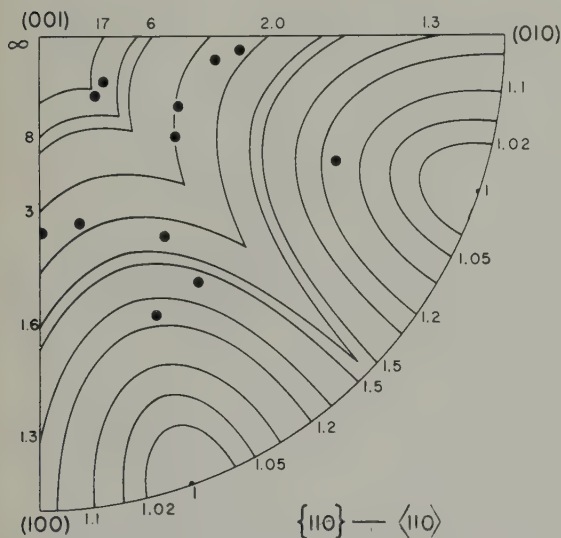


Fig. 3. Curves of constant relative resolved shear stress for $\{110\}$ – $\langle 110 \rangle$ slip. ● circles represent the orientations of the crystals studied by Calais *et al*

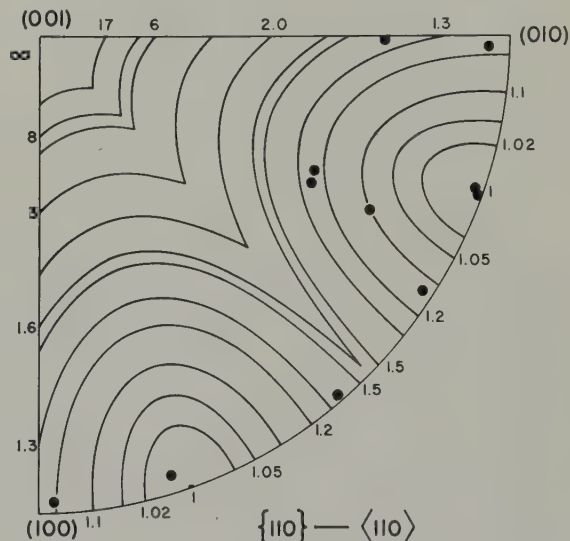


Fig. 5. Curves of constant relative resolved shear stress for $\{110\}$ – $\langle 110 \rangle$ slip. ● circles represent the orientations of crystals compressed by Lloyd at 600°C

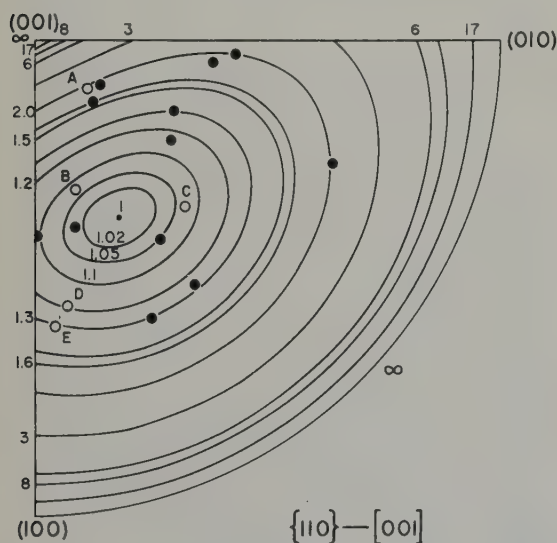


Fig. 4. Curves of constant relative resolved shear stress for $\{110\}$ – $[001]$ slip. ● circles represent the orientations of the crystals studied by Calais *et al*. and ○ represents the orientations studied by Teeg

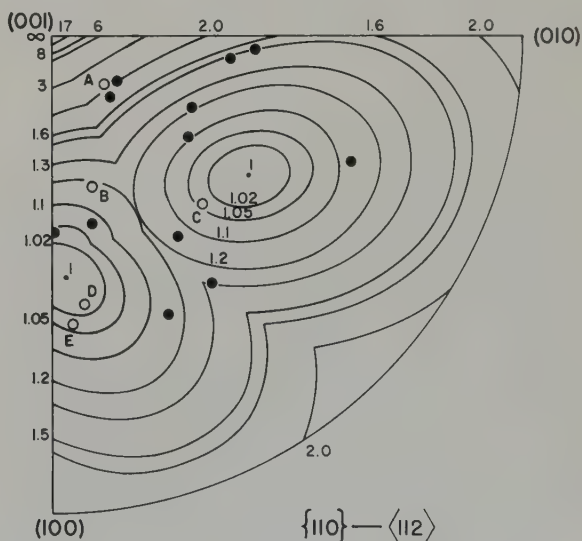


Fig. 6. Curves of constant relative resolved shear stress for $\{110\}$ – $\langle 112 \rangle$ slip. ● circles represent the orientations of the crystals studied by Calais *et al*. and ○ represents the orientations studied by Teeg

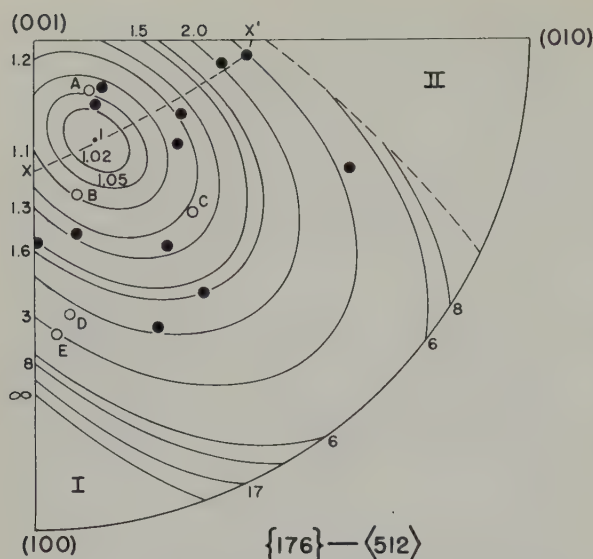


Fig. 7. Curves of constant relative resolved shear stress for $\{176\}$ twinning by compressive loading. The region limited by the dotted line around (001), $X-X'$, is forbidden for twinning in tension, and regions I and II around (100) and (010) are forbidden for twinning in compression. A, B and C represent Teeg's crystals giving $\{176\}$ twins by compression; D and E gave $\{110\}$ — $[001]$ slip by compression. ● circles represent the orientations of crystals studied by Calais *et al.*

results of Lloyd and Chiswick at room temperature and those of Lloyd at 600° C, dealing with compression, are different from the results of Calais, Lacombe and Mrs. Simenel at 20° C or those of Teeg at -196° C, both with regard to slip direction and to the correlation between crystal orientation and deformation mechanism. If one accepts that the critical shear stress concept may be extended to deformation twinning⁶), the occurrence of slip or twinning for a given crystal orientation may well depend on temperature. In general, the critical shear stress for slip is believed to diminish significantly with increasing temperature, while for twinning, in contrast, the critical shear stress varies little with temperature. This would explain the increasing predominance of slip observed by Lloyd⁴) at 600° C and by Butcher⁷) at temperatures above 400° C. On the other hand, Teeg observed $\{176\}$ twinning at -196° C for the crystal orientations A, B and C of figs. 4, 6 and 7, while Calais noted $\{110\}$ slip

for closely similar orientations. A comparison of figs. 4 and 7 shows that there would be about the same chance of obtaining slip or twinning for crystals A, B and C, if the critical shear stresses for $\{176\}$ twinning and $\{110\}$ slip are assumed to be of the same order of magnitude. These orientations fall well within the regions for which the required shear stress is at a minimum both for twinning and slip. In addition to this dynamic factor, a geometrical factor must also be considered in certain cases: crystal orientations close to (001) can give rise to twinning in compression but not in tension, hence the preference for $\{110\}$ slip noted by Calais for tensile deformation at 20° C.

A final comparison is suggested for the relative importance of the various dynamic and crystallographic factors. Teeg reported $\{110\}$ slip for only two crystal orientations, D and E. A comparison of figs. 4 and 6 with fig. 7 shows that, for these orientations, twinning is less easy than $\{110\}$ — $[001]$ slip and particularly $\{110\}$ — $\langle 112 \rangle$ slip.

Finally, the dynamic approach also explains why Calais observed $\{110\}$ slip in tension at 20° C, rather than the more frequent (010)— $[100]$ slip. Fig. 8 shows that the majority of the

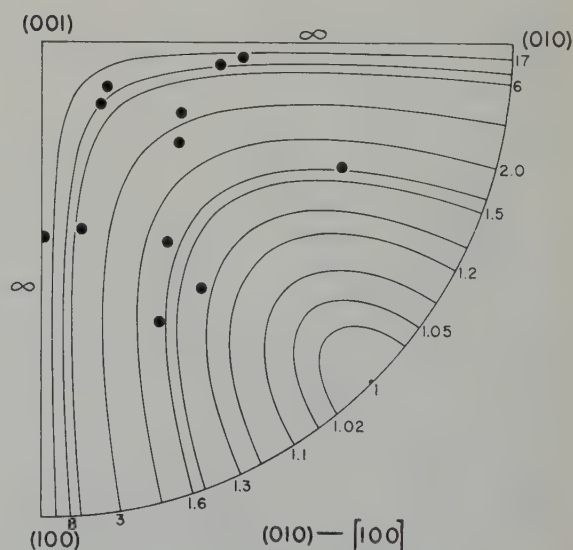


Fig. 8. Curves of constant relative resolved shear stress for (010)— $[100]$ slip. ● circles represent the orientations of crystals studied by Calais *et al.*

crystals studied by Calais *et al.* had orientations falling in a region for which the shear stress would be much higher for $(010) - [100]$ than for $\{110\} - [001]$ or $\{110\} - \langle 112 \rangle$ slip.

In conclusion $\{110\}$ slip has been observed for a wide range of temperatures, -196°C to 600°C ; at high temperatures in a $\langle 110 \rangle$ direction, and in a $[001]$ direction at room and at low temperatures. The possibility that $\{110\} - [001]$ slip may be the result of two successive $\{110\} - \langle 112 \rangle$ slips, as proposed by Teeg, is not excluded; this mechanism would suppose the occurrence of partial dislocations in uranium. To supplement the dynamic argument developed in this note to explain the different results obtained in compression and in tensile deformation at different temperatures, it would be very important to determine the critical shear

stress values as a function of temperature for the various slip mechanisms suggested.

References

- ¹⁾ R. W. Cahn, *Acta Met.* **1** (1953) 49
- ²⁾ L. T. Lloyd and H. H. Chiswik, *Trans. AIME* **203** (1955) 1206
- ³⁾ R. O. Teeg, Dissertation, Massachusetts Institute of Technology, (USA) (1958);
R. O. Teeg and R. R. Ogilvie, *J. Nucl. Mat.* **3** (1961) 81
- ⁴⁾ H. H. Chiswik, A. E. Dwight, L. T. Lloyd, M. V. Nevitt and S. T. Zegler, *Proceedings of the 2nd International Conference on the Peaceful Uses of Atomic Energy*, **6** (1958) 394
- ⁵⁾ D. Calais, P. Lacombe and N. Simenel, *J. Nucl. Mat.* **1** (1959) 325
- ⁶⁾ R. L. Bell and R. W. Cahn, *Acta Met.* **1** (1953) 752
- ⁷⁾ B. R. Butcher, AERE (Harwell) Report R 2898 (1959)

РОСТ ВЗАИМОДИФФУЗНОГО СЛОЯ В СИСТЕМЕ АЛЮМИНИЙ-УРАН

Кастлман Л. С.

Изучалась взаимодиффузия в системе алюминий-уран, в температурном интервале 400—600° Ц и при давлениях 1,25—10 тонн/дюйм² (175—1400 кг/см²), за время меньше 24-х часов. Подтвердилось что толщина слоя UAl_3 увеличивается с давлением. Было показано существование интересных зависимостей между длительностью отпуска, температурой отпуска и прикладываемым давлением, с одной стороны и природой и распределением структурных дефектов в зоне диффузии UAl_3 , с другой стороны. Было показано что количество растворенной

фазы урана в UAl_3 -фазе, равно по меньшей мере 2,6% атом. урана. Было показано что рост UAl_4 -фазы и UAl_2 -фазы в дифференциальных микропарах, гораздо более медленный, чем рост UAl_3 -фазы в микропарах алюминий-уран. В заключении предполагается что воздействие давления на образование слоя UAl_3 имеет в основном механический характер, так как повышение давления препятствует образованию макропор и тем самым фактически увеличивает поперечное полезное сечение взаимодиффузии.

ОЦЕНКА ДЕЙСТВИЯ ОБЛУЧЕНИЯ В РЕАКТОРЕ НА ТЕПЛОПРОВОДНОСТЬ БЕРИЛЛИЯ

Динес Г. Дж. и Дамаск А. С.

Изучается теплопроводность и электросопротивление бериллия при низких температурах. Из существующих данных по действию облучения в реакторе на электросопротивление бериллия выводится низкотемпературная зависимость теплопроводности от облучения. Расчет показывает что облучение в реакторе интегральной дозой в 10^{19} нейтр./см²/сек.

(быстрые нейтроны) уменьшает теплопроводность бериллия на 0,04 вт/см °К, при 20—30° К. Эта величина может быть измерена, но большого практического значения не имеет. Бериллий, высокой и низкой чистоты, реагирует одинаково. Нагрев до 250° К производит быстрое и полное восстановление прежней теплопроводности, нарушенной облучением.

НЕКОТОРЫЕ ВИДЫ РАЗВИТИЯ ДИФФУЗНЫХ СЛОЕВ В БИНАРНЫХ СИСТЕМАХ

Кидсон Г. В.

Показано что применение первого закона Фика к многофазной диффузии в бинарных системах приводит к простым но точным формулам в зависимости от времени и температуры для междуповерхностного положения. Были изучены двухфазные и трехфазные системы

и результаты обобщены на системы в H -фаз. Рассмотрено несколько видов влияния температуры на скоростные константы. В особенности определены условия при которых фазы могут или не могут достигать ширины наблюдаемой в зоне диффузии.

ВЛИЯНИЕ ФАЗОВОЙ α - β -ТРАНСФОРМАЦИИ НА ДОМИНИРУЮЩУЮ ОРИЕНТАЦИЮ В α -УРАНЕ

Бютчер Б. Р. и Баверсток Д.

Исследованы при помощи дилатометрии, металлографии и рентгеновских лучей образцы катанных стержней урана после трансформации в различной степени в β -фазе при определенном градиенте температуры. Результаты показывают что изменение фазы сопровождается полосой

трансформации смешанных α - и β -фаз проходящей через каждый образец что степень уменьшения доминирующей ориентации находится в зависимости от степени трансформации. Предлагается механизм который представляет это явление.

КОРРОЗИЯ ГЕКСАФТОРИДОМ УРАНА

Часть 1.

МЕТОД ИЗУЧЕНИЯ КОРРОЗИИ

Диксмиер Ж., Хассон Р., Мараваль С. и Венсан Л. М.

Химические свойства гексафторида урана заставили усовершенствовать новые методы для изучения коррозии металлов этим газом. Процессы коррозии характеризуются реакциями между газовой безводной фазой и твердой фазой, что может быть сравниваемо с феноменами сухого окисления металлов. После краткого обзора методов измерений, употребляемых в этой области, авторы остановились на принципе прерывистого гравиметрического метода: образцы взвешиваются перед и после коррозии гексафторидом урана. Вместе с этим они подвергаются микрографическому экзамену.

Размеры образцов были выбраны таким образом чтобы отвечать оптимальным условиям для взвешивания на микровесах. Способы приготовления и состояние поверхности точно определены. Коррозия происходит в металлических трубках формы Н с прокладками, соединениями, клапанами и седлами также металлическими. Уплотнение устройства позволяет легко получить предварительную пустоту в 10^{-6} мм рт. ст. при температуре могущей достигнуть 400°C . После откачки в аппарат впускается гексафторид урана и который подвергается тройной перегонке. Затем трубки сохраняются в термостате. Каждая трубка имеет, на конце одного из своих ответвлений, приросток для конденсации который, благодаря охлаждению позволяет иметь запас гексафторида в твердом виде и под постоянным давлением газа.

Когда трубка берется для исследования, она снова откачивается чтобы удалить остаточный гексафторид. Затем она вскрывается с перчатками в непроницаемой камере с инертным газом и, чтобы избежать повреждений, образцы манипулируются без доступа воздуха. Образцы взвешиваются на микровесах и подвергаются микрографическому исследованию, которые заключаются в изучении морфологии осадка и позволяют, кроме того, выявить различные протофториды урана. При помощи постепенного удаления осадков, металлографическое исследование выявляет изображении коррозии, которые часто принимают форму морщин в швах зерен или вид микроточечной коррозии. Изучено развитие их глубины, которое подчинено, в зависимости от времени, закону параболического хода подобному для кривых сухого окисления. Предосторожности осуществленные для приготовления образцов и перегонки гексафторида дают хорошую воспроизводимость результатов. Чувствительность микровзвешиваний позволяет оценить образование слоистого фторида.

В заключение совокупность методов коррозии и измерений была выбрана наилучшая для удобного применения в технологии гексафторида урана и в то же время большой чувствительности позволяющей вышлать серийные испытания в большом масштабе. Все это позволяет удобно изучать многие переменные факторы, а именно: время, температура, давление итд.

ВЛИЯНИЕ РАЗМЕРОВ КРИСТАЛЛА НА КИНЕТИКУ ОКИСЛЕНИЯ UO_2

Авторы: Бельбек Б., Пиекарский К. и Перио П.

Мы попробовали, учитывая специфическую поверхность, уточнить механизм окисления UO_2 при низких температурах, природу и свойства мембранальных фаз в области О/У

между 2,3 и 2,4.

Результаты правильно подтверждают ранее предложенный ⁴⁾ механизм неравномерной диффузии.

ТЕРМИЧЕСКОЕ РАСШИРЕНИЕ МОНОКРИСТАЛЛОВ α -УРАНА

Ловелл Т Ллойд

Дилатометрическим методом было измерено термическое расширение монокристаллов α -урана в интервале $25-650^{\circ}\text{C}$. Были получены уравнения для линейного расширения (L) и объемного (V) в зависимости от температур ($t^{\circ}\text{C}$):

$$L_{[100]t} = L_{[100]0} \\ (1 + 23,53 \times 10^{-6}t + 13,74 \times 10^{-9}t^2 + 9,94 \times 10^{-12}t^3).$$

$$L_{[010]t} = L_{[010]0} \\ (1 + 1,16 \times 10^{-6}t - 9,43 \times 10^{-9}t^2 - 11,79 \times 10^{-12}t^3)$$

$$L_{[001]t} = L_{[001]0} \\ (1 + 19,38 \times 10^{-6}t + 21,58 \times 10^{-9}t^2 + 3,32 \times 10^{-12}t^3) \\ V_t = V_0 \\ (1 + 43,98 \times 10^{-6}t + 26,88 \times 10^{-9}t^2 + 1,00 \times 10^{-12}t^3).$$

Разные значения коэффициентов расширения полученные для плоскостей [010] и [001] дилатометрическим методом, которые сравнивались со значениями вычисленными из параметрических характеристик решетки определенных рентгенометрическим методом, приписываются упругим напряжениям в поликристаллических образцах.

САМОДИФФУЗИЯ В β -УРАНЕ

Ротман С. Дж., Грэй Жр., Хайг Дж. П. и Хэркнес А. Л.

Коэффициент самодиффузии в уране уменьшается на величину 150 когда кристаллическая структура урана переходит из кубической центрированной γ -фазы в сложную тетрагональную β -фазу. Даже при повышенной темпе-

ратуре графическое изображение $\log C$ в зависимости от X^2 представляется кривой, которая показывает что причиной самодиффузии является не только внутризеренная изотропная диффузия.

ДИФФУЗИЯ ЗОЛОТА В γ -УРАНЕ

Ротман С. Дж.

Диффузия золота в γ -уране была измерена при помощи радиоактивного индикатора применяя технику секционирования. Значения D_0

и энергии активации равны соответственно $4,86 \times 10^{-3}$ см²/сек и 30 400 кал/моль, они очень близки к значениям самодиффузии в γ -уране.

ВЛИЯНИЕ НАПРАВЛЕНИЯ И ТЕМПЕРАТУРЫ НА ХАРАКТЕР ДЕФОРМАЦИЙ В α -УРАНЕ

Тиг Р. О. и Оджилви Р. Е.

Изучалось скольжение в α -уране в плоскости {110}, при -196°C при помощи двухплоскостного анализа; оказалось что скольжение происходит в направлении $\langle 001 \rangle$. Приводятся некоторые данные позволяющие утверждать что механизм скольжения заключается в движении по двум направлениям $\langle 112 \rangle$ и сводится к общему сдвигу по направлению $\langle 001 \rangle$. Критическое срезающее напряжение при скольжении по {010} $\langle 100 \rangle$ и при поперечном скольжении существенно возрастает, при низких температурах, по сравнению с другими механизмами скольжения. Прямое подтверждение скольжения

в направлении $\langle 100 \rangle$ было получено методом "исчезающих следов". Наблюдались полосы сбросов разного вида на плоскости (100). Наблюдались полосы не шире 5 мк. и высотой до 100 мк; кроме того был обнаружен новый механизм микросбросов. Ось вращения сбросов направлена по $\langle 001 \rangle$. Наблюдалось двойникование по плоскостям {130}, {176}, и {172}, причем плоскость {130} оказалась гораздо более активной и при -196°C , и при 350°C . Зоны скольжений в образцах соответствовали предсказанным теоретически. Других плоскостей двойникования не наблюдалось.

ПРОЧНОСТЬ МЕТАЛЛИЧЕСКИХ ПОКРЫТИЙ НА ГРАФИТЕ ПРИ ВЫСОКИХ ТЕМПЕРАТУРАХ

Бокрос Дж. С.

Изучались многие металлы и сплавы в смысле возможности их применения в виде покрытий на графите, в гелиевой атмосфере, при температурах до 1010°C . Было показано что жаропрочные сплавы на основе никеля, различные сорта нержавеющей стали и молибден быстро обуглероживались при температурах выше 816°C . В случае ниобия, очень активного металла, полученные данные указ-

ывают на необходимость поддерживать высокую чистоту гелия, чтобы избежать появления хрупкости.

Из всех опробованных сплавов самым перспективным для жаропрочных покрытий графита является никель-медный сплав. Данные по старению покрытий указывают что монель имеет большую сопротивляемость графитизации, чем никель.

АНИЗОТРОПИЯ ПЛАСТИЧЕСКОЙ ДЕФОРМАЦИИ И РАЗРУШЕНИЕ БЕРИЛЛИЯ

Грин А. П. и Савкилл Дж.

Изучена зависимость между анизотропией пластической деформации и тягучестью бериллия при температурах от 20 до 400°C . Рассматриваются характеристики пластической деформации и разрушения монокристаллов. Они заключаются в скольжении по основным плоскостям, образовании плоскостей перегиба, зарождение и развитие разрушения. Делается сравнение с разрушением по основным плоскостям,

которое наблюдается в цинке. Применяется для бериллия теория Штроха для разрушений такого рода. Обсуждается также деформация и разрушение поликристаллического и предлагается качественное объяснение для роста тягучести в зависимости от температуры. Кратко излагаются возможные средства для улучшения тягучести.